# The Assessment of a Number of Different Meso-porous Silica Nanoparticles for Delivery of Chemotherapeutics and siRNAs


*A thesis submitted for the degree of*
*DPhil in Engineering Science*

**Xinyue HUANG**

Supervisors: Dr. Helen Townley, Professor Ian P Thompson

Hertford College

Department of Engineering Science

University of Oxford

October 2015

# Abstract

Mesoporous silica nanoparticles (MSNPs) are of interest as effective drug carriers because of their controllable physical properties and biomedical compatibilities. A number of different MSNPs have been assessed for their suitability as intracellular nano-scale carriers of chemotherapeutics and siRNAs.

Four morphologically different MSNPs were synthesised after optimisation of existing protocols. The MSNPs were characterised with regards to size, porosity, surface area, surface charge, cytotoxicity and biodegradability. Their suitability as drug carrier *in vivo* was examined in terms of cargo loading, ability to be endocytosed by cells and take advantage of the Enhanced Permeability and Retention effect.

The loading and unloading profiles of two model compounds and a potential chemotherapeutic agent LY294002 were investigated. The release behaviours of the cargoes were altered by modifying the particle surface with polymeric capping agents. In addition, the particles were capped with pH-sensitive molecules, and the release behaviour in low pH was assessed since tumours are known to have an acidic microenvironment.

The physiological function of LY294002 on selected cancer cell lines was also studied. LY294002 was shown to affect the proliferation, survival, and metabolism of selected cells under different oxidative conditions. The effect differed when cells were under oxidative stress and/or glucose stress. Cell viability was also compromised after treatment with LY294002 loaded MSNPs. The sensitivity to each LY294002 loaded MSNP differed between cell lines.

Engulfment and cell motility 1 (ELMO1) - targeted siRNA was also delivered using MSNPs to two distinct rhabdomyosarcoma lines. Significant knock-down of the ELMO1 gene was shown, illustrating that MSNPs could be efficient transfection agents for siRNA. In particular, the two MSNP candidates were shown to be significantly better than a current commercial product.

A co-delivery system for LY294002 and ELMO1-targeted siRNA was established. Cell viability and ELMO1 expression were both suppressed after treatment with the co-delivery system.

# Table of Contents

# Abbreviation

| | |
|---|---|
| ABC | ATP-binding cassette |
| ACTB | Beta (β) - actin |
| ADP | Adenosine diphosphate |
| AIBA | 2,2'-Azobis (2-Methylpropionamide) Dihydrochloride |
| Akt | Alpha serine/threonine-protein kinase |
| Amplex Red | 10-acetyl-3,7-dihydroxyphenoxazine |
| approx. | Approximately |
| ARMS | Alveolar rhabdomyosarcoma |
| ATCC | American Type Culture Collection |
| ATP | Adenosine triphosphate |
| BAD | B-cell lymphoma -2-associated death promoter |
| BCA assay | Bicinchoninic acid assay |
| BET theory | Brunauer, Emmett, and Teller theory based on multilayer gas adsorption hypothesis |
| BJH method | Barrett-Joyner-Halenda method; or pore size calculation method based on multilayer gas adsorption theory |
| BMSNP | Blackberry-like Mesoporous Silica Nanoparticle |
| CMSNP | Chrysanthemum-like mesoporous silica nanoparticles |
| CNT | Carbon Nanotube |
| CTAB | Hexadecyl-Trimethylammonium Bromide |
| CV | Crystal Violet |
| $ddH_2O$ | Double-distilled water |
| DMEM | Dulbecco's Modified Eagle Medium |
| DMF | Dimethylformamide |
| DMSO | Dimethyl sulfoxide |
| DNA | Deoxyribonucleic acid |
| duo@BMSNP | ELMO1-targeted siRNA and LY294002 loaded PEI-BMSNP |
| duo@CMSNP | ELMO1-targeted siRNA and LY294002 loaded PEI-CMSNP |
| duo@HMSNP | ELMO1-targeted siRNA and LY294002 loaded PEI-HMSNP |
| duo@MSNP | ELMO1-targeted siRNA and LY294002 loaded PEI-MSNP |
| duo@WMSNP | ELMO1-targeted siRNA and LY294002 loaded PEI-WMSNP |
| ECAR | Extracellular acidification rate |

| | |
|---|---|
| EDTA | Ethylenediaminetetraacetic acid |
| EDX | Energy Dispersive X-Ray Spectroscopy |
| e.g. | *exempli gratia,* for example |
| ELMO1 | Engulfment and cell motility 1 |
| ELMO1@BMSNP | ELMO1-targeted siRNA loaded PEI-BMSNP |
| ELMO1@CMSNP | ELMO1-targeted siRNA loaded PEI-CMSNP |
| ELMO1@HMSNP | ELMO1-targeted siRNA loaded PEI-HMSNP |
| ELMO1@MSNP | ELMO1-targeted siRNA loaded PEI-MSNP |
| ELMO1@WMSNP | ELMO1-targeted siRNA loaded PEI-WMSNP |
| ELMO1@LY@HMSNP | ELMO1-targeted siRNA and LY294002 loaded PEI-HMSNP |
| ELMO1@LY@WMSNP | ELMO1-targeted siRNA and LY294002 loaded PEI-WMSNP |
| EMA | European Medicines Agency |
| Emi. | Emission wavelength |
| EPR effect | Enhanced Permeability and Retention Effect |
| ERMS | Embryonal rhabdomyosarcoma |
| EtOH | Ethanol |
| Ex. | Excitation wavelength |
| FBS | Fetal bovine serum |
| FDA | Food and Drug Administration, United States |
| FFT | Fast Fourier transform |
| FITC | Fluorescein isothiocyanate |
| FOXOs | Forkhead box proteins |
| GFP | Green fluorescent protein |
| GLUT4 | Glucose transporter 4 |
| HA | Hyaluronic acid |
| HAADF-STEM | High angle annular dark field scanning transmission electron microscopy |
| HMSNP | Hexagonal Symmetric Mesoporous Silica Nanoparticle |
| i.e. | *id est*, that is |
| keV | Kilo-electron volt; $10^3$ electron volt |
| kx | 1000 times |
| LbL | Layer-by-Layer |

| | |
|---|---|
| LY | LY294002 |
| LY294002 | 2-Morpholin-4-yl-8-phenylchromen-4-one |
| [LY294002] | Concentration of LY294002 in solution |
| LY@BMSNP | LY294002 loaded BMSNP |
| LY@CMSNP | LY294002 loaded CMSNP |
| LY@HMSNP | LY294002 loaded HMSNP |
| LY@MSNP | LY294002 loaded MSNP |
| LY@SNP | LY294002 loaded SNP |
| LY@WMSNP | LY294002 loaded WMSNP |
| mg/mL | Milligram per millilitre |
| M | Mole per litre |
| mM | Millimole per litre |
| MRI | Magnetic resonance imaging |
| μm | micrometre; $10^{-6}$ metre |
| μM | Micromole per litre |
| μL | Microlitre |
| MDR | Multi-drug resistance |
| min | minute / minutes |
| MSNP | Mesoporous Silica Nano-Particle |
| MTT | 3-(4,5-dimethylthiazol-2-yl)-2,5-diphenyltetrazolium bromide |
| NADPH | Nicotinamide adenine dinucleotide phosphate |
| nm | nanometre; $10^{-9}$ metre |
| nM | nano-mole per litre; $10^{-9}$ mole per litre |
| NOX | Nicotinamide adenine dinucleotide phosphate-oxidase |
| NP | Nanoparticle |
| n.s. | not significant |
| OCR | Oxygen consumption rate |
| OXPHOS | Oxidative phosphorylation |
| PAGE | Polyacrylamide gel electrophoresis |
| PAH | Polycyclic aromatic hydrocarbons |
| pAkt-ser473 | Akt phosphorylated at serine 473 |
| PBS | Phosphate buffered saline |
| PCR | Polymerase chain reaction |
| PDI | Polydispersity Index |

| | |
|---|---|
| PDK1 | phosphoinositide-dependent kinase 1 |
| PEG | Polyethylene glycol |
| PEI | Polyethylenimine |
| PEI-BMSNP | PEI capped BMSNP |
| PEI-CMSNP | PEI capped CMSNP |
| PEI-HMSNP | PEI capped HMSNP |
| PEI-MSNP | PEI capped MSNP |
| PEI-WMSNP | PEI capped WMSNP |
| PI | Phosphatidylinositol |
| PI3K | Phosphatidylinositol 3-kinase |
| PL | poly-(l-lysine) |
| PMPC-PDPA | Poly(2-(methacryloyloxy)ethyl phosphorylcholine)–poly(2-(diisopropylamino)ethyl methacrylate) |
| PMPC-ELMO1@HMSNP | PMPC-PDPA coated ELMO1@HMSNP |
| PMPC-ELMO1@LY@HMSNP | PMPC-PDPA coated ELMO1@LY@HMSNP |
| PMPC-ELMO1@LY@WMSNP | PMPC-PDPA coated ELMO1@LY@WMSNP |
| PMPC-ELMO1@WMSNP | PMPC-PDPA coated ELMO1@WMSNP |
| PS | Polystyrene |
| PSS | Polystyrene sulfonate |
| qPCR | Quantitative real-time PCR |
| RMS | Rhabdomyosarcoma |
| RNA | Ribonucleic acid |
| RNase | Ribonuclease |
| RNAi | RNA interference |
| ROS | Reactive oxygen species |
| RT | Room temperature |
| RT-PCR | Reverse transcription polymerase chain reaction |
| SDS | Sodium dodecyl sulfate |
| siRNA | small-interference RNA |
| siRNA@HMSNP | siRNA loaded PEI-HMSNP |

| | |
|---|---|
| siRNA@MSNP | siRNA loaded PEI-MSNP |
| siRNA@WMSNP | siRNA loaded PEI-WMSNP |
| SNP | Non-porous Silica Nano-Particle |
| SOD | Superoxide dismutase |
| STEM | Scanning transmission electron microscopy |
| TCA cycle | Tricarboxylic acid cycle |
| TEM | Transmission Electron Microscopy |
| TEOS | Tetraethyl orthosilicate |
| THMP | 3-(Trihydroxysilyl) propyl methylphosphonate |
| TR-F | Time-Resolved Fluorescence |
| VEGF | Vascular endothelial growth factor |
| U87-MG-cGFP cells | GFP expressing U87-MG cells |
| WMSNP | Wrinkle-structured mesoporous silica nanoparticle |

# List of Figures

**Appendix**

# List of Tables

# Acknowledgements

First, I would like to express my deepest thank to my supervisor, Dr. Helen Townley for giving me all the opportunities, advices and instruction, and for helping me to get through many difficulties I met throughout my DPhil years. She has always delighted me with the knowledge, vison and positive attitude. It is my great fortune to have her as my supervisor. I thank Prof. Ian Thompson for giving me so many supports and advices on both academic and personal matters. I also would like to acknowledge Dr. Karl Morten for his kindly help in biomedical field, especially in experiments and data interpretation about cell metabolism.

I want to give my appreciation to every collaborator whom I worked with. I particularly wish to thank Dr. Neil Young for the TEM training, data mining and conference opportunity he provides; thank Dr. Ben Pilgrim and Prof. Tim Donohoe for providing and analysing LY294002; thank Prof. Giuseppe Battaglia for providing PMPC-PDPA co-polymer. I am also very appreciate to all the technicians I worked with, particularly Greg Cook and Richard Turner.

I also would like to thank the Williams fund for partially funding this research.

Thank all my colleagues in my laboratories for their encouraging, and for the fun we experienced together. I should have a harder time without them.

Finally, I would like to express my special thanks personally to my family. I would not have the chance to pursue science without their unconditional love, understanding and financial support. Particularly thanks to my husband, Xi Chen, for the company, encouragement and love. I would also appreciate my lovely friends. They always cheer me up when I feel hesitated and tired.

# Publications

Parts of Chapter 2 and Chapter 4 have been published on:

Xinyue Huang, Neil P Young and Helen E Townley. **Characterization and Comparison of Mesoporous Silica Particles for Optimized Drug Delivery**. *Nano-materials and Nanotechnology*, 1, 2014.

Parts of Chapter 3 have been under review:

Xinyue Huang, Michelle Potter, Ben S. Pilgrim, Ruchuta Ardkhean, Mikail A. Kabeshov, Tim Claridge, Matt Wiseman, Karl Morten, Timothy J. Donohoe, Helen E Townley. **The efficacy of the Quercetin analogue LY294002 is related to the bioenergetic profiles of the test cells *in vitro***.2015

Parts of Chapter 5 are under preparation for publication:

Xinyue Huang, Helen E Townley. **Knockdown of ELMO1 in paediatric Rhabdomyosarcoma cells by nanoparticle mediated siRNA delivery**

Also co-authored:

Natalia Barkalina, Celine Jones, Junaid Kashir, Siobhan Coote, Xinyue Huang, Rachel Morrison, Helen Townley, Kevin Coward. **Effects of mesoporous silica nanoparticles upon the function of mammalian sperm *in vitro***; *Nanomedicine*. 2014

# Chapter 1

# Introduction

Cancer, a group of diseases caused by uncontrollably proliferating genetically mutated cells, has become one of the major causes of death that claims more than 8,000,000 lives annually in the 21$^{st}$ century (Murphy *et al.*, 2013). A considerable number of studies and developments have focused on the understanding, diagnosis and treatment of cancers. However, the mortality of cancer remains high due to the complexity of cancer and the limitations in the current approaches to deliver anti-cancer agents.

Nanomaterials provide a new means to overcome those existing limitations and enable a more efficient delivery of chemotherapeutics and other anti-cancer agents to tumour sites without causing severe damage to healthy tissues. Many of the unique physical and chemical properties of nanoparticles are ideal for chemotherapeutic carriers and are un-matched by normal bulk materials.

## 1.1 NANOPARTICLES IN INTRACELLULAR DRUG DELIVERY

### 1.1.1 The unique properties of nanoparticles

Nanoparticles are small. The officially accepted definition of nanoparticles is that they are particles with a size of 1 to 100 nm on at least one dimension (Auffan *et al.*, 2009). Their extremely small scale helps them to overcome many biological barriers in human body, and is especially beneficial for chemotherapeutics delivery into solid tumours due to the Enhanced Permeability and Retention effect (EPR effect).

The specific surface area of nano-particulates is enormous and the activity of the particles' surface is always much higher than their bulk form counterpart. Such unique surface properties not only enable a high capacity for cargo molecule adsorption, but also show a great potential for surface functionalisation. Functionalised nanoparticles could fulfil different purposes such as specific cell targeting, controlled release of cargo, and reduced cytotoxicity (Cho *et al.*, 2008).

Furthermore, many nanomaterials express unique physiochemical properties in the nano-scale that are distinctive from that in macro-scale. For example, the magnetic properties of iron oxide nanoparticles are different from their bulk form due to the quantum size effect and large surface area (Gupta and Gupta, 2005b).

### 1.1.2 The criteria of nanoparticles as anti-cancer agent carrier for intracellular delivery

As the development of nanotechnology, the synthesis and manipulation approaches of nanoparticles have been greatly improved. Therefore, many physical and/or chemical properties, such as size, shape, aspect ratio, morphology, surface charge, composition and

porosity, are controllable to achieve different goals or fit the function of different applications. A successful drug nano-carrier for *in vivo* delivery of anti-cancer agents requires the following criteria to be met (Thakor and Gambhir, 2013):

1) Biocompatibility and biostability (Buzea *et al.*, 2007): Such a nano-scaled drug carrier should cause no or little harm to healthy tissue before and after the cargo unloading. The particle-drug complex should be relatively stable in body fluid without rapid disassembly or vast premature cargo release;

2) Particle size between approx. 50 nm to 200 nm (Gaumet *et al.*, 2008): such a nanoparticle should be able to fenestrate blood vessels *in vivo* without unnecessary accumulation in healthy tissues. Also, the particle within such a size range is beneficial for the EPR effect;

3) Capability to encapsulate, conjugate or absorb cargo molecules (Davis *et al.*, 2008): such a nanoparticle should be porous or hollow in order to encapsulate cargo molecules into the particle, or present an active or functionalisible surface to conjugate or absorb guest molecules on the surface;

4) Capability to release or detach loaded molecules (De Jong and Borm, 2008): such a nanoparticle should be able to release the payload in a desired environment, e.g. only at tumour sites. The release can be triggered by a diffusion of guest molecules, the degradation of nanoparticles, or the disassembly of the coatings.

### 1.1.3 Existing nano-scaled drug delivery platforms

A number of different types of nanoparticle drug delivery systems have been investigated to meet those criteria in recent years. Some of them have achieved marvellous success.

Such nano-scaled drug delivery platforms can be broadly classified as liposomes, dendrimers, polyelectrolyte nanocapsules, virosomes and inorganic nanoparticles.

### *1.1.3.1 Liposomes*

Liposomes are closed lipid nano-spherical drug carriers, and can be functionalised with a variety of chemical groups on the surface. They are first introduced in 1965 and have become one of the most important and successful drug nano-carriers (Bangham *et al.*, 1965, Allen and Cullis, 2013).

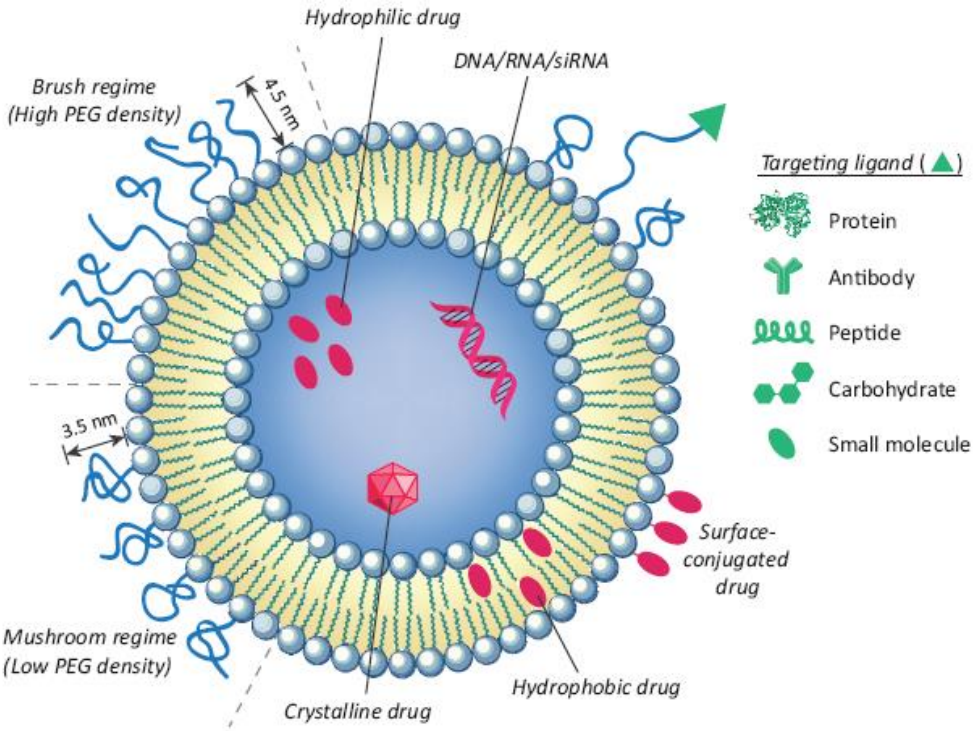


Figure 1.1 Schematic illustrations of a liposome in drug delivery [Image taken from (Çağdaş *et al.*, 2014)]

The functionalisible lipid bilayers and the large cavity enable liposomes to carry a variety of drugs: cargo molecules can be either encapsulated in the cavity, conjugated on the lipid surface, or entrapped within the lipid bilayers (various eligible cargo molecules were coloured in red in Figure 1.1). Therefore, liposomes are eligible to deliver a wide range

of anti-cancer agents or cancer diagnostic agents, including many hydrophobic chemotherapeutics, peptides, antibodies, and genetic therapeutics (such as DNA plasmid and siRNA) (Buyens *et al.*, 2012).

The surface of liposomes is easily functionalised with a wide range of molecules. Many polymeric coatings, such as polyethylene glycol (PEG, coloured in blue in Figure 1.1), can increase the biocompatibility of liposomes, and reduce systemic clearance and immune reactions (van Etten *et al.*, 1998). With different chain structures and molecular weight, the coatings can also manipulate the rigidness and cellular uptake of liposomes. Liposomes are also frequently functionalised with many types of targeting ligands (coloured in green in Figure 1.1), such as folate receptors, enabling a target delivery of their cargo molecules.

Moreover, the outer size of liposomes is largely controllable by tuning the synthesis methods. Therefore the size of a liposomal drug delivery system can be optimised to take advantage of the EPR effect (Gabizon and Papahadjopoulos, 1988). With an optimal size and biocompatible surface, liposomes can be easily accumulated in tumours without cell membrane penetration and physical damage to target cells.

These properties of liposomes lead to success in liposome development and applications. They have been explored in the clinic for applications such as imaging, diagnostics agents, vaccine, gene therapeutics and other advanced anti-cancer agents. In 2014, there were more than 50 liposomal pharmaceutical applications that have been approved by the FDA and EMA or in clinical trials (Fan and Zhang, 2013).

Despite the great success of liposomes development, the applications are still limited due to the remained problems. Liposomes can be hydrolysed, oxidized, or even dissolved easily in normal physiological environments, leading to drug leakage and delivery failure.

Liposomes also have poor extravasation into human tissues with tight endothelial junctions, resulting in poor delivery of drug targeting to those regions. Poor reproducibility and low drug entrapment efficiency has also limited the further development of liposomes.

### *1.1.3.2 Dendrimers*

Dendrimers are dendritic-branched polymeric macromolecules.

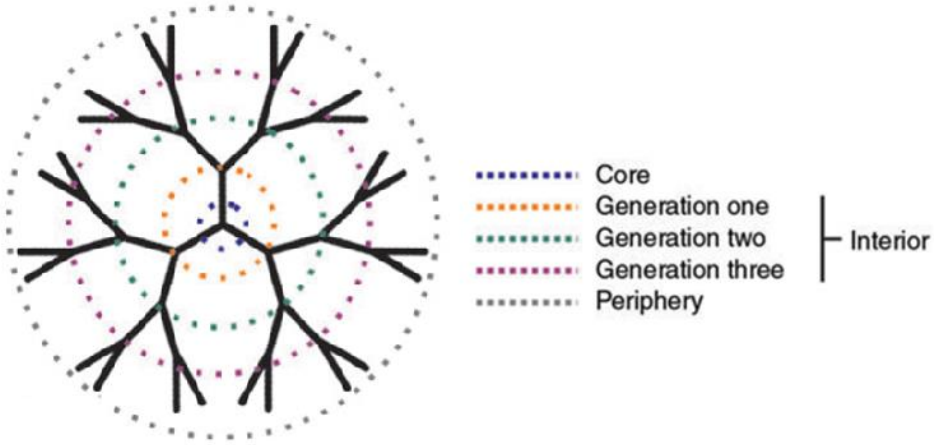


Figure 1.2 Schematic illustrations of a dendrimer. The coloured dot lines identify the various key regions of a dendrimer. [Image modified from (Lee *et al.*, 2005)]

Dendrimers possess a very unique tree-like hyperbranched architecture, leading to distinctive physical and chemical properties: (1) A large enclosed hydrophobic cavity and a functionalisible hydrophilic periphery makes dendrimers valid candidates as drug nanocarriers for a wide range of molecules, from DNA to small hydrophobic anti-cancer drug; (2) The size and shape of dendrimers is easily determined during synthesis, hence the size can be optimised to maximise the EPR effect; (3) The synthesised dendrimers are highly monodispersed with unparalleled uniformity; (4) The exposed terminal groups (periphery) of a dendrimer are multivalent and reactive, and can be easily modified with

a variety of targeting ligands and functional groups (Esfand and Tomalia, 2001, Xu *et al.*, 2014).

Dendrimers can be used as solubility enhancers for certain hydrophobic drugs (Gupta *et al.*, 2007), cellular uptake enhancers (Kitchens *et al.*, 2005), biosensors (Algarra *et al.*, 2013, Karadag *et al.*, 2013, Staneva *et al.*, 2012), and functional carriers for many chemotherapeutics and gene therapeutics (Biswas *et al.*, 2013, Cheng *et al.*, 2008b, Kesharwani *et al.*, 2014).

There are, however, a number of issues with dendrimer use. One of the most critical but challenging problems concerns biosafety. The cytotoxicity of dendrimers is highly dependent on the chemical composition, generations, concentrations, surface groups, and also cell line. Although many attempts have been tried to increase the biocompatibility (including surface modification), it has been shown in mammalian cells, in laboratory and in animal models (Wu *et al.*, 2015, Roberts *et al.*, 1996) to remain a challenge. Another major problem with dendritic applications is the low drug encapsulation efficiency due to the current loading methods. Some research has focused on overcoming this limitation by attempting to attach the guest molecules onto the surface of dendrimers for delivery, but this method would invariably induce an unfavourable immune reaction.

#### *1.1.3.3 Hollow nanocapsules*

Nanocapsules are polymeric hollow nanoparticles with a relatively thin shell and large encapsulation cavity. The most studied ones are made from Layer-by-Layer (LbL technique: alternatively capping oppositely charged molecules on the surface of each other)

assembled polyelectrolytes (Figure 1.3a) and self-assembled amphiphilic co-polymersome (Figure 1.3b) (Ariga *et al.*, 2007).

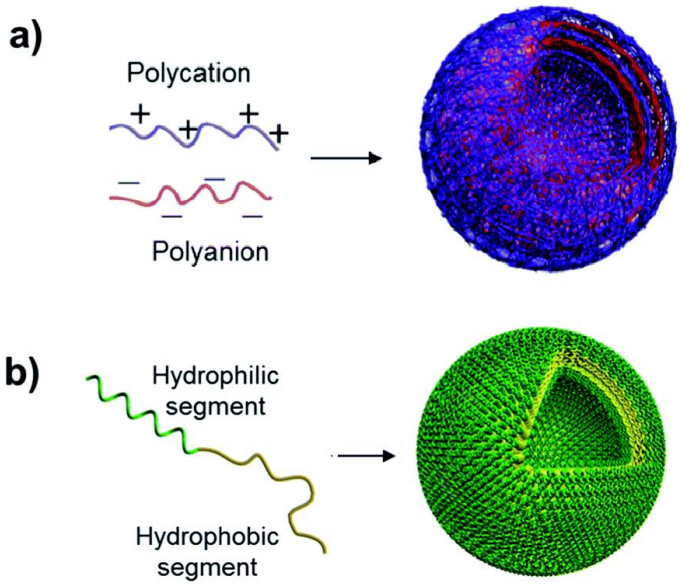


Figure 1.3 Schematic illustrations of organic hollow nanocapsules [Image modified from (Jang *et al.*, 2014)]: a) polyelectrolyte nanocapsule assembled with LbL technique; b) polymersome nanocapsule self-assembled from amphiphilic co-polymers

Cargo molecules are able to be loaded within nanocapsules *via* three different routes: in the inner cavity, entrapped between the shell layers, or conjugated on the outer surface. Furthermore, the outer dimension and surface properties of hollow nanocapsules are easily controlled by changing the composition and layers of polymers absorbed. The biocompatibility can be enhanced through further surface modification. Target ligands may also be onto the surface of nanocapsules, offering opportunities for targeted delivery.

#### *1.1.3.4 Virus-based nano-carriers*

Virosomes are attractive for drug delivery, due to the unique properties to overcome major biological barriers it possesses. A virosome is a protein shell of a deactivated virus

(has the viral genetic materials removed), which is commonly a hollow nanoparticle consisting of hundreds protein molecules (Figure 1.4). The size of virosomes varies from 10 nm to over 1000 nm due to the different scaffold virus species. The shape of virosomes is also very different from each other for the same reason.

Figure 1.4 Schematic illustrations of a spherical virosomes [Image taken from (Crisci *et al.*, 2013)]

A great advantage of virosomes is their ability to targeting cells and bypassing many different biological barriers (e.g. tight endothelial junction, blood brain barrier) due to the viral nature of virosomes which is unparalleled to other drug nano-carriers. Moreover, virosomes are claimed to be broadly applicable to a number of drugs, including siRNA and peptides which are difficult to deliver using common existing approach. A small number of virosomes have been approved by the FDA or in clinical trial phases.

However, the biosafety of virosomes is still a major limitation. Although a number of studies have concluded that many virosomes are biocompatible with low cytotoxicity (Kalra *et al.*, 2013, Huckriede *et al.*, 2003), the immunogenicity still exists and limits the development and application of virosomes (Yoo *et al.*, 2011).

#### *1.1.3.5 Inorganic nanomaterials*

Porous or hollow inorganic nanomaterials are another class of popular drug carrier. Compared to organic drug vehicles, they are relatively more reproducible. Furthermore, some unique physiochemical properties of many inorganic nanomaterials are unparalleled to other drug carriers. Size and porosity of these inorganic nanomaterials is normally controllable during synthesis, and their cytotoxicity is either minor, or can be eliminated by functionalising with biocompatible molecules.

Despite the success in research and the great potential, inorganic drug nano-carriers are still mostly under investigation and research in laboratory. Compared to well-established organic nano-carriers platform, inorganic drug nano-carriers are often challenged with regards to biocompatibility and clearance route. In 2012, only one inorganic nanoparticle (ultra-small silica quantum dot) has been approved by the FDA, and two cases are in clinical trial phase two (Bradbury *et al.*, 2013).

The most studied and successful inorganic candidates (noble metals, titanium dioxide ($TiO_2$), silica ($SiO_2$), iron oxide ($Fe_2O_3$), zinc oxide (ZnO) and carbon nanotubes) are discussed in further detail below.

##### 1.1.3.5.1 Noble metal based drug carriers

Noble metal nanoparticles (e.g. gold, silver, platinum) have their own unique virtues in drug delivery (Bhattacharya and Mukherjee, 2008).

Gold nanoparticles are the most well studied of the noble metal nanomaterials. They are biocompatible and relatively easy to synthesize with a tunable size and shape. More im-

portantly, gold nanoparticles are able to form strong bonds with thiols and amine groups which can be used for functionalization and targeted delivery. By virtue of the strong bond to amine group, gold nanoparticles can easily bind to proteins which present cysteine or lysine residue.

Silver is famed for its antibacterial property and therefore is beneficial in anti-inflammation treatment. It has been found that the loading of certain anti-infection compounds such as cerium nitrate in silver nanoparticles could exploit the antibacterial property of silver and synergistically enhance the effectiveness of the drug (Saha *et al.*, 2014, Franci *et al.*, 2015).

#### 1.1.3.5.2 Iron oxide based drug carriers

The synthesis and size / shape manipulation of iron oxide has been well established over the last 20 years and may now be fabricated at low cost. The magnetic properties of such nanoparticle can be simply altered during the synthesis. By virtue of the quantum size effects and the large surface area of iron oxide nanoparticles, every particle can be considered as a single magnetic domain and exhibits superparamagnetic properties which are not only useful in biomedical imaging, but also in targeted drug delivery.

#### 1.1.3.5.3 Titanium dioxide based drug carriers

$TiO_2$ nanoparticles are biocompatible and have been proven to be harmless to normal cells *in vitro* and *in vivo* (Bernard *et al.*, 1990). One of the most unique properties of $TiO_2$ is photocatalysis under UV. The energy band gap within the $TiO_2$ crystalline structure (especially in the anatase form) is small and comparable to the energy preserved in

UV photons. After UV excitation, surface electrons in $TiO_2$ nanoparticles can be excited and active electron holes are created. The excited electrons and active electron holes quickly migrate, combine with each other or react with environmental oxygen and water, leading to the generation of reactive oxygen species (ROS). This photocatalytic phenomenon enables $TiO_2$ nanoparticles to induce irreparable oxidative damage to unfavourable micro-organisms and/or cancer cells specifically after activation with UV (Kubota *et al.*, 1994).

However, due to the limited research into $TiO_2$ nanoparticle synthesis methods, it is still challenging to manipulate the size, shape, crystalline structure and porosity of $TiO_2$ nanoparticle. Thus, $TiO_2$ nanoparticles synthesised by the current available methods always exhibit a low drug loading capacity and limited surface functionalisation (Devanand Venkatasubbu *et al.*, 2013).

#### 1.1.3.5.4 Zinc oxide based drug carriers

Cytotoxicity of ZnO materials have been shown to be size-dependent, but the cytotoxicity can be easily tuned and limited due to the controllable size and morphology. The drug loading capacity may also be large and controllable.

ZnO nanoparticles also possess a unique pH-dependent surface charge which can be beneficial in surface modification and targeted delivery: ZnO nanoparticles exhibit a negatively charged surface at very high pH and a positively charged surface at a lower pH (lower than 9). Thus ZnO is strongly positively charged under physiological conditions which assists nanoparticle attachment onto cells, and cellular uptake due to the negatively charged phospholipids of cell membrane (Degen and Kosec, 2000).

Like $TiO_2$, ZnO is also photocatalytic, and can induce the production of ROS under the excitation of certain wavelengths of visible and UV light (Li and Haneda, 2003). The produced ROS can induce oxidative cell damage and subsequently cell death. The photocatalytic properties of ZnO nanoparticle can be further enhanced by doping with transition metal ions such as $Ni^{2+}$ and $Fe^{3+}$ (Rasmussen *et al.*, 2010).

However, ZnO nanoparticles exhibit a much higher cytotoxicity to cells compared to most drug nano-vehicles (Wang *et al.*, 2009a). It was found that the toxicity of ZnO nanoparticle is size-dependent, and that smaller nanoparticles exhibiting greater toxicity (Guo *et al.*, 2008). Considered as a drug carrier, ZnO nanoparticle may be used to deliver chemotherapeutics after functionalisation, resulting in an enhanced cancer cell killing efficiency. In this regard, the surface modification of ZnO nanoparticle is essential to rendering them benign to normal cells while still retaining their cancer targeting and killing properties.

#### 1.1.3.5.5 Carbon nanotube (CNT) based drug carriers

CNTs are allotropes of carbon, a class of nanomaterials made of graphite in a cylindrical structure. Aside from being a potent structural or semiconductor materials in engineering, CNTs (including single-wall CNTs and multi-wall CNTs) are also considered to be a valid drug carriers by virtue of their large surface area, functionalizable surface, low cytotoxicity and tunable size (He *et al.*, 2013, Ali-Boucetta *et al.*, 2011).

Due to their unique structure, large surface area, and electronic structure, a large variety of payloads can be conjugated or encapsulated on/into CNTs, including anti-cancer drugs, gene therapeutics, target ligands, peptides and antibodies (Jain, 2012, Shankar *et al.*,

2014, Kamalha *et al.*, 2012). CNTs have been found to efficiently deliver those cargo molecules to different tissues (Chahine *et al.*, 2014, Newman *et al.*, 2013).

The size of CNTs is controllable such that the length (size) can be easily tuned from < 10 nm to the macroscale (Wang *et al.*, 2009b). The surface of CNTs can be functionalised using covalent or non-covalent (such as electrical interaction) modification. Particularly, CNTs are able to deliver cargo molecules to specific aims *in vivo* when functionalised with environmental-stimuli materials and targeting ligands (Mittal, 2011).

Although the potential of CNT-based nanomaterials is often claimed to be limitless, there are currently few application where CNTs would be used as a drug carrier due to the high cost and difficulty in reproducible synthesis.

#### 1.1.3.5.6 Silica-based drug carriers

Following the development of bulk mesoporous silica materials in 1990 (Yanagisawa *et al.*, 1990), a number of studies have focused on the potential of this materials in many areas, such as catalyst chemistry, chemical adsorption, imaging, sensors, biomedical applications. Mesoporous silica in nanoparticle form was first introduced in 1997, and in the following years the synthesis methods and applications have been further developed.

To date, all published synthesis methods for the mesoporous material have been using a bottom-up strategy: MSNPs are produced from a sol-gel system with removable templates. During a synthesis process, many physical properties of MSNPs can be easily controlled by manipulating the conditions of the sol-gel system (see Chapter 2.1.2 for further details). For example, the outer dimension of MSNPs can be controlled by chang-

ing the composition of the sol-gel system and/or by controlling the aging time of silica condensation (Suteewong *et al.*, 2010, Moon and Lee, 2012, Nandiyanto *et al.*, 2009). Many synthesis routes have been well-established and proven to be effective, flexible and reproducible, but despite this success, a few limitations remain. The structure-directing templates (often surfactant molecules) play an important role in guiding silica condensation and porous structure formation, yet the choice of such templates is very limited in current protocols. Furthermore, the pore size is only controllable in a small range due to the restrained choices of the templates, leading to further process when attempted to achieve larger pores. In addition, the most commonly used ones (e.g. quaternary ammonium surfactant molecules) all show cytotoxicity and/or immunogenicity.

Since 2001, MSNPs have attracted attention as multifunctional drug delivery candidates due to their well-established synthesis methods, high biocompatibility, low cost, high drug loading capacity, controllable size and porosity, and functionalizable surface (Vallet-Regi *et al.*, 2001). MSNPs have been reported to be safe in the body after short term incubation and show high biocompatibility and low allergenicity (Mamaeva *et al.*, 2011a, Hudson *et al.*, 2008, Lin and Haynes, 2009, Trewyn *et al.*, 2008, Lu *et al.*, 2010). MSNPs can be taken up by cells, mainly through endocytosis, without damaging healthy tissue or inducing inflammation (Chu *et al.*, 2011, Akbar *et al.*, 2011).

However, it must be considered that the biocompatibility of MSNPs will be affected by a number of factors such as the particle concentration, size, morphology, surface functionalisation and chemical residue (Lin and Haynes, 2010). The biocompatibility of MSNPs may be further improved by modification of the surface with bio-friendly polymers, such as polyethylene glycol (PEG) (Rampazzo *et al.*, 2013).

A number of different approaches can be used in loading cargo molecules onto MSNPs. Drugs can be absorbed onto the outer surface or within the pores, attached on the functionalised surface or entrapped in pores (Figure 1.5). The different modes of drug loading enable the loading of MSNPs with a variety of cargo molecules that may be difficult to deliver *via* conventional routes. Examples of this include the use of MSNPs for the delivery of hydrophobic drugs such as camptothecin (loaded on the surface of MSNPs via adsorption), or nucleic acid delivery (carried by MSNPs via conjugation to a functionalised surface) (Lu *et al.*, 2007, Slowing *et al.*, 2008).

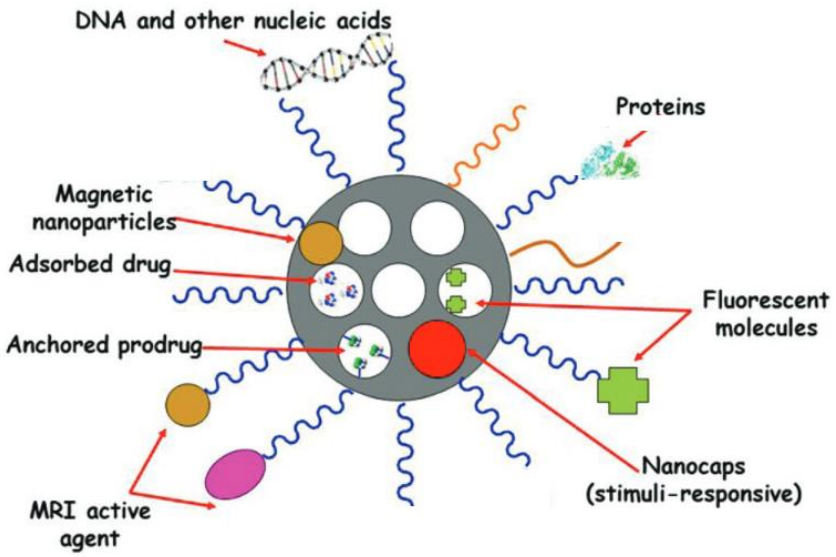


Figure 1.5 Schematic illustration of mesoporous silica nanoparticle as a drug nano-carrier. [Image modified (Colilla *et al.*, 2013)]. A large variety of drugs or other cargo molecules, such as nucleic acid, proteins, drugs, dyes and MRI active agents, can be absorbed, anchored or entrapped to the surface or within pores of MSNPs

The surface of MSNPs is easily functionalised with different chemical groups, a variety of molecules and even smaller nanoparticles (details in Chapter 2.1.3) *via* chemical modification, surface coating or grafting. For instance, the surface of MSNPs can be capped with multilayers of polyelectrolytes to prevent rapid premature drug release (for further details see Chapter 4.3.2).

From the first publication on the use of MSNPs in drug delivery, much of the research has focused on the potential of MSNPs for efficient delivery of anti-inflammatory drug molecules (Gonzalez *et al.*, 2013), chemotherapeutics (Vivero-Escoto *et al.*, 2010), proteins (Mamaeva *et al.*, 2011b) and gene therapeutics (Hom *et al.*, 2010). In particular, stimuli-responsive delivery and tumour-targeted delivery has attracted the most attention in the latest MSNP research (Croissant *et al.*, 2015, Yilmaz *et al.*, 2015, Cheng *et al.*, 2015). Many publications demonstrate promising results, and claim to be ready to move to pre-clinical studies.

Despite the large number of publications and research time spent developing MSNPs over the last ten years to date, there are no MSNPs-based drug delivery systems that have reached clinical trial stage; and even *in vivo* studies are few. Most research to date has been limited to the hexagonal-aligned MSNPs (often called MCM-41 in publications), a limited choice of drugs as cargo, and *in vitro* studies. It will be important for the field to research a wider variety of different MSNPs and drug candidates. *In vivo* studies will be mandatory before the synthesis of MSNPs can be industrialized for use as drug delivery carriers.

## 1.2 CANCER

Cancer is a group of severe diseases caused by cells growing abnormally and uncontrollably. Since the last century, cancer has become one of the major causes of death globally and is currently the third most frequent cause of death (Jemal *et al.*, 2008), particularly in the most developed countries, including the United Kingdom (American Cancer Society, 2011). In 2012, there were approximately 8.2 million deaths worldwide from cancer and

associated complications, including 161,823 cancer deaths in the UK, which accounted for more than 29 % of all deaths (Stewart and Wild, 2014).

In recent decades, many successful means of diagnosis and treatments have been developed. This success has resulted in a significant increase in the one-, five-, and ten-year survival rate (Cancer Research UK, 2013). For example, the one-year age-standardised net survival for all cancers combined in England and Wales has increased from approx. 50.0 % during 1971-1972 to 70.4% during 2010-2011 in all adults (Figure 1.6).

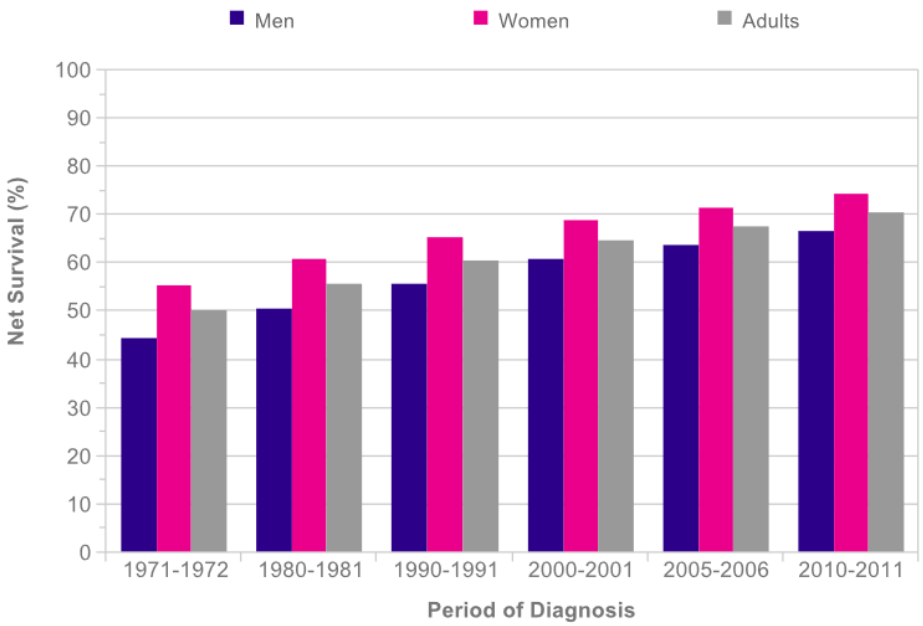


Figure 1.6 Age-standardised one-year net survival rate in England and Wales for all cancers excluding non-melanoma skin cancer (c00-c97 excl. c44): 1971-2011 [Image taken from Cancer Research UK]

Despite the success in diagnosing and managing cancer, mortality rates remain at an unacceptable level: The ten-year survival of all cancers is still about 50% in the UK. For more aggressive cancers such as liver cancer, lung cancer and pancreas cancer, the ten-year survival rate still remains lower than 10% in England and Wales (Quaresma *et al.*, 2015).

## 1.3 THE NATURE OF CANCER

Cancer cells are defined as genetically mutated autogenic cells with distinctive physiological hallmarks (Weinberg, 2007) (Figure 1.7). With the intention of developing successful cancer treatments which can eradicate cancer without damaging healthy tissue, many studies have focused on the anatomical and pathophysiological properties of cancerous tissue.

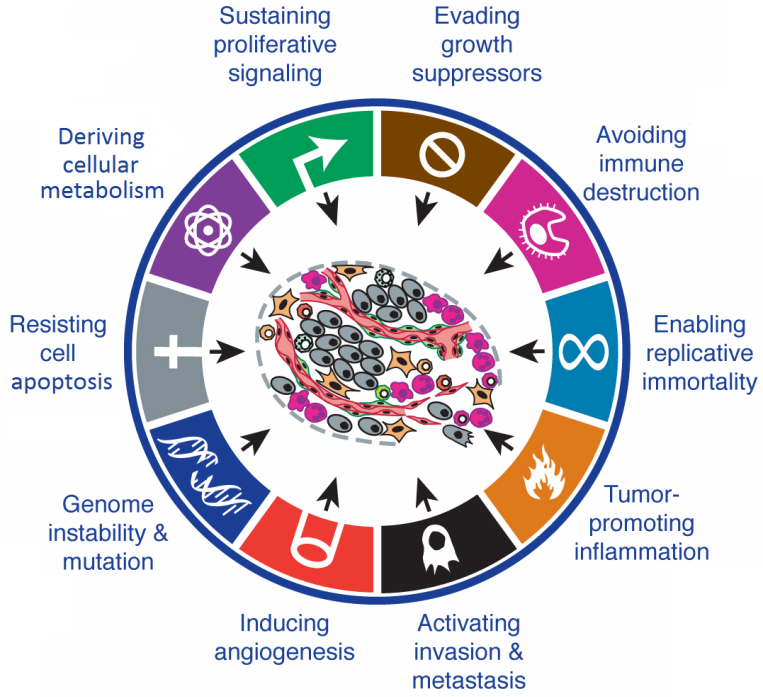


Figure 1.7 Acquired capabilities of cancers [Image modified from (Hanahan and Weinberg, 2000)]

### 1.3.1 Genetic mutation and loss of genetic error repair

In cancer cells, the ability to repair genetic errors (or defects) is inhibited or lost, leading to preserved and accumulated mutations (Jackson and Bartek, 2009). Such instable genomic and preserved mutations result in an over-expression of many oncogenes, and

down-regulation of tumour suppressors (such as p53 or PTEN) (Chalhoub and Baker, 2009, Lucci *et al.*, 2010).

### 1.3.2 Limitless proliferation and cell immortality

The growth and proliferation of cancer cells is rapid and sustainable. In healthy non-stem cells, cell growth and proliferation cycles are precisely regulated by many growth factors and cell signalling, to maintain a homeostasis in cell number and function. Such homeostasis is lost in cancer cells due to self-stimuli proliferative signals (from intrinsic cells or even surrounding normal cells), and de-regulation of anti-proliferative signals (Cheng *et al.*, 2008a). Meanwhile, the ability for cell apoptosis is irreversibly lost or de-regulated (Adams and Cory, 2007, Lowe *et al.*, 2004). These phenomena lead to an aberrant cell cycle, cell immortality and limitless proliferation in cancers.

### 1.3.3 Derived metabolism and the Warburg effect

Cell metabolism is both altered and aberrant in cancer cells due to both the defective function of mitochondria, and the mis-regulation of many cell signalling pathways (Jones and Thompson, 2009).

One of the most unique characteristics of altered cellular metabolism in cancer is the Warburg effect. In normal healthy cells, oxidative phosphorylation (OXPHOS) is the predominant respiration mechanism enabling efficient adenosine-5'-triphosphate (ATP, a substance that transports chemical energy) generation and higher oxygen consumption than in glycolysis. However, many cancer cells generate energy predominantly using glycolysis in the cytoplasm even when sufficient oxygen is available (i.e. aerobic glycol-

ysis), rather than using OXPHOS (Alfarouk *et al.*, 2014, Warburg, 1956, Warburg *et al.*, 1927). This derived metabolic effect, the Warburg effect, leads to insufficient energy generation in cancer cells.

However, the claim by Warburg that aerobic glycolysis results from compromised mitochondrial OXPHOS in cancers has been challenged in recent years. Some hypotheses suggest that the effect is actually an adaptation of cancer cells to the damaged mitochondria (Lopez-Lazaro, 2008). Others claimed that aerobic glycolysis may arise from upregulated oncogenes, downregulated tumour suppressors. Thus, the mechanism of the Warburg effect is not fully understood to date.

### 1.3.4 Induced angiogenesis and the enhanced permeability and retention (EPR) effect

Many types of cancer cells tend to aggregate together and form clusters which consume large amounts of oxygen and nutrients for rapid growth. These tumour cells excrete the signalling molecule vascular endothelial growth factor (VEGF) which promotes angiogenesis (blood vessel generation) (Folkman *et al.*, 1971).

This sustained angiogenesis allows tumour growth beyond the limitations of passive nutrient diffusion from surrounding blood vessels (Fang *et al.*, 2011). However, the rapidly formed blood vessels surrounding tumours are defective; comprising poorly-aligned defective endothelial cells lacking a smooth muscle layer supporting, which leads to wide fenestrations and enhanced permeability. In addition, there is inadequate lymphatic system connected with the tumour thereby making it difficult to filter large molecules or nanoparticles out from the system. This effect is called the enhanced permeability and re-

tention (EPR) effect and can be important to nanoscale anti-cancer drug carriers (Matsumura and Maeda, 1986).

### 1.3.5 The tumour microenvironment

As a result of the aberrant cellular metabolic processes and defective angiogenesis, the tumour cell microenvironment differs significantly from healthy cells. Due to the rapid and limitless growth of tumours, and massive oxygen consumption *via* aerobic glycolysis, the supply of $O_2$ to tumours is always inadequate (especially in the core), which leads to hypoxia (Olin *et al.*, 2011). Furthermore, defective angiogenesis causes the accumulation of acidic molecules (e.g. $CO_2$, lactic acid), resulting in an acidic microenvironment with a pH as low as 6.5 (Spence and Johnston, 2001). This has far-reaching implications since anti-cancer reagents must perform effectively in the hypoxic and acidic microenvironment of the tumour.

### 1.3.6 Tumour metastasis

In many aggressive cancers, the cell-to-cell attachment or adhesion is found to be reduced or inhibited, causing an enhancement of cellular mobility, tumour metastasis and invasion (Goldberg, 2013, Folkman, 1995, Weidner *et al.*, 1991). Cancer cells can leave the primary tissue sites and migrate to nearby, or even distant, tissues *via* the circulatory and/or lymphatic systems because of the down-regulation of certain cell-to-cell adhesion molecules (such as cadherins, radixin), the degradation of extracellular matrix, and the up-regulation of lamellipodia formation (Berx and van Roy, 2009, Santy *et al.*, 2005, Cancer Research UK, 2014).

Metastasis has been considered one of the most important differences between benign tumours and malignant tumours (Koten *et al.*, 1993, Cancer Research UK, 2014), and the most life-threatening aspect of cancer (Liotta *et al.*, 1991).

## 1.4 CURRENT MANAGEMENTS OF CANCER

In order to treat cancer and/or relieve the symptoms of cancers, many cancer managements have been developed to remove the tumorous lesions, reduce the tumour size, and ease the discomfort caused by cancer and the complications. Because of the vastly diverse phenotypes, stage, and drug resistance of cancers, the approaches to manage cancer are largely varied (Miller *et al.*, 1981).

The most commonly used methods to treat cancers, including surgical removal, radiotherapy, chemotherapy, and gene therapy are discussed in further detail below.

### 1.4.1 Surgical removal

Surgical removal is available for many types of cancers allowing a promising cure by removing solid tumours and their vasculature partially or entirely. This approach is especially effective when the solid tumours are isolated, well defined and not yet metastasised. This approach is especially efficient in early stage cancers.

With the improvement of diagnostic techniques and surgical methods (such as gamma knifes), surgical oncology has been greatly improved and can be applied to more types of cancers, and even used in some metastased cases. The survival rate after a tumour extraction surgery has greatly increased since last century.

Although the application of surgical oncology is wide, it still cannot be employed to all types of cancer. Not all tumours are operable because surgeries could introduce irreparable damage to certain organs, particularly in the brain. Also, the effectiveness of surgery can be significantly compromised due to the propensity of invasion and metastases of cancers which leads to undefined tumour margins, especially in the terminal stages. Furthermore, microscopic cancer cells may not be removed completely during surgery, resulting in cancer recurrence.

Due to the limitations of cancer surgery, patients are always treated with additional radiotherapy and/or chemotherapy before and after the surgery.

### 1.4.2 Radiotherapy

Radiotherapy is another widely applied treatment which uses ionizing radiation to limit malignant cell growth. It works by damaging the DNA of exposed tissue, and causing cell death. Cancer cells replicate much more rapidly than most healthy mature cells, and it is known that their ability to repair damaged genes is reduced. When the DNA of cancer cells is impaired in radiotherapy, the damage is not corrected, but maintained and accumulates when the cells replicate, resulting in reduced proliferation and cell death (Kapiteijn *et al.*, 2001).

Healthy cells, however, are able to repair a limited amount of DNA damage and so would not proliferate genetic errors. Hence, radiotherapy specifically targets cancerous cells. This technique is widely applicable to many types of cancers, including haematological cancers (cancer in blood which does not form solid tumours), and can also be used post-surgery to prevent recurrence.

However, the challenges of radiotherapy remain and limit the applications in cancer management. Radiotherapy may also damage healthy tissues near to irradiated lesions, leading to possibly irreversible damage or long-term side effects, such as tissue fibrosis, epilation (hair loss) and infertility (NHS, 2015).

### 1.4.3 Chemotherapy

Chemotherapy is a cancer management approach using pharmaceuticals to cure cancers, and/or ease the symptoms of cancers. The use of a chemotherapeutic is often associated with surgery, radiotherapy and/or other types of chemotherapeutics.

Chemotherapeutics can be broadly classified into hormonal therapeutics, cytotoxic chemotherapeutics, and molecularly targeted therapy.

#### *1.4.3.1 Hormonal therapy*

Since the growth of certain cancers (including some breast cancers and ovarian cancers) is hormone-dependent, the manipulation (or disturbance) of the endocrine system can reduce tumour growth or even lead to cancer cell death (Boothby *et al.*, 2004).

Hormonal therapeutics include hormone synthesis inhibitors (such as Letrozole™, an estrogen synthetase inhibitor), hormone antagonists (such as Tamoxifen™, an estrogen receptor antagonist) or supplementary hormone agonists (such as using estrogen to inhibit growth of prostate cancer; using progesterone-like drugs to treat breast cancer).

However, the applications of hormonal therapy are very limited.

#### *1.4.3.2 Cytotoxic chemotherapy*

Cytotoxic chemotherapeutics are the most conventional and widely used chemotherapeutics to date. They damage and kill cells that are dividing and growing rapidly through different strategies, such as inhibiting mitosis, or disturbing DNA synthesis.

The most studied and widely used examples include Doxorubicin™ (intercalating DNA), Paclitaxel™ (constraining mitosis by inducing microtubules polymerization and inhibiting the mitotic spindle formation) and Camptothecin™ (inhibiting the topoisomerase activities in DNA, preventing DNA re-ligation and leading to DNA damage and cell death (Hsiang *et al.*, 1985)).

Most cancer cells proliferate much faster than healthy ones, therefore cytotoxic chemotherapeutics could work efficiently to specifically kill cancers. However, they also do great damage to those healthy cells which reproduce rapidly, e.g. stem cells in bone marrow. It can therefore lead to severe side effects such as the decreased production of blood cells, epilation and infertility.

#### *1.4.3.3 Molecular targeted therapy*

Instead of disturbing all rapidly dividing cells, molecular targeted therapeutics can target specific enzymes (such as some kinases) or oncogenes which are associated with tumour growth and/or carcinogenesis.

A number of enzymes and oncogenes can be the 'target' in molecular targeted therapy. For example, bevacizumab™ targets VEGF and reduces tumour angiogenesis (details in section 1.3.4). Many therapeutics targeting poly-ADP-Ribose polymerase, folate receptor,

and epidermal growth factor have been studied with a number of them reaching clinical trial phases, or receiving approval by the FDA or EMA (Campos and Ghosh, 2010).

A number of studies have investigated therapeutics targeting PI3K/Akt/mTOR pathways (Arcaro, 2014). The aberrant and elevated physiological function of PI3K/Akt/mTOR pathways is found in many cancers, responsible to enhanced cell growth, evaded apoptosis, and mis-regulated metabolism (details in section 3.1.3). Therapeutics targeting these pathways are being considered promising anti-cancer agents to treat many cancers. In fact, some cases, such as GDC-0941 (Roche) and BKM120 (Novartis), have reached clinical trial phases.

#### *1.4.3.4 Challenges in current chemotherapy*

Limitations still remain in all classes of chemotherapies.

Cancer cells can be resistant to one or more chemotherapeutics, leading to reduced drug efficacy (Kapse-Mistry *et al.*, 2014). This is called Multi-Drug Resistance or MDR. MDR resulted from poor drug uptake, enhanced efflux from cancer cells, drug inactivation due to environmental stress, and off-target effect (for molecular targeted therapy) (Stewart, 2010). A number of previous studies have shown that MDR is one of the most important reasons for tumour recurrence and poor prognosis (Dean *et al.*, 2005, Kanwar *et al.*, 2012).

Furthermore, many chemotherapeutics, especially cytotoxic chemotherapeutics, have a non-specific action upon both cancerous and healthy cells. Poor drug specificity often leads to high cell mortality in healthy cells and severe adverse effects in normal tissues and organs.

#### *1.4.3.5 Delivery systems of chemotherapeutics*

In recent years, many studies have been focused on the use of nanomaterials to deliver chemotherapeutics. An appropriate nano-scaled drug carrier may overcome many current obstacles and offer an opportunity to increase the internalisation of chemotherapeutics, improve the specificity (*via* particle functionalisation), and bypass MDR (Liang *et al.*, 2010).

### 1.4.4 Gene therapy

Another newly emerging method for cancer treatment is gene therapy. Gene therapy is a promising approach in which a nucleic acid (in the form of DNA plasmid, dsRNA, microRNA, siRNA, etc.) is delivered into cancer cells to interfere with gene expression, introducing tumour-suppressor genes, or even correcting genetic errors. In particular, small interfering RNA (siRNA) is one of the most attractive gene therapeutics in the last decade (Whitehead *et al.*, 2009).

However, the use of siRNA is challenging. Unmodified siRNA is unstable in the bloodstream, can be immunogenic and does not readily cross cell membranes (Hickerson *et al.*, 2008). It is vital that the siRNA be delivered to the interior of the target cells in order to be incorporated into the RNAi machinery. However, siRNA molecules are too large and too hydrophilic to cross most mammalian cell membranes. Therefore, it always requires chemical modification or a carrier material for siRNAs to enter the cells.

Currently, several techniques have been developed to increase cellular uptake of siRNA.

- Enhanced siRNA internalisation by stimulating cells

Although research concerning the cellular uptake of siRNA is limited, there are studies to suggest that siRNA cellular uptake could be enhanced after chemical stimulation of mammalian cells with compounds, such as phosphorothioate (Detzer *et al.*, 2009, Overhoff and Sczakiel, 2005). Electroporation is an alternative technique which can be used to enhance siRNA cellular uptake (Fyrberg and Lotfi, 2010). During a powerful electric pulse, the negatively charged groups on the lipid bilayer of cell membranes reorient and undergo thermal phase transitions due to heating, resulting in the transient creation of hydrophilic pores and localised perturbations in the integrity of the cell membrane. The temporary loss of the semi-permeability of cell membranes leads to the escape of intracellular contents, and simultaneous uptake of extracellular molecules, such as siRNA. Electroporation shows a high cellular uptake efficiency of siRNA, but, it also induces a high level of cell mortality, and therefore applicable cell lines are very limited.

- Enhanced siRNA internalisation by chemically modifying siRNA

Chemical modification is useful in certain circumstances, especially for systemic delivery. It was well-known that uncomplexed siRNA (or 'bare' siRNA) delivered systemically after intravenous administration would be rapidly degraded from the RNases *in vivo* and/or cleared from the kidney. Chemical modification (Braasch *et al.*, 2003) on siRNA (normally on the nucleobases, or the phosphate ester backbone) (Manoharan, 2004) could reduce siRNA sensitivity to nucleases and enhance membrane permeation.

Despite the possibility to enhance the internalisation of siRNA through different strategies, the applications are still very limited and mortality is always extreme. An ideal siRNA carrier would enable high delivery efficiency and low fatality.

## 1.5 AIM AND OBJECTIVES

In this thesis the focus of the research will be on the assessment of MSNPs for the delivery of chemotherapeutics and siRNAs to cancer cells. A drug delivery system based on surface functionalised mesoporous silica nanoparticles is developed, which efficiently delivers small drug molecules (including LY294002, a hydrophobic chemotherapeutic), and siRNAs.

- Synthesise, characterise, and analyse four morphologically different MSNPs.
- Demonstrate the biocompatibility and bio-degradability of the MSNPs.
- Demonstrate whether the MSNPs are suitable as drug nano-carriers.
- Characterise and analyse the chemical properties of LY294002, a typical hydrophobic chemotherapeutic that requires a delivery system for *in vivo* use; Assess the physiological effect of LY294002 on different cancer cell lines.
- Evaluate the loading and unloading behaviours of different cargo molecules (including LY294002) on MSNPs.
- Alter the drug unloading behaviours with capping polymers onto MSNPs
- Deliver LY294002 loaded MSNPs to cancer cells and demonstrate the cell survival after treatment.
- Deliver siRNA to cancer cells using functionalised MSNPs.
- Establish a chemo- / gene therapeutics co-delivery system based on functionalised MSNPs and demonstrate the efficiency of such a co-delivery system in reducing cell survival and gene knock-down.

# Chapter 2

# Mesoporous Silica Nanoparticles: Synthesis and Characterisation

Mesoporous silica nanoparticles (MSNPs) are a class of silica materials with outer dimension under 100 nm and pores in the range of 2-50 nm (definition from IUPAC (Physical Chemistry Division Commission on Colloid *et al.*, 2003)). MSNPs have been of interest in many fields, e.g. catalytic chemistry, ion exchange (Davis, 2002), pharmaceutical industry, biosensing, drug delivering, due to their high porosity and large surface area (Ozin *et al.*, 2005).

In this study, MSNPs were generated *via* different synthesis routes, and the resulting MSNPs fully characterized for their suitability as drug carriers. A number of particles with anticipated different overall size and shape were chosen. The chosen MSNPs were also assessed for ease of synthesis, reproducibility, and homogeneity of the product.

## 2.1 INTRODUCTION

### 2.1.1 History of mesoporous silica

Mesoporous silica materials was first introduced into the chemical engineering industry for their potential as efficient catalyst matrices and/or molecular sieves (Yanagisawa *et al.*, 1990). Mesoporous silicates have been described as zeolite-like bulk materials with a very large surface area (up to 1500 $m^2/g$ based on BET theory; (Bucknall, 2012)) and mesoscopic pores. The field has seen rapid development and mesoporous silica has been used in many different forms such as films and particles, and the porosity can be tuned with respect to size and alignment.

### 2.1.2 Silica nanoparticles synthesis routes

Following the first reports of a synthesis method for MSNPs (Di Renzo *et al.*, 1997), a number of alternative MSNP synthesis routes were derived. The architecture of the MSNPs can be vastly varied using different synthesis techniques. The size, shape and distribution of pores can also be varied, as well as the overall size and morphologies of the particles.

All found synthesis methods have been using bottom-up strategy based on sol-gel system. In a most classic route, the sol-gel / micro-emulsion was composited from an oil-water-surfactant system, in which the surfactant played a role as a removable structure-directing template. A silica resource, typically an orthosilicate, was then added into the system, hydrolysed, and condensed around the template, forming a silica nanoparticle before the template is removed.

This synthesis strategy is simple, reproducible and very flexible. Therefore many MSNPs synthesis methods based on this strategy have been developed and published. The architecture and size of MSNPs can be easily tuned by changing the composition of the sol-gel system or by controlling the aging time of orthosilicate hydrolysis (Suteewong *et al.*, 2010, Moon and Lee, 2012, Nandiyanto *et al.*, 2009). The pore size can also be manipulated by controlling the concentration or the types of the scaffold molecules (Sponchia *et al.*, 2014, Büchel *et al.*, 1998).

Drying and etching processes are also common in MSNP synthesis methods. Silica particles can be obtained by spray drying or freeze drying silica gels / colloids (Ide *et al.*, 2011, Urata *et al.*, 2008). Etching is normally used to generate or enlarge pores or even cavities from silica nanoparticles.

In this study, all four types of MSNPs were reproduced using methods based on sol-gel routes. With the different sol-gel compositions, template molecules and reaction conditions, the size, morphology, porosity and surface properties of synthesised MSNPs were distinct. The silica precursor used was tetraethyl orthosilicate (TEOS). The hydrolysis reaction of TEOS described thus:

$$Si(OC_2H_5)_4 + 2\ H_2O \underset{}{\overset{\text{-OH}}{\rightleftharpoons}} SiO_2 + 4\ C_2H_5OH$$

### 2.1.3 Functionalisation of MSNPs

MSNPs are easily functionalised with a variety of fluorophores, polymers, targeting ligands, peptides, and even smaller nanoparticles *via* chemical modification, surface coating or grafting. The modified/functionalised MSNPs may be used in different applications

and to fulfil different tasks in drug delivery, such as visualisation, improvement of biocompatibility, specific targeting or controllable cargo release.

MSNPs can be conjugated with a variety of fluorophores, such as Rhodamine 6G, on the surface or within the silica matrix. Since fluorescence can be easily tracked, fluorescently labelled MSNPs can be widely used in research, biomedical imaging, and even surgical procedures (Chen *et al.*, 2013). Such particles may also be used for *in vitro* work to determine the internalisation of the MSNP and sub-cellular localisation (Cho *et al.*, 2010).

MSNPs can be functionalised with different polymer coatings. For example cyto-friendly polymers, such as polyethylene glycol (PEG) have been grafted on to the surface to improve the biocompatibility of MSNPs (Rosenholm *et al.*, 2011). Since the cellular uptake is affected by the surface charge of MSNPs (also see section 2.5.4), uptake can be enhanced by alteration of the surface charge with polycation coatings. Coating with poly-(l-lysine) (PL), poly(ethyleneimine) (PEI) or chitosan has been shown to successfully improve the cellular uptake of the coated MSNPs (Asefa and Tao, 2012). A layer-by-layer coating of PL and hyaluronic acid (HA) was also shown to effectively increase the biocompatibility and cellular uptake of MSNPs by cancer cells (Gary-Bobo *et al.*, 2012).

Furthermore, cargo release from MSNPs has been shown to be controllable after surface functionalisation with a variety of stimuli-responsive materials and targeting ligands (detailed in section 4.1.2 and 4.1.3).

## 2.2 MATERIALS AND METHODS

### 2.2.1 Synthesis methods

#### *2.2.1.1 Synthesis method of HMSNP*

HMSNPs were synthesized using the method by Hom *et al.*(Hom *et al.*, 2010). Briefly, 100 mg CTAB (99%; Aldrich,) was dissolved in 48 mL dd$H_2O$ and 350µL of 2M NaOH and vigorously stirred in a round-bottom flask at 80 °C. After temperature stabilization, 500 µL TEOS (Aldrich) was added. After a further 2 hours incubation, the nanoparticles were collected by centrifugation and washed twice with methanol. The CTAB surfactant was removed by overnight reflux in acidic methanol (20 mL methanol, 1 mL 37% hydrochloric acid) at 80°C.

#### *2.2.1.2 Synthesis method of BMSNP*

BMSNPs were synthesized by a modification of the method by Nandiyanto *et al.* (Nandiyanto *et al.*, 2009). In a typical synthesis 100 mg CTAB was dissolved in 30mL dd$H_2O$, and incubated at 60°C. After temperature stabilization 9.6 mL octane (Sigma-Aldrich), 81.34 µL styrene solution (5000 µg/mL in methanol solution; Sigma), 22 mg L-lysine (SAFC), 1.07 mL TEOS and 34.23 mg AIBA (Sigma) was added. The reaction was incubated with stirring for a further 3 hours under $N_2$ at 60°C. The reaction was then cooled to room temperature and stirred overnight. Nanoparticles were collected by centrifugation, and washed three times with absolute ethanol. To remove the organic templates, particles were washed with toluene in a Soxhlet extractor at 150 °C for 48 hours.

#### *2.2.1.3 Synthesis method of CMSNP*

CMSNPs were synthesized by a modification of the method by Zhang *et al.* (Zhang *et al.*, 2010). Briefly, 8 mL dd$H_2O$ was mixed with 40 mL diethyl ether (Sigma), and 1 mL 28 % ammonia solution (Alfa Aesar) in a closed flask with vigorous stirring at room temperature. After the mixture became homogeneous, 2 mL TEOS was added into the solution

dropwise. After a further 3 hours stirring, another 2 mL TEOS was added in dropwise, and 1g CTAB added. The mixture was then stirred at room temperature overnight. Particles were washed three times with $ddH_2O$ and dried under vacuum at 60 °C overnight. To remove the template, the particles were fired at 550 °C for 6 hours.

#### *2.2.1.4 Synthesis method of WMSNP*

WMSNPs were synthesized by a modification of the method by Moon *et al.*(Moon and Lee, 2012). In a typical synthesis, 0.5 g CTAB and 0.3 g urea were dissolved in 15 mL $ddH_2O$ in a round bottom flask. 15 mL cyclohexane and 0.46 mL iso-propanol were added subsequently to the solution. With vigorous stirring, 1.25 g TEOS was added dropwise to the mixed solution and the stirring was kept for 30 min at RT. Then, the mixture was heated to 70 °C for 12 h. The nanoparticles were collected by centrifugation and wash with acetone and water for three times each. The CTAB surfactant was removed by overnight reflux in acidic methanol (20 mL methanol with 1 mL 37% hydrochloric acid) at 80°C.

#### *2.2.1.5 Synthesis method of SNP*

Non-porous silica NP (SNP) was synthesized as a control / comparison when investigating if MSNPs are efficient drug carrier. SNP was synthesized using the method reported by Rao *et al*. (Rao *et al.*, 2005). As such, 36.8 mL absolute ethanol was mixed with 20.25 mL $ddH_2O$ in a flask in a sonicating water bath at room temperature. After 10 min, 0.5 mL TEOS was added in. The mixture was sonicated for a further 20 min before the dropwise addition of 54.44 mL 28% ammonia solution. The reaction was continued for another 1 hour with sonication. Particles were collected by centrifugation and washed twice with $ddH_2O$.

### 2.2.2 Characterisation techniques

#### *2.2.2.1 TEM*

Specimens for TEM analysis were made by drop-casting particles onto holey carbon coated TEM grids (Agar). Bright field imaging and single tilt series imaging (-10º to +20º about the planar orientation with images taken at 10º intervals) was performed using a JEOL JEM-2010 operating at 200kV.

Images were taken and analysed with DigitalMicrograph™. The size measured on TEM images were obtained from a contrast profiling tool with DigitalMicrograph™. Calibration (size per pixel) was achieved with a standardised gold nanoparticle measured with the same TEM on 15th Sep 2011. The associated FFT graphs were also obtained from DigitalMicrograph™

#### *2.2.2.2 SEM*

Backscattered electron images of the specimens were taken from a JEOL JSM-840A instrument operating at a primary energy of 10kV. The specimens were sprayed on the stage and sputter-coated with 3 nm gold before the testing.

#### *2.2.2.3 Surface area analysis*

The specific surface area of MSNPs was tested with nitrogen adsorption-desorption isotherm measurement on a Gemini VI (Micromeritics, GA, USA) surface analyser at -196 $^{o}$C and calculated with Brunauer-Emmett-Teller (BET) theory (Brunauer *et al.*, 1938). Specimen was degassed by nitrogen at 50 $^{o}$C overnight before testing. BET surface area was adopted with isotherm adsorption data at P/P0 from 0.05 to 0.30 (linear region):

$$SA_{BET} = \frac{CSA \times N_A}{22414 \times 10^{18} \times (S+ Y_{INT})}$$

Where $SA_{BET}$ is BET surface area ($m^2/g$); CSA is the analysis gas molecular cross-sectional area (0.162 $nm^2$ for $N_2$); $N_A$ is Avogadro constant $6.023 \times 10^{23}$; S is the slope ($g/cm^3$); $Y_{INT}$ is the Y-intercept ($g/cm^3$).

Porosity can be evaluated from TEM imaging in some MSNPs when the pores were shown to be well-defined on the images. Otherwise, pore volume and pore size distributions were obtained by using the Barrett, Joyner, and Halenda (BJH) method from both absorption and desorption branch (Barrett *et al.*, 1951).

#### *2.2.2.4 ζ (zeta) potential*

The surface charge of MSNPs was measured using a Zetasizer Nano ZS (Malvern, UK). To determine the electrokinetic potential, or ζ potential (which represents the surface charge of a colloidal suspension), the MSNPs were suspended in PBS buffer (pH 7.4) prior to the measurement. 30 runs were read before the calculation of electrophoretic mobility, zeta potential and zeta potential distribution.

#### *2.2.2.4 Disc Centrifuge*

The hydrodynamic particle size distributions were measured using a Disc Centrifuge (DC 18000; CPS instrument) based on the technique of Differential Centrifugal Sedimentation (DCS). The machine operated stably at 24,000 rpm. Prior to measurements, a sucrose gradient was built and PVC particle calibration standards (0.377 μm and 0.022 μm) were applied. All the particles were measured in triplicate. The main peak, standard deviation and polydispersity index (PDI) were collected.

### 2.2.3 Particle degradation

A study of MSNPs degradation was undertaken in physiological buffer since the MSNPs were designed for biomedical applications. The particles were re-suspended in PBS (pH 7.4) at 37 $^{o}$C. The suspension was shaken every two days. TEM images were taken using JEOL JEM-2010. The size of degraded MSNPs was plotted against the degradation duration.

### 2.2.4 Biocompatibility of MSNPs assessed with MTT assay

In order to evaluate the biocompatibility of MSNPs, cell viability was measured using the MTT assay in the presence of the different MSNPs. Details regarding cell types and cell culture methods are stated in Chapter 3.2.2 and Chapter 3.2.3.1.

After selected cell lines were treated with 0.05 mg/mL MSNPs or SNP suspension for a defined period of time, cells were washed twice with pre-warmed PBS and 100 µL 0.5 mg/mL MTT solution (0.5 mg/mL dissolved in a mixture of PBS: growth medium, 1:9 v/v) was added to each well and incubated at 37 $^{o}$C, in darkness. After 4 hours incubation the supernatant was removed, and the formazan was solubilized with 100 µL DMSO per well. The absorbance was read at 570 nm using Tecan INFINITE 200 plate reader.

## 2.3 RESULTS OF SILICA NANOPARTICLES CHARACTERISATION

### 2.3.1 Morphology of MSNPs

The nanoparticle morphology is an important parameter in determining the utility of synthesised nanoparticles in drug delivery applications. Four MSNPs were synthesised and compared in this research.

They were all found to be broadly spherical in shape with an aspect ratio nearly 1:1. The size and alignments of pores were seen to be vastly different due to the distinct synthesis methods (Figure 2.1, Figure 2.2).

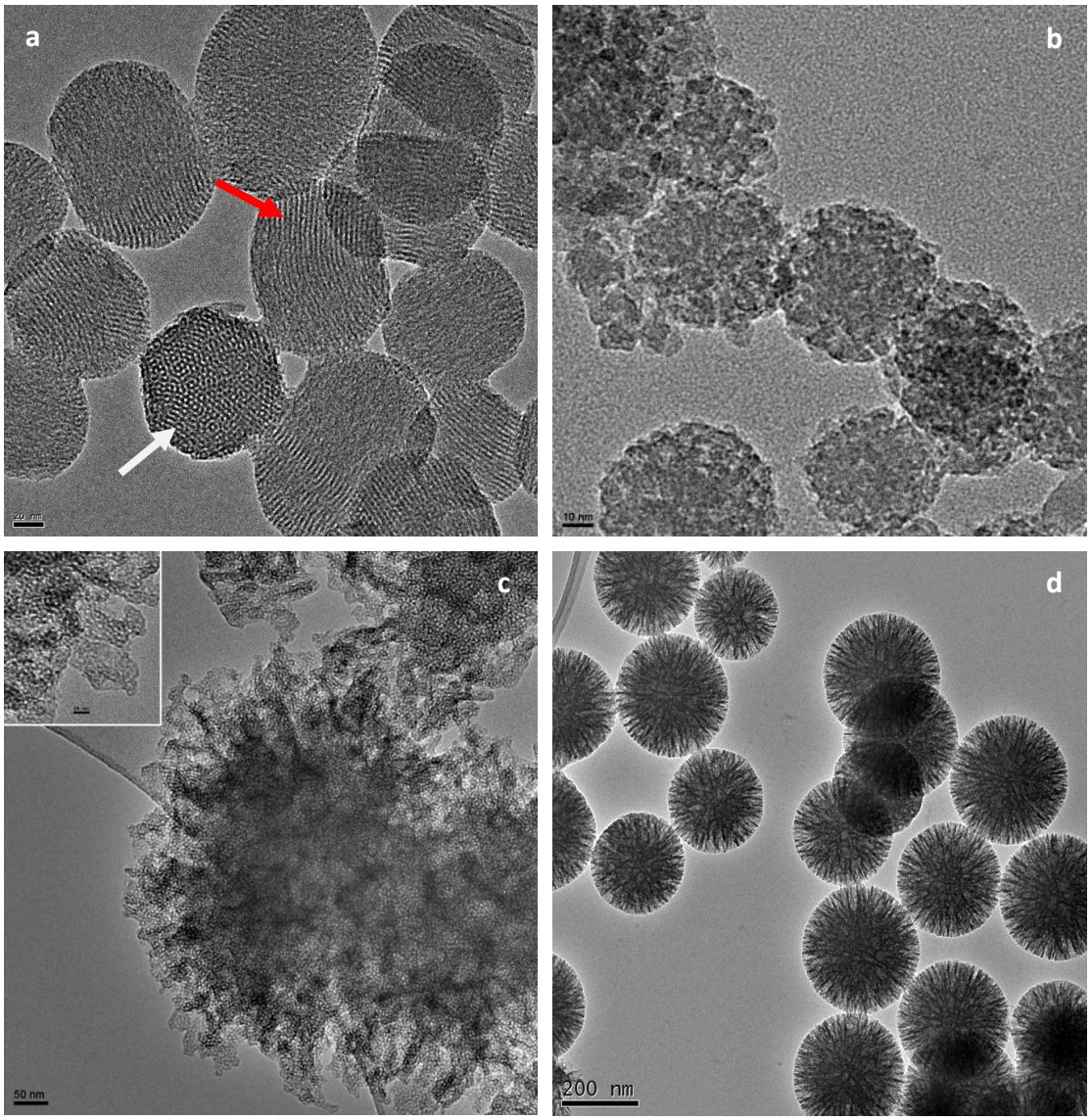


Figure 2.1 Typical TEM images of MSNPs synthesised for this study as drug delivery candidates: a) HMSNP (scale bar: 20 nm, arrows point out two views of HMSNP); b) BMSNP (scale bar: 10 nm); c) CMSNP (scale bar: 50 nm; higher magnification inset [scale bar: 10 nm] details the pores on the 'petal' structure) and d) WMSNP (scale bar: 200 nm)

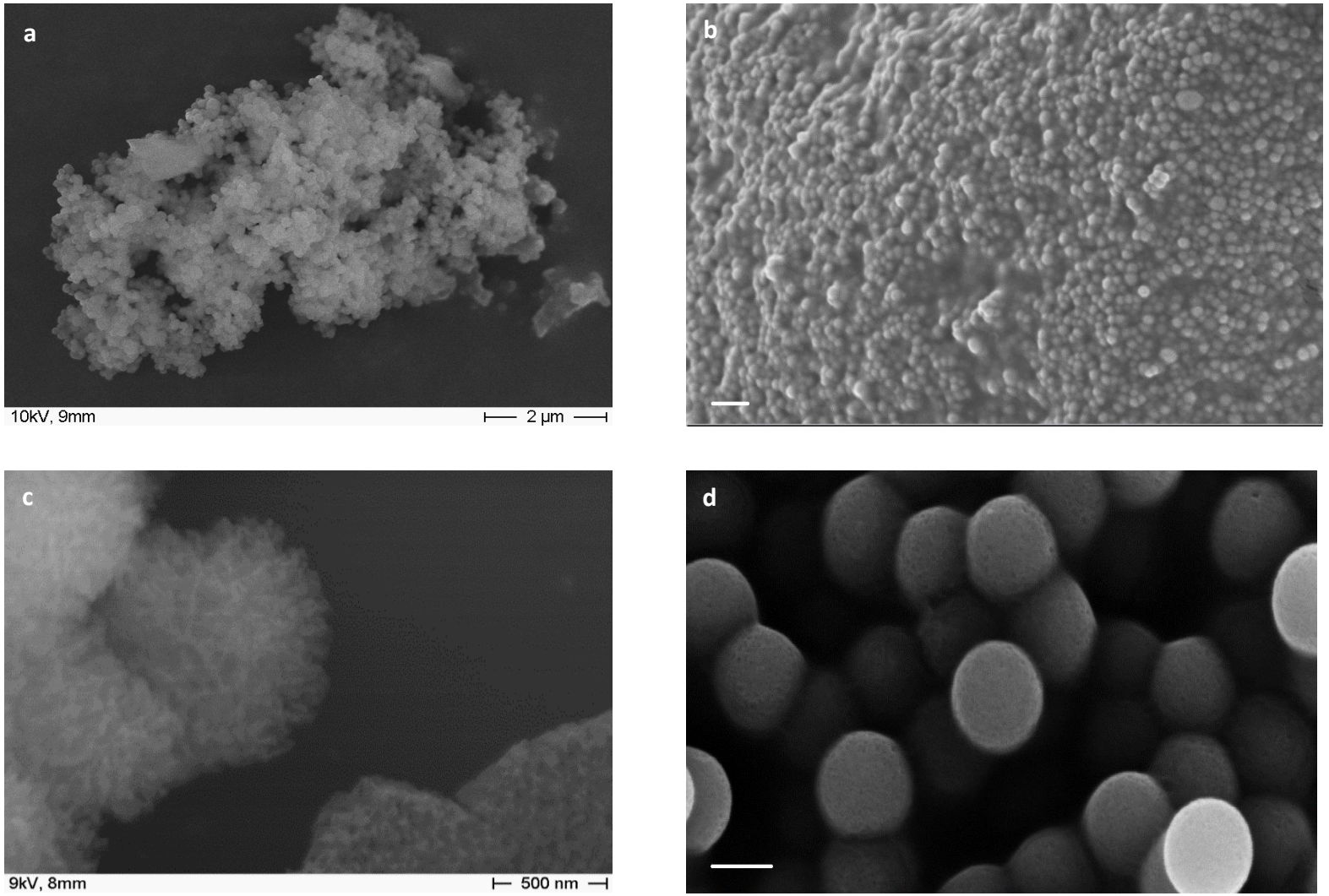


Figure 2.2 Typical SEM images of MSNPs synthesised: a) HMSNP (scale bar: 2000 nm); b) BMSNP (scale bar: 200 nm); c) CMSNP (scale bar: 500 nm) and d) WMSNP (scale bar: 200 nm)

### *2.3.1.1 Morphology of HMSNP*

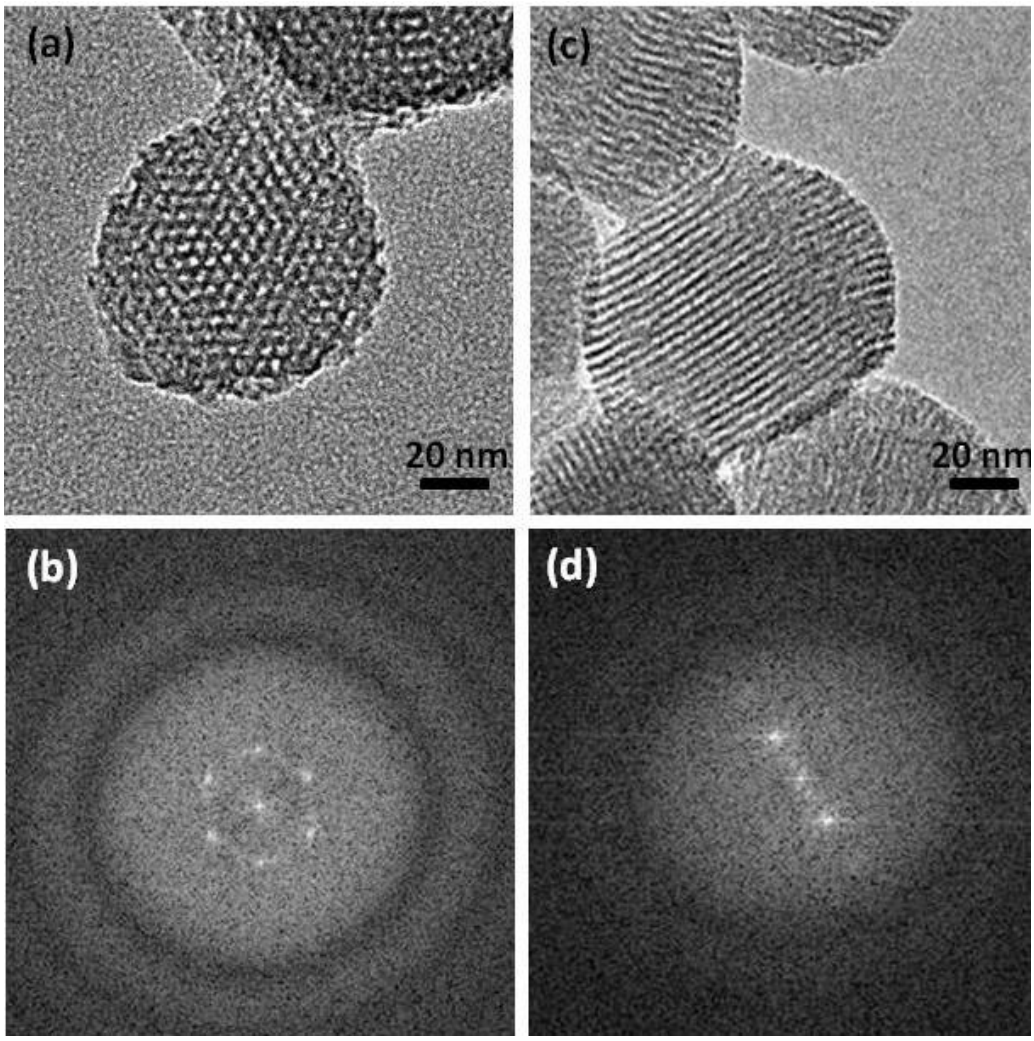


Figure 2.3 TEM images of HMSNP imaged from different orientations and their corresponding FFT's. (a) TEM image and (b) associated FFT of a HMSNP orientated with high-symmetry pore axis aligned parallel with the electron beam. (c) TEM image and (d) associated FFT of a HMSNP aligned with pores orientated normal to the direction of the electron beam.

HMSNPs were shown to be porous and roughly spherical with little elongation (Figure 2.1 a). The pores showed high rotational symmetry about the centre axis (white arrow in Figure 2.1 a), and were aligned in a hexagonal pattern with a central pore surrounded by six further pores when imaged in transmission through the axis of the centre pore (<110> direction). Meanwhile, if the electron beam is perpendicular to the symmetrical axis (red arrow in Figure 2.1 a), many particles displayed an ordered line array of pores, which run

through the entire volume of particle. As an approximation of the structure, the particle may be described as a slightly elongated sphere with individual pores running through the length of the particle, and are arranged in a quasi-hexagonal structure.

The fast Fourier transform (FFT) of the high-resolution images was performed to confirm the structure. Figure 2.3 b revealed an ordered set of reflections in reciprocal space with an overall six-fold symmetry when the electron beam was parallel to the channels. The sharpness of the spots indicated little variance of the pore size throughout the particle, as confirmed by the statistical measurements on many TEM images (Table 2.1). However, the corresponding FFT of a HMSNP imaged with the electron beam perpendicular to the symmetrical axis showed a two-fold symmetry, which confirmed the ordered pore meso-structure with a single dominant direction through the particle (Figure 2.3 d). A close inspection of the HMSNPs was also performed to confirm the porous structure on HAADF-STEM platform using small angle tilting imaging series and large angle tilting imaging series (Huang *et al.*, 2014).

#### *2.3.1.2 Morphology of BMSNP*

BMSNPs were shown to be spherical, mono-dispersed and porous with a rough surface (Figure 2.1 b, Figure 2.2 b). The pores showed no regular alignment, and were randomly embedded over the entire particle volume, forming a blackberry-like structure. The structure was also demonstrated with the associated FFT graph, in which no periodicity was displayed (Figure 2.4 b).

A close inspection of BMSNP was performed on STEM to confirm the morphology. A series of bright and dark patches was seen on the STEM image, corresponding to regions

of differing projected density (Huang *et al.*, 2014). It can be concluded that BMSNP consisted of open surface pores and randomly distributed internal voids.

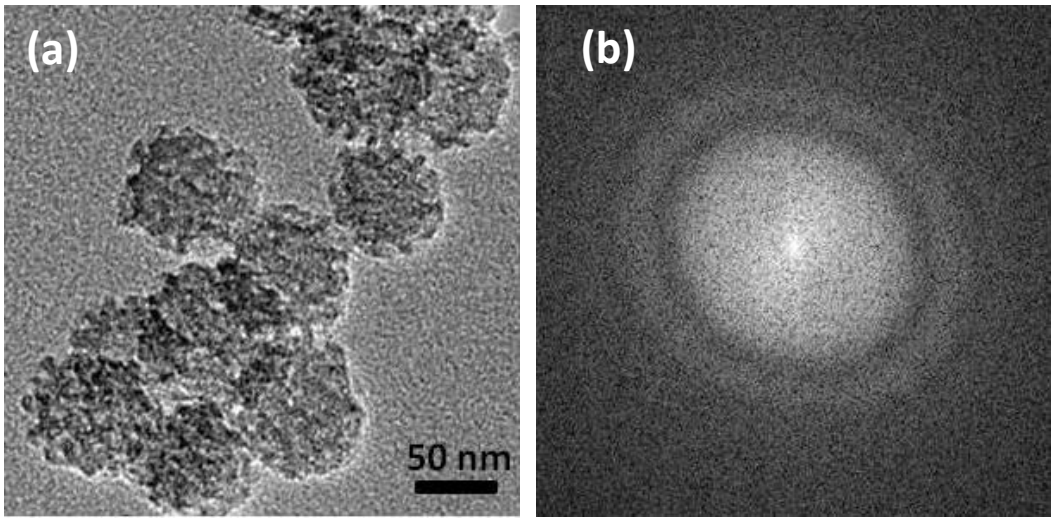


Figure 2.4 a) A representative TEM image of BMSNPs, and b) a FFT graph associated with a BMSNP

### *2.3.1.3 Morphology of CMSNP*

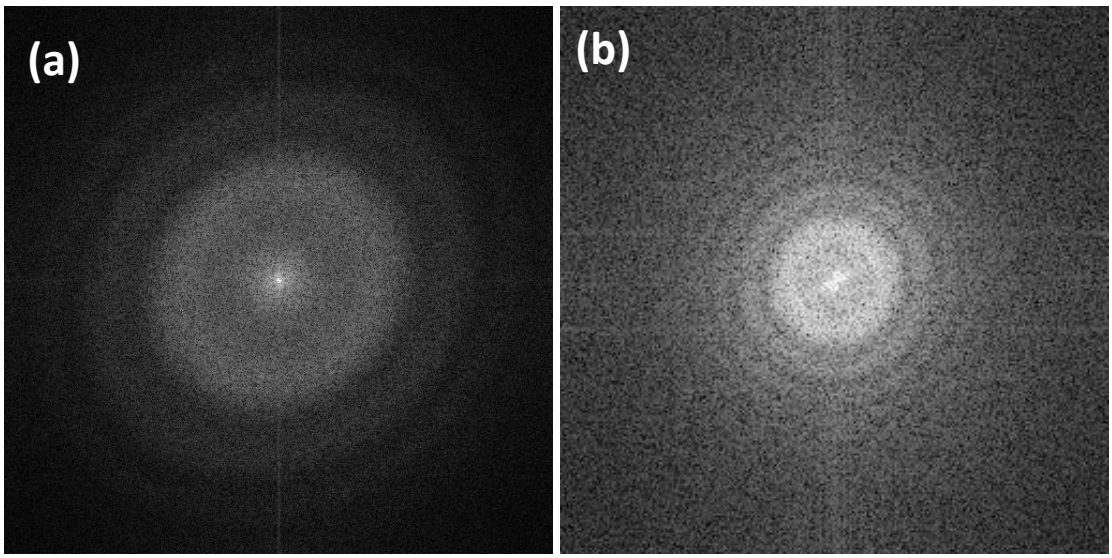


Figure 2.5 The associated FFT of (a) a CMSNP imaged with TEM in Figure 2.1 c, and (b) the 'petal' in Figure 2.1c insert

CMSNPs were shown to be large mesoporous spherical silica particles with a unique chrysanthemum-like architecture. The size of a CMSNP was found to be in excess of the

definition of ‘nanoparticle’, making CMSNPs in fact micro-particles. However, it would be still referred to as ‘Chrysanthemum-like **Nano**-Particle’ herein for convenience.

Similar to real chrysanthemums in the macroscopic world, CMSNPs were seen to be formed from multilayers of silica ‘petals’ growing from the particle core, which were closely packed and overlaid on each other (Figure 2.1 c, Figure 2.2 c). CMSNPs were found to be severely aggregated due to the petal-like structure.

The mesoscopic pores were shown to be dispersed irregularly on the ‘petals’ over the entire particle (close inspection of the ‘petals’ in Figure 2.1 c insert). There was also no periodicity seen in the associated FFT graphs corresponding to the entire particle (Figure 2.5 a) or the ‘petal’ (Figure 2.5 b).

#### *2.3.1.4 Morphology of WMSNP*

WMSNPs were shown to be spherical mesoporous silica nanoparticles with a wrinkle-like structure over the entire volume (Figure 2.1 d, Figure 2.2 d).

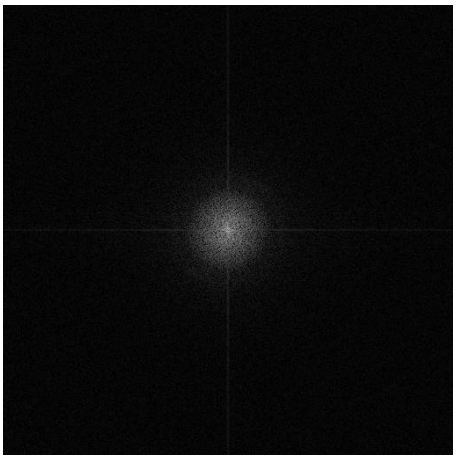

Figure 2.6 The associated FFT graph of a WMSNP imaged with TEM in Figure 2.1 d

Pores were formed between the wrinkles and aligned in a radial manner (Figure 2.1 d). The pores on the surface of WMSNPs appeared to be large and were even visible on

SEM images (Figure 2.2 d). TEM images also displayed lighter contrast near the core region of WMSNPs, representing internal voids in the particle (Figure 2.1 d). This indicated that the pores of WMSNP were dispersed over the entire particle.

The associate FFT graph of WMSNP also confirmed the irregularity of pore alignment (Figure 2.6).

### 2.3.2 Physical properties of non-porous silica nanoparticles

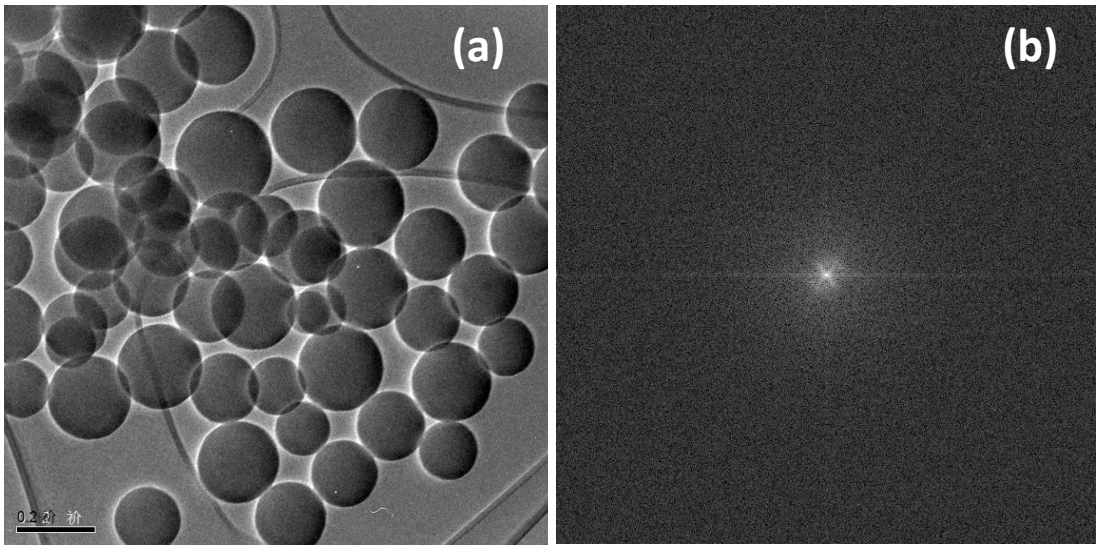


Figure 2.7 a) A representative TEM image of SNPs, and b) an associated FFT graph of a SNP

SNPs appeared to be spherical particles with a rough surface, as determined by TEM images (Figure 2.7 a). No porous structure was observed with TEM up to 200 kx magnification. The associated FTT (Figure 2.7 b) also confirmed that there was no porous or crystalline structure.

The size of SNPs was determined to be 63.56 ± 14.83 nm (72 particles were measured) using TEM contrast profile measurement. The specific surface area was found to be 89.69 $m^2/g$ based on BET theory.

### 2.3.3 Physical properties of the MSNPs

Many physical properties of nanoparticles, such as size and surface area, are considered to be very important parameters of a successful drug nano-carrier, and would influence drug loading efficiency, affect biocompatibility of nanoparticles and contribute significantly to overcoming the biological barriers in the human body (Albanese *et al.*, 2012, Chen *et al.*, 2005, Gaumet *et al.*, 2008, He *et al.*, 2010, Kulkarni and Feng, 2013).

In this study, the outer dimension of the nanoparticles, their porosity and surface properties were characterised and analysed. These physical properties of MSNPs were compared to SNP.

Along with the various morphologies and synthesis methods, the physical properties of the studied silica nanoparticles differed from each other greatly (Table 2.1, Table 2.2):

1) The sizes of most MSNPs varied from 63 nm to 232 nm (measured from the contrast profiles of representative TEM images), which were almost in the range of the optimal size for an *in vivo* drug nano-carrier. The only exception was CMSNPs that showed an unexpectedly large size.
2) SNPs and most of the studied MSNPs were seen to be mono-dispersed, except CMSNPs which showed a relatively broad size distribution.
3) All studied MSNPs were very porous with differently aligned mesoscopic pores.
4) All studied MSNPs exhibited a huge specific surface area; much larger than SNPs.
5) All studied MSNPs presented a negative or nearly neutral surface charge.

| | Particle Size (nm) | | | | Pore size (nm) | | | |
|---|---|---|---|---|---|---|---|---|
| | TEM | | CPS | | TEM | | BJH | |
| | Size | No. measured | Size | PDI | Size | No. measured | Adsorption | Desorption |
| HMSNP | 105.66 ± 23.11 | 431 | 98.77 | 1.32 | 2.13 ± 0.21 | 544 | 2.87 | 2.89 |
| BMSNP | 63.82 ± 7.39 | 47 | 57.47 | 1.90 | Not measurable | | 7.30 | 6.09 |
| CMSNP | 754.75 ± 313.69 | 7 | 998.81 | 3.20 | 2.03 ± 1.22 | 83 | 3.28 | 3.22 |
| WMSNP | 231.73 ± 17.84 | 91 | 234.53 | 1.08 | Not measurable | | 6.95 | 6.17 |

Table 2.1 Summary of particle and pore size of MSNPs. Particle size (nm) was measured *via* TEM image contrast profile (TEM) and CPS disc centrifuge (CPS); pore size (nm) was measured *via* TEM image contrast profile (TEM) and calculated with BJH theory based on measurement from Gemini VI surface analyser

| | Specific surface area ($m^2/g$) | |
|---|---|---|
| | BET | Zeta-potential (mV) |
| HMSNP | 1110.89 ± 1.73 | -31.43 ± 0.61 |
| BMSNP | 303.02 ± 1.00 | 1.13 ± 0.35 |
| CMSNP | 934.18 ± 1.03 | -18.00 ± 0.62 |
| WMSNP | 511.56 ± 1.99 | -59.27 ± 2.22 |

Table 2.2 Summary of specific surface area and zeta-potential of MSNPs. Specific surface area was calculated with BET theory based on measurement from Gemini Vi surface analyser; Zeta-potential was measured with Zetasizer in water suspension (pH = 7)

#### *2.3.3.1 The physical properties of HMSNP*

The average external diameter of HMSNPs was 105.66 nm. The porous structure can be described as a polyhedral solid with the constituent channels being 2.04 nm in diameter. The particles showed a typical type IV isotherm linear plot indicate that the HMSNPs were mesoporous (Figure S2.3 a) (Tóth *et al.*, 1999).

The specific surface area of the HMSNPs appeared to be very large (1110.89 $m^2/g$ , based on BET theory) due to the porous structure and small particle size. The surface charge of HMSNPs was determined to be -31.43 mV.

#### *2.3.3.2 The physical properties of BMSNP*

The outer dimension of BMSNPs can be easily tuned by changing the oil/water ratio of the sol-gel system in synthesis. The chosen BMSNPs were small (63.82 nm in diameter by TEM) with large and disordered pores. The type V isotherm linear plot (Figure S2.3 b)

indicated that the surface of the BMSNPs had little interaction with the liquid nitrogen in the test, and that the BMSNPs were mesoporous. Although the randomly aligned pores were not measurable from TEM imaging, the pore size was determined to be approx. 7.30 nm based on the BJH pore size calculation (absorption).

The specific surface area of BMSNPs was found to be 303.02 $m^2/g$ based on BET theory, which was smaller than other tested MSNPs. The surface charge is +1.13 mV.

#### *2.3.3.3 The physical properties of CMSNP*

The synthesised CMSNPs were in fact was on the microscale as the average diameter was shown to be approx. 700 nm as assessed by both TEM imaging and Disc Centrifuge. The size distribution was broad and the PDI was measured to be 2.51 (Disc Centrifuge).

The isotherm linear plot of CMSNPs (Figure S2.3 c) showed a typical type IV curve, indicating that CMSNPs are mesoporous with a pore size 3.28 nm based on the BJH adsorption calculation. The pore size can be also determined from TEM images, which was 2.03 nm on average from TEM imaging.

The large specific surface area of 934.18 $m^2/g$, based on BET theory, was virtue of the unique chrysanthemum-like architecture and small pore size. The surface charge of CMSNP was determined to be -18.00 mV.

#### *2.3.3.4 The physical properties of WMSNP*

The external diameter of the WMSNPs was determined to be 231.73 nm by TEM imaging, making it larger than HMSNPs and BMSNPs but much smaller than CMSNPs. The type V isotherm plot of WMSNPs suggested a mesoporous structure (Figure S2.3 d). The

pores were not well-defined and not measurable from TEM images, but could be calculated from BJH theory. The pore size was demonstrated to be 6.95 nm from the absorption curve and 6.17 nm from the desorption curve, which appeared to be larger than the pores on HMSNPs and CMSNPs, and comparable with BMSNPs.

The relatively large particle size and the unique porosity led to a moderate specific surface area of 511.56 $m^2/g$. The surface was found to be very negatively charged, with a very low zeta potential of -59.3 mV.

### 2.3.4 Degradation of the MSNPs

The degradation patterns of the different MSNPs were studied by monitoring changes of each MSNP in size and morphology during incubation in a simulated physiological environment (warm PBS). All of the MSNPs showed signs of degradation under the experimental conditions, suggesting that the silica was gradually dissolved into the buffer.

#### *2.3.4.1 Degradation of HMSNP*

HMSNPs were seen to be degraded during the incubation in warm PBS. The external diameter of HMSNPs was seen to decrease from an average of 105 ± 23 nm to 71 ± 10 nm over the course of 180 days incubation (Figure 2.8). An increasingly rougher surface was seen over the course of the degradation, suggesting that HMSNPs can be degraded from the outer surface (Figure 2.9 a). Furthermore, the degradation of HMSNPs appeared to also have progressed internally due to the buffer which was presented within the pores (Figure 2.9 b).

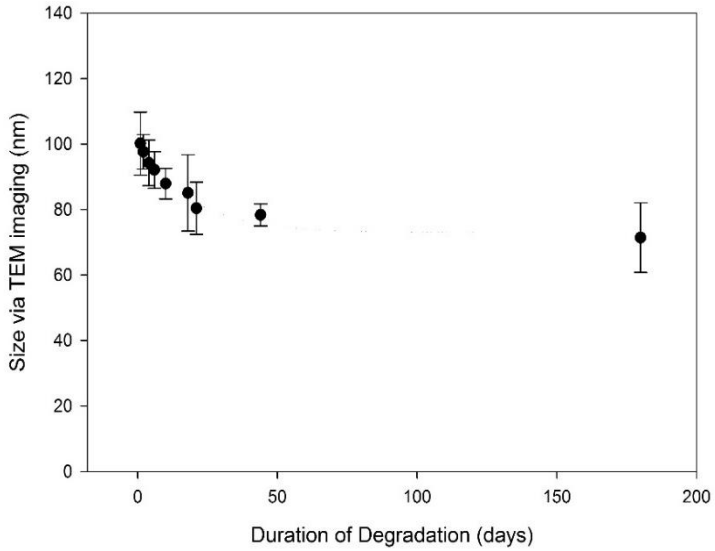


Figure 2.8 The size change of HMSNP measured with TEM over 180 days degradation in a simulated physiological environment

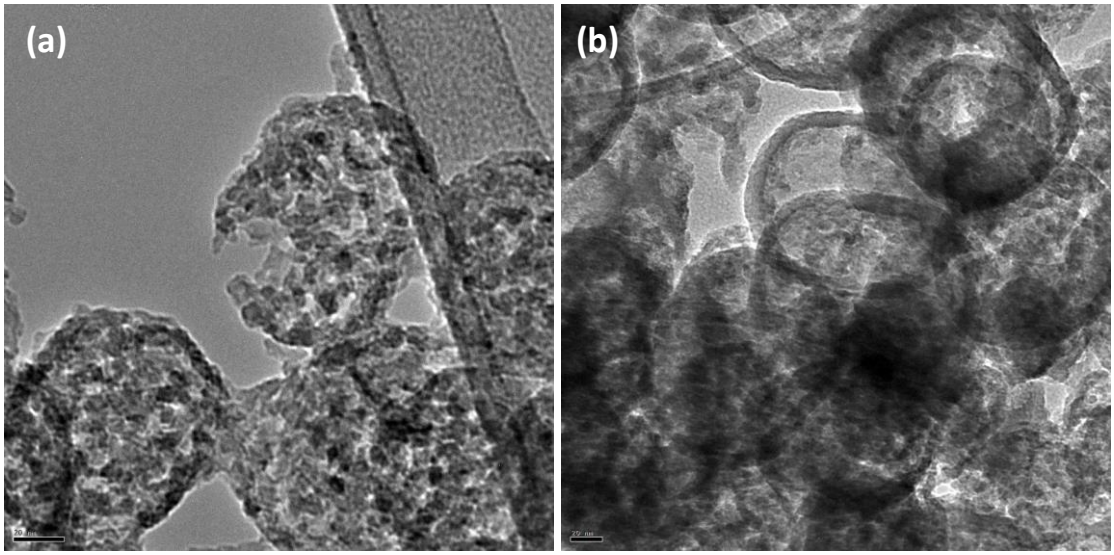


Figure 2.9 HMSNPs were incubated in physiological buffer and samples were imaged over 21 days, showing dissolution from either (a) the external or (b) the internal

### *2.3.4.2 Degradation of BMSNP*

BMSNPs also appeared to be degraded in a simulated physiological environment. They showed a decrease in overall diameter from 52.46 ± 6.64 nm to 35.12 ± 6.95 nm over 180 days of incubation (Figure 2.10). There was very little morphological change seen over the first 30 days of the incubation as the size decrease was not significant ($P > 0.05$)

(Figure 2.11). However, the degradation became more marked after further incubation, up to 180 days.

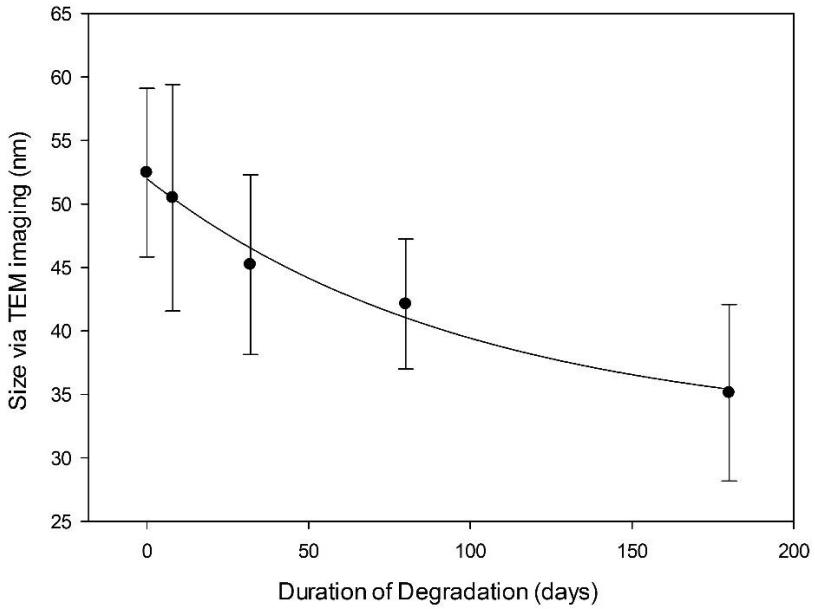


Figure 2.10 The size change of BMSNPs measured with TEM over 180 days degradation in a simulated physiological environment

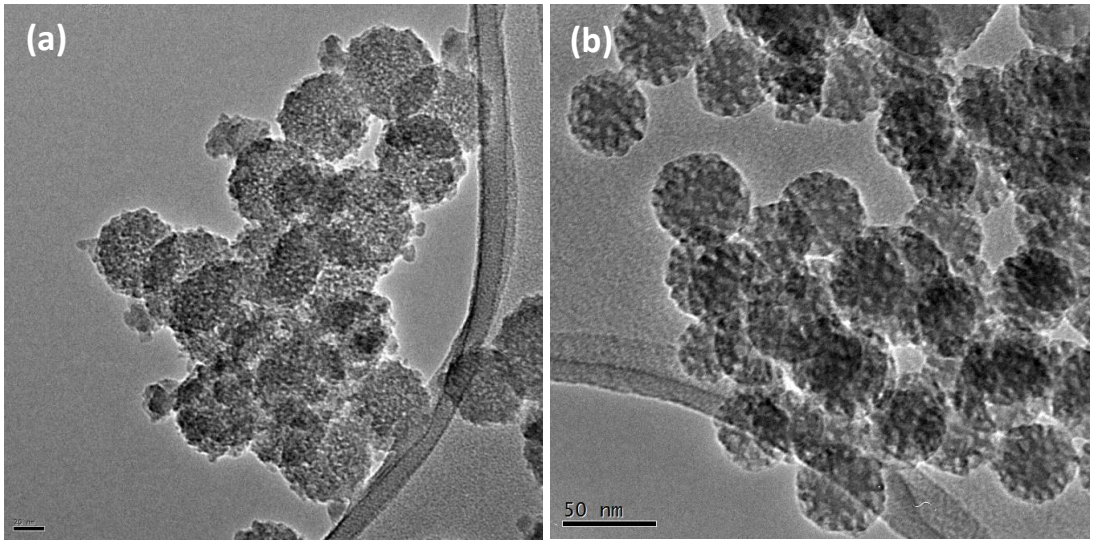


Figure 2.11 BMSNPs were incubated in physiological buffer and samples were imaged (a) before and (b) after 32 days degradation

### *2.3.4.3 Degradation of CMSNP*

CMSNPs also changed in size and morphology over the course of degradation.

After 32 days incubation, it can be seen that the structure of the 'petals' was very different from the pre-degraded ones, and the discrete pores were replaced with an open lacy structure (Figure 2.12 a). After 173 days incubation, it can be seen from TEM images that there was significant inter-particle conglutination (Figure 2.12 b). Individual particles can no longer be discerned at this point.

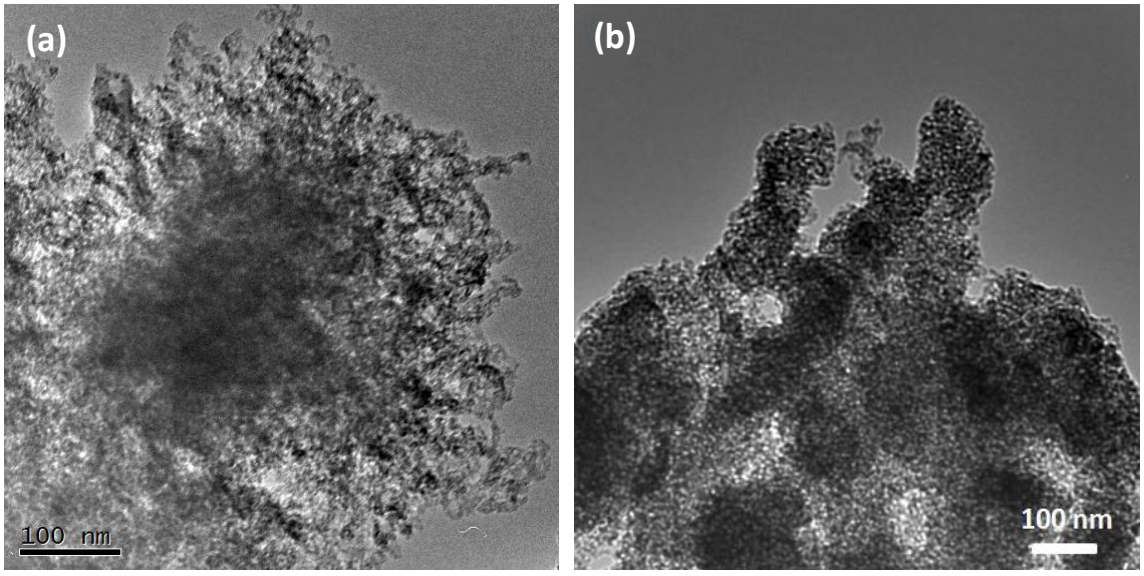


Figure 2.12 CMSNPs were incubated in physiological buffer and samples were imaged after (a) 32 days and (b) 173 days degradation

### *2.3.4.4 Degradation of WMSNP*

Despite having a large pore size, WMSNPs did not show any apparent degradation in a simulated physiological environment over 180 days.

The morphological change was hardly noticeable during the whole degradation (data not shown). WMSNPs showed only a small reduction in size after incubation in warm PBS over the whole 180 days degradation (Figure 2.13).

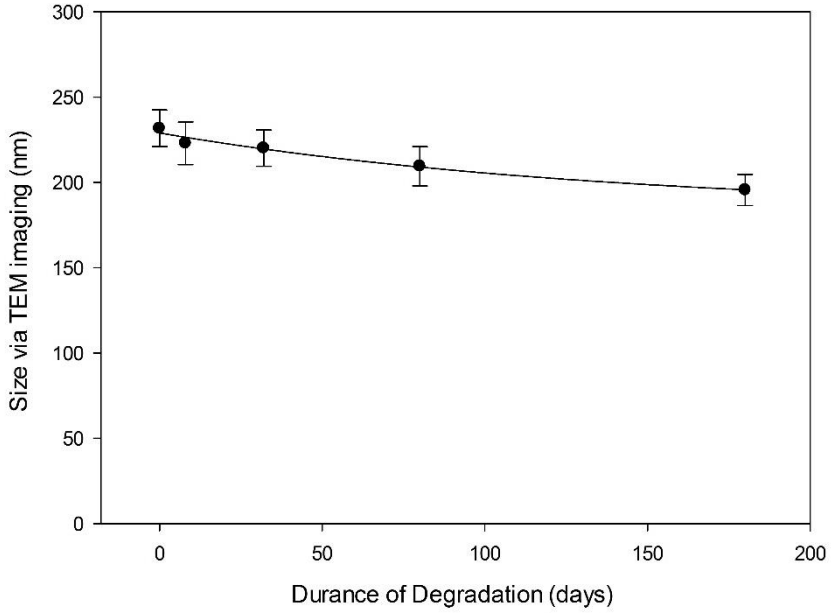


Figure 2.13 The size change of WMSNPs measured with TEM over 180 days degradation in a simulated physiological environment

## 2.4 BIOCOMPATIBILITY OF MSNPS

The biocompatibility of the synthesised MSNPs was assessed on four cell lines: RH30, RD, U87-MG and MCF7 cells (further details about the cell lines in section 3.2.2). The MSNPs showed varied cytotoxicity to these cell lines (Figure 2.14).

HMSNPs showed low toxicity to all four cell lines. After 24 hours, the cell viability was higher than 85 % against the control (untreated) in all cell lines. Long-time cytotoxicity was noticed on RD and U87-MG cell lines, as the viability dropped further to 78.92 % and 75.62 % against control respectively.

The biocompatibility of BMSNPs was seen to be lower than HMSNPs in all cell lines. In RH30, RD, U87-MG and MCF7 cells, the viability was decreased remarkably to 79.98 %, 72.14 %, 73.40 % and 62.99 % of the control, respectively, after long-time incubation. Comparing to other silica nanoparticles, BMSNPs appeared to be the least biocompatible

candidate for RD, U87-MG and MCF7 cells (Figure 2.14 b, c & d). This may result from an insufficient template removal of PS.

The cytotoxicity of CMSNPs was not seen to be significantly different from HMSNPs on all cell lines after 24 hours incubation. However, an increased toxicity to RH30 cells was seen after a long-time incubation, and the cell viability was reduced to 77.85% of the control ($P < 0.001$). CMSNPs were the most harmful MSNP to RH30 cells (Figure 2.14 a). The other three cell lines seem to be more adaptable to CMSNPs, and cell viability recovered slightly after 24 hours treatment up to 96 hours. This phenomenon was mostly obvious on MCF7 cells, as the viability was 81.99 % after 24 hours treatment, but recovered to 97.34 % of the control after a longer incubation time with CMSNPs ($P < 0.01$).

The cytotoxicity of WMSNPs was seen to be moderately low in RH30 and RD cells, as the cell viability remained higher than 84% with WMSNPs, even after 96 hours incubation. However, WMSNPs appeared to be more harmful to U87-MG and MCF7 cells after a long-time incubation (96 hours), as the viability was reduced to 78.31 % and 76.27 % of the controls, respectively (Figure 2.14 c & d).

The control particle, non-porous silica nanoparticles (SNPs) appeared to be the most biocompatible particles in this research against all four cell lines tested. The cell viability was as high as 91.65 %, 97.55 %, 107.49 % and 112.11 % of the controls after 96 hours SNP treatment in RH30, RD, U87-MG and MCF7 cells, respectively. It was noticed that the SNPs even encouraged cell survival rate in U87-MG and MCF7 cells after a long-time incubation, which is in fact not a desired property for a chemotherapeutics delivery vehicle.

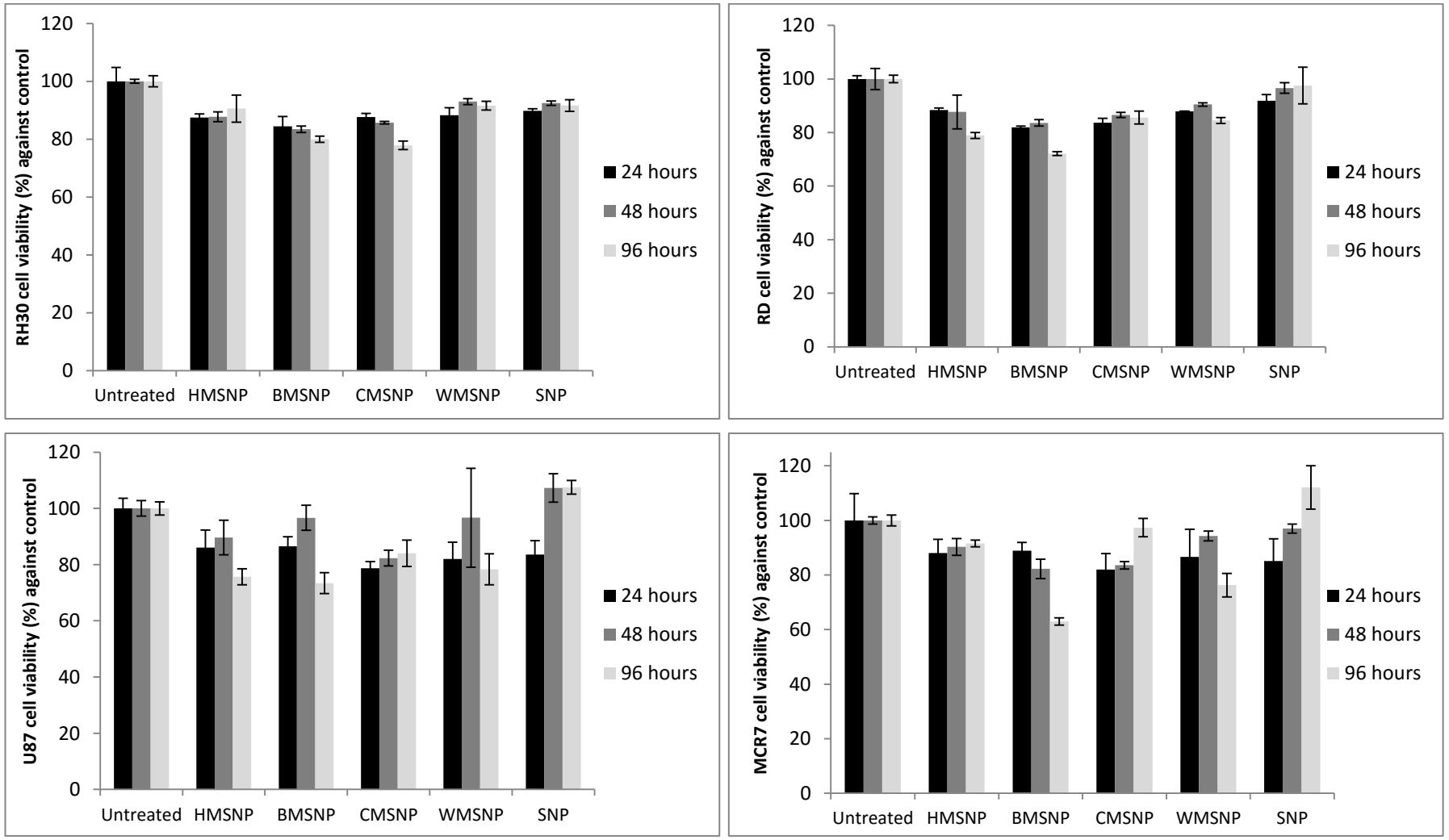


Figure 2.14 Viability of a) RH30; b) RD; c) U87-MG or d) MCF7 cells after treatment with 0.05 mg/mL MSNPs was assessed using an MTT assay. Values are expressed as a percentage of the untreated control for each time point. (The data are presented as the means ± standard deviation, n= 3)

| 24 hours | HMSNP | BMSNP | CMSNP | WMSNP | SNP |
|---|---|---|---|---|---|
| RH30 | * | * | * | * | * |
| RD | *** | *** | *** | *** | ** |
| U87-MG | * | ** | ** | * | ** |
| MCF7 | n.s. | n.s. | n.s. | n.s. | n.s. |
| | | | | | |
| 48 hours | HMSNP | BMSNP | CMSNP | WMSNP | SNP |
| RH30 | *** | *** | *** | *** | *** |
| RD | * | *** | *** | * | n.s. |
| U87-MG | n.s. | n.s. | ** | n.s. | n.s. |
| MCF7 | ** | ** | *** | * | n.s. |
| | | | | | |
| 96 hours | HMSNP | BMSNP | CMSNP | WMSNP | SNP |
| RH30 | * | *** | *** | ** | ** |
| RD | *** | *** | *** | *** | n.s. |
| U87-MG | *** | *** | ** | ** | * |
| MCF7 | ** | *** | * | *** | * |

Table 2.3 The significance test was performed on the data describing the viability of RH30, RD, U87-MG and MCF7 cell lines after treatment with 0.05 mg/mL MSNPs versus their own controls. n.s. = not significant, * $P < 0.05$, ** $P < 0.01$, *** $P < 0.001$

## 2.5 DISCUSSION

### 2.5.1 Template removal in MSNPs

Template removal is an important procedure in MSNPs synthesis affecting the biocompatibility, surface area, surface charge and drug loading efficiency. A number of different methods were used to maximise / optimise the template removal.

The structure-directing scaffold molecule in HMSNPs and WMSNPs was CTAB. This compound is known to be cytotoxic, causing phospholipid bilayer instability, quenched ATP synthase and increased cell death (Schachter, 2013). Furthermore, due to the positive charge of CTA+, a nanoparticle with insufficiently removed CTAB template would

present an overall positively charged or neutral surface (Domb and Khan, 2014, Lüderitz, 2012). Previous literature has demonstrated a number of protocols for efficient CTAB removal. In this study, refluxing the particles in acidic methanol for no less than 24 hours was elected. While HMSNPs were refluxed for the minimum 24 hours, WMSNPs were refluxed for 48 hours due to the higher CTAB concentration. It was found that CTAB was efficiently removed since the surfaces of HMSNPs and WMSNPs were both negatively charged after template removal.

Although CTAB was one of the structure-directing templates in CMSNPs, the water-insoluble diethyl ether also played an important role in CMSNPs fabrication and needed to be removed. After the ammonia was washed off, CTAB and diethyl ether was to be burnt out under high temperature. The calcinated CMSNPs product was found to be white (suggesting no/trivial carbon residue), and the powder was determined to be negatively charged with a very large specific surface area. This indicated that the template was removed. However, the surface charge of CMSNPs, although negative, appeared to be significantly higher than that found for HMSNPs and WMSNPs, possibly suggesting incomplete template removal. Other methods were also attempted to remove the CTAB/diethyl ether in CMSNPs, including optimisation of calcination conditions, refluxing the particles in a variety of organic solvents, and chemical extraction. However, the delicate 'petal-like' structure was lost with other template removal methods.

PS (the structure-directing template in BMSNPs) is known to be cytotoxic. Incubation with nano-scaled PS has shown damage and oxidative stress to cytoplasmic organelles (Cheng-Yu *et al.*, 2008). Furthermore, it is possible that the surface of BMSNPs became positively charged due to the insufficient removal of AIBA and PS, which would result in unfavourable cellular uptake and increased cell damage (details in Chapter 2.5.4). Previ-

ous literature has suggested burning out the organic template with high temperatures (Nandiyanto *et al.*, 2009). However, this method led to severe particle aggregation and carbon residue. Other methods, including refluxing in different organic solvents, tuning calcination conditions and chemical extraction, were attempted to remove the PS template. The template removal efficiency was evaluated using a Gemini VI surface analyser: before template removal, the pores of BMSNP were all occupied by PS templates leading to a relatively small specific surface area; the specific surface area ought to be increased after successful template removal due to the exposed inner surface of pores. It was found that the specific surface area of calcinated BMSNPs was 163.30 ± 0.39 $m^2/g$, much higher than that of BMSNPs before template removal (102.04 ± 0.33 $m^2/g$), indicating a successful template removal. And, the specific surface area of chemically extracted BMSNPs was 269.50 ± 0.98 $m^2/g$, much greater than that of the sintered BMSNPs. This indicated a more successful template removal using chemical extraction. The reason could be that the chemical extraction method not only successfully removes the organic template but also avoids sintering and aggregation of the BMNSPs. Therefore, the chemical method was applied to remove the PS template in the BMSNPs fabrication protocol. However, BMSNPs were still found to be slightly positively charged and the cytotoxicity of BMSNP remained the highest among all. This suggested that the current template removal method was still not effective enough.

### 2.5.2 The effect of particles size

Size matters, particularly for a drug nano-carrier. Not only is the cytotoxicity of a nanoparticle size-dependent, but the outer dimension also affects the enhanced permeability

and retention (EPR) effect, organ distribution and cellular uptake of nanoparticles (Oberdorster *et al.*, 2005).

The distribution of nanoparticles to organs after systemic administration is known to be size-dependent (Vonarbourg *et al.*, 2006). As the nanoparticles circulate through the body and enter into the various organs, large nanoparticles (>1μm) are easily removed from the circulating blood, where they accumulate in the kidneys and are excreted in the urine. Meanwhile, when nanoparticles are too small (< 10 nm), they can penetrate the tight junctions of endothelial cells (Schwab and Pang, 2000) leading to a nanoparticle accumulation in the liver and/or spleen and causing long-term toxicity (Buzea *et al.*, 2007). Therefore the optimal size of nanoparticles to avoid rapid system clearance and long term toxicity is from 10 to 1000 nm.

The complement system is a series of biochemical process in the immune system that clear foreign agents, such as drug delivery nanoparticles, from the body (Neun and Dobrovolskaia, 2011). The activation of the complement system is affected by the size of nanoparticles that the clearance of nanoparticles from the blood stream is slower when the size is smaller than 1μm (Mosqueira *et al.*, 2001).

While nanoparticles tend to accumulate in organs largely due to a filtration effect, a further mechanism promotes accumulation in tumour tissue: the EPR mechanism (Iyer *et al.*, 2006). In malignant tumour tissue, angiogenesis is induced by VEGF which is secreted from cancerous cells (see section 1.3.4) (Senger *et al.*, 1983). This newly formed tumour vasculature is extensive, but defective, irregular, and leaky with poorly aligned endothelial cells. Fenestrations between endothelial cells in tumours are also larger than in normal tissues, allowing macromolecule and/or nanoparticle entry. Moreover, cancerous tissues commonly have poor lymphatic drainage due to the wide lumen of their vasculature

(Skinner *et al.*, 1990), causing poor lymphatic filtration and clearance. This means that nanoparticles tend to accumulate in tumour tissue and the retained nanoparticles are not rapidly cleared by the lymphatic system. The EPR effect can be very significant: resulting in 10 to 50 times higher concentration of nanoparticles in tumours than in normal cells. The effectiveness can be enhanced by the introduction of certain proteins or drugs, such as VEGF and nitric oxide (Maeda *et al.*, 1994).

Cellular uptake is highly dependent on tissue and cell type, and also influenced by the physical properties of nanoparticles. While extremely small nanoparticles (< 10 nm) are able to penetrate the cell membrane by inducing holes formation on the membrane, larger nanoparticles are commonly internalised into mammalian cells *via* endocytosis and/or phagocytosis (Leroueil *et al.*, 2008, Lesniak *et al.*, 2013). Both the elasticity of cell membrane and ligand-receptors on the membrane affect the endocytotic uptake of nanoparticles (Lu *et al.*, 2009). The endocytosis of larger particles would induce larger local membrane disruption and deformation, thus the dynamic of this process is lower. When particles are larger than 500 nm, the elasticity of the membrane of most non-phagocytic mammalian cells reaches the limitation, leading to difficulty in the endocytotic uptake of particles (He *et al.*, 2010, Verma *et al.*, 2008). Therefore, a particle which is larger than 10 nm but smaller than 500 nm would be ideal for maximising cellular uptake of a nanoscaled drug carrier (Oberdorster *et al.*, 2005).

Therefore, for minimal cytotoxicity, maximal cellular uptake, optimal organ distribution and taking advantage of the EPR effect, MSNPs with a size between 50 to 200 nm could be an efficient drug carrier *in vivo*. In this research, both HMSNPs and BMSNPs are in the optimal size range, suggesting that they are more likely to be accumulated in tumours

and cells without rapid clearance. The size of WMSNPs (approx. 232 nm) is slightly over the optimal range which may lead to a more rapid system clearance and difficulty in cellular uptake.

CMSNPs may be considered to be less appropriate as a candidate for nano-scaled drug carrier, since it was shown to be much larger than the optimal size range (although reported to be 200 nm approx. in previous literatures; (Zhang *et al.*, 2010)). The high cytotoxicity of CMSNPs to certain lines may result from its large size (Figure 2.14 a).

### 2.5.3 The effect of shapes

Although the shape of a drug nano-carrier has not been considered a physical property as important as its outer dimension in many studies, shapes in fact are found to affect many parameters, such as cellular uptake, cell adhesion, viability and apoptosis (Gupta and Gupta, 2005a, Park *et al.*, 2008b, Chithrani *et al.*, 2006). For example, a rod-shaped MSNP with high aspect ratio would have a larger contact interface area with the cell membrane than the spherical counterpart, therefore causing more efficient cellular uptake in non-phagocytic cells; but it would also cause disturbance of the cytoskeleton and a reduced cell viability (Huang *et al.*, 2010). The mechanism is poorly understood to date.

All tested MSNPs were seen to be roughly spherical in shape with small aspect ratios and therefore the influence of particle shape is likely to be negligible.

### 2.5.4 The effect of surface properties

Surface properties are considered to be important parameters in nano-medicine, and would be expected to affect drug loading, particle functionalisation and biocompatibility.

Since the main drug loading mechanism for MSNPs is surface adsorption, a larger nanoparticle surface area would allow more cargo molecule attachment; clearly a desirable property for a drug carrier (Walkey *et al.*, 2012). Surface functionalisation is also found to be more effective on MSNPs with a relatively larger surface area since more reactive groups would be exposed on the surface (Chen *et al.*, 2005).

The specific surface area of HMSNPs and CMSNPs was shown to be exceptionally large (Table 2.2), and may therefore result in a more effective drug loading and surface modification than BMSNPs, WMSNPs and SNPs.

Nanoparticles with higher absolute values of zeta potential have been found to be more stable in suspension and can be more efficiently taken by tumour cells (Win and Feng, 2005, Chung *et al.*, 2007). Negatively charged nanoparticles have been found to be more stable in suspension and beneficial for efficient endocytosis into cells (He *et al.*, 2010).

After the deprotonation of silica in a neutral buffer, the negatively charged silanol group ($SiO^-$) is exposed on the particle surface. Therefore, bare MSNPs ought to present an overall negatively charged surface. However, the surface charge of synthesised MSNPs can be altered by adding chemicals during synthesis, and varied due to insufficient template / surfactant removal. On BMSNPs, in particular, the surface charge was found to be slightly positive (Table 2.2), which was possibly because of the insufficient removal of the positively charged PS template. This positively charged surface and small absolute value of zeta potential might be the cause of high agglomeration and cytotoxicity of BMSNPs to most tested cell lines. HMSNPs, CMSNPs and WMSNPs were determined to have negatively charged surfaces with relatively high absolute values of zeta potential, which was seen to be an advantage as a drug carrier *in vivo*.

### 2.5.5 The effect of porosity

The degree of porosity affects the surface area of a nanoparticle and therefore biocompatibility and absorbance of compounds. The pore diameter of MSNPs will also influence the drug loading capability. Drug loading and release is sustained when the pore diameter and drug molecule are approximately the same size (He and Shi, 2011). Since the size of most chemotherapeutic molecules is less than 2 nm, a small pore size of around 2 nm is desirable for efficient loading of chemotherapeutics. However, a large pore size can also be beneficial to load large molecules, such as peptides and nucleic acids.

HMSNPs and CMSNPs had the largest specific surface area and smallest pore sizes. Their pore sizes were smaller than 3 nm, which was roughly comparable to the size of most chemotherapeutic molecules. This could result in a high cargo molecule loading capacity for most chemotherapeutics. BMSNPs and WMSNPs presented larger pore sizes, thereby a smaller specific surface area. The loading capacity of chemotherapeutics in them might be not as efficient as in HMSNPs and CMSNPs. However, BMSNPs and WMSNPs could be more suitable to load larger molecules, such as siRNA.

### 2.5.6 MSNPs degradation

The solubility of amorphous silica in water at a neutral pH has been shown to range from 70 to more than 250 ppm at 25 °C (Iler, 1979, Tarn *et al.*, 2013). Therefore MSNPs were expected to be degraded gradually in aqueous solution such as cytoplasm and/or extracellular matrix.

It was found that the degradation patterns in the tested MSNPs varied greatly (section 2.3.4). This variation may result from the electrolyte concentration, differences in particle

size and surface area, the state of internal hydration, or impurities in the silica (Marshall and Chen, 1982). All of these factors would lead to a difference in the biodegradability of MSNPs.

### 2.5.7 Factors affecting biocompatibility other than the physical properties of MSNPs

It has been demonstrated that the biocompatibility of MSNPs can be affected by the outer dimension and surface properties. The sensitivity to silanol groups can vary greatly in different cell lines, leading to a different response to the MSNPs. However, the biocompatibility of tested MSNPs was also seen to be affected by other factors, such as impurities and insufficient template removal.

Impurity elements may be introduced into the nanoparticles from minor impurities in the reagents used and leaching from glass used during the synthesis. For example, elemental analysis of HMSNPs by EDX mapping (Figure S2.1, Figure S2.2) showed a number of elements in the particles other than Si, O (in silica), C and Cu (on the grid). Although the amounts of these elements may seem trivial, it is possible that ions, such as $Al^{3+}$, could result in disturbance in some cellular functions and reduced cell viability (Alshatwi *et al.*, 2015) and so synthesis for clinical use would have to be carefully controlled.

Another possible cause of reduced biocompatibility of MSNPs is the insufficient template removal. No template was used in the synthesis procedure of non-porous SNP and SNPs showed the highest biocompatibility in all the tested cell lines. Meanwhile, the synthesis of all MSNPs included a template removal procedure which could be incomplete. HMSNPs, CMSNPs and WMSNPs used CTAB as structure-directing template which

was proven to be cytotoxic (Yasun *et al.*, 2015). This may result in reduced biocompatibility of those MSNPs. The cationic bio-hazardous PS template residue in BMSNP was thought to be responsible for the highest cytotoxicity seen in the cell lines tested.

### 2.5.8 Evaluation of cytotoxicity of MSNPs and cell survival

Four different techniques were used to evaluate cell number depending upon the particular experiment.

1) Crystal violet (CV) is a triphenylmethane dye which intercalates with DNA in both live and dead cells in a similar manner to ethidium bromide but is less mutagenic and detectable in the visible range. CV staining therefore provides a simple method for obtaining quantitative data on the number of cells based on the absorbance of the dye by DNA in the cells. It was confirmed that the absorbance reading of CV was linearly correlated to cell number in all tested cell lines with concentrations between 25,000 to 250,000 cells / mL (data not shown).

   However, CV was found to stain the silica nanoparticles used in this research. With increasing concentration of MSNPs, the absorbance reading of CV increased. Therefore the CV assay was not suitable for the evaluation of cytotoxicity in the presence of MSNPs.

2) Trypan blue is a live / dead stain. The dye is not able to traverse intact membranes of live cells and stain them, whereas it can pass through the damaged cell membranes of dead cells and colour them blue. The live / dead cells can be distinguished under a microscope and the live / dead cell number can be counted with a

haemocytometer. Furthermore, stained MSNPs were microscopically distinguishable from live cells.

However, the cell counting procedure was time-consuming and cell viability may change during the experiment. Trypan blue is not suitable for an experiment compositing too many samples, including assessments in 96-well microplates, as the cell viability can be largely altered during the experiment.

3) 3-(4, 5-dimethylthiazol-2yl)-2, 5-diphenyl tetrazolium bromide (MTT) assay is a colourimetric assay based on the capacity of the cellular mitochondrial dehydrogenase in living cells to reduce the yellow water-soluble substrate MTT into a water insoluble dark blue/purple formazan product. It was confirmed that the absorbance reading of MTT was linear with respect to cell number in the range of 25,000 to 250,000 cells / mL (data not shown) after MTT was dissolved in DMSO.

   Although MTT was also found to stain MSNPs (data not shown), the purple coloured formazan was produced from cellular reactions. The absorbance of MTT was shown to be unchanged with increasing concentration of MSNPs. The MTT assay is suitable for measuring cell viability after treatment with MSNPs, loaded MSNPs, or drug only.

   It should be noted that the results in U87-MG cells showed a large standard deviation due to severe cellular agglomeration.

4) Hoechst 33342 is a fluorescent dye that stains DNA and provides a bright blue fluorescence under UV excitation. The Hoechst assay enables a simple and fast means to obtain cell number from the fluorescence of the dye. It was confirmed

that the fluorescence reading of Hoechst 33342 showed a linear correlation with cell number for concentrations between 25,000 to 250,000 cells / mL (data not shown). Similar to CV, Hoechst 33342 was also found to stain MSNPs and not suitable for the evaluation of cytotoxicity in the presence of MSNPs.

## 2.6 CONCLUSION

HMSNPs, BMSNPs, CMSNPs and WMSNPs were synthesised to enable full characterization and analysis for their suitability as drug carriers.

In depth analysis showed that HMSNPs were the most suitable candidates for an intracellular and/or intercellular nano-scaled chemotherapeutics carrier *in vivo*, due to the high loading capacity, appropriate size and surface properties and low cytotoxicity to many cell lines. Meanwhile, WMSNPs could also be successful drug nano-vehicle candidate by virtue of their biocompatibility and desirable surface properties. However, WMSNPs were slightly larger than the optimal size range which may lead to fast clearance from the system *in vivo*. The pore size of WMSNP was also shown to be too large for loading the majority of chemotherapeutics, but could be suitable for siRNA or peptide loading.

The remaining two MSNPs tested may not be suitable drug nano-carrier without further modification or improvement. BMSNPs were found to be toxic to many cell lines. Furthermore, the nearly neutral surface charge of BMSNPs may cause severe agglomeration and difficulty in surface functionalisation. CMSNPs were also not seen as a suitable chemotherapeutics carrier since the size was too large for efficient endocytosis into cells, and may also show fast clearance from the system *in vivo*.

# Chapter 3

# The physiological study of a potent hydrophobic chemotherapeutic: LY294002

MSNPs have been shown to have suitable properties to carry chemotherapeutics to a tumour. To develop the system further, it is useful to show effective loading with a specific drug molecule. Since one of the potential advantages of the MSNPs is the ability to overcome drug delivery barriers and to deliver anti-cancer agents with poor solubility and/or specificity, the anti-cancer drug, LY294002 was chosen as a representative model of a hydrophobic drug in this research.

The physiological function of free LY294002 was therefore extensively assessed and discussed in this Chapter. The cellular response after packaging in MSNPs will be discussed in Chapter 4 and Chapter 6.

## 3.1 INTRODUCTION

### 3.1.1 LY294002

LY294002 is a potential anti-cancer drug which has shown anti-tumour activity *in vitro* and *in vivo* for many different types of cancers (Hu *et al.*, 2000, Su *et al.*, 2003).

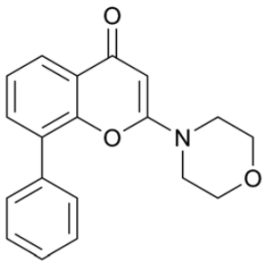


Figure 3.1 The chemical structure of LY294002

LY294002 is a small synthetic organic molecule which is a derivative of quercetin with a functional morpholine ring (Figure 3.1). The molecular formula is $C_{19}H_{17}NO_3$; the molecular weight is 307.343; and the molecular size is less than 5Å (from spatial modelling by Dr. Ben Pilgram, Cambridge), which is much smaller than the pore size of the MSNPs.

As a widely used phosphatidylinositol-4,5-bisphosphate 3-kinases (PI3Ks) inhibitor, LY294002 shows inhibition to all classes of PI3Ks even at low concentrations: the half maximal inhibitory concentration ($IC_{50}$) is as low as 1.4 μM (Garlich *et al.*, 2008).

### 3.1.2 PI3K pathways

PI3Ks are a family of enzymes that phosphorylate 3'-hydroxyl groups of phosphatidylinositols (PIs) at the inositol ring (Angyal *et al.*, 1989). The lipids generated from PIs activate many cellular functions such as cell survival, cell cycle, cellular trafficking, growth

proliferation and metabolism by binding to many downstream proteins at the Pleckstrin homology (PH) domain, a lipid-binding protein domain (Jiang *et al.*, 2001).

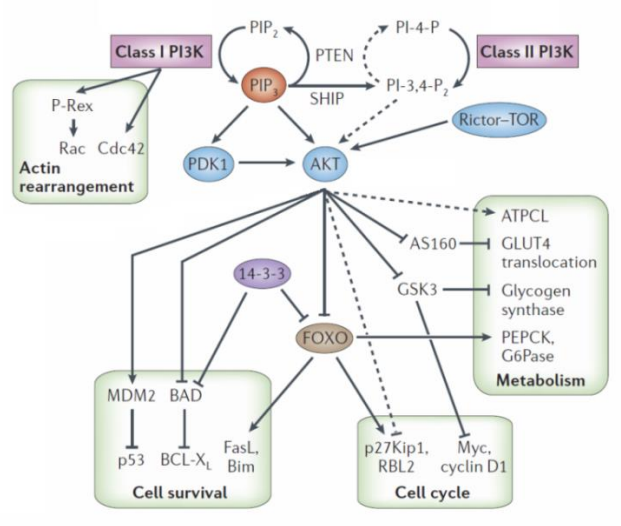


Figure 3.2 Schematic illustrations of PI3K signalling pathways in mammalian cells. Class I PI3K catalyses PI into phosphatidylinositol-3,4,5-trisphosphate (PIP3, shown in an orange balloon) that activates PDK1, Akt and their downstream proteins involved in metabolism, cell survival, cell cycle and other cell signalling pathways. [Image modified from (Engelman *et al.*, 2006)]

One particularly important target of PI3K is Akt (also called protein kinase B, or PKB). With an active PI3K on the cell membrane, Akt can be activated by phosphorylation within the carboxy terminus at Serine 473 (ser-473) and by phospholipid binding and activation loop phosphorylation at Threonine 308 (Thr-308) by PDK1. The phosphorylation at ser-473 and Thr-308 works in parallel (Alessi *et al.*, 1996).

The activity of PI3K-Akt and their downstream signalling pathways are involved in many cellular processes, such as cell survival and metabolism (Figure 3.2).

### 3.1.3 PI3Ks in cancer

PI3K pathways are often over-expressed in cancers due to the amplification or the mutation of genes that encode some of the essential components of the PI3K family. The over-

expression of PI3Ks usually leads to aberrant activation or inhibition of downstream effectors, such as Akt and FOXOs, resulting in cellular malignancy and dysregulation of many cell function cascades (Mahajan and Mahajan, 2012).

PI3K-Akt pathways are found to promote cell survival by supressing pro-apoptotic proteins or tumour suppression. For example, Akt has been shown to downregulate p53 (an important tumour suppressor) and BCL2-antagonist of cell death protein (BAD, a pro-apoptotic protein) (Gottlieb *et al.*, 2002, Song *et al.*, 2005, Cardone *et al.*, 1998, Datta *et al.*, 1997). Therefore, active Akt would inhibit p53-dependent and/or BAD-dependent apoptosis in cancer and enhances cell survival.

Over-expressed PI3K-Akt signalling is also involved in cell metabolism in cancers (Barthel *et al.*, 2005, Osorio, 2012, Nakae *et al.*, 2001). Glucose uptake (membrane translocation of glucose molecules) is regulated by PI3K-Akt pathways *via* insulin signalling pathways through the stimulation of different glucose transporters, such as GLUT4. PI3K-Akt also affects glycolysis by mediating glycogen synthase, which generates glycogen from glucose. The glycogen synthase kinase 3 (GSK3) is inhibited by active Akt, leading to the activation of glycogen synthase and enhanced glycogen generation. Some publications even reported that PI3Ks affect the Warburg effect *via* HIF1 in cancer (Courtnay *et al.*, 2015).

Furthermore, PI3K mutations play a role in the malignancy of certain cancers. For example, the gain-of-function mutation of p85α results in the loss of the c-terminal inhibitory domain of PI3K and is responsible for multiple cancers of the brain, colon and ovaries (Engelman *et al.*, 2006).

Due to the essential roles of PI3Ks and the over-expression of PI3Ks in many cancers, they are considered to be a drug target for cancers (Courtney *et al.*, 2010).

## 3.2 MATERIALS AND METHODS

### 3.2.1 LY294002

LY294002 used in this study was provided by Prof. Donohoe's group (University of Oxford) and Cambridge Bioscience (Cat. CAY70920, Cambridge, UK). The compound from both suppliers was all characterised with NMR (Bruker DPX200, UK) to confirm the molecular structure.

The fluorescence of LY294002 was measured with Cary Eclipse Fluorescence Spectrophotometer (Agilent Technologies, LA, USA). The excitation wavelength was ranged from 300 nm to 600 nm, and the emission wavelength was ranged from 320 to 700 nm.

### 3.2.2 Cell lines

Four different immortalized cell lines were tested in this study. They were:

RH30 (American Type Tissue Culture Collection [ATCC] no. CRL-2061), an alveolar rhabdomyosarcoma (RMS) derived from the bone marrow metastatsis of 17-year-old male. Alveolar RMS (ARMS) commonly occurs during adolescence in the limbs, chest, genitalia, and abdomen.

RD (ATCC no. CRL-7763), an embryonal RMS (ERMS) derived from the muscle carcinoma of a 7-year-old female. The ERMS is a childhood maligant tumour and more likely to occur in children with a high birth weight. Tumours often arise in the head, neck, and genitourinary tract. The cells are adherent with spindle shape and histologically resemble foetal muscle.

U87-MG (ATCC  no. HTB-14), an astrocytoma cell line derived from human malignant glioblastoma. The cells are adherent epithelial cells. It was noticable that U87-MG cells are likely to agglomerate rather than form a monolayer on a microplate.

MCF7 (ATCC no. HTB-22), an adenocarcinoma cell line, derived from a metastatic site (pleural effusion) of invasive breast ductal carcinoma isolated from a 69-year-old female. The cells are adherent epithelial cells.

### 3.2.3 Cell culture and treatment with LY294002

#### *3.2.3.1 Subculture*

Cells were plated at a density of $1 \times 10^4$ cells per well (96-well microplate, Nunc) in 200 µL of growth medium (Dulbecco's Modified Eagle's Medium (DMEM) with 25 mM glucose, 1 mM pyruvate [Sigma], supplemented with 10% foetal bovine serum [Sigma], 2 mM L-Glutamine [Gibco], 100Ū/mL Penicillin and 0.1 mg/mL Streptomycin [Gibco]) in 96-well microplates and incubated at 37 °C in 5% $CO_2$ atmosphere.

#### *3.2.3.2 Treatment with LY294002*

LY294002 was dissolved in ethanol solution before the treatment. After 24 hours cell incubation, the culture media was replaced with fresh media and LY294002 solution was added. The percentage of ethanol was kept below 0.5%.

- Different oxidative conditions:

In order to simulate the hypoxic tumour microenvironment, LY294002 treated cells were incubated under both hypoxic (1% $O_2$, 5% $CO_2$) and normoxic condition (21% $O_2$, 5%

$CO_2$). Cell number and cell viability assessments were performed after 24-hour treatment; western blots were performed after 4-hour treatment.

- Hypoglycaemia:

In the experiments on cells under glucose stress, cells were seeded in microplates for 24 hours before the media was replaced with low glucose media (DMEM without glucose, pyruvate or glutamine [Gibco], supplemented with 10 % FBS [Sigma], 1 mM pyruvate [Sigma], 2 mM L-Glutamine [Gibco], 100Ū/mL Penicillin and 0.1 mg/mL Streptomycin [Gibco], and desired concentration of glucose [Sigma]). After 24 hours incubation in low glucose media, LY294002 was added to the cells reaching a final concentration of 50 µM. Further experiments were performed after 24 hours treatment.

### 3.2.4 Western blot

Cells were lysed in tissue extraction buffer (TEB, 50 mM Tris-HCl (pH 7.4), 150 mM NaCl, 1 mM EDTA, 1% Triton X-100, 0.1% SDS, add 1 tablet of protease inhibitor in every 10 mL buffer before use). Each extract was collected and transferred to a 1.5 mL sterile tube (Eppendorf). Protein concentrations were determined using a Bicinchoninic acid assay (BCA assay; Pierce™, Thermo SCIENTIFIC).

5 µg of protein from each sample was resolved by SDS-PAGE (gel: Thermo SCIENTIFIC 8-16% Precise Protein Gel, 1 mm x 15 wells; running buffer: Thermo SCIENTIFIC BupHTM Tris-HEPES-SDS running buffer) at 50 V for 2 hours, and transferred to nitrocellulose membranes in cold transfer buffer (200 mM Glycine, 25 mM Tris, 20% Methanol) at 100 V for 1 hour. To visualise the protein bands and confirm the success of

SDS-PAGE, the membranes were stained in Ponceau S solution (0.1% (w/v) Ponceau S in 5% acetic acid) for 5 min, and de-stained in water before next step.

Membranes were washed in TBST buffer (10 mM Tris-HCl, 150 mM NaCl, 0.05% Tween-20), and blocked in 5% milk (non-fat) - TBST solution overnight.

The primary antibody, pAkt-ser473 (#4060 Cell Signaling Technology™) or Akt (pan) (#4691 Cell Signaling Technology™), was diluted to 1/1000 in 5% milk (non-fat) - TBST solution. Membranes were incubated in a primary antibody dilution for 1 hour at room temperature. After the membranes were washed 3 times in TBST, they were incubated in 1/2000 secondary anti-rabbit antibody in 5% milk (non-fat) - TBST solution for 30 min. The membranes were washed 3 times and incubated in 4 mL working solution of Pierce™ ECL Western Blotting Substrate (Life technologies™) for 5 min.

The chemiluminescence was detected by exposure on Amersham Hyperfilm ECL (#28-9068-35 GE Healthcare Life Technology™).

### 3.2.5 Densitometry of western blot

The band intensity on the western blots was quantified using Fiji™ software (based on ImageJ). On each blot, the density of both pAkt-ser473 and Akt (pan) were divided by the density of the house-keeping protein β-actin. Samples were then normalized against β-actin. Values are expressed as % of the zero drug control.

### 3.2.6 Cell survival number assessed with CV assay

After cell lines were incubated with the drug under hypoxic (1% $O_2$) or normoxic condition (21% $O_2$), the surviving cell number was quantified using a crystal violet (CV) assay.

Cells were rinsed with pre-warmed PBS and fixed with 1% glutaraldehyde solution for 30 min. Fixed cells were stained with crystal violet solution (1% crystal violet [Sigma] dissolved in a mixture of methanol: glacial acetic acid: $H_2O$, 5:1:4 v/v/v) for 1 hour at room temperature. After staining, the supernatant was removed and cells washed carefully three times with water. The microplate was then drained and dried overnight. Before reading, 100 µL solubiliser (1% SDS in 10% glacial acetic acid) was added to each well and re-suspended vigorously. The absorbance was read at 540 nm.

### 3.2.7 Cell viability assessed with MTT assay

After cell lines were incubated with LY294002 under hypoxic (1% $O_2$) or normoxic condition (21% $O_2$), the cell viability was evaluated using MTT assay. The procedures of MTT assay was described in section 2.2.4.

### 3.2.8 Lactate assay

Lactate generation was evaluated with BM-lactate strips [Roche]. For each sample, 25 µL media was added on to the reactive pad of a new lactate strip. The result was read by an Accutrend Lactate Meter [Roche] after incubation for 1 min.

In order to eliminate the influence of cell number, Hoechst 33342 stain was immediately performed after the measurement of lactate generation. Cells were incubated in 1 µg/mL Hoechst-culture media solution for 30 min at 37 °C. Immediately before reading, the Hoechst containing culture media was removed and the microplate was washed with PBS

once carefully. After 100 µL warm PBS was added to each well, the fluorescence signal was read with FLUOstar OPTIMA plate reader (exc. 350 nm; emi. 461 nm; well-scan mode) without shaking. Blank wells with only PBS were set as a control.

### 3.2.9 Oxygen consumption rate assay

#### *3.2.9.1 Oxygen consumption rate (OCR) assessed with MitoXpress-Xtra*

The OCR was assessed with MitoXpress-Xtra probe (Luxcel™). The probe is oxygen sensitive and its phosphorescence is quenched in high oxygen.

Each well of the treated cells was rinsed once with warm PBS before 150 µL probe containing culture media (Media: MitoXpress-Xtra (v/v) = 14:1) was added. The wells were then sealed from the atmosphere using 100 µL highly viscous HS Mineral Oil (Luxcel). TR-F intensity was read on a plate reader (BMG FLUOstar) at 37 °C, and 18 % $O_2$ at Ex. 340 ± 50nm, Emi. 650 ± 50nm.

The lifetime is evaluated using dual delay time resolved measurements (Figure 3.3). The lifetime (τ) can be calculated as:

$$\tau\ (\mu s) = \frac{t2-t1}{Ln(\frac{W_2}{W_1})}$$

Where $W_1$ and $W_2$ represent the dual measurement windows while t1 and t2 represent the delay time prior to measurement of $W_1$ and $W_2$ respectively

As the cells respire, oxygen was depleted from the sealed wells resulting in increasing signal on the plot of lifetime. Select the linear portion of the signal profiles and apply linear regression to determine the slope and correlation coefficient (quality control of the fit)

for each of the lifetime profiles. OCR was obtained by the mean of the slope values of the linear region.

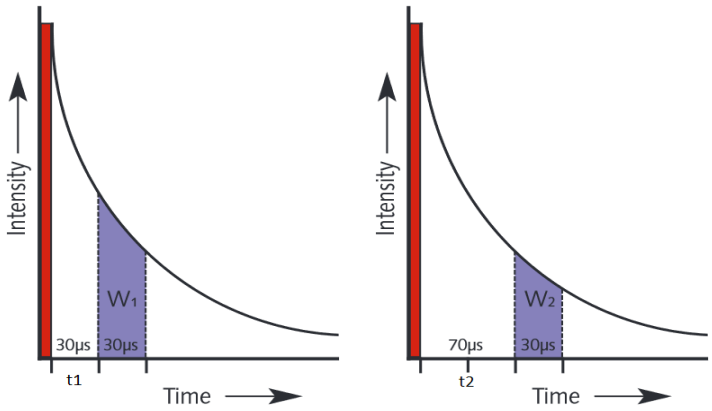


Figure 3.3 Illustration of the principle for the dual delay time resolved measurements [Image modified from (Luxcel, 2015)]

### *3.2.9.2 Intracellular oxygen level assessed with MitoXpress-Intra*

Intracellular oxygen was evaluated with MitoXpress-Intra ($NANO_2$, [Luxcel]) probe which consists of cationic hydrogel nanoparticles loaded with Pt(II)-5,10,15,20-tetrakis-(2,3,4,5,6-pentafluorophenyl)-porphyrin) dye. After the probes are internalised, the phosphorescence of the oxygen sensitive dye is quenched with increasing concentrations of oxygen. Drug induced changes in mitochondrial activity can be seen as changes in the probe signal overtime (data not shown). As $NaNO_2$ assays are unsealed, equilibrium is reached between oxygen consumption by the cells and back diffusion into the well from the environment. Cells will reach a "resting state" characterised by a plateau signal in lifetime plot.

Treated cells were washed once with warm PBS and incubated with probe-containing culture media (Media: MitoXpress-Intra (v/v) = 10:1) overnight.

Immediately before read, probe-containing culture media was replaced with respiration media (normal culture media with 4500 mg/L glucose). TR-F intensity was read on a

plate reader (BMG FLUOstar) at 37 °C and an appropriate oxygen level (either 2% $O_2$ as hypoxia or 18% $O_2$ as normoxia) at Ex. 340 ± 50nm, Emi. 650 ± 50nm every 3 min till signal stabilised.

The lifetime is evaluated using dual delay time resolved measurements as described in section 3.2.9.1 (Figure 3.3).

More than 10 points were taken from the plateau region of the lifetime (μs) plot for each sample. Intracellular oxygen can be calculated from lifetime using the equation:

$$Y = a + e^{(bx + c)}$$

where Y is the measured lifetime value; x is the intracellular oxygen (%); parameters a, b, c can be obtained from a calibration curve for each individual cell line. The calibration equation was fit using SigmaPlot 12.0.

### 3.2.10 ADP/ATP assay

ADP/ATP ratios were measured to differentiate the status of cell death and viability with ADP/ATP Ratio Bioluminescent Assay Kit (ELDT-100, EnzyLight™)

The Assay Buffer, Substrate and Co-substrate were thawed at RT and ATP, ADP enzymes were thawed on ice before the experiments.

ATP Reagent was prepared by mixing 95 μL Assay Buffer with 1 μL Substrate, 1 μL Co-substrate and 1 μL ATP Enzyme for each well. ADP Reagent was prepared by mixing 5 μL $ddH_2O$ with 1 μL ADP Enzyme for each well.

The treated cells in multiwell microplate were washed with warm PBS before the assay. 90 μL ATP Reagent was added to each well. The microplate was tapped gently for 1 min

to encourage the reaction. Luminescence (RLU A) of each well was then read on plate reader.

Ten min after reading the luminescence for ATP (RLU A), the luminescence of the samples was read again (RLU B) providing the residual ATP signal prior to measuring ADP. Immediately following reading RLU B, 5 μL ADP Reagent was added to each well and mixed by tapping the microplate gently. 1 min after mixing, luminescence (RLU C) was read on a plate reader.

ATP production has a linear correlation to the read of RLU A, whereas ADP production has a linear correlation to the read of (RLU C - RLU B). Therefore, the ADP/ATP ratio was calculated by:

$$\text{ADP/ATP ratio} = \frac{\text{RLU C} - \text{RLU B}}{\text{RLU A}}$$

### 3.2.11 Amplex Red assay

The Amplex Red assay was used to determine the production of reactive oxygen species (ROS) before and after LY294002 addition. Amplex™ Red reagent is a colourless substrate that reacts with hydrogen peroxide ($H_2O_2$) with a 1:1 stoichiometry to produce highly fluorescent resorufin (excitation/emission maxima=570/585 nm)

In experiments, culture media was removed completely from black multiwell microplates before the assay. Each well was washed with PBS once carefully. Then 50 μL warm clear DMEM (no phenol red, no serum, no antibiotics) was added. 1X Reaction Buffer was set as a negative control, and 1 to 10 μM $H_2O_2$ solution as standard.

The Amplex Red working solution comprised 100 μM Amplex Red 0.2 U/mL HRP separately. 50 μL Amplex Red working solution was added to each well including experiment, standard, and control groups. The microplate was when incubated at room temperature for 30 min, protected from light.

Fluorescence of each well was read at 542 nm excitation and 590 nm emission for 30 min at 5 min intervals. To quantify the concentration of $H_2O_2$ produced by treated cells, a standard curve was established between the concentrations of $H_2O_2$ (ROS) against the fluorescence signal of Amplex Red.

Levels of ROS ($H_2O_2$) at each time point were calculated from the calibration curve. The ROS Endpoint was picked at the $30^{th}$ minute read.

### 3.2.12 Data analysis and statistic test

Significance tests were performed using a two-tailed homoscedastic Student's t test on Microsoft™ Excel platform.

## 3.3 RESULTS

### 3.3.1 Characterisation of LY294002

Both the synthesised and the commercially supplied LY294002 were analysed. The chemical structure was assessed using NMR (data not shown) while the PI3K inhibition was assessed using SDS-PAGE western blot (data not shown). It was confirmed in both analyses that the compound presented the same chemical structure from both supplier; and they expressed the same function in inhibiting Akt phosphorylation.

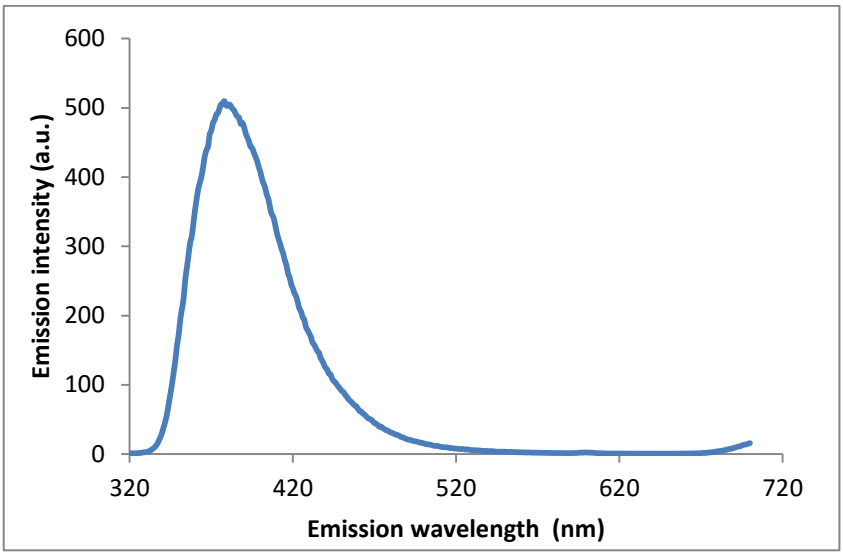


Figure 3.4 The emission intensity of LY294002 at different wavelengths (excited at 305 nm)

A spectrophotometer was used to determine the fluorescence of the LY294002 molecule at different wavelengths. It was found that after excitation at 305 nm the peak emission was at 392 nm for both the compounds (Figure 3.4).

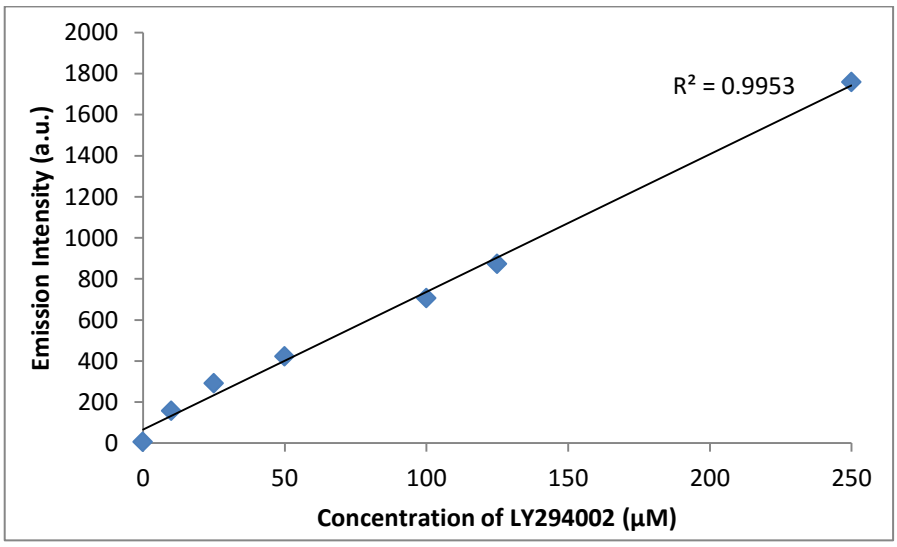


Figure 3.5 Concentration dependence of the emission intensity of LY294002 at 392 nm under an excitation at 305 nm

With Ex. 305 nm / Emi. 392 nm, the emission intensity was shown to be linear with respect to the concentration of the compound (Figure 3.5). No self-quenching was found in the tested range of concentrations.

Therefore, it was confirmed that the concentration of LY294002 can be evaluated by measuring the emission intensity of LY294002 at 392 nm when excited at 305 nm.

### 3.3.2 Inhibition of Akt phosphorylation

LY294002 acts upon all classes of PI3Ks and therefore affects the phosphorylation status of downstream targets. Since Akt is one of the most important downstream effectors of PI3Ks, the inhibition of PI3Ks by LY294002 was evaluated by determining the phosphorylation state of Akt at Serine 473 (pAkt-ser473).

Due to the hypoxic nature of the real tumour micro-environment, the phosphorylation status of Akt was investigated using cell lysates collected from cells treated with increasing amounts of LY294002 under both hypoxic (1% $O_2$) and normoxic (normal condition in laboratory, 21% $O_2$) conditions.

Cells were seen to respond differently to LY294002. The response was found to be dependent upon the cell type, LY294002 concentration, and environmental oxygen level.

In RH30 cells, treatment with the highest dose of LY294002 (50 µM) resulted in a large decrease in the level of phosphorylation of Akt at Ser473 (reduced to approx. 11.48 % relative to the zero drug control; $P < 0.001$) under normoxic condition. Conversely, the level of phosphorylation dropped to approx. 39.45 % of the control under hypoxic conditions (Figure 3.6 a, Figure 3.7 a).

In RD cells, the level of phosphorylation of Akt was seen to decrease to approx. 15.39 % ($P < 0.001$) relative to the zero drug control after treatment with 50 µM LY294002 under normoxic conditions (Figure 3.6 b, Figure 3.7 b). However, Akt can be seen to be phos-

phorylated in the presence of LY294002 under hypoxic conditions. Even when treated with the highest dose of LY294002 (50 µM), the level of phosphorylation of Akt at ser473 merely reduced by 30.83 % relative to the zero drug control (Figure 3.6 b, Figure 3.7 a).

In the presence of LY294002, U87-MG cells, the glioblastoma line, showed a large decrease in levels of Akt phosphorylation (Figure 3.6 c, Figure 3.7). After treatment with the highest dose of LY294002, the level of Akt phosphorylation was reduced to 12.35 % of the control under normoxic conditions ($P < 0.001$), and to approx. 38.08 % of the control under hypoxic conditions ($P < 0.05$).

Meanwhile, the phosphorylation status of Akt in MCF7 cells reduced with increasing concentration of LY294002 (Figure 3.6 d, Figure 3.7). The decrease was up to approx. 14.07 % of the control after treatment with 50 µM LY294002 under normoxia and to approx. 37.03 % of the control under hypoxia.

In summary, it was clearly shown that pAkt-ser473 was significantly reduced after treatment with LY294002 while the amount of pan Akt remained the same (blots in Figure 3.6; densitometry in Figure 3.7; significance test in Table 3.1) in all four tested cell lines. The inhibition of Akt phosphorylation was seen to be more marked with increasing concentration of LY294002.

This effect was shown to be more significant when the treatment was performed under normoxic conditions than under hypoxic conditions. In particular, LY294002 appeared to be the least effective in inhibiting PI3K functions in RD cells under hypoxic conditions.

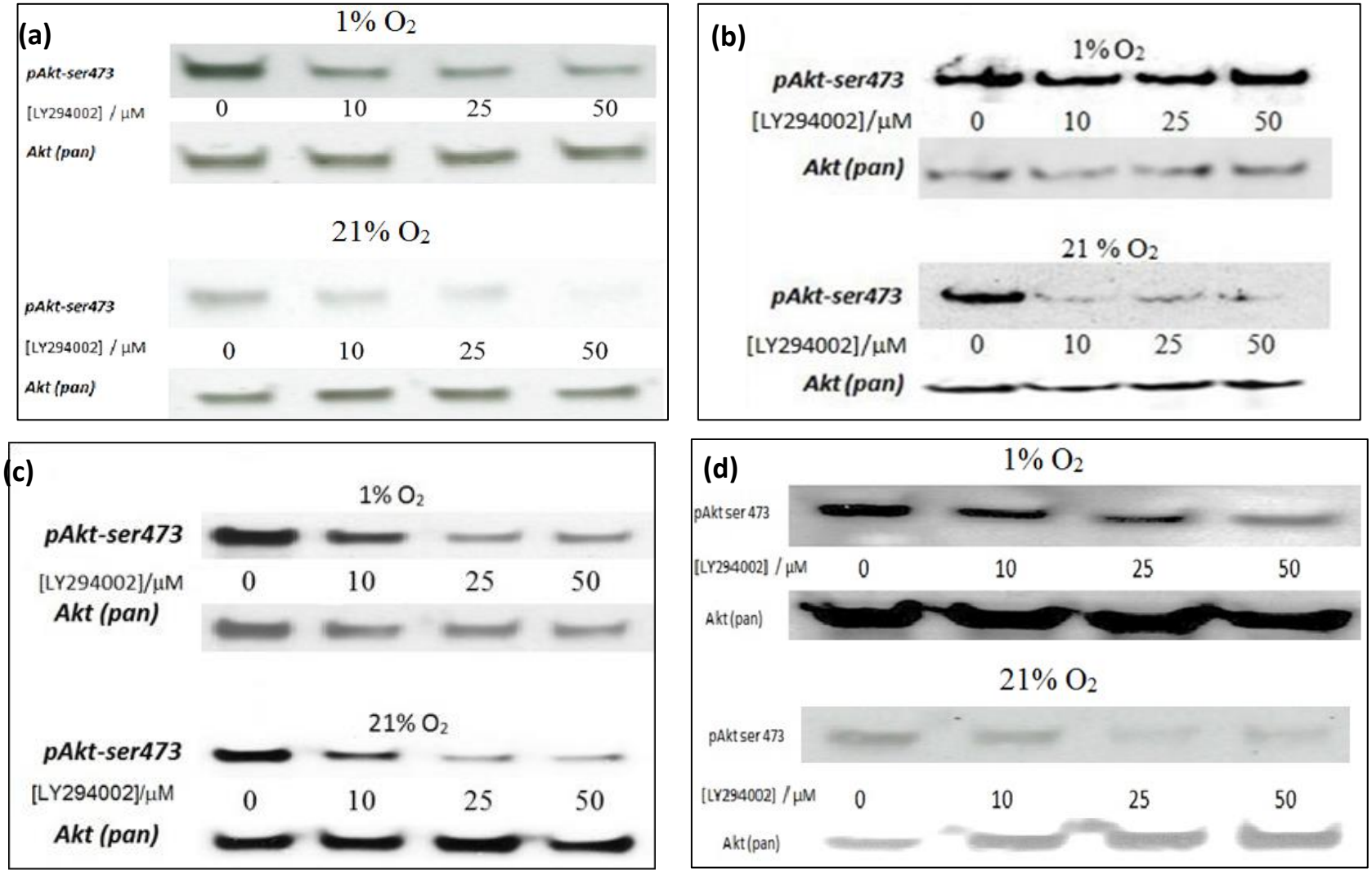


Figure 3.6 Representative western blots of cell lysate from a) RH30; b) RD; c) U87-MG or d) MCF7 cells incubated with increasing amounts of LY294002 under either 1% $O_2$ or 21% $O_2$ condition. Blots were probed with anti-Akt (pan) or anti-pAkt-ser473 antibodies

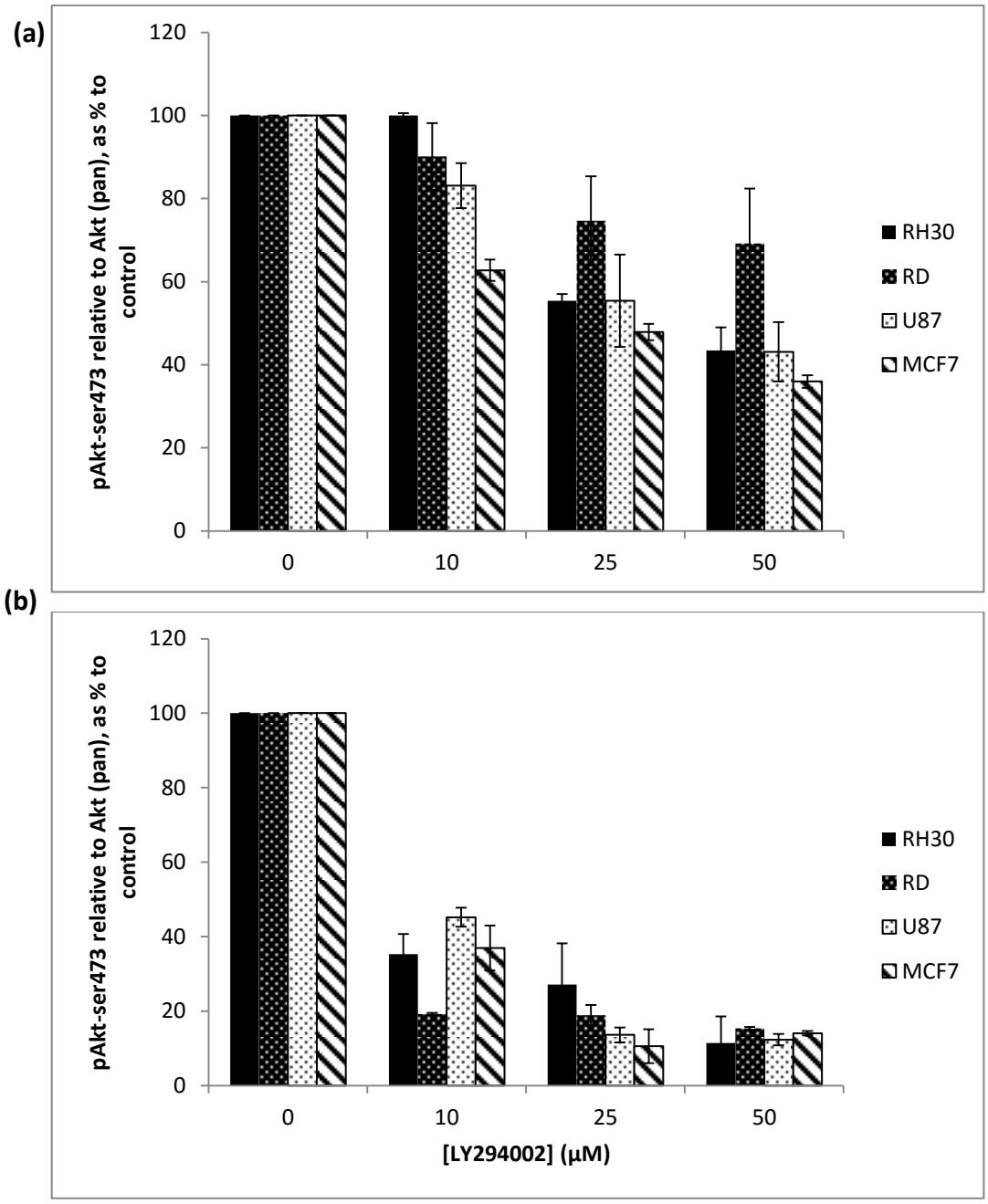


Figure 3.7 Densitometry data taken western blot of cell lysate from RH30, RD, U87-MG and MCF7 cells incubated with increasing amounts of LY294002 under a) 1% $O_2$ or b) 21% $O_2$ (The data are presented as the means ± standard deviation, n= 3)

| vs. controls in Hypoxia | RH30 | RD | U87-MG | MCF7 |
|---|---|---|---|---|
| 10 µM LY294002 | n.s. | *** | n.s. | *** |
| 25 µM LY294002 | *** | *** | * | *** |
| 50 µM LY294002 | *** | *** | * | *** |
| | | | | |
| vs. controls in Normoxia | RH30 | RD | U87-MG | MCF7 |
| 10 µM LY294002 | ** | *** | *** | *** |
| 25 µM LY294002 | ** | *** | *** | *** |
| 50 µM LY294002 | *** | *** | *** | *** |
| | | | | |
| Hypoxia vs. Normoxia | RH30 | RD | U87-MG | MCF7 |
| 10 µM LY294002 | *** | *** | *** | ** |
| 25 µM LY294002 | *** | ** | ** | ** |
| 50 µM LY294002 | ** | ** | ** | *** |

Table 3.1 Results are shown from the student t-test showing the significance of data taken from western blot densitometry on RH30, RD, U87-MG and MCF7 cells incubated with increasing amounts of LY294002 under hypoxic or normoxic condition. The significance test were performed between each data point against its own control, and performed between groups treated under hypoxia against treated under normoxia. (n.s. = not significant,* $P < 0.05$, ** $P < 0.01$, *** $P < 0.001$)

### 3.3.3 Treatment with LY294002 affects cell number under both hypoxic and normoxic conditions

Because PI3Ks are involved in cell proliferation and cell survival, it is likely that the cell number would be affected after treatment with LY294002. However, a very different response to LY294002 was seen in the four test cell lines.

In RH30 cells, the cell number decreased after treatment with increasing concentration of LY294002 under either hypoxic or normoxic conditions. There was approx. 41.70 % decrease in cell number after treatment with 50 µM LY294002 over 24 hours under normoxic conditions (Figure 3.8 a). Under hypoxic conditions, there was approx. 42.40 % decrease in cell number after treatment with 50 µM under hypoxic condition, which is very similar to its counterpart under normoxia. This shows that the compound caused a

similar reduction in proliferation of RH30 cells under either high or low levels of oxygen, despite the fact that LY294002 appears to be more efficient in inhibiting the phosphorylation of Akt in the same cell line under normoxic conditions. Furthermore, it was also found that RH30 cells were sensitive to the drug at low concentrations. Cell number started to decrease even when incubated with a low concentration of drug (5 μM), but did not reduce much further as the concentration increased to 50 μM. This observation was more apparent under normoxic conditions.

The paediatric ERMS line, RD, behaved differently from RH30 cell, an ARMS line, after treatment with LY294002. RD cell showed approx. 23.53 % reduction in cell number after treatment under normoxia (Figure 3.8 b) which is seen to be less susceptible than RH30, despite the fact that they are both RMS lines. Under hypoxic condition, the sensitivity to LY294002 was reduced: merely approx.13.45 % reduction in cell number after 24 hours treatment, and the difference was not significant against control ($P > 0.05$). This indicated that RD cells were less susceptible to LY294002 under low oxygen condition than under normoxic condition.

The different sensitivity to LY294002 was not only observed in the two different RMS lines, but also in the other two studied cancer cell lines. Cell number was seen to be negatively correlated with the concentration of LY294002 under both oxygen conditions. U87-MG presented approx. 63.57 % decrease in cell number treated with a high dose drug (50 μM) under normoxic condition while the survival cell number only dropped approx. 17.52 % after treatment with the same concentration of the drug under an hypoxic

environment (Figure 3.8 c). This indicated that U87-MG cell proliferation was less sensitive to LY294002 under hypoxic conditions than under normoxia.

In the MCF7 line, cell number was seen to decrease to 59.81 % of the control after a high dose treatment under hypoxia. MCF7 cell proliferation also appears to be more sensitive to the drug under a normoxic environment, where the cell number dropped to 47.92 % of the control which is significantly lower than the number of MCF7 cells after treatment under hypoxia ($P < 0.001$). A similar phenomenon was also observed in the other cell lines (Figure 3.8 d).

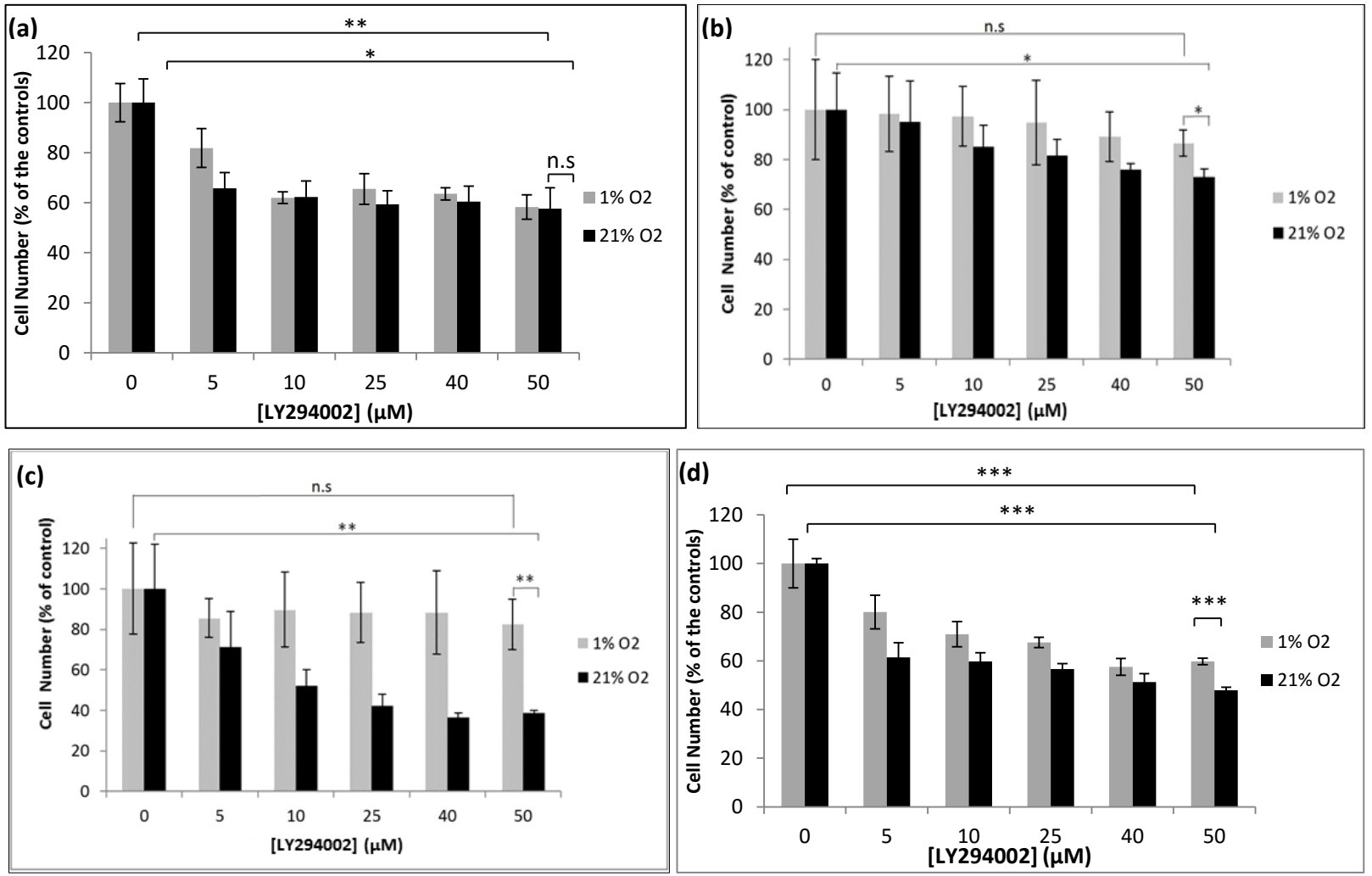


Figure 3.8 Cell number of a) RH30; b) RD; c) U87-MG; d) MCF7 cells assessed using crystal violet staining, in the presence of increasing concentrations of LY294002, either under 1% or 21% oxygen, after incubation for 24 hours (Using Student's t test, n.s. = not significant, * P< 0.05, ** P < 0.01, *** P < 0.001; the data are presented as the means ± standard deviation, n= 3)

### 3.3.4 Treatment with LY294002 affects cell viability under both hypoxic and normoxic conditions

In addition to evaluating the cell proliferation and survival after a treatment of LY294002, the cell viability of LY294002 treated cells was assessed using an MTT assay.

Under normal oxygen levels, the viability of RH30 cells decreased significantly with increasing concentrations of LY294002, and was reduced to only 45.75 % of the control ($P < 0.01$) when the LY294002 concentration reached 50 µM (Figure 3.9 a). Meanwhile, the reduction in cell viability was not as great when the treatment was performed under hypoxic conditions. The cell viability dropped to 85.24 % approx. in the presence of low concentrations (5 µM) of LY294002 and did not decrease much further as the dose increased up to 50 µM.

The viability of RD cells also decreased with an increasing concentration of LY294002 under either 1% $O_2$ or 21% $O_2$ environment. RD cells appeared to be less vulnerable to the drug than RH30 under normoxic conditions; the viability decreased to 69.08 % approx. of the control with 50 µM LY294002 (Figure 3.9 b). Under low oxygen concentrations, the RD cells were seen to be less sensitive to the compound, and the viability decreased to 86.51 % approx. of the control in the presence of 50 µM LY294002.

U87-MG cells showed a more significant reduction in cell viability than the RMS lines under normoxic conditions, with a reduction of 72.37 % compared to control after a treatment of 50 µM LY294002 ($P < 0.01$). Cells were less susceptible to the presence of

LY294002 under hypoxic conditions, with a reduction in viability of 23.14 % compared to control (Figire 3.9 c).

As the viability of U87-MG cells decreases with incresing concentrations of LY294002 under normoxic conditions, MCF7 showed a high sensitivity to the drug at low doses (5 µM): the viability dropped to 31.55 % approx. of the control after treatment with 5 µM LY294002, and remained to this low level with the increasing dose of LY294002. MCF7 also showed less vulnerbility to the compound when the treatment was performed under hypoxic conditions (Figure 3.9 d).

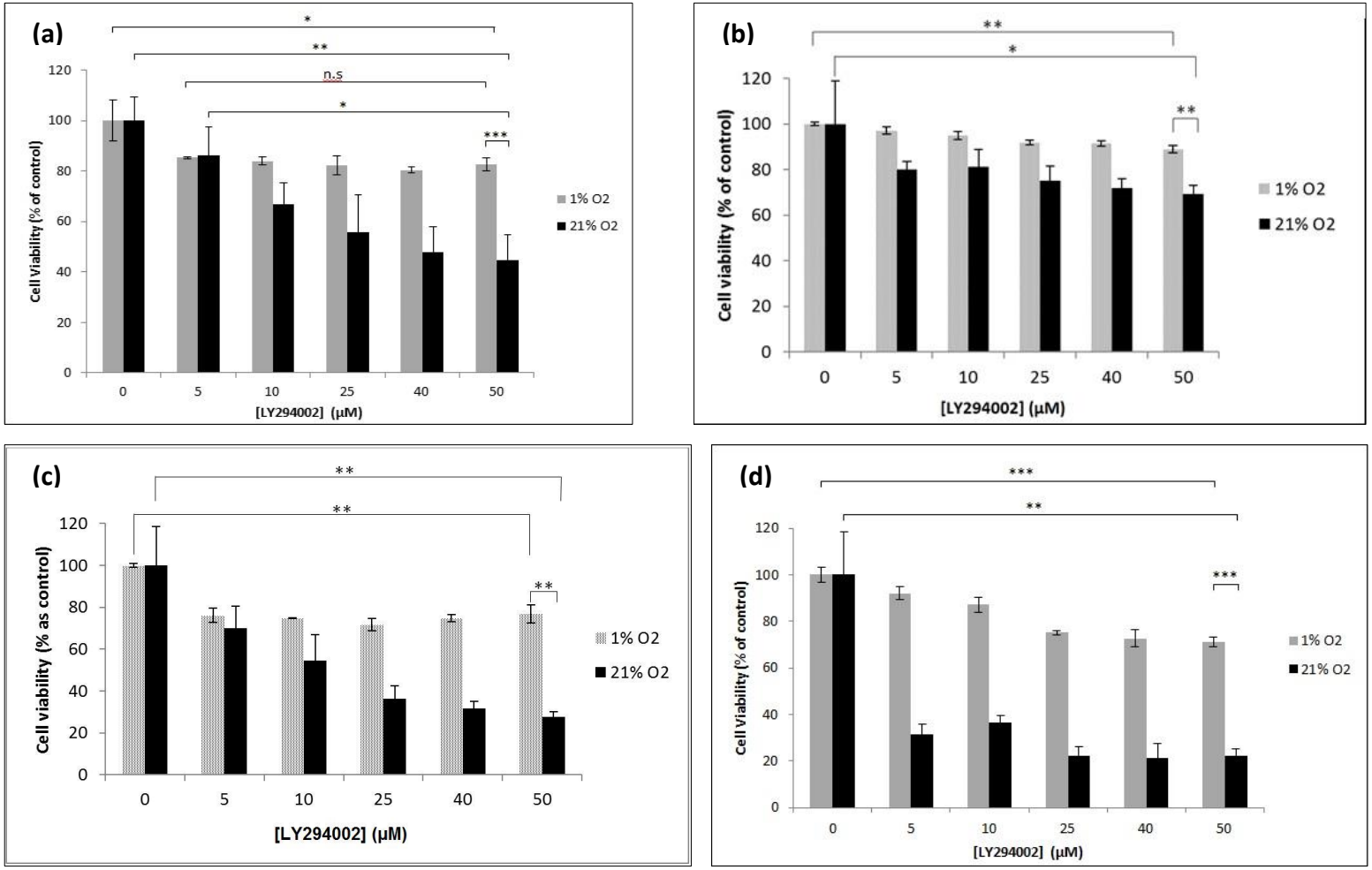


Figure 3.9 Cell viability of a) RH30; b) RD; c) U87-MG; d) MCF7 cells assessed using MTT assay, in the presence of increasing concentrations of LY294002, either under 1% or 21% oxygen, after incubation for 24 hours (Using Student's t test, * P< 0.05, ** P < 0.01, *** P < 0.001; the data are presented as the means ± standard deviation, n= 3)

In summary, the PI3K inhibitor, LY294002, was found to affect cell proliferation (cell number) and survival (cell viability) of all four cell lines tested (Figure 3.8, Figure 3.9). The sensitivity to LY294002 was reduced when the treatment was performed under low oxygen conditions.

### 3.3.5 Alteration in metabolism with the presence of LY294002

Cellular respiration and metabolism of cancer cells differs from healthy cells due to defective mitochondria and altered regulation in certain cell signalling pathways (also see section 1.3.3). A series of assessments was performed on selected cancer cell lines to evaluate their metabolism, and the alteration in metabolism in the presence of LY294002.

#### *3.3.5.1 Respiration profile before treatment*

A bioenergetics profile screen obtained by Dr. Michelle Potter (NDOG, University of Oxford) showed the respiration pattern of many immortalised cancer cell lines (Figure S3.1). Two lines at bioenergetics extremes, RD and U87-MG, were chosen from the screening for further metabolism assessments with LY294002. RD expressed a high OCR coupled with a very low ECAR, whereas U87-MG presented an opposite extreme with a low OCR and a high ECAR. This suggested that RD and U87-MG cells use very different metabolic mechanism under the same environmental conditions.

To confirm this finding, lactate production and OCR of RD and U87-MG cells was assessed in normal culture media. The assessment was performed under normoxic conditions to quantify the mitochondrial respiration of those cell lines, and to give an indica-

tion of glycolysis. OCR was assessed with the MitoXpress-Xtra assay which gave a direct indication of consumed oxygen in a closed environment.

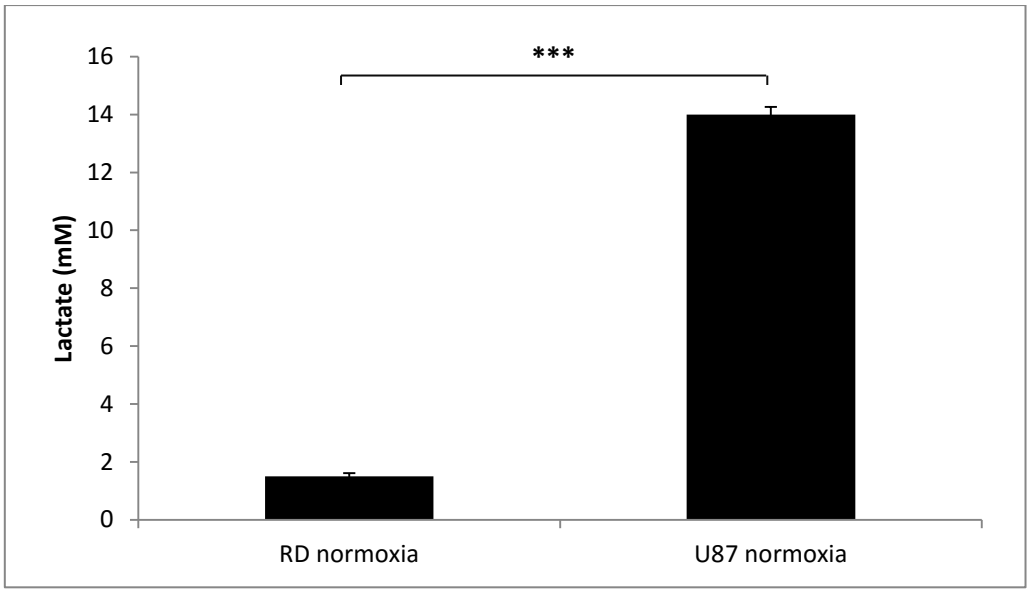


Figure 3.10 Lactate productions detected from the cell culture medium after 24 hours culture for RD and U87-MG cells in normal culture under normoxia (Using Student's t test, *** $P < 0.001$; the data are presented as the means ± standard deviation, n= 3)

It was shown that RD cells produced 1.5 mM lactate into the culture media compared to 14 mM lactate seen in the culture media of U87-MG cells, more than 9 times the former (Figure 3.10). In addition, the OCR of RD cells was more than twice that of U87-MG cells under the same conditions (Figure 3.11). Therefore, the results showed that RD cells consumed a high level of oxygen coupled with a relatively low level of acidification, while U87-MG showed a reduced respiration rate (low OCR) and significantly high acidification rates under the same experiment conditions ($P < 0.001$).

Therefore, U87-MG's metabolism is more glycolytic even under normoxic condition whereas RD cells are more aerobic with more robust oxidative phosphorylation.

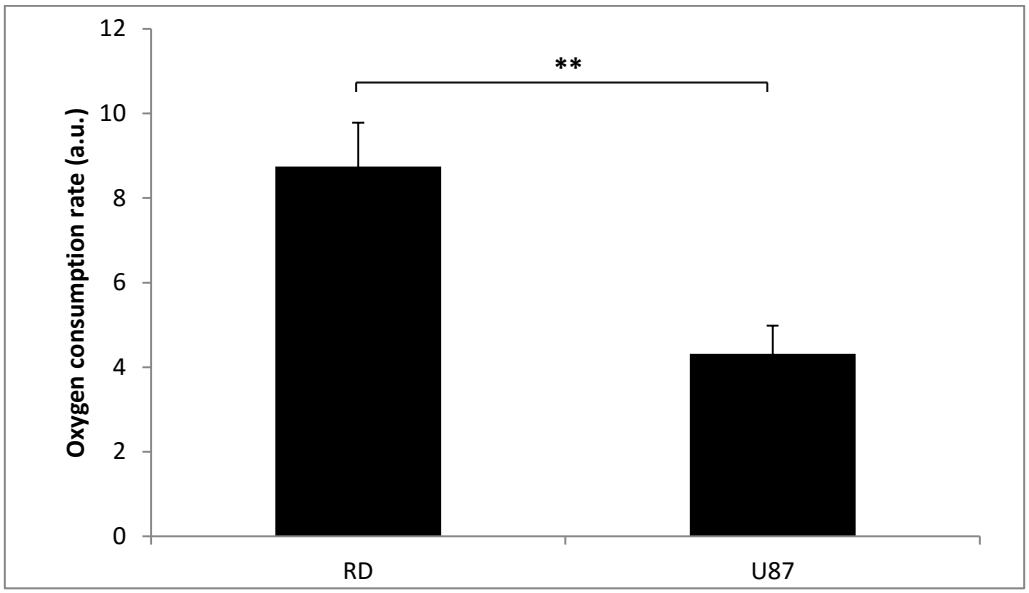


Figure 3.11 Oxygen consumption rate of RD and U87-MG cells in normal culture media under normoxia. (Using Student's t test, ** $P < 0.01$; the data are presented as the means ± standard deviation, n= 3)

### *3.3.5.2 Cellular metabolism after a treatment of LY294002*

Cellular metabolism was evaluated from cellular lactate production. Because the total lactate production in culture was affected by the cell number, the results were expressed relative to cell number.

Cellular metabolism was also evaluated from the intracellular oxygen level. The intracellular oxygen concentration of treated cells was evaluated using the MitoXpress-Intra ($NaNO_2$) assay. A calibration curve was built for each cell line by plotting the equilibrium lifetime against ambient oxygen (Figure S3.2 a & c). To validate the assay, both cell lines were treated with mito-poisons (1 µM rotenone and 4 µM Antimycin-A) to produce a calibration curve. Cellular respiration is inhibited in the presence of mito-poisons if the measurement is valid, resulting in increasing intracellular oxygen, and lifetime reduction (Figure S3.2 a & c).

Unlike the MitoXpress-Xtra probe, the $NaNO_2$ probe can be internalised by the tested cells *via* endocytosis. Therefore the results are independent of cell number (which would be changed after LY294002 treatment) (Figure S3.2 b & d).

It was found that in the presence of 50 µM LY294002, lactate production and intracellular oxygen levels were significantly altered in both cell lines under both hypoxic and normoxic conditions (Figure 3.12, Figure 3.13).

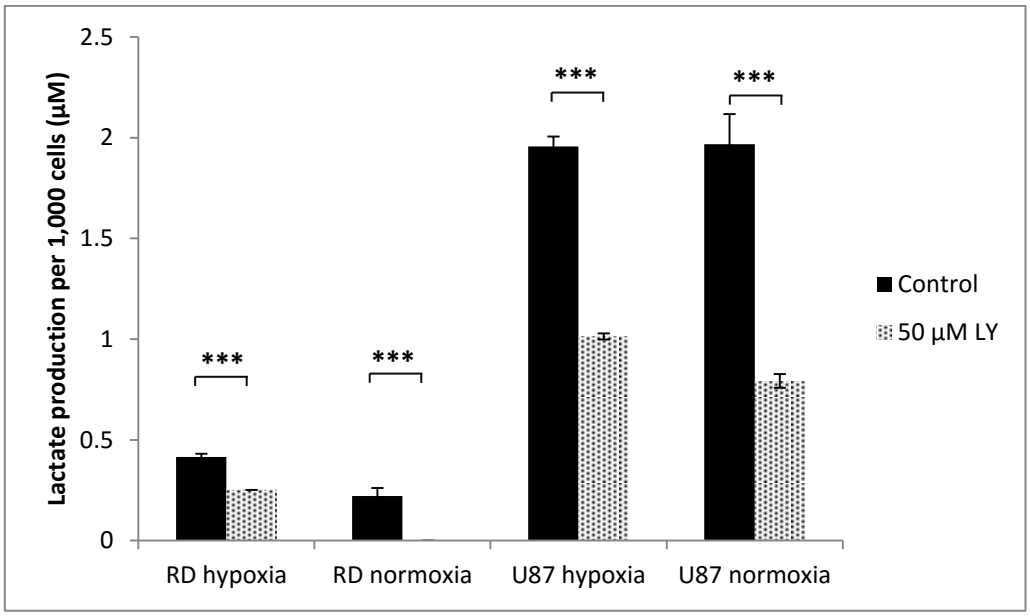


Figure 3.12 Lactate detected in the culture medium after 24 hours in the presence and absence of LY294002 for RD and U87-MG cells under 1% and 21% oxygen. The results were calibrated with relative cell number. (Using Student's t test, *** $P < 0.001$; the data are presented as the means ± standard deviation, n= 3)

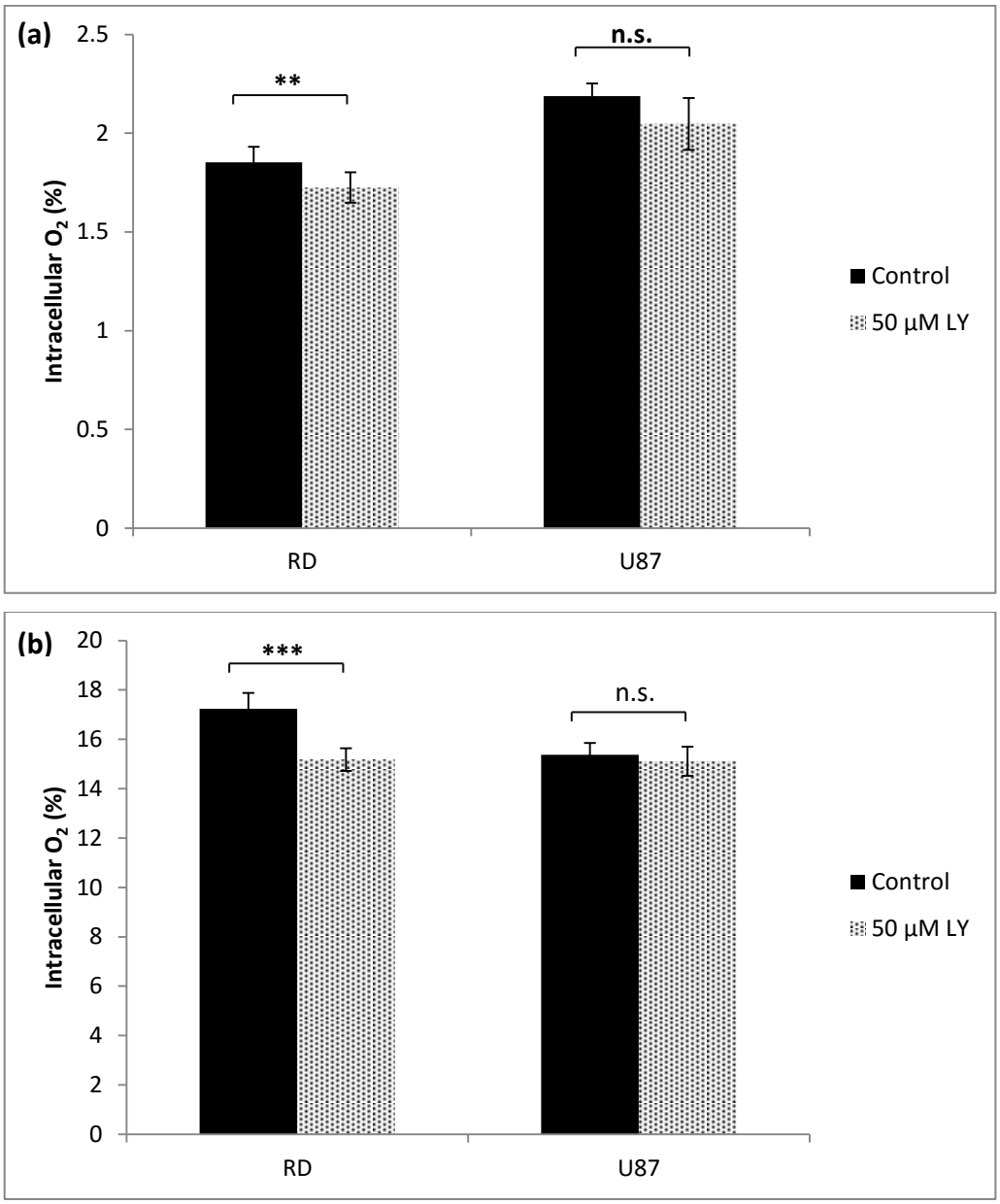


Figure 3.13 Intracellular oxygen level assessed using MitoXpress-Intra assay on RD and U87-MG cells after treatment with 50 µM LY294002 for 24 hours under a) hypoxic (2 % $O_2$) or b) normoxic condition (18 % $O_2$) (Using Student's t test, * $P < 0.05$, ** $P < 0.01$, *** $P < 0.001$; the data are presented as the means ± standard deviation, 60 points were taken from the plateau region from n = 6 replicates)

Under hypoxic conditions, it was seen that lactate production was significantly reduced in the presence of 50 µM LY294002 in both cell lines. RD cells showed an approx. 39.62 % reduction in lactate generation compared to the control ($P < 0.001$), while the lactate generated from U87-MG cells was also reduced 48.21 % compared to the control

(Figure 3.12; $P < 0.001$). Meanwhile, intracellular oxygen was significantly reduced in RD cells after treatment with 6.91 % reduction of the control ($P < 0.01$), while it remained in U87-MG cells (Figure 3.13; $P > 0.05$). This suggested that under hypoxic conditions, glycolysis would be remarkably reduced after inhibition of the PI3K pathway. Such an effect was seen to be less significant in cell lines using predominantly OXPHOS respiration.

Under normoxic conditions, intracellular oxygen was reduced by 11.95 % compared to the control in RD cells while the reduction in the intracellular oxygen of U87-MG cells was negligible. RD cells predominantly respire using OXPHOS with limited glycolysis and low lactate generation, particularly under normoxic conditions. After inhibition of PI3K, lactate generation from RD cells was reduced to an undetectable level (lower than 0.8 mM) after treatment. Meanwhile, U87-MG cells showed a 59.73 % reduction in lactate production compared to control under the same condition (Figure 3.12). This result showed that glycolysis in U87-MG cells was compromised when the PI3K pathway was inhibited. Such an effect appeared to be more significant under normoxic conditions.

Therefore, these results suggested glycolysis could be impaired in the presence of LY294002. Such an effect was seen to be more significant in cell lines using predominantly glycolytic respiration or under normoxic conditions.

#### *3.3.5.3 The energy transformation profile assessed with ADP /ATP ratio*

The alteration of the cellular bioenergetic profile after treatment with LY294002 suggested that the energy transformation may also change in the presence of the drug. Therefore,

the energy production was assessed with ADP/ATP assay under hypoxic and normoxic conditions. It should be noted that the production of ATP and ADP was affected by the cell number. Hence the change of ADP/ATP ratio, not the absolute value of ATP and ADP, would give an indication of energy transformation profile.

In RD cells, the production of ATP remained at a low level while the change in ADP level was also negligible after a treatment of LY294002 under hypoxic conditions (Figure S3.3 a). The change in ADP/ATP ratio was also low (9.41 % decrease of the control) after treatment, meaning cells were in growth arrest (Figure 3.14 a).

Under normoxic conditions, the level of ATP was markedly decreased (80.03 % decrease compared to control) after treatment, while the decrease in ADP level was seen to be less (68.17 % compared to control) (Figure S3.3 a). This resulted in a significant increase in the ADP/ATP ratio (59.01 % compared to control; $P < 0.05$) after treatment (Figure 3.14 a) which possibly indicated that the treated cells suffered from apoptosis due to efficient inhibition of the PI3Ks pathway.

These results showed that the energy production and energetic status was not significantly changed in RD cells under hypoxia. However, cells were going through apoptosis when the PI3K pathways were inhibited under normoxic conditions. One possible reason is that RD cells respire mainly using OXPHOS, despite the low levels of oxygen, which was not significantly impaired by the presence of LY294002.

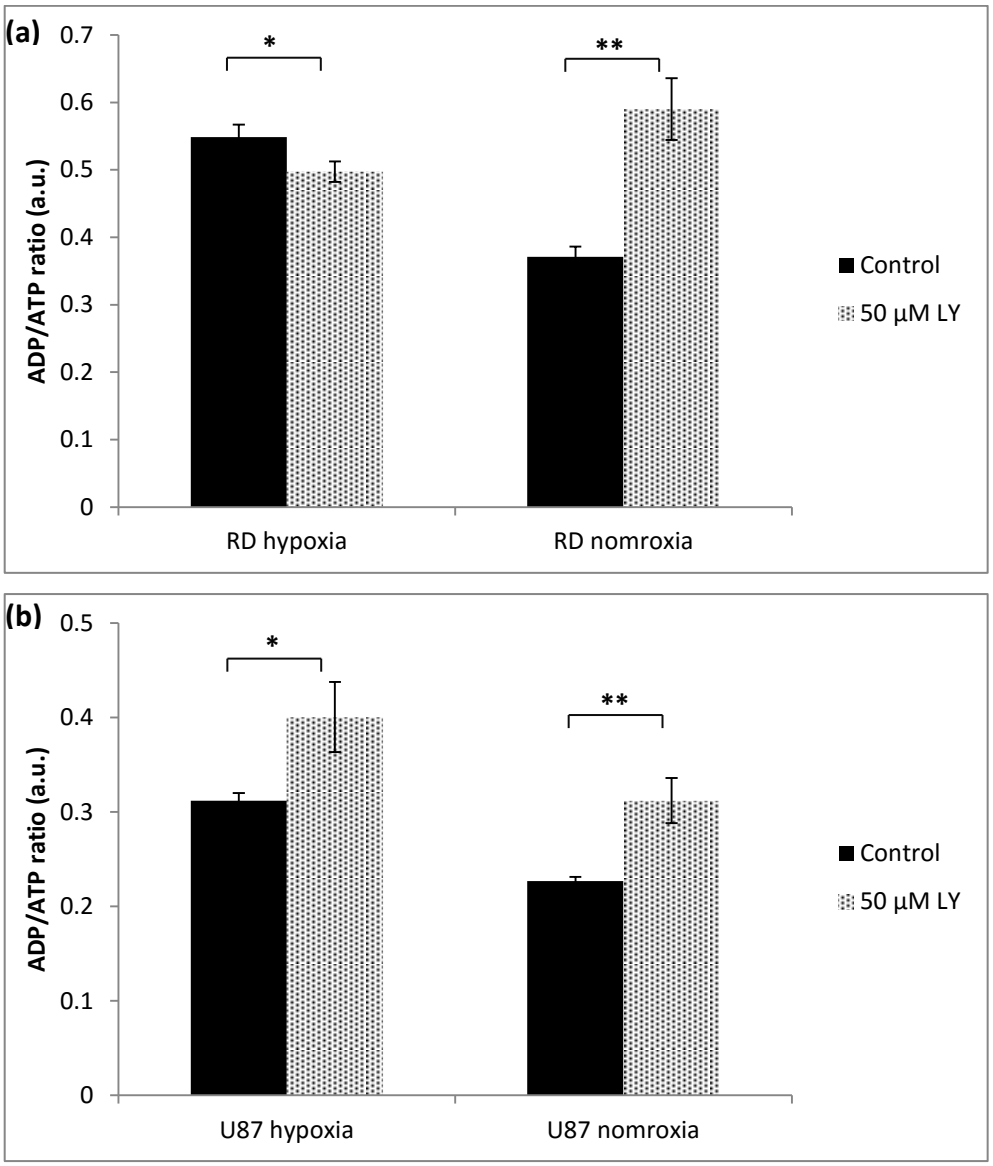


Figure 3.14 ADP/ATP production ratio in a) RD or b) U87-MG cells after treatment with 50 µM LY294002 for 24 hours under either hypoxic (1% $O_2$) or normoxic (21% $O_2$) environment (Using Student's t test, * $P < 0.05$, ** $P < 0.01$; the data are presented as the means ± standard deviation, n= 3)

U87-MG, a more glycolytic cancer cell line, behaved differently from RD cells due to a different metabolic profile. Under hypoxic conditions, both ATP and ADP levels were greatly reduced after treatment with an elevated ADP/ATP ratio with a 28.46 % increase compared to control (Figure S3.3 b, Figure 3.14 b). This indicated the treated cells were in an apoptotic or necrotic stage (Data interpretation, EnzyLight™).

Under normoxic conditions, the ADP/ATP ratio was also raised significantly after treatment (37.75 % increase compared to control; $P < 0.01$). This also indicated that the treated cells were going through an apoptotic process (Figure 3.14 b).

These results are consistent with the previous results, showing that the cells suffered from mitochondrial dysfunction and apoptosis with an efficient inhibition of PI3Ks and remarkable reduction in glycolysis, the predominant metabolic process in U87-MG cells.

#### *3.3.5.4 The generation of reactive oxygen species*

ROS generation was monitored using the Amplex Red assay. To eliminate the influence of cell number, the ROS production level was expressed by per 1,000 cells. It should be noted that it was impossible to differentiate the source of ROS from this assessment. The results only indicate the ROS level (represented by $H_2O_2$ equivalents) released in culture media.

In RD cells, the production of $H_2O_2$ equivalent was reduced from 0.83 µM to 0.31 µM in 1,000 RD cells (61.94 % reduction compared to the control) when treated under hypoxic conditions, and from 0.50 µM to 0.11 µM (77.56 % decrease compared to the control) under normoxic conditions (Figure 3.15 a).

In U87-MG cells, ROS generation was elevated after the more successful inhibition of PI3K. Under a hypoxic environment, the production of $H_2O_2$ equivalents was significantly promoted from 1.40 µM to 3.02 µM in 1,000 U87-MG cells with more than 100 % increasing ($P < 0.01$). The produced ROS per 1,000 cells was also seen to be increased

when the treatment was performed under normoxic conditions, with a 29.4 % increase compared to the control from 1.47 µM to 1.90 µM in U87-MG cells (Figure 3.15 b).

It was also noted that RD cells generated more ROS under hypoxic conditions than under normoxic conditions ($P < 0.001$), whereas there was no significant difference between the production of ROS in U87-MG cells under different oxidative conditions (Figure 3.15 b; $P > 0.05$).

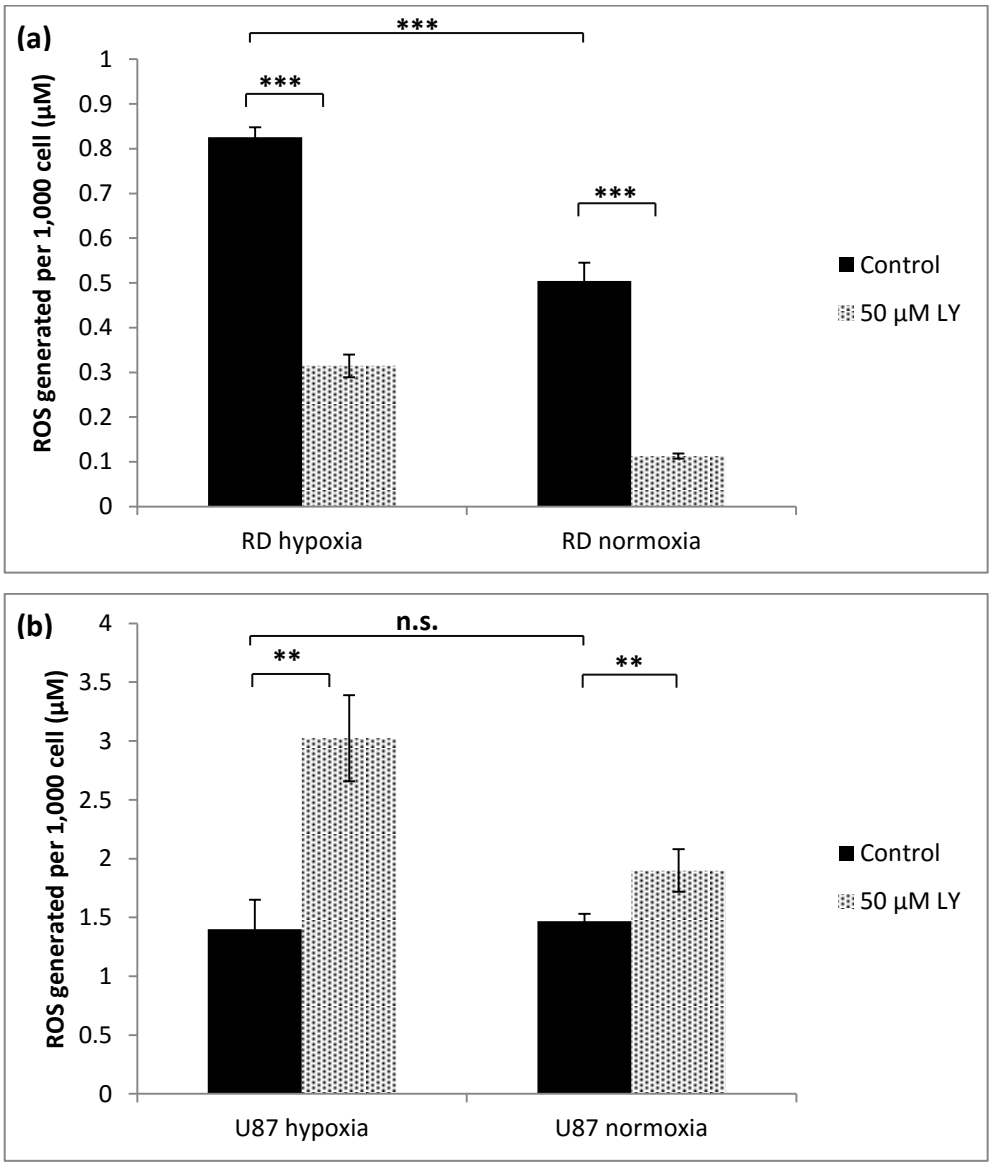


Figure 3.15 ROS generated per 1,000 a) RD or b) U87-MG cells after treatment with 50 µM LY294002 for 24 hours under either hypoxic (1% $O_2$) or normoxic (21% $O_2$) environment (Using Student's t test, *** $P < 0.001$, ** $P < 0.01$; the data are presented as the means ± standard deviation, n= 3)

### 3.3.6 Cell adaptation to glucose stress

In order to simulate a more physiological environment, RD and U87-MG cells were incubated and treated in low glucose media. Cell number, intracellular oxygen levels and ROS production were assessed to evaluate the adaptation of RD and U87-MG cells to limited glucose supply under both hypoxic and normoxic conditions.

Under hypoxic conditions, RD cells failed to thrive in culture media containing low concentration of glucose. The number of RD cells was reduced to approx. 4.51 % and 13.74 % of the control (20 mM glucose in media) in 1 mM and 5 mM glucose media, respectively (Figure 3.16a, Table 3.2a). Under normoxic conditions, RD cell number was also found to be lower than the control in culture media with low glucose concentrations (Figure 3.16 b, Table 3.2 b).

(a)

| Glucose concentration | 5 mM | 20 mM |
|---|---|---|
| 1 mM | n.s. | *** |
| 5 mM | | *** |

(b)

| Glucose concentration | 5 mM | 20 mM |
|---|---|---|
| 1 mM | n.s. | *** |
| 5 mM | | ** |

Table 3.2 The significance test associated with Figure 3.16 a & b, performed on cell number of untreated RD cells incubated in different media under a) hypoxic or b) normoxic condition. (n.s. = not significant, * P < 0.05, ** P < 0.01, *** P < 0.001)

(a)

| Glucose concentration | 5 mM | 20 mM |
|---|---|---|
| 1 mM | n.s. | *** |
| 5 mM | | *** |

(b)

| Glucose concentration | 5 mM | 20 mM |
|---|---|---|
| 1 mM | n.s. | *** |
| 5 mM | | *** |

Table 3.3 The significance test associated with Figure 3.17a, performed on intracellular oxygen level of untreated RD cells incubated in different media under a) hypoxic or b) normoxic condition. (n.s. = not significant, * P < 0.05, ** P < 0.01, *** P < 0.001)

(a)

| Glucose concentration | 5 mM | 20 mM |
|---|---|---|
| 1 mM | * | *** |
| 5 mM | | *** |

(b)

| Glucose concentration | 5 mM | 20 mM |
|---|---|---|
| 1 mM | n.s. | n.s. |
| 5 mM | | n.s. |

Table 3.4 The significance test associated with Figure 3.18 a & b, performed on ROS generation per cell of untreated RD cells incubated in different media under a) hypoxic or b) normoxic condition. (n.s. = not significant,* P < 0.05, ** P < 0.01, *** P < 0.001)

In addition, intracellular oxygen levels of cells cultured in low glucose media were seen to be significantly lower than the control (20 mM glucose in media) under either hypoxic ($P < 0.001$) or normoxic condition ($P < 0.001$) (Figure 3.13 and Figure 3.17a; Table 3.3). This indicated that RD cells consumed *more* oxygen in low glucose media.

ROS production was found to be significantly increased with the decrease in glucose concentration under hypoxic conditions: RD cells in 1 mM glucose media generated 15.36 times more ROS than in 20 mM glucose media ($P < 0.001$), while cells in 5 mM glucose media generated 5.58 times more ROS than in normal glucose media ($P < 0.05$) (Figure 3.18a, Table 3.4a). Under normoxic conditions, however, there was no significant difference in ROS production from cells cultured in media with different glucose concentration ($P > 0.05$) (Figure 3.18b, Table 3.4b).In U87-MG cells, the cell number remained unchanged after a 24-hour incubation in different glucose concentrations under either hypoxic or normoxic conditions (Figure 3.16 c & d, Table 3.5).

Intracellular oxygen was found to be significantly lower when U87-MG cells were cultured in media with low glucose concentrations (1 mM or 5 mM) under both hypoxic and normoxic conditions, indicating *more* oxygen consumption under glucose stress (all four $P < 0.001$) (Figure 3.13 and Figure 3.17 b; Table 3.6).

Under hypoxic conditions, U87-MG cells generated more ROS in high glucose media (20 mM glucose) than in 1 mM or 5 mM glucose media ($P < 0.05$). This observation was the converse of that seen in RD cells. Under normoxic conditions, there was no significant difference in ROS production between cells cultured in media with different glucose concentrations ($P > 0.05$) (Figure 3.18 d, Table 3.7 b).

(a)

| Glucose concentration | 5 mM | 20 mM |
|---|---|---|
| 1 mM | n.s. | n.s. |
| 5 mM | | n.s. |

(b)

| Glucose concentration | 5 mM | 20 mM |
|---|---|---|
| 1 mM | n.s. | n.s. |
| 5 mM | | n.s. |

Table 3.5 The significance test associated with Figure 3.16 c & d, performed on cell number of untreated U87-MG cells incubated in different media under a) hypoxic or b) normoxic condition. (n.s. = not significant,* $P < 0.05$, ** $P < 0.01$, *** $P < 0.001$)

(a)

| Glucose concentration | 5 mM | 20 mM |
|---|---|---|
| 1 mM | n.s. | *** |
| 5 mM | | *** |

(b)

| Glucose concentration | 5 mM | 20 mM |
|---|---|---|
| 1 mM | n.s. | *** |
| 5 mM | | *** |

Table 3.6 The significance test associated with Figure 3.17b, performed on intracellular oxygen level of untreated U87-MG cells incubated in different media under a) hypoxic or b) normoxic condition. (n.s. = not significant,* $P < 0.05$, ** $P < 0.01$, *** $P < 0.001$)

(a)

| Glucose concentration | 5 mM | 20 mM |
|---|---|---|
| 1 mM | n.s. | * |
| 5 mM | | * |

(b)

| Glucose concentration | 5 mM | 20 mM |
|---|---|---|
| 1 mM | n.s. | n.s. |
| 5 mM | | n.s. |

Table 3.7 The significance test associated with Figure 3.18 c & d, performed on ROS generation per cell of untreated U87-MG cells incubated in different media under a) hypoxic or b) normoxic condition. (n.s. = not significant,* $P < 0.05$, ** $P < 0.01$, *** $P < 0.001$)

It was noted that the adaption of U87-MG cells to glucose and oxidative stress differed greatly from RD cells. U87-MG cells appeared to survive better than RD cells in media with limited glucose concentration (Figure 3.16). Such phenomenon was more significant under hypoxic conditions (Figure 3.16 a & c).

Under hypoxic conditions, ROS production in U87-MG cells was much lower than in RD cells in hypoglycaemic culture media (Figure 3.18 a & c): RD cells generated 18.30 times and 5.94 times more ROS than U87-MG cells in media with 1 mM and 5 mM glucose, respectively. Under normoxic conditions, however, the difference in ROS production between RD and U87-MG cells cultured in low glucose media was negligible.

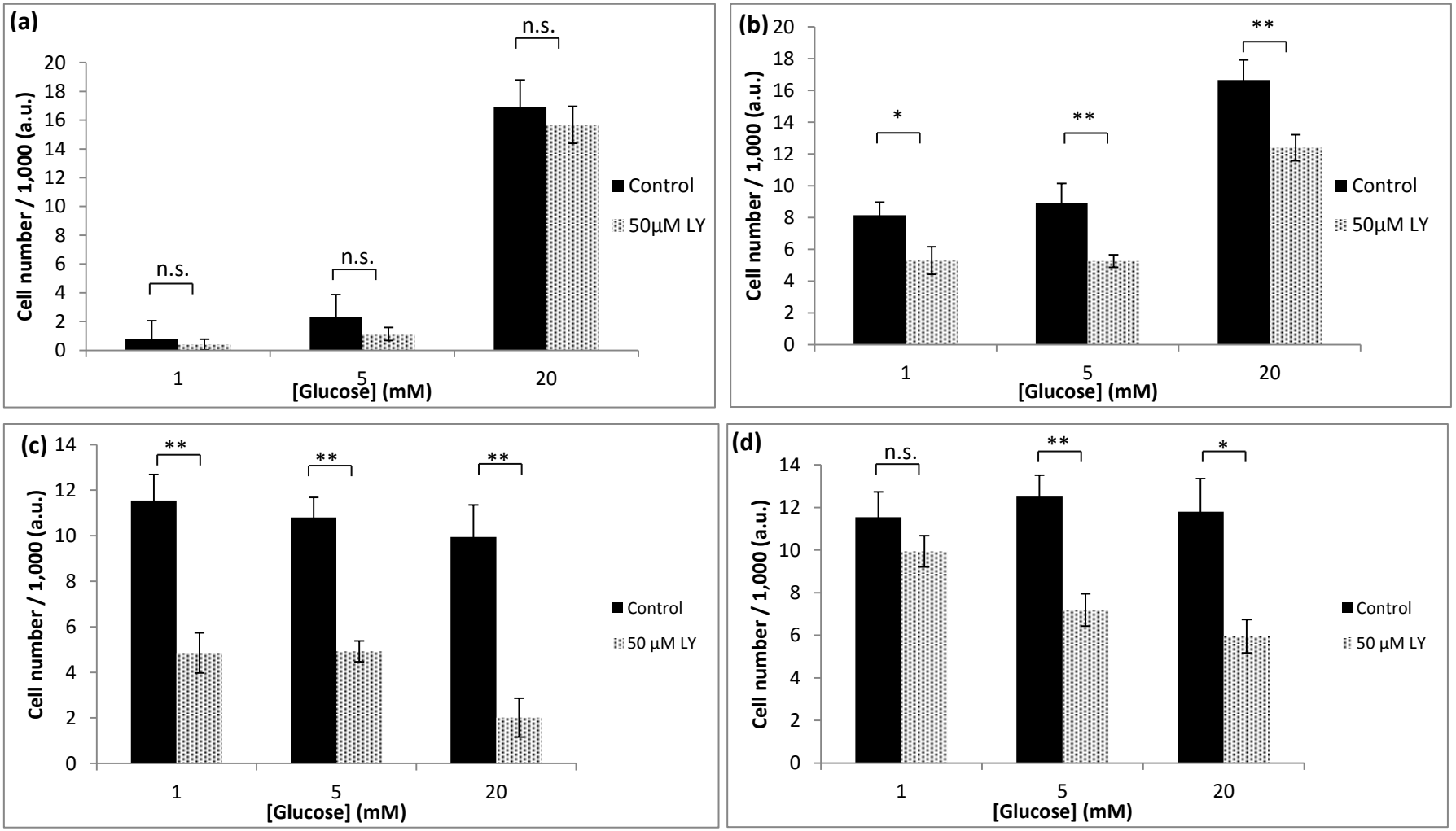


Figure 3.16 Cell number of RD (a & b) and U87-MG (c & d) assessed with Crystal Violet assay after a treatment of 50 µM LY294002 under hypoxic (a & c) or normoxic (b & d) condition for 24 hours in culture media with different glucose concentrations (Using Student's t test, n.s. = not significant,* $P < 0.05$, ** $P < 0.01$, *** $P < 0.001$; the data are presented as the means ± standard deviation, n= 3)

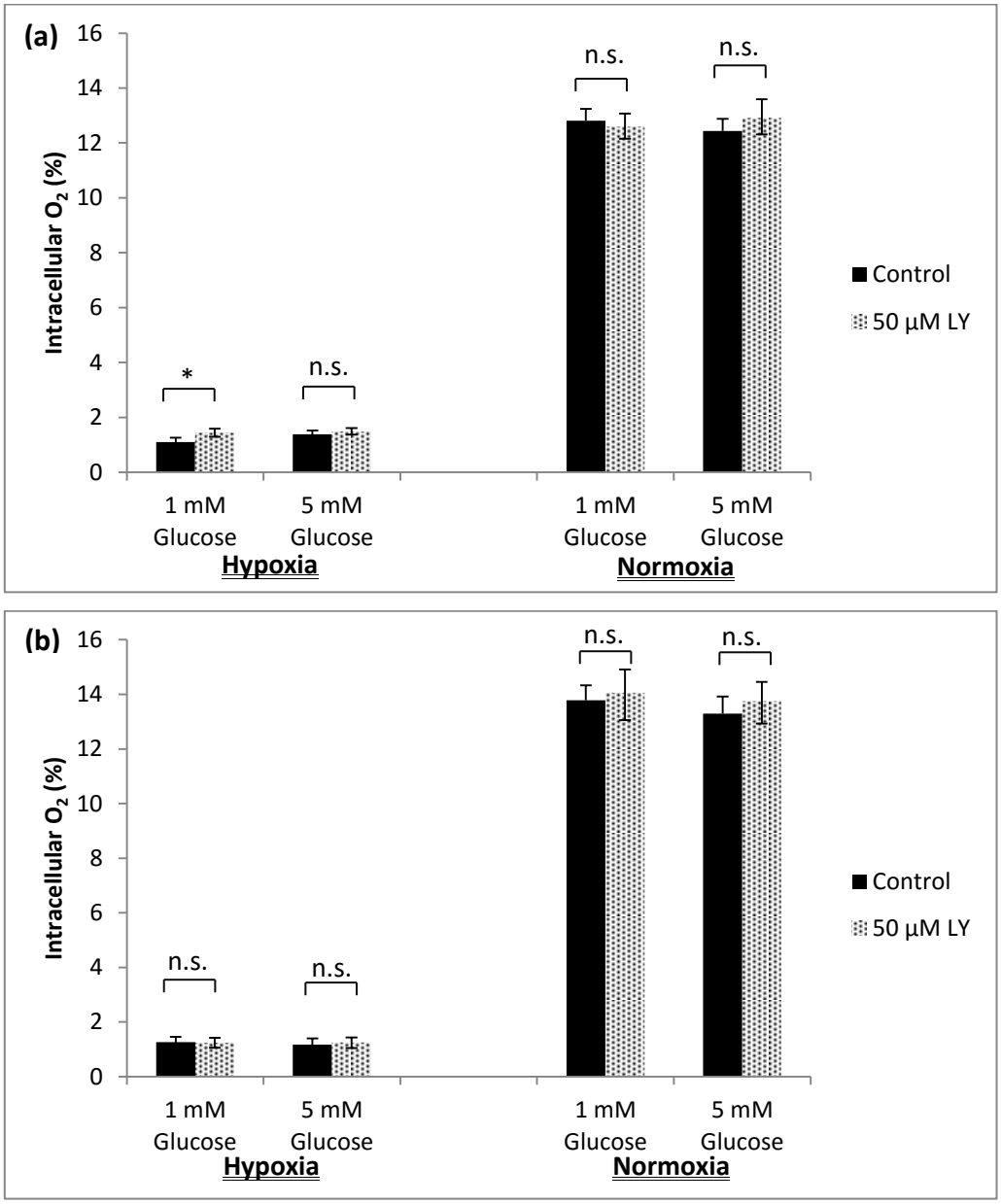


Figure 3.17 Intracellular $O_2$ level in a) RD and b) U87-MG cells after a treatment of 50 µM LY294002 under hypoxic or normoxic condition for 24 hours in culture media with low glucose concentrations (the data are presented as the means ± standard deviation, 60 points were taken from the plateau region from n = 3 replicates, Using Student's t test, n.s. = not significant,* $P < 0.05$, ** $P < 0.01$, *** $P < 0.001$; the data are presented as the means ± standard deviation, n= 3)

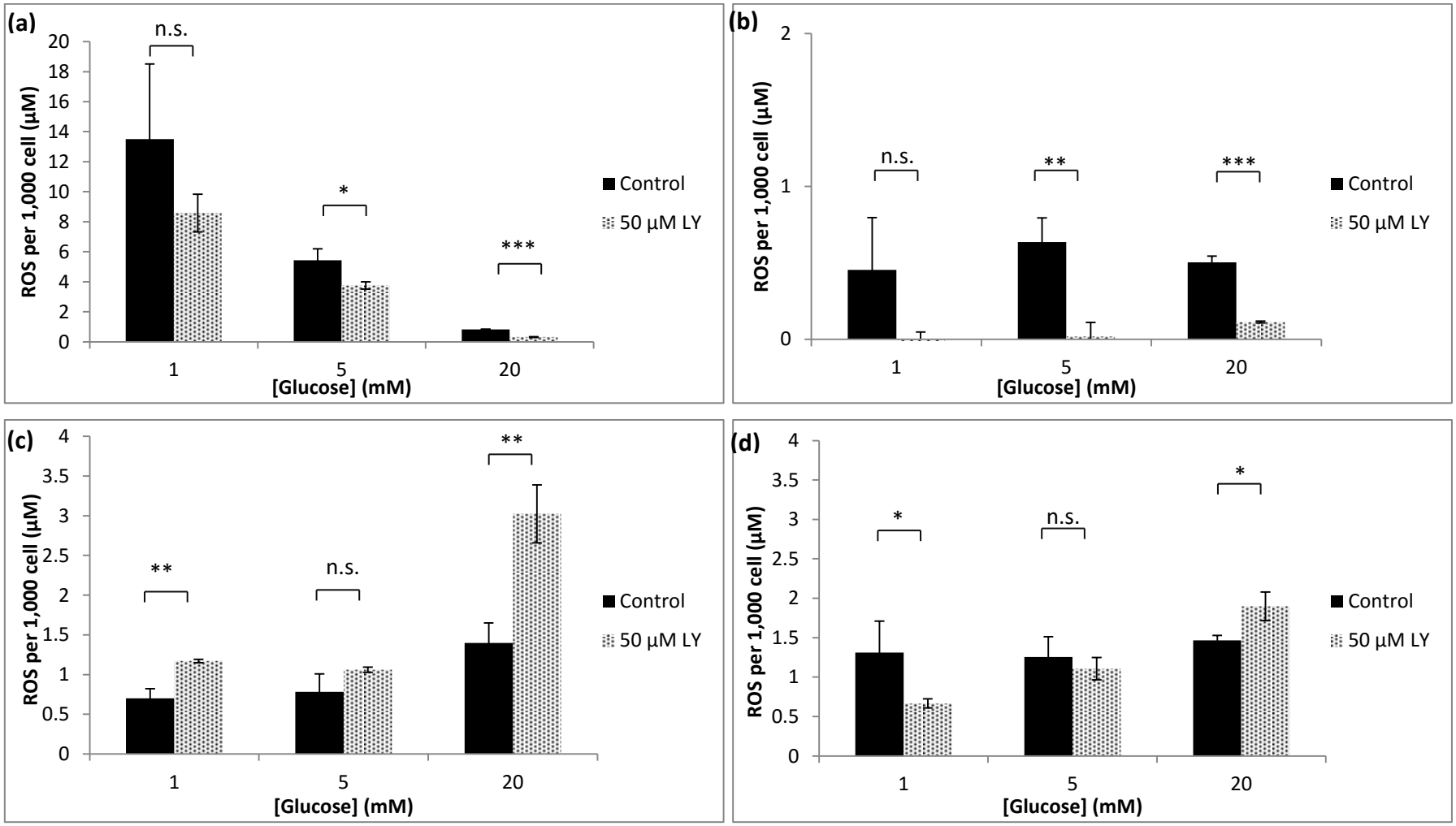


Figure 3.18 ROS generation in RD (a & b) or U87-MG (c & d) cells after a treatment of 50 µM LY294002 under hypoxic (a & c) or normoxic (b & d) condition for 24 hours in culture media with different glucose concentrations (Using Student's t test, n.s. = not significant,* $P < 0.05$, ** $P < 0.01$, *** $P < 0.001$; the data are presented as the means ± standard deviation, n= 3)

### 3.3.7 The effect of LY294002 to cells under glucose stress

Under hypoxic conditions, no significant change in cell number was found after RD cells were treated with LY294002 in any of the media conditions tested (Figure 3.16 a; $P > 0.05$). Intracellular oxygen levels after treatment remained unchanged when the glucose concentration was lowered to 5 mM. However, LY294002 treatment was seen to result in lower oxygen consumption in RD cells when cultured in media with 1 mM glucose.

Despite the small change in cell number and intracellular oxygen, ROS production dropped significantly after treatment with the drug. ROS production per cell decreased to approx. 69.06 % of the control ($P < 0.05$) and 37.35 % of the control ($P < 0.001$) after treatment with LY294002 in 5 mM and 20 mM glucose media, separately (Figure 3.18 a).

Under normoxic conditions, cell proliferation in RD cells was significantly compromised in the presence of LY294002 in all three culture media conditions tested ($P < 0.05$) (Figure 3.16 b). Intracellular oxygen was not seen to change after treatment with LY294002 ($P > 0.05$), at the same time.

In addition, ROS was barely detected after treatment and significantly lower than the untreated counterparts ($P < 0.01$) (Figure 3.18 a & b). This indicated that the presence of LY294002 would significantly reduce the production of ROS in RD cells under normoxic conditions.

The tested U87-MG glioblastoma cell line responded to LY294002 differently from RD cells under glucose stress. Under hypoxic conditions, U87-MG cell number was seen to be significantly decreased after treatment with LY294002 in all culture media tested ($P < 0.01$). Intracellular oxygen levels, however, were not seen to be changed ($P > 0.05$).

Furthermore, ROS production was not suppressed, but actually increased in the presence of LY294002 in all media tested; the opposite to the observation in RD cells. These results showed that LY294002 would stimulate the production of ROS and reduce cell proliferation in U87-MG cells while not consuming more oxygen.

Under normoxic conditions, U87-MG cell number was not seen to be significantly reduced after treatment of LY294002 when cells were cultured in 1mM glucose media ($P > 0.05$). The decrease in cell number became significant when U87-MG cells were treated in media with a more available glucose supply (5 mM vs. 20 mM glucose; $P < 0.05$). Intracellular oxygen levels were not changed after treatment, and ROS generation was also not significantly changed after treatment in low glucose media (Figure 3.18 c & d; $P > 0.05$, in 5 mM glucose media).

## 3.4 DISCUSSION

### 3.4.1 Reactive oxygen species

Reactive oxygen species (ROS) are a by-product of cell respiration from many sources such as oxidative stress, stimulated superoxide dismutase (SOD) and NADPH oxidase (NOX) (Bae *et al.*, 2011). The generation of ROS depends upon a number of factors such as the cell types, ambient oxygen level, metabolic profile, environmental stress and the activity of enzymes and cell signalling pathways. The PI3K-Akt pathway also contributes to ROS production both directly and indirectly. By directly suppressing FOXOs, active PI3K would lead to the promotion of ROS generation (Weinberg *et al.*, 2010). PI3K would also reduce cell number and alter cellular metabolism, therefore indirectly affecting the level of ROS generated. However, the overall function of PI3K in ROS produc-

tion remains inconclusive due to the regulation of ROS being complicated and can be vastly varied from different cell lines.

ROS plays a unique and complicated role in many cellular processes; especially in the cancer cells. ROS is required in some cell lines to activate certain growth factors and kinases (Irani *et al.*, 1997). Therefore a reduction in ROS production would result in a decrease in cell proliferation (Gupta *et al.*, 2011). However, over-production of ROS can induce DNA damage, tumorigenesis, metastasis, and apoptosis in many lines (Ozben, 2007, Hampton and Orrenius, 1997, Waris and Ahsan, 2006).

### 3.4.2 Respiration patterns in RD and U87-MG cells

Glycolysis and OXPHOS are closely co-operative (Zheng, 2012). In the cytoplasm, each glucose molecule can convert to two pyruvate molecules through the reactions in glycolysis, while the released energy leads to the formation of two ATPs. Pyruvate would enter mitochondria and participate in aerobic respiration, the TCA cycle and OXPHOS, and produce much more energy. Oxygen is not necessary for the reactions involved in the glycolytic pathway, but it is required for OXPHOS. Under hypoxic (or anoxic) conditions, glycolysis is normally enhanced to compensate for the limited OXPHOS, leading to excess production of pyruvate. Due to the limited oxygen levels and OXPHOS, pyruvate would not participate in the TCA cycle, but convert to lactate resulting in an increase in lactate production and a decrease in pH value (Pfeiffer *et al.*, 2001).

Due to aberrant or defective cell membranes and mitochondria, metabolism in cancer cells is often found to be different from that found in normal cells. In contrast to normal cells which produce ATP *via* aerobic respiration (OXPHOS) in their mitochondria, can-

cer cells produce most of their ATP through aerobic glycolysis generating less ATP, and producing lactate (Warburg *et al.*, 1927, Koppenol *et al.*, 2011) (detailed in section 1.3.3). However, cancers are heterogeneous with extremely broad diversity, and this is also reflected in their metabolic profile. In some cancer cell lines (e.g. RD cells), the Warburg effect has not been observed and OXPHOS is still the predominant respiration pathway (Zu and Guppy, 2004).

In this study, it was also shown that RD cells primarily use OXPHOS when oxygen supply is sufficient, while in contrast U87-MG cells were found to use glycolysis. Under hypoxic conditions, lactate production was significantly enhanced in RD cells ($P < 0.001$) indicating an enhanced glycolysis. Glycolysis in U87-MG cells, however, was not seen to be promoted ($P > 0.05$).

### 3.4.3 Alteration in cell survival and metabolism after treatment with LY294002

Despite LY294002 affects various cell signalling targets, PI3K/Akt was reported to be the main target of LY294002 (Gharbi *et al.*, 2007).

Activation of the PI3k/Akt pathway was found in all cell lines tested before treatment with LY294002, in agreement with literature (Wysoczynski *et al.*, 2010, Kilic-Eren *et al.*, 2013, Yang *et al.*, 2014, Glorieux *et al.*, 2014). In the presence of LY294002, PI3K activation was seen to be inhibited with different effectiveness (Figure 3.6, Figure 3.7). The inhibition of PI3K was found to be more marked under normoxic conditions. The sensitivity to the drug was therefore dependent on (i) the environmental oxygen level, (ii) drug concentration and (iii) cell types.

Treatment with LY294002 also reduced cell proliferation and viability, indicating that a lower level of Akt phosphorylation was associated with lower cell proliferation and viability. The assessment of the ADP/ATP ratio also indicated that the cells were in an apoptotic stage after PI3K inhibition. One possible reason for this is that the inhibition of PI3K leads to the promotion of p53- and/or BAD-dependent apoptosis. The reduction in cell proliferation and viability was seen to be more marked under normoxic conditions in certain cell lines. Akt phosphorylation of RD cells remained at a high level after treatment under hypoxic conditions, and the cell number and viability also remained relatively high after treatment. Successful inhibition of U87-MG and MCF7 cells after treatment under hypoxic conditions was associated with a greater reduction in cell number and/or viability than in RD cells. This suggests that the different response to LY294002 is potentially caused by a different metabolic mechanism under different oxidative conditions.

In previous literature, PI3K has been shown to affect metabolism by regulating glucose transporters and glycogen synthase (Vesely and Michigan, 2009). In this study, it was found that lactate production was significantly decreased in the presence of LY294002 in both cell lines tested (Figure 3.12). Furthermore, intracellular oxygen was reduced in RD cells while it remained at the same level in U87-MG cells under either low or atmospheric oxygen. One possible explanation is that PI3K inhibition could compromise glycolysis and lactate production. Impaired glycolysis leads to lower pyruvate production and also causes pyruvate stress. To compensate for the glucose / pyruvate stress, other metabolites, such as glutamine, participate in cellular metabolism with higher oxygen consumption.

ROS production was significantly reduced in RD cells in the presence of LY294002 under either oxygenic condition ($P < 0.001$), while the generated ROS was increased in U87-MG cells ($P < 0.01$). Due to the complexity of ROS production, it is difficult to propose a mechanism for these results. One possible explanation is that the major source of ROS was not the same in RD cells and U87-MG cells. In RD cells, the inhibition of PI3K leads to a down-regulation of FOXOs which results in a reduction of cytoplasmic ROS as seen in (Luo *et al.*, 2013). Conversely, in U87-MG cells ROS may be produced primarily from other pathways, such as NOX. Such pathways may be not affected by oxidative stress, but can be altered when the activity of PI3K was inhibited (Figure 3.15).

Furthermore, the elevated level of ROS production in U87-MG cells may be associated with cell death. In the presence of LY294002, the cellular ROS production in U87-MG cells was seen to be much higher than in RD cells, particularly under hypoxic conditions. High levels of ROS may induce apoptosis and lower cell viability, which is consistent with the results obtained in section 3.3.5.4.

### 3.4.4 Cell survival and metabolism under glucose stress

The tested cancer cell lines (RH30, RD, U87-MG, and MCF7 cells) were maintained in DMEM media with high glucose concentration according to the supplier's instruction (ATCC). In such culture media, sufficiently supplied glucose, pyruvate and glutamine all play a role as metabolites and participate in cellular respiration. However, the levels of the metabolites found in cell culture media are not those found physiologically in the body. For example, the glucose concentration is approx. 6 - 8 mM in normoglycemic plasma in the mammalian brain (Silver and Erecinska, 1994), approx. 5 mM in the skeleton muscle (Cline *et al.*, 1998) and approx. 4 - 7 mM in the human blood

(American.Diabetes.Association, 2000). In cancerous tissues, the supply of metabolites, including glucose, may be even lower leading to glucose stress (Navratilova *et al.*, 2013). The efficacy of anticancer drugs may be compromised under such oxidative / glucose stress (Onozuka *et al.*, 2011).

In order to mimic the tumour microenvironment, RD and U87-MG cells were cultured and treated under hypoxic / hypoglycaemic conditions. Cell survival, oxygen consumption and ROS production were all seen to be altered when RD and U87-MG cells were under glucose stress. Their response to LY294002 was also found to be altered (Figure 3.16, 3.17, and 3.18).

Under hypoxic conditions, RD cells consumed more oxygen in hypoglycaemic media, associated with a significantly lower cell survival rate ($P < 0.01$) and large increase in ROS generation ($P < 0.01$). The treatment of LY294002 was not seen to significantly affect either cell number or intracellular oxygen ($P > 0.05$), only contribute to reduce the ROS generation. One possible explanation is that neither glycolysis nor OXPHOS work normally when oxygen (required in OXPHOS) and glucose (required in both pathways) are both insufficient. Instead of efficiently generating energy, RD cells produced excessive amounts of ROS and consumed more oxygen due to aberrant metabolic pathways, resulting in cell death. The treatment of LY294002 compromises the aberrant metabolism leading to reduced ROS generation (for example, by inhibiting SOD and/or NOX pathways), but not effectively enough to influence cell survival rate.

Under normoxic conditions, RD cell number was lower in hypoglycaemic media, and more oxygen was consumed per cell. These results indicated a stimulated OXPHOS coupled with lower cell survival. One possible reason is that the adaptation to glucose stress

leads to an abnormally high but inefficient consumption of oxygen, and therefore RD cells fail to thrive. In RD cells, the presence of LY294002 caused a significant reduction in cell number ($P < 0.01$) and ROS generation ($P < 0.001$) under normoxic conditions. The reason might be similar to that discussed in section 3.4.3 (when RD cells were treated in normal culture media under normoxic condition), as altered metabolism from glucose stress may not affect cell survival and ROS production. PI3K was not found to contribute directly in OXPHOS (which is found primarily used in RD cells) in many cell lines (Arcaro, 2014). This was consistent with the results that sufficient PI3K inhibition was not seen to affect oxygen consumption of RD cells after treatment in either tested culture media.

U87-MG cells were shown to survive better than RD cells under the same glucose stress, as the cell number was barely affected under metabolite stress under either low or atmospheric oxygen levels. One possible explanation is that U87-MG cells may efficiently use other metabolites (such as glutamine or pyruvate) in the media to survive. Furthermore, the oxygen consumption under glucose stress was found to be higher than when U87-MG cells were cultured in 20 mM glucose media. This result is also consistent with the assumption that the respiration was enhanced with metabolites other than glucose. ROS generation was lower when cultured in low glucose media under hypoxic conditions. It was also noted that ROS production induced by normoxia was much lower compared with hypoxia (Figure 3.18 c & d). These results indicate that U87-MG cells consumed more oxygen in low glucose media under hypoxic conditions, associated with a decrease in ROS production. However, the converse was found in RD cells. One possible reason is that the mitochondrial respiration and TCA cycle are not the major source of ROS gener-

ation in U87-MG cells, since OXPHOS metabolism is not predominantly used in U87-MG cells. Under normoxic conditions, ROS remains at the same level when cultured in media with different glucose concentrations, possibly also resulting from compensated metabolism depending on metabolites other than glucose.

The treatment of LY294002 was seen to significantly reduce the cell number when U87-MG cells were suffering from glucose stress under hypoxic conditions ($P < 0.01$). However, the cell number was not found to decrease in the presence of LY294002 when U87-MG cells suffered from metabolite stress under normoxic conditions ($P > 0.05$, in 1 mM glucose media). This may be because respiration using other metabolites is not affected by PI3K inhibition.

### 3.4.5 Difficulty in clinical use and drug carrier

The difficulty of LY294002 delivery has been a major challenge in the clinical use of this drug. Although LY294002 is soluble in many common organic solvents such as DMSO, ethanol and DMF, it is a very hydrophobic chemical, and is insoluble in aqueous solutions (<50 µg/ml in PBS pH 7.2; Cayman Chemicals), such as body fluids.

Furthermore, LY294002 is unstable in aqueous solutions with a half-life of only approx. 3.5 hours (Jones *et al.*, 1999, Malaiyandi *et al.*, 2005). This insolubility and short half-life often leads to poor pharmacokinetics both *in vitro* and *in vivo*. Moreover, the tissue specificity of LY294002 is low, which may cause high cytotoxicity to healthy cells when administered systemically (Hennessy *et al.*, 2005).

Despite the low specificity, hydrophobicity and instability in aqueous solutions, LY294002 is still a potential candidate for use as an anti-cancer agent with an appropri-

ate drug carrier. It has been reported that MSNPs are able to protect hydrophobic/instable drug from rapid clearance and overcome drug delivery barriers in the body (Lu *et al.*, 2007). Therefore, LY294002 was chosen as a representative model of a drug with high anti-cancer potential, but which would be difficult to use without an appropriate carrier.

## 3.5 CONCLUSION

In summary, the PI3K inhibitor, LY294002, was found to be capable of inhibiting the phosphorylation of Akt in the tested cell lines under either hypoxic or normoxic conditions. However, the inhibition efficiency varied greatly between different cells under different oxygen levels. It was observed that LY294002 appeared to be more functional in cells which use glycolysis predominantly in metabolism.

In the future, the use of LY294002 needs to be cautiously evaluated when treating tumours, since cancer cells may respond differently to LY294002 under various metabolite concentrations and under different oxygen conditions.

Due to the insolubility of LY294002 in aqueous solution, organic solvents, such as ethanol (Brown, 2007) or DMSO (Abdul-Ghani *et al.*, 2005), have to be used when treating cells with LY294002. The toxicity and low tolerance of such organic solvents constrains the usage of the drug *in vivo*. Therefore a biocompatible carrier of LY294002, such as MSNPs, is highly desirable.

A drug delivery system that encapsulates LY294002 molecules within MSNPs is detailed and discussed in Chapter 4.

# Chapter 4

# Drug carrying and release

An important parameter to determine for a drug delivery system is the way in which encapsulated drugs migrate from their initial position in a nano-carrier to the release buffer. This seemingly simple process is affected by many factors such as the relative size of the drug molecules to pore size (He and Shi, 2011), the physicochemical properties of the drugs against the surface of nanocarriers and the release buffer (Kosmulski, 2004), and the release environment (Fu and Kao, 2011).

As such, the drug loading and unloading behaviours of the different MSNPs were assessed.

## 4.1 INTRODUCTION

### 4.1.1 The theory of drug release

Previous studies have generated a number of mathematical models which are able to provide theoretical explanations of drug release behaviour. The majority of models are based on Fick's first law of diffusion and the Noyes-Whitney dissolution law.

Fick's first law of diffusion describes the relationship between the solute concentrations to the diffusive flux under the assumption of steady state. It is proposed that the solute flux diffuses from regions of high concentration to regions of low concentration across the concentration gradient (Raval *et al.*, 2010).

The Noyes–Whitney dissolution law describes the dissolution rate of a solute in relation to both the properties of the solute and the solvent. This is expressed mathematically as:

$$\frac{dW}{dt} = \frac{DA(C_s - C)}{L}$$

Where: $\frac{dW}{dt}$ is the dissolution rate, A is the surface area of the solute, C is the solute concentration in the bulk solvent, $C_s$ is the solute concentration in the diffusion layer surrounding the solute, D is the diffusion coefficient, L is the diffusion layer thickness (Sherrill, 1936).

### 4.1.2 Controllable release of drug

MSNPs have been demonstrated to be effective nano-carriers of many clinical drugs (Huang *et al.*, 2014, Kwon *et al.*, 2013), including doxorubicin (Shen *et al.*, 2011), paclitaxel (Jia *et al.*, 2013), and ibuprofen (Zhang *et al.*, 2011). The release of cargo can be controllable from surface functionalization and/or capping with a variety of stimuli-

responsive materials (Lee *et al.*, 2011b) and targeting ligands (Rosenholm *et al.*, 2010). Such modifications enable control over the drug release profile, but also spatial control which could potentially avoid off-target effects.

A number of methods have been reported to control drug release in MSNPs. For example, MSNPs can be capped with small nanoparticles, such as CdS, which are removable with disulfide bond-reducing molecules such as dithiothreitol (DTT), and the loaded cargo will be released if the uncapping effect is triggered (Lai et al., 2003). MSNPs capped with stimuli-responsive polymeric materials that enable drug release to be triggered under specific environmental conditions have also been developed.

Such a system allows loaded MSNPs to release chemotherapeutics only in the tumour and eliminate damage to healthy tissues, as the microenvironment in a malignant tumour differs from normal healthy tissue in the pH, temperature and redox condition (section 2.1.3). For example, the pH in cancerous tissue is normally slightly lower than in healthy tissue. Therefore pH-responsive materials can be used to control drug unloading behaviour in chemotherapeutics delivery with MSNPs.

Since the tumour microenvironment is hypoxic and acidic, pH- or redox-responsive capping can be used for specific drug unloading in tumours. To date, known redox-responsive molecules are rare and toxic. Therefore MSNPs in this study will be capped with pH-sensitive coating.

The capping molecules need to be biocompatible and sensitive at physiological range (which is pH 6.5 to pH 7.5). Therefore PMPC-PDPA co-polymer has been chosen because of its biocompatibility and sensitivity range (Wang *et al.*, 2005). Ideally, the

capped MSNPs will only release drug/siRNA specifically in the tumour, and minimise damage to healthy tissue.

### 4.1.3 Target release

MSNPs can be functionalised with targeting ligands that direct drug-loaded MSNPs specifically to cancerous cells. For example, it was reported that folic acid can act as an effective targeting ligand due to a higher abundance of folate receptors in many cancer cells compared to normal cells (Liong *et al.*, 2008). Other targeting ligands such as monoclonal immunoglobulin G (IgG) could also target MSNPs to tumours and avoid non-specific particle distribution *in vivo*, thereby enhancing the efficiency of drug delivery (Angelatos *et al.*, 2006).

## 4.2 MATERIALS AND METHODS

### 4.2.1 Model drug loading and releasing

Calcein and Rhodamine B were used as model drugs in the study of the loading and unloading behaviours of MSNPs. In a typical experiment, 20 mg MSNP was re-suspended in 7 mL dd$H_2O$ while 18 mg calcein was dissolved in 2 mL loading solvent dimethylformamide (DMF). The MSNP suspension and calcein solution was mixed and stirred robustly in a glass vial, resulting in a final calcein concentration of 2 mg/mL. The stirring was maintained at room temperature for 24 hours. The calcein loaded particles were collected by centrifugation and washed with washing buffer (methanol: dd$H_2O$ (1:1 v/v)) twice. The loading process was similar when loading Rhodamine B (RB), except ethanol

was used as the loading solvent instead of DMF and dd$H_2O$ was used for the washing step. SNPs were included as a control.

The unloading behaviours were determined by measuring the fluorescence of calcein / RB loaded MSNPs in water. For assessment of the unloading characteristics of the particles, the MSNPs were diluted to low concentrations to avoid self-quenching of the dye. The release behaviour of the MSNPs was monitored with an INIFINITE 200 plate reader (Tecan, Switzerland) with single fluorescence read with 10 min intervals over 60 hours. Filter sets used for Calcein were Excitation 465(35), Emission 510(10), and for Rhodamine B Excitation 544(25), Emission 612(10). All samples were set in triplicate.

The loaded amount was calculated by subtracting the remaining amount of dye in the residue from the total amount before loading. The immobilised dye amount was calculated by subtracting the total released amount over 120 hours from the loaded amount of dye.

### 4.2.2 Controlling MSNPs releasing behaviour

#### *4.2.2.1 Controlling release behaviour of HMSNPs by capping with polyelectrolytes*

HMSNP was capped using a layer-by-layer technique (Pearson *et al.*, 2013) with a polycation, poly-allylamine hydrochloride (PAH) and a polyanion, poly-sodium 4-styrene sulfonate (PSS). Before capping, PAH or PSS was dissolved in Capping Buffer (20 mM Tris, 20 mM NaCl, pH 8.5) at 20 mg/mL. 200 mg HMSNP was re-suspended in 20 mL Capping Buffer, and sonicated in a water bath for 3 min. 0.5 mL PAH solution was added to the HMSNP suspension and incubated with stirring for 30 min at RT. The PAH capped HMSNPs were then collected by centrifugation and washed three times with

dd$H_2O$. Alternate PAH/PSS layers were added to the particles, until eight layers of poly-electrolytes had been capped.

The capped particles were incubated in PBS (pH 7.4) at 37 $^oC$ over 8 days. TEM images were taken at the start of the experiment and during the incubation period.

The release profiles were built using the same technique as the drug release from uncoated particles that was described in section 4.2.1.

#### *4.2.2.2 Controlling release behaviour of HMSNPs by capping with the pH-sensitive co-polymer PMPC-PDPA*

HMSNPs were capped with PMPC-PDPA (provided by Prof. Giuseppe Battaglia, University of Sheffield) in order to study the stimuli-responsive drug release behaviour. The molecule was synthesised as $PMPC_{100}$-$PDPA_{120}$ with $M_n$ (measured with Gel permeation chromatography) 62,000 and $M_n/M_w$1.38.

Before capping, siRNA@HMSNP was synthesised (procedures detailed in section 5.2.1) and was re-suspended in RNase-free water (Sigma-Aldrich) at a concentration of 5 mg/mL. PMPC-PDPA co-polymer solutions were made up at a concentration of 5 mg/mL (0.05 wt %) in PBS and adjusted to pH 5 with 0.1 M HCl.

100 µL siRNA@HMSNP complex suspension was added dropwise in 10 mL co-polymer solution. The solution was vortexed during addition of the siRNA@HMSNP complex. The pH was continuously monitored and maintained below 6.3 after each droplet.

10 µL 2M NaOH was then added to the system dropwise after 100 µL suspension was all added in. The system was shaken for 15 min and sonicated for 5 min in a water bath prior to measuring the pH. This process was repeated until a pH jump from 5.0 to 7.5 was ob-

tained. The particles were washed with PBS twice and collected by centrifugation at 8500 rpm for 5 min.

The release profile was built with the same techniques in section 4.2.1, in water at pH 5 and pH 9.

### 4.2.3 LY294002 loading and releasing

In a LY294002 loading experiment, 15 mg MSNPs were re-suspended in 4 mL PBS (pH 7.4) while 10.5 mg LY294002 was dissolved in 1 mL ethanol: DMF (1:1 v/v). Other solvents were also tested to load LY294002 into the nanoparticles (details in Chapter 4.4.1.3). The MSNP suspension and LY294002 solution was mixed and stirred robustly in a glass vial. The mixture was sonicated in a water bath for 1h and stirred for 23h each day, for five days. The loaded MSNPs were collected by centrifugation and washed with 10% DMSO in PBS.

The release of LY294002 was monitored with Cary Eclipse Fluorescence Spectrophotometer (Agilent Technologies, USA) at Ex. 392 nm / Emi. 305 nm over 24 hours in 10% DMSO in PBS at 37 $^{o}$C.

### 4.2.4 Cell viability after a treatment of LY294002 treated MSNPs

The cell viability of RD and U87-MG cells was determined after a treatment with LY294002 loaded MSNPs (LY294002@MSNPs or LY@MSNPs) under hypoxic (1% $O_2$) and normoxic (21% $O_2$) environments. The cells were cultured in a 96-well microplate at a concentration of $1 \times 10^4$ cell / mL for 24 hours in humid 37 $^{o}$C incubator (5% $CO_2$, 21% $O_2$) before treatment. Then the cells were washed once with warm PBS and treated with

LY294002 loaded MSNPs at a final concentration of 0.05 mg loaded MSNPs / mL of culture media.

The cell viability was evaluated using the MTT assay as detailed in section 2.2.4.

## 4.3 RESULTS

### 4.3.1 Model drugs loading and releasing

The fluorescent probes calcein and Rhodamine B were used as model drugs in the investigation of drug encapsulation and releasing from the MSNPs. Calcein is a water-soluble fluorophore that self-quenches easily: the fluorescence signal reaches a maximum in a relatively low concentration (70 to 100 mM). However, when the concentration of calcein was kept below 0.04 mg/mL (Figure S4.1 insert), the fluorescence was linear related to the concentration. Rhodamine B is also a water-soluble fluorophore that also self-quenches, but the quenching commences at a higher concentration than calcein (> 1 M): when the concentration was lower than 0.5 mg/mL (Figure S4.2 insert), the relation of the fluorescence against the concentration was linear. Therefore, the concentration of both calcein and Rhodamine B can be determined by measuring the fluorescence at low concentration.

For the negatively charged model drug, calcein, the MSNPs had a various loading capacity: BMSNPs and CMSNPs were loaded with 21.48% and 18.85% of the total of which they were exposed (which was 2 mg/mL), respectively. HMSNPs and WMSNPs were less efficient calcein carriers (with only 12.63% and 9.03% loading capacity). Virtually no calcein was detected on SNPs, as would be expected (Figure 4.1a). The absolute amounts of calcein loaded in different MSNPs were listed in Table 4.1.

BMSNPs, CMSNPs and WMSNPs released calcein rapidly such that almost all cargo was unloaded within the first 10 hour period, and the release became much slower during the end of the studied release period (Figure 4.1b). On the contrary, there is no rapid cargo unload from HMSNPs. The release was seen to have a steady release during the whole experiment. The release was not fit in normal drug release kinetic theory due to the non-Fick diffusion.

Release profiles for Rhodamine B from the different MSNPs showed variations. Rhodamine B is a positively charged dye at neutral pH (Patel *et al.*, 2009), thereby it was expected to be more likely to be attracted to silica nanoparticles whose deprotonated surface is negatively charged in a neutral environment. It was shown that the Rhodamine B loading of the MSNPs was higher than seen for calcein loading (Figure 4.1a, Figure 4.2a; Table 4.1, Table 4.2). HMSNPs showed a 12.63 % loading of calcein whereas Rhodamine B loading was as high as 63.10 %. For all other MSNPs, similar phenomena were also noticed. The absolute amounts of Rhodamine B were listed in Table 4.2.

Rhodamine B release profiles of the MSNPs differed from those seen with calcein loading (Figure 4.2b). BMSNPs and CMSNPs released Rhodamine B rapidly while the cargo release from HMSNP was much more stable during the entire time. WMSNPs showed an initial small decrease in the fluorescence signal over the first 2 hour, following by a stable release over the next 30 hours to reach a plateau. The reason for the initial decrease was not very clear, but could be due to de-agglomeration causing re-attachment of the dye molecules. Similar to unloading calcein, all the Rhodamine B release profile also showed a non-Fick diffusion pattern and did not fit any standard theoretical models.

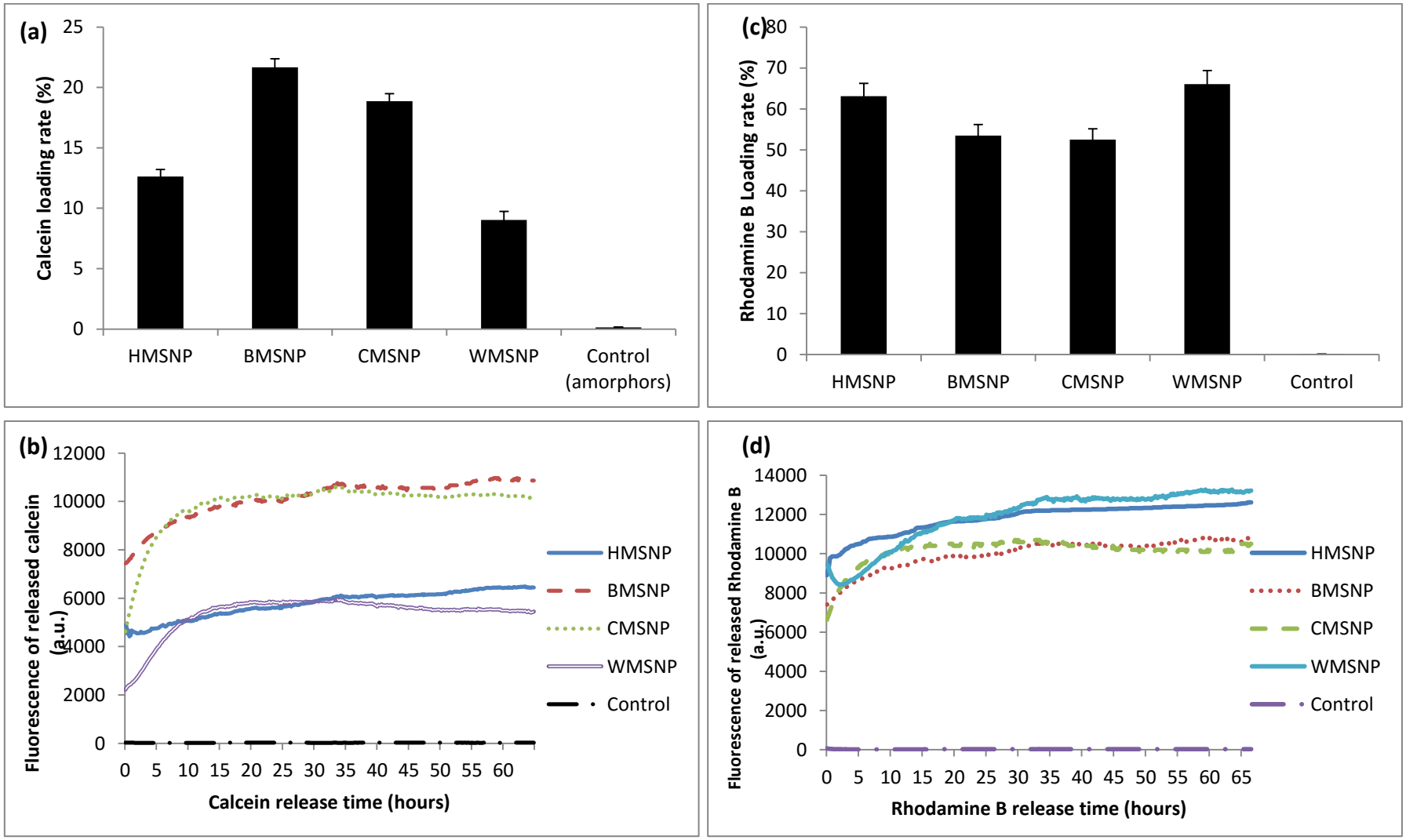


Figure 4.1 Loading and unloading characteristics of the various MSNPs with the model drugs calcein (a & b) and Rhodamine B (c & d): drug loading rate in the MSNPs presented in percentage (a & c) and the model drugs release profiles from the MSNPs (b & d)

| | HMSNP | BMSNP | CMSNP | WMSNP | Control |
|---|---|---|---|---|---|
| Total loaded Calcein / µg | 1136.48 | 1950.80 | 1697.26 | 812.31 | 13.24 |
| Release Calcein in 65 hours / µg | 316.24 | 582.91 | 931.91 | 576.22 | 0.72 |
| Immobilised Calcein / µg | 820.23 | 1367.89 | 765.35 | 236.09 | 12.53 |
| Release percentage of total loaded Calcein / % | 27.83 | 29.88 | 54.91 | 70.94 | 5.44 |
| Calcein loaded per $cm^2$ exposed silica / µg | 1.02 | 6.44 | 1.82 | 1.59 | 0.21 |

Table 4.1 Absolute amounts of the model drug calcein loaded and unloaded on different silica nanoparticles; drug release percentage and calcein loaded per exposed silica were calculated from both uptake and release profiles

| | HMSNP | BMSNP | CMSNP | WMSNP | Control |
|---|---|---|---|---|---|
| Total loaded RB / µg | 5679.00 | 4815.00 | 4725.00 | 5945.85 | 14.19 |
| Release RB in 65 hours / µg | 1674.00 | 1297.23 | 1565.02 | 2283.17 | 0.06 |
| Immobilised RB /µg | 4005.00 | 3517.77 | 3159.98 | 3662.68 | 14.13 |
| Release percentage of total loaded RB / % | 29.48 | 26.94 | 33.12 | 38.40 | 0.42 |
| RB loaded per $cm^2$ exposed silica / µg | 5.11 | 15.89 | 5.06 | 11.62 | 0.22 |

Table 4.2 Absolute amounts of the model drug Rhodamine B (RB) loaded and unloaded on different silica nanoparticles; drug release percentage and RB loaded per exposed silica were calculated from both uptake and release profiles

### 4.3.2 Controlled drug release with degradable polymers capped MSNPs

#### *4.3.2.1 Release controlled with multilayers polyelectrolyte coating*

Cargo release may be controlled by a number of different methods. One of the easiest and most effective approaches is to cap the particle with degradable polymeric materials. To study this possibility, a layer-by-layer PAH/PSS coated HMSNP was assembled.

Rhodamine B release was used to test the system. Since the silica is negatively charged, the first-layer coating was with the positively charged polycation PAH, followed by the negatively charged PSS. After coating the particle with each layer, a small sample was removed and zeta potential measurements (Figure 4.2) were taken to check the success of each polyelectrolyte layer in coating the particle. This confirmed that each layer (PAH or PSS) was successfully layered on the HMSNP.

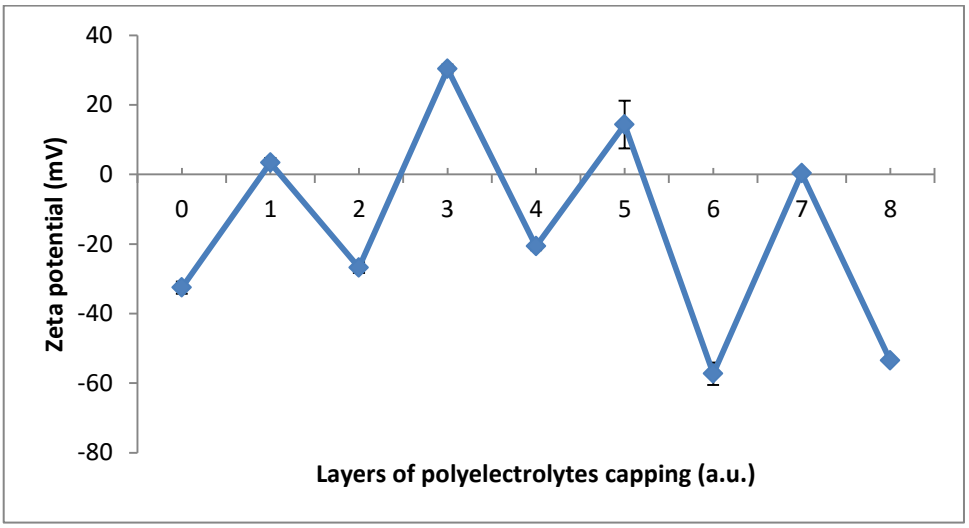


Figure 4.2 Zeta potential of HMSNP measured after each layer of polyelectrolyte capped

The 8-layer polyelectrolyte capped HMSNP was imaged with TEM (Figure 4.3 a). It can be clearly seen that there is a thick layer of material coated on the surface of each particle (seen as a pale grey coating surrounding each particle). A darker region between the coating and the core was seen in some particles (highlighted with a white arrow in Figure 4.3 a). It was suggested that this resulted from polymer immersed into the silica particle through pores. The polymer layer was up to 28.65 ± 3.77 nm (n = 64). A pale grey region can also be found in the centre of some of the particles. This was because the coating was polymeric and easily burnt with the electron beam during TEM imaging.

After an incubation in a simulated physiological environment (37 $^{o}$C in PBS buffer), the polymer coating became thinner over time. After 8 days incubation, the coating was completely absent from the surface of the particle (Figure 4.3 b), leaving a bare and rough surface of silica nanoparticle.

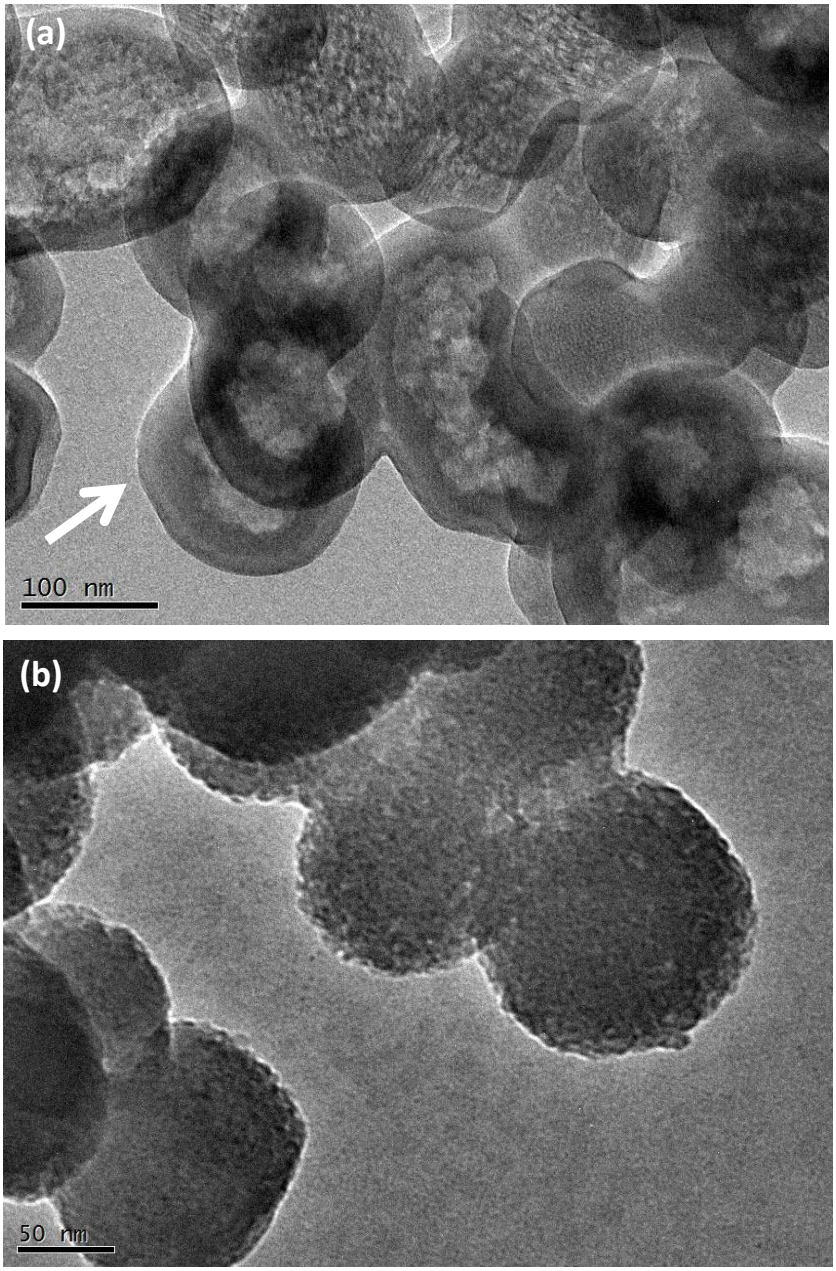


Figure 4.3 Degradation of HMSNPs coated with 8 layers of PAH/PSS (a) Before degradation clearly showing a thick polyelectrolyte layer on the surface (b) After 8 days incubation in physiological buffer at 37 °C the polyelectrolyte layer is no longer present and the pores are indistinct.

The Rhodamine B release profile of polyelectrolyte coated and uncoated HMSNP was compared. The release profiles for the coated and uncoated HMSNPs were different; as would be expected. Coated particles showed a slow release over the first 70 hours, following an inflection point, and a more rapid sustained release over the next 40 hours (Figure 4.4). It was assumed that the polymeric layer was too thick to allow effective Rhodamine B molecule diffusion in the first 70 hours. As the polymer coating degraded, the thickness was reduced to a low enough level to allow Rhodamine B release. The total amount of Rhodamine B released was similar for both coated and uncoated HMSNPs after 110 hours.

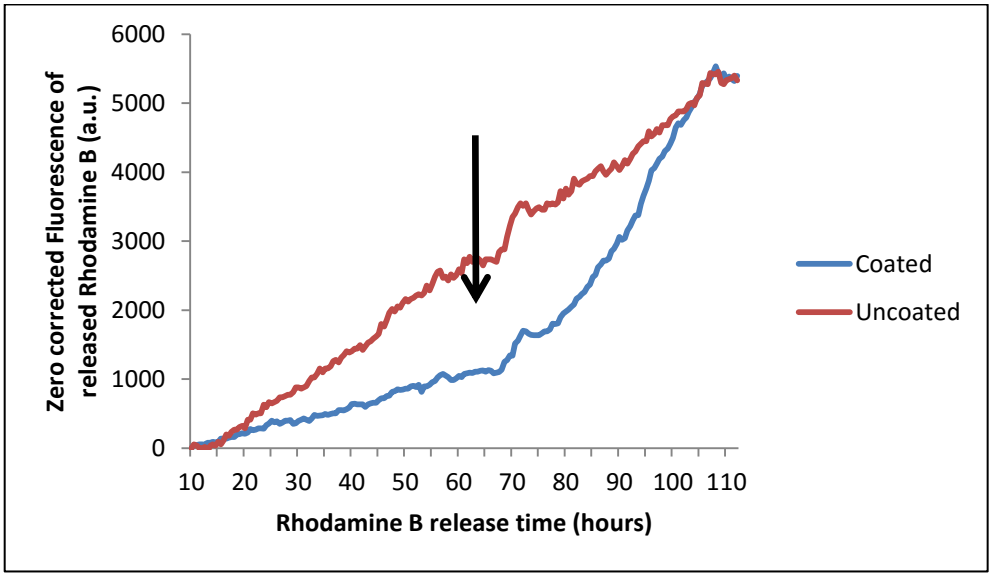


Figure 4.4 Zero corrected Rhodamine B release profile of uncoated and 8-layer PAH/PSS coated HMSNP over 110 hours, the release was taken from the 10$^{th}$ hour to 110$^{th}$ hour

Therefore, the drug unloading behaviour can be controlled with coating degradable polymeric materials on the silica nanoparticle nano-carrier.

#### *4.3.2.2 Release controlled with a PMPC-PDPA co-polymer coating*

The Rhodamine B release profile of PMPC-PDPA coated, and uncoated HMSNP was compared (Figure 4.5). The release profiles for the coated and uncoated HMSNPs were shown to be different under different pH due to the pH sensitivity of PDPA blocks (discussed in section 4.4.2). Over the first two hours, Rhodamine B release in high pH buffer (pH 9) was seen to be much slower than it was in acidic buffer (pH 5). There was approx. 112.53 % difference after the 1$^{st}$ hour release (see the black arrow in Figure 4.5). However Rhodamine B released in pH 5 or pH 9 buffers eventually reached the same level over 24 hours (Figure S4.3).

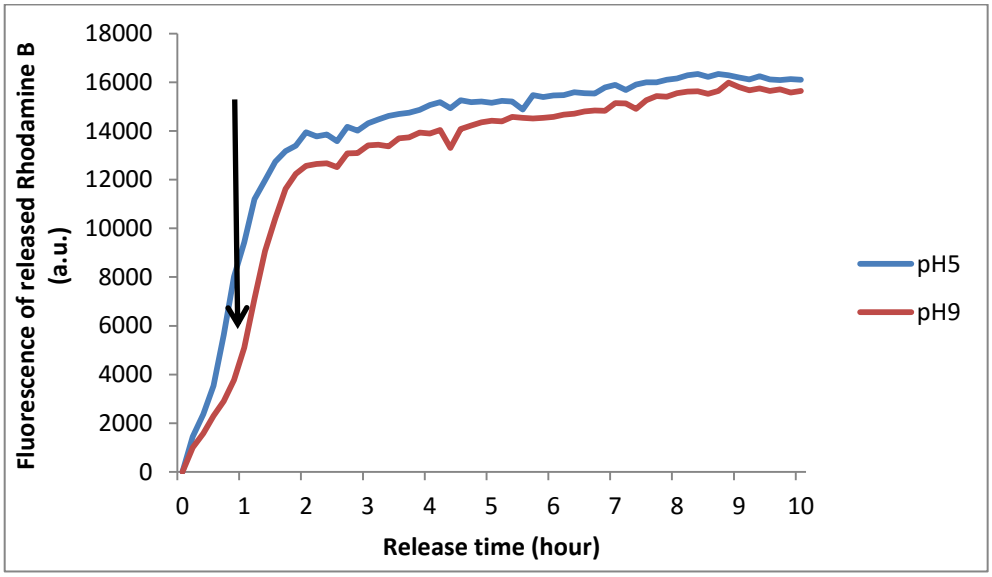


Figure 4.5 The Rhodamine B release profile from PMPC-PDPA capped siRNA@PEI-HMSNP in release buffers with pH 5 or pH 9 over 10 hours

### 4.3.3 LY294002 loading and releasing

HMSNPs, BMSNPs and WMSNPs showed a high loading capacity: holding 693.3 μg, 555.1 μg, and 518.0 μg LY294002 per mg nanoparticles. The loading capacity was

slightly lower in CMSNPs such that 396.9 μg LY294002 was loaded per mg nanoparticles. LY294002 loaded on SNPs was negligible.

The release profiles showed a rapid release for all MSNPs and nearly all the cargo was released in the first 60 min (Figure 4.6). However, the different MSNP architectures showed very different release profiles.

In HMSNPs, the LY294002 release behaviour was unexpected: after a rapid initial unloading, release LY294002 dropped from a peak at the $60^{th}$ min and remained at a low level. The same phenomenon was observed in multiple repeats, and has also been observed by other researchers in the laboratory, with a number of different compounds. One possible explanation is that the released LY294002 either self-quenched or decomposed over the time course. However, NMR results indicated LY294002 was not decomposed after exposed to 305 nm UV light over 24 hours in a normal laboratory environment (data not shown). It was also possible that the LY294002 was re-adsorbed by HMSNPs. Another possible reason is the precipitation of HMSNPs interrupting optical detection by the spectrophotometer.

The release profiles of other MSNPs were seen to be as expected and similar to those releasing model drugs. After a rapid surge of LY294002 release in the first 40 min, a plateau was seen in BMSNPs, CMSNPs, and WMSNPs, and remained fairly constant thereafter. The LY294002 loading on SNPs was negligible and the release profile was seen to remain at a very low level during the whole course.

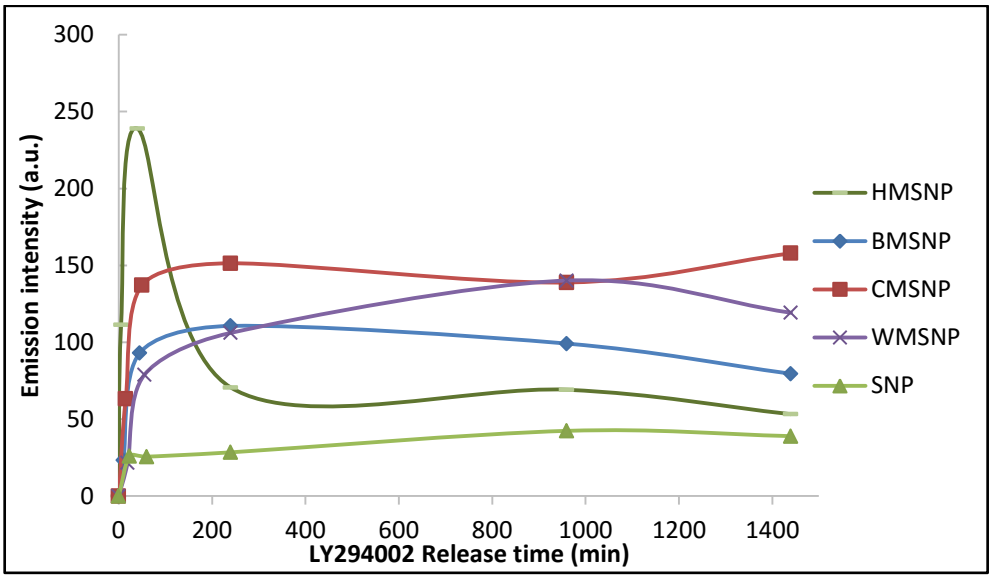


Figure 4.6 LY294002 release curve assessed with spectrophotometer from morphologically different MSNPs over 24 hours

In summary, all the MSNPs tested were seen to be effective nano-carriers to load and un-load LY294002.

### 4.3.4 Cell viability after a treatment of LY294002 treated MSNPs

The viability of RH30, RD, U87-MG and MCF7 cells was measured after they were treated with LY294002 loaded MSNPs (labelled as LY@MSNPs in later context), to evaluate the effectiveness of MSNPs unloading LY294002 over 120 hours. To eliminate any potential influence of inherent MSNPs toxicity, all viability results of the loaded MSNPs were compared /calibrated with their unloaded counterparts separately.

In RH30, all MSNPs were seen to be able to deliver LY294002 to cells and reduce the viability after treatment under hypoxic or normoxic condition.

Under hypoxia, CMSNPs appeared to be the most efficient carrier in the first 24 hours in RH30 cells and the viability decreased to 71.12 % of the control after treatment with LY@CMSNPs. All other LY294002 delivery systems showed a decrease in viability of RH30 cells after treatment for 24 hours under hypoxic conditions, except for SNP. After a longer period of incubation, LY@HMSNPs and LY@BMSNPs caused a further decrease in RH30 viability. BMSNPs became the most efficient candidate as the viability reached 54.41 % of the control after 120 hours treatment (Figure 4.7a).

Under normal oxygen levels (21% $O_2$), all the LY294002 delivery systems were seen to be more effective compared to hypoxia over long incubation periods. The cell viability was decreased to 30.35 % of the control after treatment with LY@BMSNPs for 120 hours incubation. HMSNPs and CMSNPs were also shown to be very efficient carriers of LY294002 under the same experimental environment (Figure 4.7b): LY@HMSNP and LY@CMSNP caused a decrease in RH30 viability to 41.40 % of the control and approx. 35.09 % of the control, respectively.

LY@SNPs caused negligible reduction in RH30 cell viability over 24 or 120 hours incubation under either hypoxic and normoxic condition.

MSNPs were also found to deliver the drug to RD cells. In hypoxia, BMSNPs were seen to be the most efficient LY294002 nano-carrier: RD cell survival reached a minimum to 81.49 % of the control after a 24 hours treatment with LY@BMSNPs, and dropped further to 38.68 % of the control after 120 hours (Figure 4.8a). Other MSNPs were all seen to effectively deliver the compound to RD cells and cause a reduction in cell viability.

Under normal oxygen condition, the tendency was seen to be similar as all MSNPs were shown to be effective LY294002 carriers. When compared to hypoxia, cell viability was decreased even more in normoxia over a long time treatment with LY@MSNPs. Cell viability dropped to just 36.82 % of the unloaded control after treatment with LY@BMSNPs for 120 hours. LY@HMSNPs appeared to be more efficient in reducing RD cell viability under normoxia than under hypoxia. They successfully delivered LY294002 to RD cells and caused the viability to decrease to 36.67 % of the control after 120 hours incubation under normoxic condition, comparing to 65.97 % of the control under hypoxic condition.

The non-porous SNP was not a successful carrier of the compound and the viability of RD was hardly changed after treatment with LY@SNP under either oxidative condition.

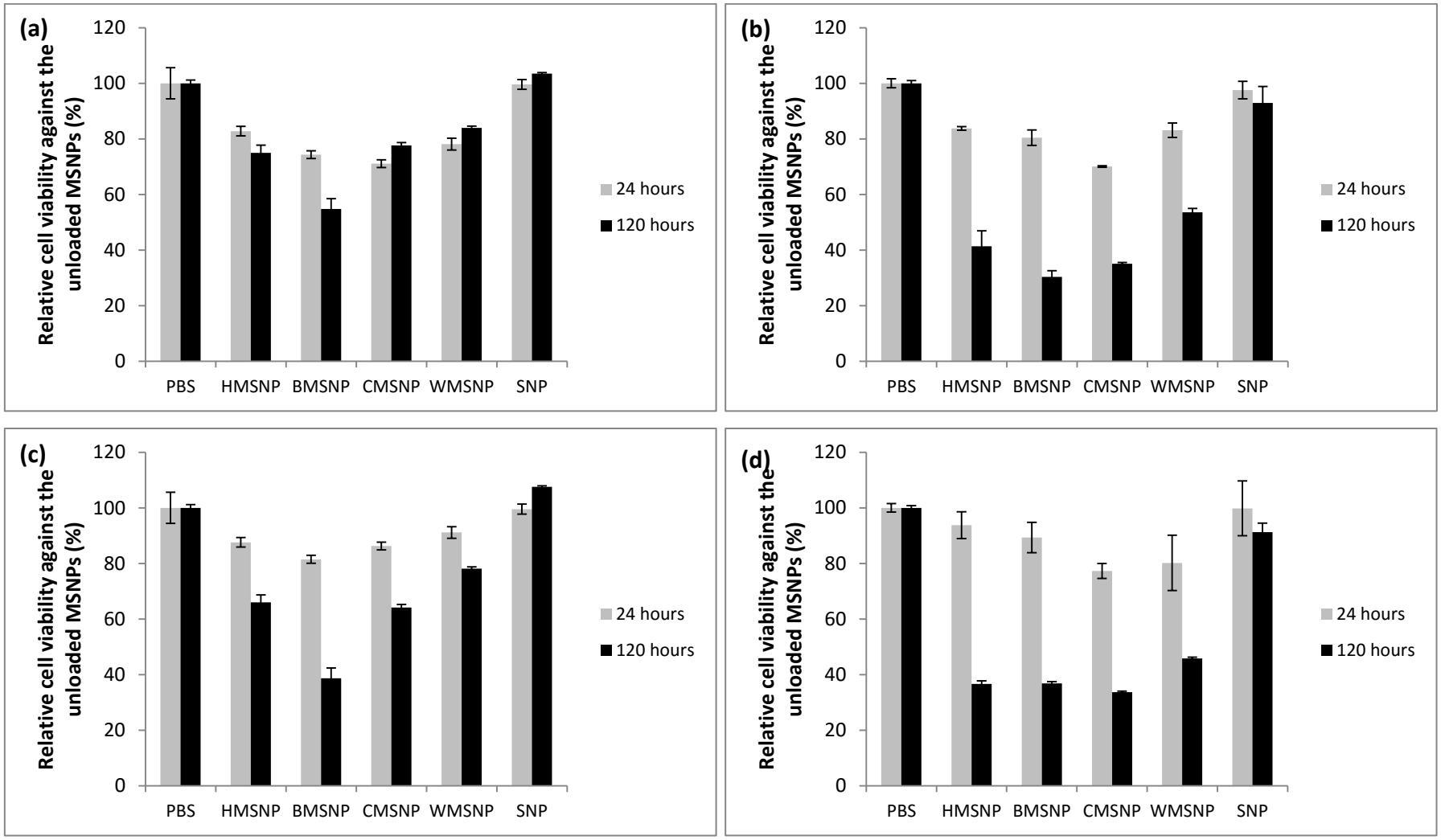


Figure 4.7 Relative RH30 (a & b) and RD (c & d) cell viability after a treatment of LY294002@MSNPs calibrated with unloaded MSNPs separately under hypoxic (a & c) or normoxic (b & d) conditions (the data are presented as the means ± standard deviation, n= 3)

Under hypoxic conditions, WMSNPs were seen to be the most efficient carrier of LY294002 to U87-MG cell line: a treatment of LY@WMSNPs managed to reduce U87-MG cell viability to78.99 % of the control after 24 hours treatment. The viability was further reduced to 42.38 % after a long period of incubation. Other MSNPs were also shown to be effective carrier for LY294002: LY@BMSNPs reduced the U87-MG cell viability to 59.65 % of the control after treatment for 120 hours, while LY@HMSNPs and LY@CMSNPs also efficiently caused a decrease in cell viability to 71.11 % of the control and 66.32 % of the control separately under the same experimental condition.

WMSNPs were also found to be the most efficient vehicle to deliver LY294002 to U87-MG under normoxic conditions after treatment for 24 hours. However, over a long period of incubation, BMSNPs became the best LY294002 carrier as the LY@BMSNPs caused a reduction in viability down to 37.29 % of the control. Other MSNPs were also seen to be able to deliver the compound and result in reduced U87-MG cell viability.

Control SNP showed negligible delivery of LY294002, and U87-MG did not show any decrease in cell viability after treatment with LY@SNPs under either hypoxic or normoxic conditions.

It should be noted that the results from U87-MG cells showed a large standard deviation due to the severe agglomeration of the cells that may introduce errors into the MTT assays.

Under hypoxic conditions, all MSNPs were shown to be efficient drug carriers of LY294002, and MCF7 cell viability was reduced to similar levels after 24 hours treatment. LY@HMSNPs and LY@CMSNPs were not seen to decrease the viability much

further after the first 24 hours, while LY@BMSNPs and LY@WMSNPs caused a further reduction in MCF7 cell viability to approx. 51.82 % of the control and 41.92 % of the control, respectively, over the course of 120 hours.

The delivery systems were seen to be more efficient under normoxic condition. MCF7 viability reached 32.98 % of the control after treatment with LY@BMSNPs over the course of 120 hours. All other LY@MSNPs, despite their lower efficiency, were also found to cause reduction in cell viability under the same experimental condition.

Control SNPs showed negligible delivery of LY294002 and LY@SNPs did not show any decrease in MCF7 cell viability under either condition.

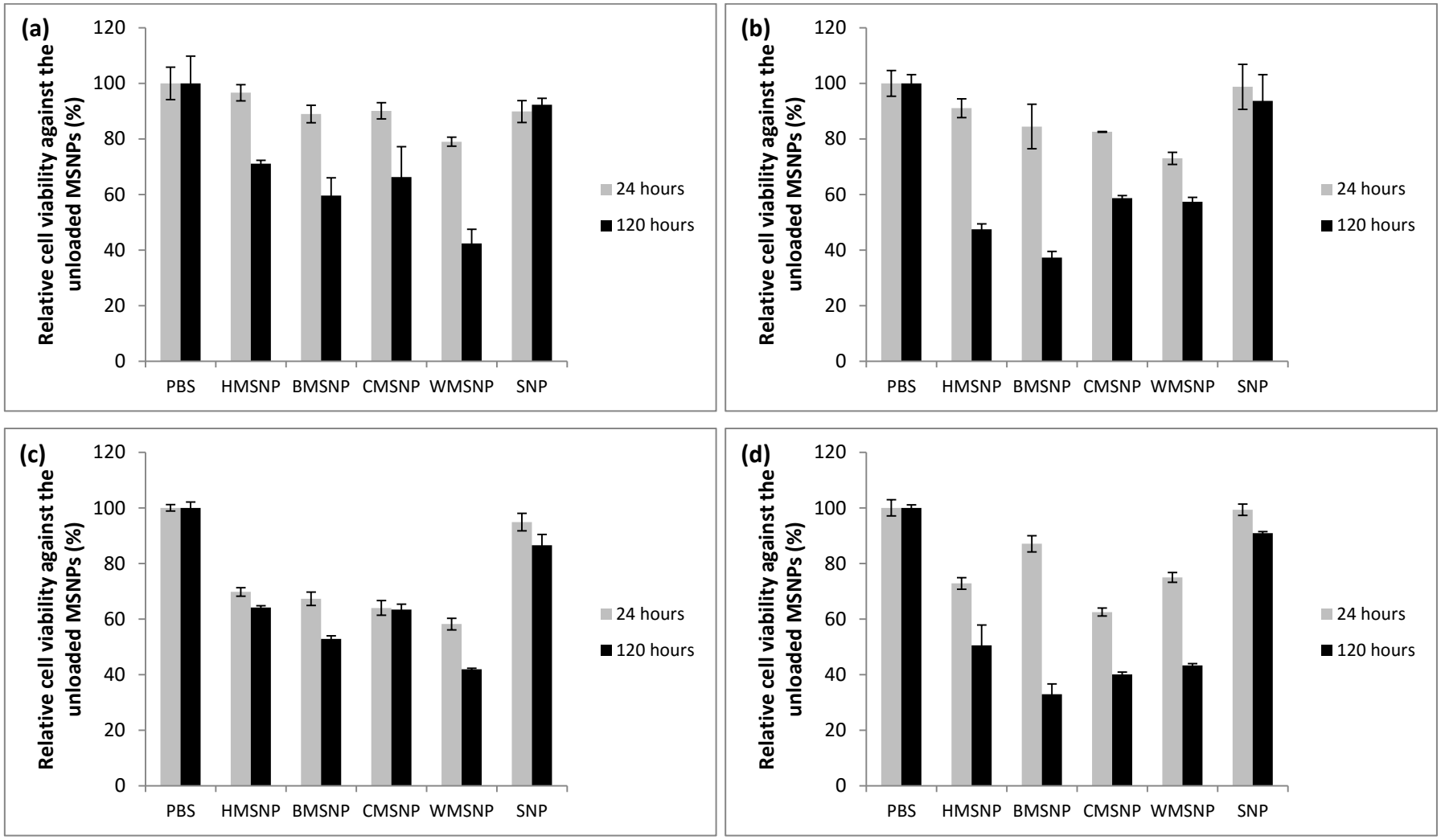


Figure 4.8 Relative U87-MG (a & b) and MCF7 (c & d) cell viability after a treatment of LY294002@MSNPs calibrated with unloaded MSNPs separately under hypoxic (a & c) or normoxic (b & d) condition (the data are presented as the means ± standard deviation, n= 3)

## 4.4 DISCUSSION

### 4.4.1 Factors that affect drug loading and unloading on MSNPs

It was found that the drug loading and unloading varied depending upon the different cargo molecules and MSNPs. The load/release behaviours were shown to be affected by many factors, such as surface charge, surface area and porosity as described in further detail below.

#### *4.4.1.1 Surface properties may affect drug loading/unloading behaviours on MSNPs*

The large surface area of MSNPs allows the adsorption and desorption of the cargo (de Villiers *et al.*, 2008). Loaded and unloaded cargo was barely detected on SNP (Figure 4.1b&d, Figure 4.6), suggesting that the inner surface and pores contributes to the majority of molecule adsorption. However, there was no precise positive correlation found between surface area and cargo molecule adsorption efficiency. This indicates that total surface area was not the sole factor affecting drug loading/unloading on MSNPs.

In addition, surface charges of MSNPs and electric potential difference between MSNPs and cargo molecules may also affect loading/unloading profiles (Honary and Zahir, 2013). Although negatively charged molecules (calcein), positively charged molecules (Rhodamine B) and non-charged molecules (LY294002) were all found to be able to be loaded and unloaded on the tested MSNPs, the efficiency varied greatly. It would be expected that positively charged molecules would be more likely to be attracted to MSNPs. The loading efficiency of the positively charged Rhodamine B was indeed much higher than the negatively charged calcein for all types MSNPs tested (Table 4.1, Table 4.2).

Furthermore, it was noticed that the interaction between the exposed silica surface on the MSNPs and the drug molecules was not only dependent upon the electric potential differences but also other surface properties of MSNPs, such as exposed pore size, and chemical residues on the surface. Model drug molecules were seen to be adsorbed more easily onto the surface of BMSNPs than any of the other candidates; and the surface of the SNPs appeared to be the most recalcitrant to both calcein and Rhodamine B under the loading protocols attempted.

#### *4.4.1.2 Porosity and morphology may affect drug loading/unloading behaviours on MSNPs*

Another factor which affects loading and unloading of cargo is the relative dimensions of the pore and the drug molecule. It has been found that when the pore diameter and drug molecule are approximately the same size there is a sustained release due to the confinement effect. When the pore size is much larger than the drug molecule then the cargo may be released at a relatively higher rate (He and Shi, 2011). The Stokes-Einstein radius of calcein is estimated as 0.6 nm, and a hydrated calcein radius of 0.8 nm (Edwards *et al.*, 1995). Therefore, calcein is much smaller than the pore size of all MSNPs studied (Table 2.1), enabling an efficient loading. The size of Rhodamine B molecule is similar to calcein and will behave accordingly. The LY294002 molecule is not electrostatically charged and the molecule size was determined to be 0.5 nm in diameter from spatial modelling. LY294002 is hydrophobic so there would be little hydration during the loading procedure. Since the LY294002 molecule is much smaller than the pore size of the MSNPs, efficient loading would be expected without confinement effects.

In addition, the release percentage of loaded drugs was found to be dependent upon the morphology of the silica nanoparticles. While WMSNPs were found to un-anchor and release 70.94 % calcein or 38.40 % Rhodamine B in aqueous solution, HMSNPs only released 27.83 % loaded calcein or 29.48 % Rhodamine B. The non-porous SNPs barely released any of the adsorbed molecules. The release efficiency may be related to the degree of porosity of the structure surface (highly wrinkled surface on WMSNP against non-porous amorphous surface on SNP), the specific surface area, or the surface charge.

#### *4.4.1.3 Drug loading procedures (such as solvents and/or sonication) may affect drug loading behaviours on MSNPs*

It was also noticed that the solvents used for loading the cargo can affect the cargo molecule attachment on the MSNPs significantly. Previous studies showed that the solubility and dispersion of cargo molecules to the loading solvent(s) should be taken into consideration in the loading procedures (de Villiers *et al.*, 2008, Mohanraj and Chen, 2006).

| Solvent | Sonication | Loading efficiency / % |
|---|---|---|
| 10 % DMSO in water | No | 0.1 |
| 10 % EtOH in water | No | 12.2 |
| 10 % DMF in water | No | 34.8 |
| 10 % DMF, 10 % DMSO | No | 22.9 |
| 10 % DMF, 10 % EtOH | No | 60.5 |
| 10 % DMSO, 10 % EtOH | No | 27.4 |
| 10 % DMF, 10 % EtOH | Yes | 99.1 |

Table 4.3 Loading efficiency of LY294002 on HMSNPs, using a number of different solvent systems. Samples were incubated for 120 hours

It was also found to be important with the MSNPs. It was found in this research that the LY294002 loading is very dependent upon the loading process and loading solvent. The efficacy of loading varied vastly with different LY294002 loading solvent. After many

attempts, a mixture with 10% DMF and 10% EtOH in water was determined to be the most efficient loading solution (Table 4.3).

It was also found that sonication during loading process can enhance the LY294002 loading efficacy (Table 4.3).

### 4.4.2 PMPC-PDPA coating

PDPA is the pH sensitive block of the PMPC-PDPA co-polymer. When the environmental pH falls below the PDPA pKa of 6.4, the tertiary amine groups on the polymer chains are protonated (Figure 4.9) leading to the hydrophilic and dissolvable properties of the co-polymer. Conversely, when the pH is higher than 6.4, the PDPA tertiary amine groups are deprotonated resulting in its hydrophobicity and insolvability. PDPA can also interact with the negatively charge sugar-phosphate backbone of a nucleic acid at physiological pH. Hence PMPC-PDPA was capped onto the surface of the siRNA@MSNPs complex (Lomas et al. 2010).

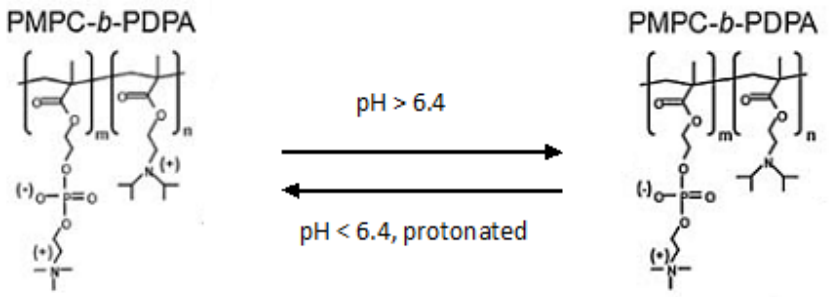


Figure 4.9 Schematic diagram of the protonation process of PMPC-PDPA co-polymer, where m = 100 and n = 120 in this research

The drug release profile from MSNPs was seen to be altered after capped with PMPC-PDPA co-polymer under different pH (see section 4.4.2). It was seen that the PMPC-PDPA co-polymer coating affected the release behaviour of entrapped cargo differently

depending upon the pH of the environment buffer: cargo was seen to be unloaded more quickly in acidic buffer than in basic buffer. This phenomenon was more obvious in the first 2 hours, and the total release amount would eventually reach the same level under different pH over time.

Despite the success in controlling cargo release under different pH, a number of issues remain.

There would be a large amount premature release of cargo molecules using current PMPC-PDPA capping procedures. The problem is particularly noticeable during calcein unloading from PMPC-PDPA capped nanoparticles: the release of calcein was almost undetectable (data not shown) due to the massive drug loss before the unloading experiments. It was not much better when using Rhodamine B as model drug. The capping method needs to be improved to minimise the premature drug release.

Another challenge is the pH sensitivity of PMPC-PDPA. It has been claimed in the previous literatures that the co-polymer coating should be dissembled when the pH is lower than 6.4. However, the process can be very slow when the pH was not significantly lower than 6.4 as in tumours. Rhodamine B unloading from PMPC-PDPA capped HMSNPs was monitored in the buffers with pH from 5 to 9, however, the difference between drug release behaviours was only obvious between pH 5 buffer and pH 9 buffer. The drug loaded in the system can diffuse through the PMPC-PDPA coating over time irrespective of the pH. Therefore, the PMPC-PDPA co-polymer capping with the current assembly approach may not be very effective to control drug release *in vivo*.

### 4.4.3 The effectiveness of LY294002@MSNPs delivery system

It was found that LY294002 was successfully delivered to RD cells causing a large decrease in cell viability. Similar phenomena were observed in both the RMS cell lines, and the more glycolytic cell lines U87-MG and MCF7 (data not shown). There are a number of factors that affect the cell viability after treatment with LY@MSNPs.

The physiological response of cells after LY294002 treatment was clearly an important factor. It was known that the cells acted differently after treatment under different oxygen level (see section 3.3.2 to section 3.3.7). It would be expected that these differences would also be reflected when the drug is loaded into MSNPs.

Other key factors include the loading capacity of the nano-carriers. The loading and unloading capacity varies greatly between MSNPs. CMSNPs were less efficient in loading LY294002 than BMSNPs, and LY@CMSNPs were found to be less efficient in reducing cell viability in all tested cell lines after a long period of incubation.

Other factors, such as the interaction between MSNPs and LY294002, cellular uptake of the delivery systems under different oxidative conditions, and the biocompatibility of the MSNPs, may also influence the efficiency of LY@MSNPs in reducing cell viability

An interesting fact was noticed that using the delivery system resulted in LY294002 becoming more effective in RD cells under hypoxia. The cell viability of LY@HMSNPs treated RD was 78.95 % in hypoxia, almost the same as in normoxia, which was 79.94 %. This was similar to BMSNPs (73.44 % in hypoxia against 77.24 % in normoxia).

One possible explanation is that LY294002 behaves differently under different oxygen levels in both metabolism (section 3.3.5) and cellular uptake. MSNPs deliver LY294002

into the cytoplasm and endoplasmic reticulum, irrespective of the environmental oxygen concentrations. Therefore the influence of cellular uptake is eliminated. Other possible reasons include the interaction between the MSNPs and LY294002, and MSNPs protecting LY294002 from degradation / decomposition.

## 4.5 CONCLUSION

All MSNPs in this study were found to be able to carry model drug molecules (calcein, Rhodamine B) and LY294002 with the current loading protocols. The cargo molecules could also be successfully released with varied profiles in different MSNPs. Due to the surface charge of the MSNPs, the molecule with a more negative charge appeared to be more difficult to load onto the silica nanoparticles than a more positively charged molecule. The loading and unloading behaviours of different molecules appeared to also be dependent upon the morphology, porosity and surface properties of the carriers.

The drug release profiles may be tuned by capping the MSNPs with polymeric coatings. A layer of polyelectrolytes (PSS/PAH in this study; approx. 10 nm thick) on the surface of a MSNP could prevent the rapid release of cargo molecules although the total release amount would be unchanged. This was successfully demonstrated using the PMPC-PDPA co-polymer as a functionalising polymeric coating of the MSNPs, and the pH-sensitive property was confirmed. However, the pH-sensitivity was not found within the physiological range (as claimed in previous literature). Further research would therefore be required before this co-polymer could be used for drug delivery applications.

LY@MSNPs were found to successfully reduce cell viability in all selected cell lines under either hypoxic or normoxic conditions. MSNPs could therefore be considered to be suitable carriers to deliver LY294002 into cancer cells. In particular, HMSNPs and BMSNPs were found to be the most efficient carrier for LY294002.

It was noted that under hypoxic conditions LY294002 can also cause efficient cell death when delivered with MSNPs (while the cell killing efficacy was compromised in the absence of a carrier; details in Chapter 3.3.3 and 3.3.4).

# Chapter 5

# siRNA delivery using MSNPs

Mesoporous silica nanoparticles have been found not only to be efficient nano-carrier of chemotherapeutics, but also able to deliver gene therapeutics, including DNA plasmid (Kim *et al.*, 2013, Jian-Tao *et al.*, 2014), oligo-DNA (Hartono *et al.*, 2014), dsDNA (Tao *et al.*, 2014) and siRNA (Li *et al.*, 2011, Hom *et al.*, 2010). In particular, the delivery of siRNA remains challenging using current delivery systems due to poor cellular uptake, low bio-stability and rapid clearance from the system. A delivery system using MSNPs could enable a novel and potentially ideal means to carry and deliver siRNA to tumours.

## 5.1 INTRODUCTION

### 5.1.1 RNA interference & small interference RNA

RNA interference (RNAi) is one of the most promising approaches in cancer gene therapy, by silencing the expression of certain genes involved in cancer and constraining cancer growth, development and invasion (Ozpolat *et al.*, 2009).

In a typical RNAi process, cells are transfected with double-stranded RNA (dsRNA), which targets the messenger RNA (mRNA) of a specific gene. This small exogenous dsRNA associates with a protein complex and forms an RNA-induced silencing complex (RISC). After an activated RISC combines cognate mRNA, a component of RISC called Argonaute 2 (a RNA endonuclease) is able to cleave the targeted mRNA and induce its degradation, silencing the specific gene expression.

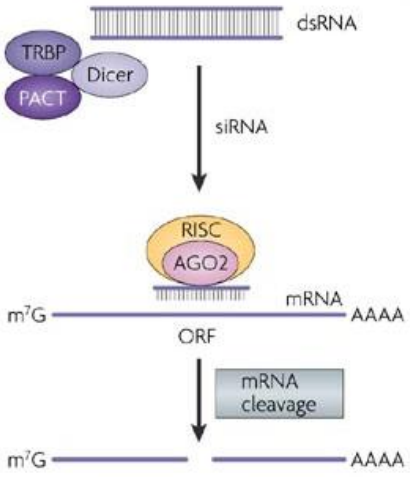


Figure 5.1 Mechanisms of RNA interference in mammalian cells [Image modified from (Kim and Rossi, 2007)]

Exogenous small interfering RNA (siRNA) is a sub-class of dsRNA, comprising 20-25 nucleotide base pairs in length with a 2-nucleotide overhang at the 3' end. siRNA is one of the most commonly used therapeutics in RNAi and other post-transcriptional gene si-

lencing (Whitehead *et al.*, 2009). Both exogenous and endogenous gene can be knocked down with siRNA (Wu *et al.*, 2004).

### 5.1.2 siRNA carriers

Although there are a few methods available to enhance siRNA uptake without a carrier (see section 1.4.4), their drawbacks, such as the high fatality, low cellular uptake efficiency and rapid systemic clearance, remain challenging. Therefore an ideal carrier is desired for the future use of siRNA. Such a carrier should fit the same criteria as a nanoscale drug carrier (detailed in section 1.1.2), and have (i) capability to package and/or absorb siRNA, and (ii) capability to protect siRNA from degradation (Pack *et al.*, 2005).

The nanocarriers which are designed for siRNA delivery can be broadly classified in to two types, viral and non-viral delivery vehicles (Oliveira *et al.*, 2006).

#### *5.1.2.1 Viral delivery systems*

Viruses are at present the most efficient delivery vectors in gene therapy. The most commonly harnessed ones in RNAi transfection are Retrovirus, Adeno-associated virus, and lentivirus (Thermo Scientific). These are all small viruses, normally < 30 kb, and present a reasonable packaging capacity but with varying efficiency depending on the particular cell type (Cross and Burmester, 2006).

Although viral delivery systems (particularly adenovirus) have achieved some success in packaging and delivering siRNA while protecting cargo degradation, a number of hurdles constrain the use of them. One of the major problems is severe immune reaction. A systemic administration of these viruses would immediately cause robust innate immune re-

sponse (including activation of complementary system and secretion of inflammatory cytokines) and adaptive immune response (i.e. produce antibodies to inactivate the vectors). Viral delivery systems are also toxic to the liver and spleen after systemic administration (Cheng and Mahato, 2013).

#### *5.1.2.2 Non-viral delivery systems*

A number of traditional organic nanoparticles are shown to be able to deliver siRNA into cancer cells, including liposomes (Buyens *et al.*, 2012), dendrimers (Biswas and Torchilin, 2013), polycation particles (Ardana *et al.*, 2014), exosome (Alvarez-Erviti *et al.*, 2011), and chitosan particles (Ragelle *et al.*, 2013). Some of them appear to have been successful in laboratory and clinical trials.

Some polymers, such as PEG, PL and PEI, have been also found to be valid transfection reagents. PEI has drawn more attention due to the high transfection efficacy and relatively low cytotoxicity (Boussif *et al.*, 1995, Park *et al.*, 2008a). As a polycation, PEI condenses negatively charged nucleic acid to the cell surface *via* endocytosis. PEI is however not completely biocompatible and can be cytotoxic and lead to cell death at high doses (Hunter, 2006). Despite this, it is widely used in research laboratories due to the much higher transfection efficacy compared to other polycation transfection reagents. For example, the transfection efficacy of PEI is 5 times greater than PL, which is another very commonly used transfection agent. PEI reacts with phosphate groups and therefore it is not only easily conjugated with gene therapeutics, but may also be capped on many inorganic surfaces.

Numerous inorganic particles have also been employed to deliver siRNA *in vitro* and *in vivo* in the last decade. An appropriate polymeric coating allows an inorganic particle to conjugate and deliver siRNA with lower nuclease degradation than conventional carriers (Conde *et al.*, 2015). Many candidates, such as iron nanoparticles (Medarova *et al.*, 2007), gold nanoparticles (Lee *et al.*, 2009), calcium phosphate nanoparticles (Li *et al.*, 2012b), MSNPs (Hom *et al.*, 2010) and carbon nanotubes (Liu *et al.*, 2007), have been studied and demonstrated as valid siRNA carriers.

In this study, siRNA was loaded onto the previously investigated MSNPs after capping with PEI. Transfection efficacy was demonstrated by transfecting GFP expressing cells with GFP-targeted siRNA, and subsequently transfecting RMS cells with ELMO1-targeted siRNA.

## 5.2 MATERIALS AND METHODS

### 5.2.1 siRNA loading efficiency on MSNPs

PEI was coated on MSNPs before transfection. In a typical PEI capping experiment, 10 mg MSNPs or SNPs were suspended in 2 mL PEI solution (2.5 mg PEI/mL solution, $Mw_{PEI}$ = 24 kD). The suspension was sonicated for 15 min and shaken for a further 30 min. The capped nanoparticles were then washed with dd$H_2O$ thrice to remove any un-capped polymer.

siRNA was re-suspended in 1x siRNA buffer (five times diluted from 5x siRNA buffer [Dharmacon], comprising 300 mM KCl, 30 mM HEPES-pH 7.5, 1.0 mM $MgCl_2$, with RNase-free water), and aliquoted into a 20 µM siRNA stock suspension.

Immediately before any further experiment (e.g. transfection), siRNA was loaded onto PEI loaded MSNPs (abbreviated as siRNA@MSNPs). In a typical siRNA loading process, 10 µL siRNA aliquot (20 µM) and 10 µL 6.25 mg/mL PEI-MSNP suspension was mixed in 5 mL DMEM (no additives) and incubated at RT for 30 min.

FITC-conjugated siRNA (Santa Cruz sc-36869) was used to measure the loading efficiency on the siRNA-MSNP delivery system. After FITC-conjugated siRNA loading, the siRNA-MSNP complex was washed once with RNase-free water. Immediately after FITC-conjugated siRNA was loaded, the fluorescence signal of the siRNA-MSNP complex ($F_c$), loading supernatant ($F_s$) and washed residue ($F_r$) was immediately determined after the complex was washed, and every 24 hours up to 72 hours. All signals were read using a Tecan INFINITE 200 plate reader.

Loading efficiency was calculated by:

$$\frac{F_c}{F_c + F_s + F_r} \times 100\%$$

### 5.2.2 siRNA protection on MSNPs

#### *5.2.2.1 Degradation in culture media*

FITC-conjugated siRNA@HMSNP complex was incubated with normal culture media and samples taken at 1, 12, 24, 48, 72 hours. The complex was collected and washed with RNase-free water before the fluorescence was read. The existence of siRNA on siRNA@HMSNP complex and in the supernatant was assessed using a 4 % agarose gel electrophoresis (data not shown).

#### *5.2.2.2 Degradation in RNase I*

FITC-conjugated siRNA@HMSNP was suspended in 0.25% RNase I (Sigma-Aldrich) and incubated in 37 °C for 1 hour. The fluorescence of the washed complex was read. As previously, gel electrophoresis was used to assess degradation.

### 5.2.3 GFP knock-down transfection system

The transfection system was assessed using U87-MG-cGFP cells with GFP-targeted siRNA on MSNPs with different morphologies. siRNA transfection procedures were modified slightly from manufacturers' instructions (Thermo Scientific™ and Santa Cruz Biotechnology™). When using MSNPs as the transfection vehicle, the protocol was adjusted from Hom *et al.* (Hom *et al.*, 2010).

U87-MG-cGFP cells were cultured in 24-well microplates at a concentration of $5 \times 10^4$ cells/well in antibiotic-free media (DMEM with glutamine and fetal bovine serum) in 37°C, 5 % $CO_2$ sterile humid incubator. GFP-targeted siRNA (Santa Cruz Biotechnology™) was used to knock-down GFP gene in this cell after 24 hours incubation. The following groups were set:

- Blank control: siRNA buffer;
- Negative controls:
    - (i) bare siRNA without carriers;
    - (ii) PEI coated HMSNP (labelled PEI-HMSNP);
    - (iii) DharmaFECT Transfection Reagent I [Dharmacon, Thermo Scientific™] (abbr. DharmaFECT in later context);
- Positive control: siRNA transfected with DharmaFECT

- Experimental groups: siRNA@MSNPs complexes.

Immediately before transfection, siRNA stock solution (10 μM in RNase-free water) was diluted with 1X siRNA buffer (Dharmacon, Thermo Scientific™).

For each well in Controls: 2.5 μL siRNA dilution (in negative control (i) and positive control) or 2.5 μL 1X siRNA buffer (in blank control and negative control (ii), (iii)) was added to 47.5 μL DMEM (serum-free) in an RNase-free tube A; in a separate tube, add 1 μL DharmaFECT (in negative control 3 and positive control) or 1 μL 1X siRNA buffer (in other control groups) with 49 μL DMEM (serum-free) in a RNase-free tube B. After gentle mixing and 5 min incubation at room temperature separately, the tube As were mixed with tube Bs for a total volume of 100 μL, and incubated for 20 min.

For experimental groups: siRNA-MSNPs complexes (described in section 5.2.1) were re-suspended in DMEM (serum-free) to make up a 100 μL suspension. In order to keep the concentration of conjugated siRNA at the same level as the control groups, the concentration of siRNA-MSNPs complexes was calculated from the siRNA loading efficacy results obtained in section 5.2.1 (Figure 5.4) and equivalent amount of siRNA added to cells, irrespective of the nanoparticle concentrations

U87-MG-cGFP cells were washed with PBS once after 24 hours incubation. 400 μL antibiotic-free media was added to each well before transfection mixture was added. The final concentration of siRNA was 25 nM in each well (in negative control (i), positive control, and experimental groups).

After 24 hours transfection, the fluorescence signal of GFP was measured with Tecan Infinite 200 plate reader using well scan mode (7X7 circle filled) at Ex 395nm./Em. 510nm after each well was washed with PBS twice.

### 5.2.4 ELMO1 knock-down

Two RMS lines, RH30 and RD cells were transfected with the following groups using the same processes detailed in section 5.2.3:

- Blank control: siRNA buffer (labelled 'Untreated'), PEI loaded HMSNP (labelled PEI-HMSNP) / PEI-WMSNP (PEI-WMSNP)
- Negative control: non-targeted siRNA (ON-TARGETplus non-targeting siRNA #1, loaded PEI-HMSNP / PEI-WMSNP (labelled 'NT@HMSNP' / 'NT@WMSNP')
- Positive control: ELMO1-targeted siRNA on DharmaFECT (labelled 'ELMO1@DharmaFECT')
- Experimental groups: ELMO1-targeted siRNA (ON-TARGETplus SMARTpool – human ELMO1, Dharmacon, Thermo Scientific™) loaded PEI-HMSNP / PEI-WMSNP (labelled 'ELMO1@HMSNP' / 'ELMO1@WMSNP')

### 5.2.5 qRT-PCR

After transfection, quantitative reverse transcription polymerase chain reaction (qRT-PCR) was used to evaluate ELMO1 expression and therefore transfection efficiency. After total RNA was extracted, two-step RT-PCR was used in this research.

#### *5.2.5.1 Total RNA extraction*

Total RNA of each sample was purified using ISOLATE II RNA Micro kit (Bioline™). According to manufacturer's instructions, all transfected RH30 or RD cells were washed with warm PBS, trypsinised and collected in an RNase-free tube. 100 µL Lysis Buffer (RLY), 2 µL TCEP and 5 µL Carrier RNA working solution (20 ng Carrier RNA) was

added separately to the collected cells, and the lysate was vortexed robustly twice after TCEP added and after Carrier RNA added. After the lysate was filtered, 100 µL 70% ethanol solution was added. The mixture was then placed on an ISOLATE II RNA Micro Column and centrifuged for 30 s at 11,000 g, and the RNA bonded to the silica membrane in the column. The membrane was then desalted with Membrane desalting buffer before DNase I reaction mixture was added to the membrane. After 15 min DNA digestion at room temperature, the column was washed with Wash Buffer RW1 once and Wash Buffer RW2 twice. Finally, total RNA was eluted with 30 µL RNase-free water. The total amount of RNA was measured with a NanoDrop 1000 (Thermo Scientific).

#### *5.2.5.2 cDNA synthesis*

cDNA was synthesised using SensiFAST cDNA Synthesis Kit (BioLINE). According to manufacturer's instructions, 1 µg purified RNA was mixed with 4 µL 5x TransAmp Buffer, 1 µL reverse transcriptase and RNase free water to make up a 20 µL mixture. The mixture was pipetted and placed in thermal cycler with following programme:

- 25°C for 10 min (primer annealing)
- 42°C for 15 min (reverse transcription)
- 85°C for 5 min (inactivation)
- 4°C hold.

#### *5.2.5.3 qPCR*

The second step of the qRT-PCR was run with SensiMix II Probe No-ROX kit (BioLINE). The testing primer/probe used was ELMO1 primer/probe set with FAM-MGB tag (TaqMan, assay ID Hs00404994_m1, Applied Biosystem) when ACTB primer/probe set with VIC-MGB tag (TaqMan, assay ID Hs01060665_g1, Applied Biosystem) was used

as control. According to supplier's instructions, each reaction sample was mixed 2 µL template (cDNA synthesised) with 10 µL 2x SensiMix™ II Probe No-ROX, 1 µL ELMO1 TaqMan primer/probe, 1 µL ACTB TaqMan primer/probe, and 6 µL DNase/RNase-free water. In a Rotor-Gene 3000 (QIAGEN) thermal cycler, a programme was set up as following:

- Cycle 1st: 10 min at 95 °C for polymerase activation
- Cycle 2nd to 46th: 10 s at 95 °C then 60 s at 60 °C (every cycle)

All samples were tested in three replicas.

#### *5.2.5.4 Data analysis*

The results obtained by qRT-PCR were quantified using the comparative threshold method. Giulietti *et al.* (Giulietti *et al.*, 2001) detailed this method as 'the amount of target, normalised to an endogenous housekeeping gene and relative to the calibrator, given by $2^{-\Delta\Delta Ct}$, where $\Delta\Delta Ct = \Delta Ct_{sample} - \Delta Ct_{calibrator}$.' In this context, Ct means threshold cycle measured in the PCR. Therefore $Ct_{sample}$ means the threshold cycle of the gene under study, while $Ct_{calibrator}$ means the threshold cycle of the housekeeping gene.

Therefore, in this experiment, the housekeeping gene was β-actin (ACTB), as the 'calibrator' in Giulietti's statement; ELMO1 was the 'sample' gene. The fold difference of ELMO1 knockout = $\log(2^{-\Delta\Delta Ct})$, where $\Delta\Delta Ct = \Delta Ct_{ELMO1} - \Delta Ct_{ACTB}$. Here, $\Delta Ct_{ELMO1}$ equals $Ct_{ELMO1}$ of given sample minus $Ct_{ELMO1}$ of un-knockout sample (blank control) on the same cell line on the same run batch; $\Delta Ct_{ACTB}$ equals $Ct_{ACTB}$ of given sample minus $Ct_{ACTB}$ of blank control.

All data was analysed with Rotor-Gene 6000 Series Software 1.7 (QIAGEN) and MicroSoft Excel 2010. The fold difference of ELMO1 expression against ACTB was plot-

ted in Figure 5.5. Significance tests were performed using two-tailed homoscedastic Student's t test on Microsoft™ Excel platform and listed separately in Table 5.1 and Table 5.2.

### 5.2.6 Scratch test

A scratch test was performed in this study to evaluate cell migration and invasion. In a typical test depicted in Figure 5.2, RH30 or RD cells were cultured into a 24-well sterile microplate (Corning). After 24 hours transfection with ELMO1-targeted siRNA on different nanocarriers, transfected cells were allowed to proliferate, spread, and form a monolayer towards confluent. A 1000 µL pipette type was used as a pin tool to scratch across the cell layer, and remove the scratched content, hence form a cell-free zone in each well.

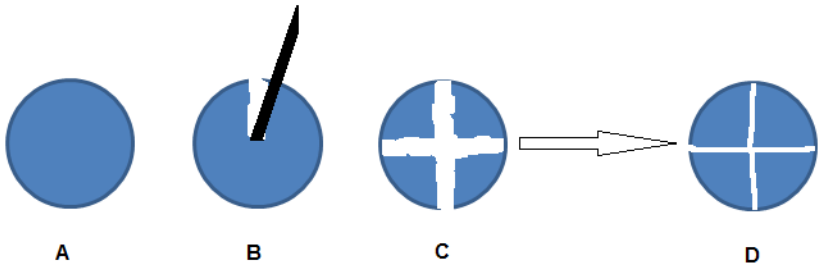


Figure 5.2 Schematic illustrations of a typical Scratch test. After a certain cell (RH30 or RD cell in this study) had proliferated and grown to a confluent monolayer (A), a scratched cross was introduced by drawing a tip across the cell layer (B, C). After a fixed time of incubation, cells would migrate inward the scratched cross (D).

After a period of cell incubation, cells migrate inward to close the wound. Pictures of cells pre- (Figure 5.2C) and post- (Figure 5.2D) migration were recorded for comparison. The average width (measured twice across the vertical and the horizontal scratches separately) in Figure 5.2C of the scratched cross was set to $W_{before}$; the average width in Figure 5.2D was set to $W_{after}$. In section 5.3.4.2 (Figure 5.7), the cell mobility was calculated from:

$$\frac{W_{before} - W_{after}}{W_{before}} \times 100\ \%$$

## 5.3 RESULTS

### 5.3.1 siRNA loading efficiency on MSNPs

In order to confirm that MSNPs were successfully capped with PEI, the surface charge of particles was measured before and after capping. It was demonstrated in Chapter 2 that MSNPs were either negatively charged (on HMSNPs, CMSNPs, WMSNPs, SNPs) or nearly neutral (on BMSNPs). Figure 5.3 shows that the surface charge of MSNPs, no matter what morphology, was altered to a positive charge after capping. This confirmed the effectiveness of PEI capping.

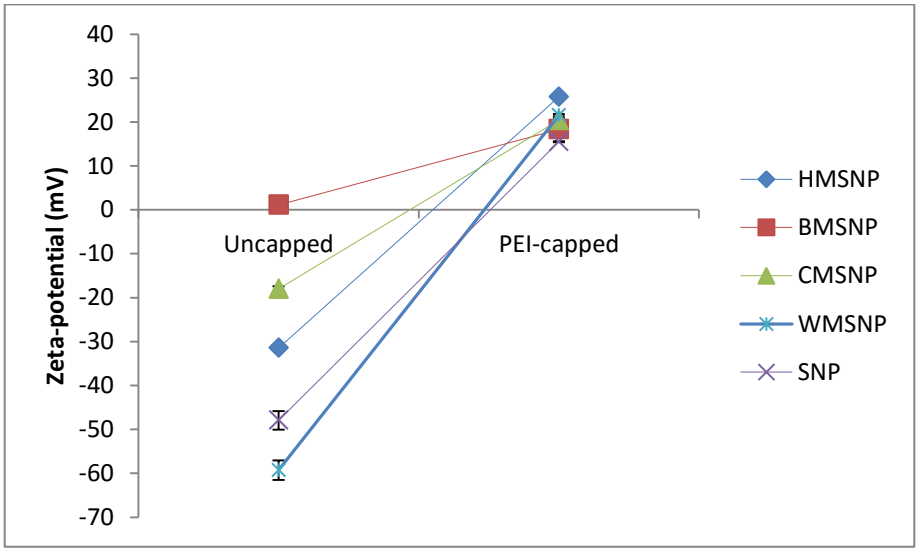


Figure 5.3 Zeta-potential of MSNPs before and after PEI capping (the data are presented as the means ± standard deviation, n= 3)

The siRNA loading efficacy was measured in all MSNPs and non-porous SNP. In HMSNPs, more than 55.04 % of the available siRNA was loaded on to the nanoparticle, while WMSNPs carried approx. 58.23 % of the available siRNA using the same proce-

dure. The other nanoparticles showed slightly lower siRNA uptake efficiency of approx. 48.28 %, 38.11 % and 30.70 % in BMSNPs, CMSNPs and SNPs separately (Figure 5.4). This showed that all MSNPs candidate presented capability to carry siRNA.

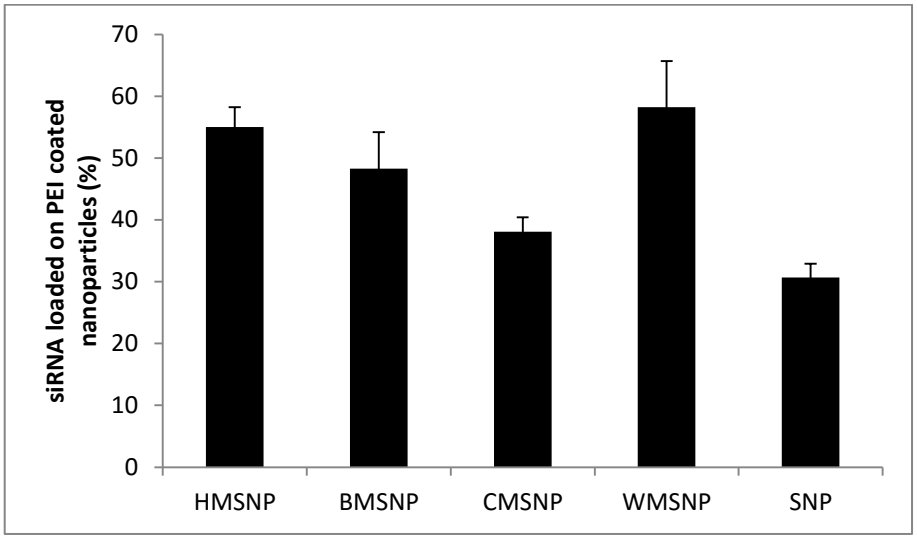


Figure 5.4 siRNA loading efficiency on morphological different MSNPs with PEI coating (the data are presented as the means ± standard deviation, n= 3)

### 5.3.2 siRNA protection

siRNA@MSNPs complexes were all found to be stable in culture media over the course of 72 hours. After 72 hours, the total siRNA found on MSNPs and in suspension was not significantly lower than the initial level for all siRNA@MSNPs complexes.

However, MSNPs were not found to protect siRNA from cleavage by RNase I as declared in previous literature (Hom *et al.*, 2010).

### 5.3.3 Validation of siRNA transfection system

In order to validate the siRNA transfection method, GFP-targeted siRNA was used to knock-down GFP expression in U87-MG-cGFP cells.

After GFP-targeted siRNA@MSNP complex was transfected on U87-MG-cGFP cells, GFP fluorescence was monitored after the 24 hour transfection period. When compared to the negative control, all carriers, including the commercial product DharmaFECT and all studied silica nanoparticles, were shown to be able to deliver siRNA to cells leading to GFP silencing. HMSNPs and WMSNPs appeared to be the most efficient carriers resulting in a significantly higher gene silencing efficacy (approx. 23.36 % and 21.36 % GFP signal reduction in HMSNPs and WMSNPs separately) than commercial product (7.60 % GFP signal reduction) and other silica nanoparticles.

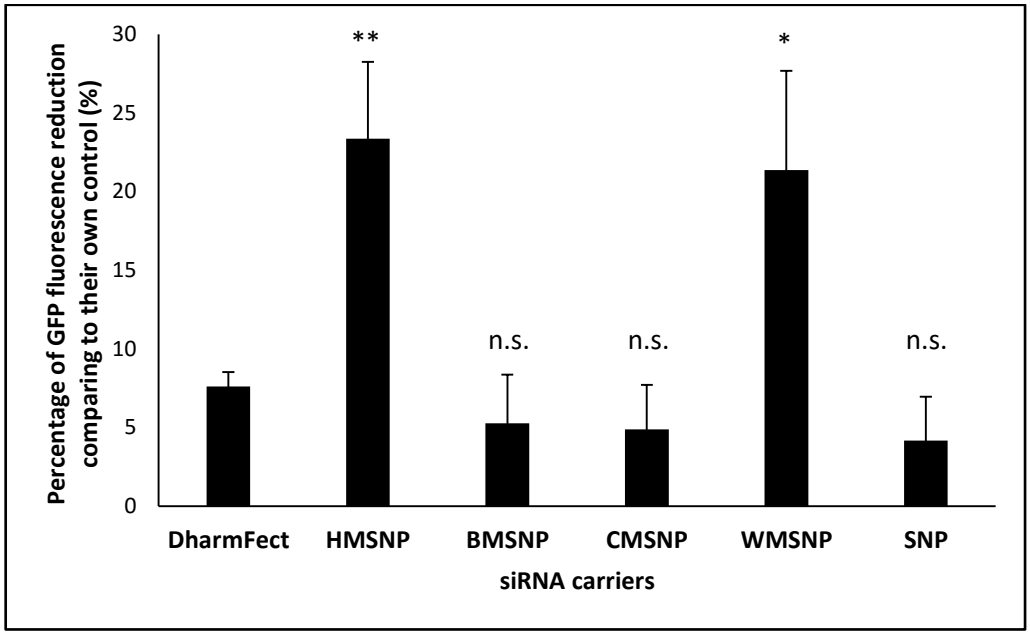


Figure 5.5 The percentage of GFP fluorescence reduction after transfection with GFP-targeted siRNA on different carriers comparing to their own controls (same carriers conjugated with non-targeted siRNA; the data are presented as the means ± standard deviation, n= 3). A student t-test was performed on each experimental group versus the positive control DharmaFECT (n.s. = not significant,* $P < 0.05$, ** $P < 0.01$, *** $P < 0.001$)

The different transfection efficacy was a result of a number of different factors. HMSNPs were the most capable candidate in carrying siRNA (Figure 5.4) and it was the most efficient siRNA carrier in transfection, knocking down 23.36 % GFP expression in U87-MG-cGFP cells after 24 hours transfection. Nevertheless, the ability of siRNA loading

was not the only factor that affects siRNA transfect efficacy. For instance, BMSNPs showed similar siRNA loading with HMSNPs, but were less efficient at transfection, only causing 5.27 % GFP knock-down. The siRNA@WMSNP complex was very efficient in knocking down GFP gene expression, resulting in a 21.36 % GFP signal reduction which was not significantly lower than the siRNA@HMSNP complex (Figure 5.5).

### 5.3.4 ELMO1 knock-down

After validation of the transfection system, the ELMO1 gene was knocked down using ELMO1-targeted siRNA@MSNPs complexes in the two RMS cell lines, RH30 and RD cells. Since ELMO1 is responsible for enhanced cell mobility and invasion, the transfection efficacy was evaluated using both qRT-PCR and a scratch test.

#### *5.3.4.1 Knock-down efficiency evaluated via qRT-PCR*

In section 5.3.3, HMSNPs and WMSNPs were found to be the most efficient siRNA carriers among all the studied silica nanoparticles. Therefore qRT-PCR was performed only on ELMO1@HMSNP and ELMO1@WMSNP.

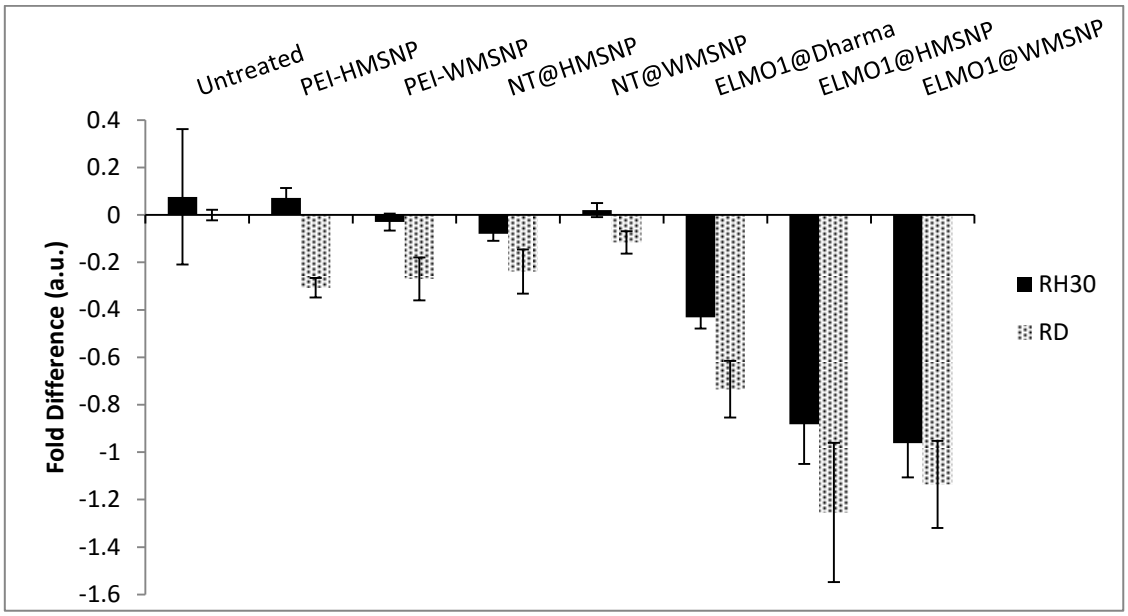


Figure 5.6 ELMO1 gene expressions evaluated with quantitative RT-PCR analysis in RH30 and RD cell lines after the cells were transfected for 24 hours with ELMO1-targeted siRNA carried by different carriers. The gene expression level was compared to β-actin as housekeeping gene. (The data are presented as the means ± standard deviation, n= 3). (Blank control: untreated / transfected with PEI capped HMSNP and PEI capped WMSNP; negative controls: transfected with non-targeted siRNA with HMSNP or WMSNP; positive control: transfected with ELMO1-targeted siRNA with DharmaFECT)

| Groups | PEI-HMSNP | PEI-WMSNP | NT@HMSNP | NT@WMSNP | ELMO1@Dhar-DharmaFECT | ELMO1@HMSNP | ELMO1@WMSNP |
|---|---|---|---|---|---|---|---|
| Untreated | n.s. | n.s. | n.s. | n.s. | ** | *** | *** |
| PEI-HMSNP | | Not tested | *** | Not tested | *** | *** | Not tested |
| PEI-WMSNP | | | Not tested | n.s. | *** | Not tested | *** |
| NT@HMSNP | | | | Not tested | Not tested | *** | Not tested |
| NT@WMSNP | | | | | Not tested | Not tested | *** |
| ELMO1@Dhar-maFECT | | | | | | *** | *** |
| ELMO1@HMSNP | | | | | | | n.s. |

Table 5.1 The significance test performed on ELMO1 gene expression evaluated with quantitative RT-PCR analysis in RH30 cells after transfection for 24 hours with ELMO1-targeted siRNA carried by different carriers. n.s. = not significant,* $P < 0.05$, ** $P < 0.01$, *** $P < 0.001$

| Groups | PEI-HMSNP | PEI-WMSNP | NT@ HMSNP | NT@ WMSNP | ELMO1 @ Dhar-Dhar-maFECT | ELMO1 @ HMSNP | ELMO1 @ WMSNP |
|---|---|---|---|---|---|---|---|
| Untreated | *** | *** | *** | ** | *** | *** | *** |
| PEI-HMSNP | | Not test-ed | n.s. | Not test-ed | *** | *** | Not test-ed |
| PEI-WMSNP | | | Not test-ed | * | *** | Not test-ed | *** |
| NT@ HMSNP | | | | Not test-ed | Not test-ed | *** | Not test-ed |
| NT@ WMSNP | | | | | Not test-ed | Not test-ed | *** |
| ELMO1@ Dhar-maFECT | | | | | | *** | *** |
| ELMO1@ HMSNP | | | | | | | n.s. |

Table 5.2 The significance test performed on ELMO1 gene expression evaluated with quantitative RT-PCR analysis in RD cells after transfection for 24 hours with ELMO1-targeted siRNA carried by different carriers, n.s. = not significant,* $P < 0.05$, ** $P < 0.01$, *** $P < 0.001$

The qRT-PCR results suggested that both HMSNPs and WMSNPs were efficient ELMO1-targeted siRNA delivery carriers in both RMS cell lines tested. After RH30 cells were transfected with ELMO1@HMSNP, ELMO1 expression was knocked down 0.88 fold. The transfection efficacy was even more marked with ELMO1@WMSNP (0.96 fold knock-down). Meanwhile, RD cells appeared to be more sensitive to these transfection systems and ELMO1 expression was reduced 1.25 fold and 1.14 fold after transfection with ELMO1@HMSNPs and ELMO1@WMSNPs, respectively (Figure 5.6). Control groups showed little influence on ELMO1 gene expression, as would be expected.

### *5.3.4.2 Knock-down efficacy evaluated via scratch test*

Previous work has shown that a higher ELMO1 gene expression leads to a higher cell mobility and increased cell invasion in RMS cell lines. Therefore, the effect of ELMO1 knock-down on RH30 and RD cells was assessed using a scratch test (Figure 5.2), as a quick and inexpensive evaluation of cell invasion, after transfection with ELMO1@MSNPs.

Cell mobility was seen to be significantly reduced in both tested cell lines after a successful knock-down of ELMO1 gene with the ELMO1-targeted siRNA delivery system. In RH30 cells, gap invasion was decreased from 85.74 % to 38.69 % after successful transfection with ELMO1@HMSNPs ($P < 0.05$); and reduced to 38.03 % with ELMO1@WMSNPs ($P < 0.05$). Other siRNA delivery carriers, except BMSNPs, were also seen to be effective vehicles to deliver ELMO1-targeted siRNA causing reduced cell mobility, although they were not as efficient as HMSNPs and WMSNPs in RH30 cells.

RD cells were seen to be less metastatic than RH30 cells before ELMO1 knock-down: gap invasion was shown to be 85.74 % in untreated RH30 cells while it was only 79.62 % in RD cells. ELMO1@WMSNPs were found to be the most effective delivery system and reduced invasion to 39.21 % ($P < 0.05$). DharmaFECT, SNPs, CMSNP based ELMO1-targeted siRNA delivery systems were also seen to successfully reduce cell invasion of RD cells.

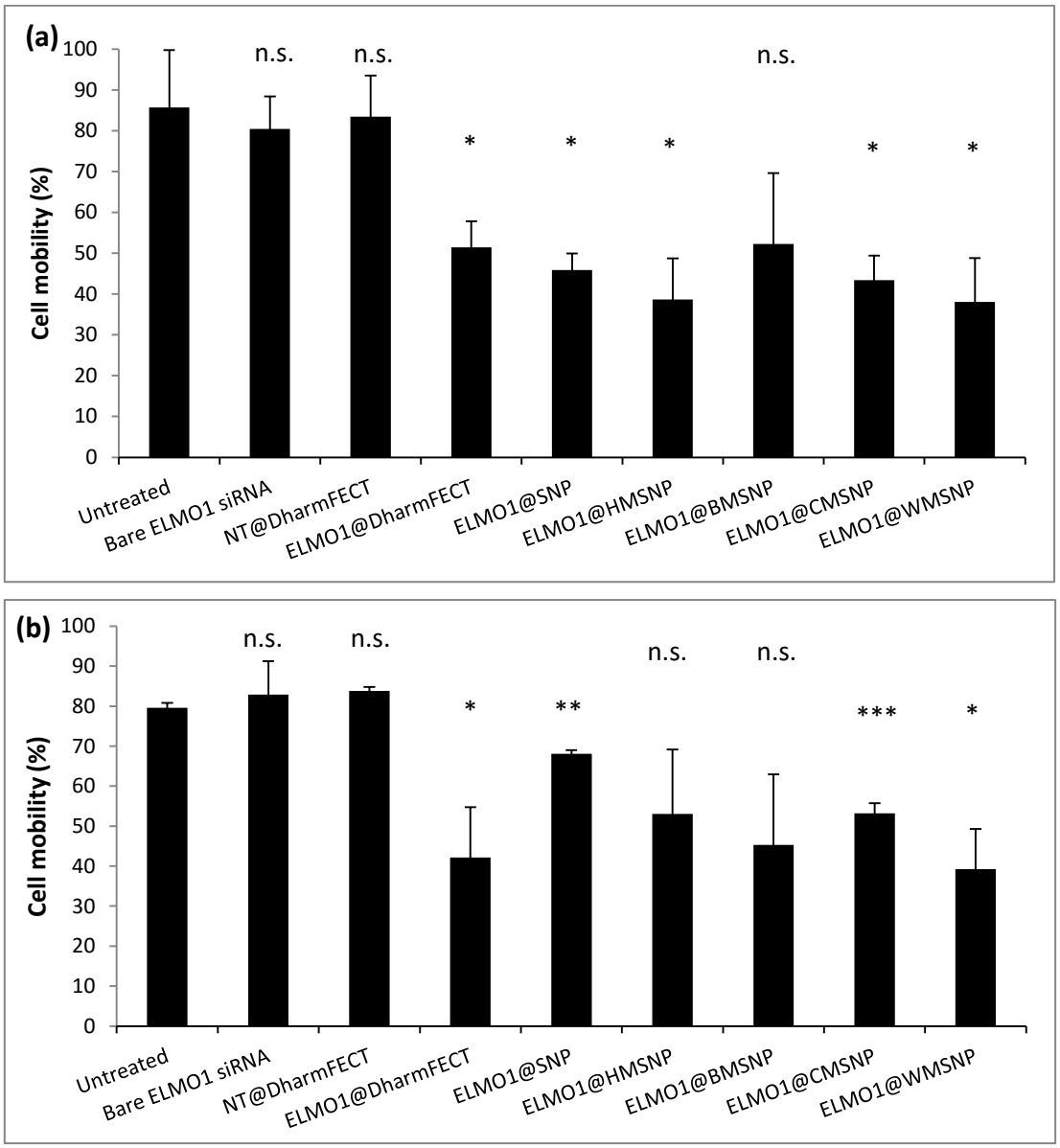


Figure 5.7 Cell mobility tested using scratch test in (a) RH30 and (b) RD cells after transfection for 24 hours with ELMO1-targeted siRNA carried by different carriers (the data are presented as the means ± standard deviation, n= 3). (Blank control: untreated / transfected with bare ELMO1 siRNA; negative controls: transfected with non-targeted siRNA with DharmaFECT; positive control: transfected with ELMO1-targeted siRNA with DharmaFECT; The student's t-test was performed on each experimental group against the blank control: untreated group (n.s. = not significant,* $P < 0.05$, ** $P < 0.01$, *** $P < 0.001$)

## 5.4 DISCUSSION

### 5.4.1 Engulfment and cell Motility protein 1 (ELMO1)

Many genetic mutations and/or over-expressions and/or inhibitions contribute to metastasis. A microarray screen undertaken by a collaborating group in Oxford identified a number of candidate genes involved in metastasis (Rapa *et al.*, 2012). Further investigations of the migratory properties of one specific gene, ELMO1, showed that it forms complexes with other kinases. Those complexes could activate down-stream genes which enable actin polymerisation and lamellipodia formation (required in cell movement) (Katoh *et al.*, 2006, Kim *et al.*, 2011).

ELMO1 expression knock-down was reported to significantly decrease the cell movement and tumour invasive ability in a number of cancer cells, including different RMS lines (Rapa, 2008). This observation was also seen in this study (Figure 5.6, Figure 5.7).

### 5.4.2 Factors affecting siRNA loading onto MSNPs

One possible reason for the difference in siRNA loading onto MSNPs may be the difference in surface charge. After capping with PEI, the surface charge of HMSNPs was slightly higher than all other particles (Figure 5.3, Table 2.2). However, there was no clear correlation between surface charge after PEI capping and siRNA loading efficacy. Thus, the differences in surface area may be another property which contributes to the differences in siRNA loading. HMSNPs showed a significantly higher specific surface area than the other MSNPs tested and was also capable of carrying siRNA very efficiently. However, this assumption was also not conclusive: despite the specific surface area of BMSNPs being only a quarter of HMSNPs, the siRNA loading efficacy was not signifi-

cantly different (Figure 5.3). This suggests that the factors affecting siRNA loading on different silica nanoparticles are multi-factorial. Surface charge, surface area and even particle and pore size may affect the siRNA loading.

### 5.4.3 Factors that may affect gene expression after transfection with siRNA

#### *5.4.3.1 Cell type*

Cancers are heterogeneous with large diverse phenotypes. Hence, initial gene expressions show large variation in different cancer cell lines and by extension will affect gene expression after transfection.

GFP expression varies depending upon the suppliers and cell selection. In order to minimise potential errors and equalise GFP expression, U87-MG-cGFP cells were selected three times with 10 μg/mL blasticidin (Invitrogen). Further gene knock-down experiments were then performed on these U87-MG-cGFP cells with uniform GFP expression.

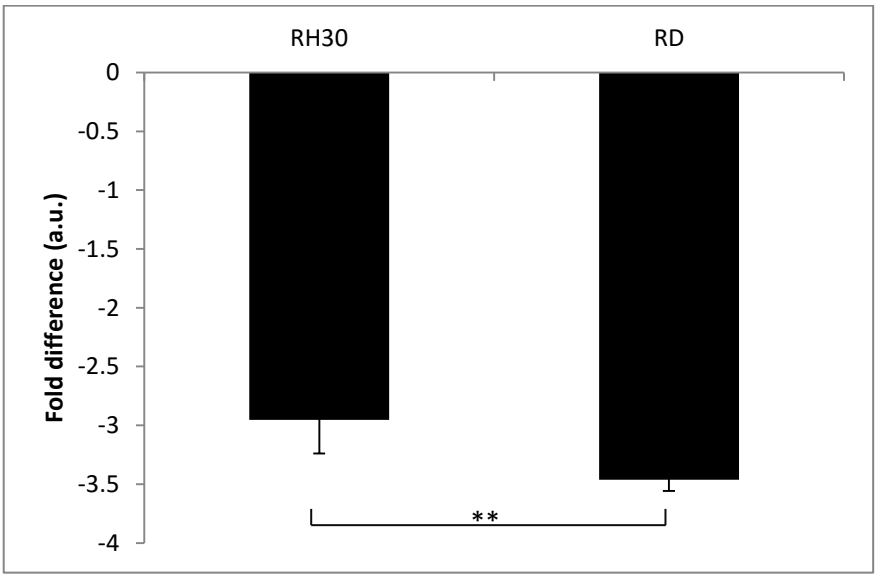


Figure 5.8 ELMO1 gene expression level compared to β-actin (as housekeeping gene) in RH30 and RD cell lines before transfection (The data are presented as the means ± standard deviation, n= 6).

Initial ELMO1 expression also varied in different RMS cell lines (Rapa *et al.*, 2012): in RH30 cells ELMO1 expression was approx. 0.51 fold higher than in RD cells before any treatment (Figure 5.8). Similar results were also found in Rapa's work (Rapa, 2008). After transfection, ELMO1 expression in RD cells was reduced more significantly than in RH30 cells.

### *5.4.3.2 Cell viability*

Previous literature suggests that transfection efficacy is closely related to cell viability (Roche). Therefore U87-MG cell viability was evaluated after treatment with PEI capped MSNPs (Figure 5.9).

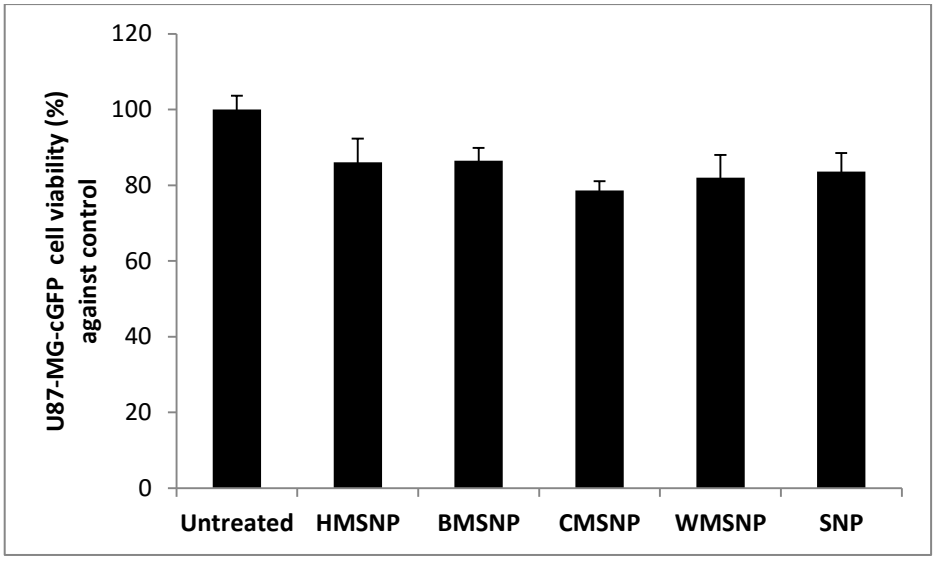


Figure 5.9 U87-MG-cGFP cell viability compared to the control (untreated) after 24 hours treatment of different MSNPs with PEI capping. The concentration of PEI capped MSNPs was the same to each experiment group in Figure 5.5 (the data are presented as the means ± standard deviation, n= 3)

It was found that there was no significant difference in U87-MG-cGFP cell viability after treatment with the different PEI capped MSNPs ($P > 0.05$ between every two experimental groups); whereas transfection efficacy varied greatly using different MSNPs as

transfection agents. Therefore, there was no relation found between cell viability and transfection efficacy.

#### *5.4.3.3 The physical properties of siRNA carriers*

The physical properties of the siRNA carriers were not only shown to influence the siRNA loading efficacy (Figure 5.4), but also the gene expression (Figure 5.5). For example, BMSNPs were found to be very efficient siRNA carrier and not significantly different to HMSNPs in terms of loading efficacy (Figure 5.4). Yet the transfection efficacy with GFP-targeted siRNA on BMSNPs was significantly lower than on HMSNPs (when final loaded siRNA levels in media were the same) ($P < 0.01$; Figure 5.5). One possible explanation is that the cellular uptake of MSNPs, determined by the physical properties of nanoparticles, affects transfection efficacy.

#### *5.4.3.4 Transfection procedures*

The siRNA transfection procedures vary in the literature with regards to siRNA concentration and transfection time (ThermoFisher, Santa Cruz Biotechnology, BIOLINE, (Hom *et al.*, 2010)). In order to achieve a maximum transfection efficacy, many attempts were performed to optimise the final transfection protocols.

Research showed that a commonly used siRNA concentration in gene silencing was approx. 30 nM (Sigma-Aldrich). The fluorescence of GFP was read after transfecting U87-MG-cGFP cells with a final concentration of 25 nM, 50 nM and 100 nM siRNA using DharmaFECT. There was no significant difference found among these groups (data not shown), indicating that the influence of final siRNA concentration was negligible be-

tween 25 nM to 100 nM. Previous literature also showed a similar conclusion (ThermoFisher).

Furthermore, previous literature suggested a transfection time from 4 hours to 72 hours (Promega, Santa Cruz Biotechnology). RH30 and RD cells were transfected with ELMO1-targeted siRNA on DharmaFECT, HMSNPs and WMSNPs for 4, 24, 48 and 72 hours. The qRT-PCR results revealed that the transfection efficacy reached a maximum after transfection for 24 hours (data not shown). One possible explanation is a shorter transfection time leads to incomplete siRNA release from the carriers and/or insufficient RNAi processing. When the transfection time was too long, gene expression may start to recover after the RNAi process has finished.

### 5.4.4 Future potential of MSNPs as gene therapeutics carriers

One of the greatest benefits of MSNPs as a gene therapeutics carrier is the relatively low and controllable cytotoxicity. Most commercial products to date, viral or non-viral, have showed high fatality (Lappalainen *et al.*, 1994, Cheng and Mahato, 2013). Therefore PEI-capped MSNPs offer a new possibility as a gene therapeutics carrier with low toxicity (Figure 5.8). Although the MSNPs siRNA delivery system in this study were still seen to be slightly toxic to tested lines, the cytotoxicity may be enhanced by many processes, such as extra coating with cell-friendly polymers, PEI modification before capping or capping with other polycations on MSNPs (Arbab *et al.*, 2004, Thomas and Klibanov, 2002, Malek *et al.*, 2008). Moreover, the tested MSNPs, especially HMSNPs and WMSNPs, appeared to be more efficient siRNA carriers than current products on the market (Figure 5.6, Figure 5.7).

Furthermore, MSNPs also allowed a targeted delivery of gene therapeutics to specific sites. The siRNA-loaded MSNPs could be further functionalised with peptides, targeting ligands or environmentally-sensitive molecules, therefore enabling a targeted release of cargo siRNA to tumours.

A further advantage of the MSNPs platform compared to current commercial products is the possibility of co-delivery of gene therapeutics and other anti-cancer reagents (Meng *et al.*, 2013). This possibility is studied in Chapter 6.

## 5.5 CONCLUSION

The MSNPs tested were found to be able to successfully load siRNA after coating with PEI. The loading efficacy appeared to be affected by the specific surface area of the carrier MSNP candidates, making HMSNPs and WMSNPs the most efficient siRNA carriers among all six candidates in this study.

The MSNP based siRNA delivery system was seen to successfully knock-down target genes (GFP / ELMO1) in different cancer cell lines. After transfection with ELMO1-target siRNA using functionalised MSNPs, the ELMO1 expression was proven to be significantly reduced ($P < 0.001$). The transfection efficacy of HMSNPs and WMSNPs was found to be better than one of the current popular products on the market (DharmaFECT reagent 1) under the same experimental protocols ($P < 0.001$).

# Chapter 6

# A chemo- / gene- therapeutics co-delivery system using multifunctional MSNPs

In order to constrain the viability, proliferation and invasion of cancer at the same time, many multifunctional drug delivery platforms have been developed to co-deliver two or more chemotherapeutics or even different classes of anti-cancer agents.

The previous chapters demonstrated the utility of MSNPs as vehicles to deliver different drug molecules (Chapter 4) and siRNA (Chapter 5) independently. The possibility of a combined system for chemo- and gene- therapeutics is studied in this Chapter.

## 6.1 INTRODUCTION

A number of nano-scaled delivery platforms have been found to be able to carry and deliver multiple classes of cargo molecules, including liposomes, polymersomes, dendrimers, iron oxide nanoparticles and MSNPs (Han and Gao, 2013).

Organic nanoparticles have been widely investigated in the research of co-delivery systems. Dendrimers are able to conjugate both microRNAs and small molecule drugs (including different chemotherapeutics, photosensitizers) at the same time and efficiently deliver those cargoes to tumours (Ren *et al.*, 2010). Cationic liposomes/polymersomes are also promising platforms that present a large inner cavity allowing encapsulation of anticancer drugs, while gene therapeutics (such as DNA plasmid, siRNA and microRNA which are negatively charged) can be attached on the surface (Saad *et al.*, 2008, Wang *et al.*, 2010, Chen *et al.*, 2014, Koganti *et al.*, 2013, Laing *et al.*, 2006). A number of these carriers have reached clinical trial stage (Tsouris *et al.*, 2014).

Many composite delivery systems based on liposome or polymersomes are also developed to co-deliver small molecules, peptides, gene therapeutics, and enzymes. For example, gel-liposome nanoparticles were found to successfully deliver doxorubicin and proteins to cancer cells (Jiang *et al.*, 2014) and porous silicon-liposomes were used to deliver doxorubicin and DNA (Kong *et al.*, 2015).

Inorganic platforms have also been shown to be a useful co-delivery system. Surface modified CdSe/ZnSe quantum dots have been shown to deliver doxorubicin and siRNA to Hela cells successfully (Li *et al.*, 2012a). Calcium carbonate apatite nanoparticles were reported to be able to overcome MDR in breast cancer by co-delivering an ATP-binding

cassette transporter (ABC)-targeted siRNA and a chemotherapeutic agent (Li *et al.*, 2012a). Other nano-scaled vehicles, including gold nano-rods (Xiao *et al.*, 2012), iron oxide nanoparticles (Yen *et al.*, 2013), and mesoporous silica nanoparticles (Meng *et al.*, 2013), have also been described in the previous literature.

In the previous chapters, it was found that MSNPs were effective carriers of small molecules (Chapter 4) and siRNA (Chapter 5). Therefore, it was investigated whether a multi-functional delivery system could be built to deliver both chemotherapeutics (LY294002) and gene therapeutics (ELMO1-targeted siRNA) at the same time. The co-delivery system was further functionalised with a pH-sensitive polymer, PMPC-PDPA. The effectiveness of the co-delivery system was assessed using a cell viability assay (MTT) and gene expression levels (qRT-PCR).

## 6.2 MATERIALS AND METHODS

### 6.2.1 Assembly of the chemo- / gene- therapeutics co-delivery system

LY294002 was loaded onto all MSNPs following protocols in section 4.2.3. PEI was then capped on the LY@MSNPs (described in section 5.2.1).

ELMO1-targeted siRNA was loaded onto PEI loaded LY@MSNPs (PEI-LY@MSNPs). In a typical loading process, 10 µL ELMO1-targeted siRNA (20 µM, described in section 5.2.1) and 10 µL 6.25 mg/mL PEI-LY@MSNPs suspension was mixed in 5 mL DMEM (no additives) and incubated at RT for 30 min. Non-targeted siRNA was loaded onto PEI-LY@MSNPs with the same protocol. The co-delivery systems were washed once with RNase-free water.

Since the non-porous SNPs were found not to be an efficient carrier for either LY294002 or siRNAs, a co-delivery system based on SNPs was not investigated.

### 6.2.2 Assembly of the pH-stimuli co-delivery system

The co-delivery system was re-suspended in RNase-free water at a concentration of 5 mg/mL. PMPC-PDPA co-polymer was added as a cap using the procedure detailed in section 4.2.2.2.

### 6.2.3 Cell viability

After RH30, RD, U87-MG and MCF7 cells were treated with the co-delivery systems, the viability of the cells was evaluated using the MTT assay. The procedure for the MTT assay is detailed in section 2.2.4. ELMO1-targeted siRNA loaded on PEI-LY@MSNPs were called duo@MSNPs in later context.

### 6.2.4 ELMO1 knock-down

In order to evaluate the gene knock-down effect following co-delivery with LY294002 and siRNA, RD cells were transfected as follows:

- Blank control: Untreated;
- Negative control: NT@HMSNP / NT@WMSNP;
- Positive control: ELMO1@DharmaFECT; ELMO1@HMSNP / ELMO1@WMSNP;
- Experiment:
    - LY@HMSNP / LY@WMSNP;

- Non-targeted siRNA loaded on PEI-LY@HMSNP (NT@LY@HMSNP) / Non-targeted siRNA loaded on PEI-LY@WMSNP (labelled NT@LY@WMSNP);
- ELMO1-targeted siRNA loaded on PEI-LY@HMSNP (labelled ELMO1@LY@HMSNP or duo@HMSNP) / ELMO1-targeted siRNA loaded on PEI-LY@WMSNP (labelled ELMO1@LY@WMSNP or duo@WMSNP);
- PMPC-PDPA co-polymer capped ELMO1@HMSNP (labelled PMPC-ELMO1@HMSNP)/ PMPC-PDPA co-polymer capped ELMO1@WMSNP (labelled PMPC-ELMO1@WMSNP);
- PMPC-PDPA co-polymer capped ELMO1@LY@HMSNP (labelled PMPC-ELMO1@LY@HMSNP) / PMPC-PDPA co-polymer capped ELMO1@LY@WMSNP (labelled PMPC-ELMO1@LY@WMSNP);

The transfection procedure is detailed in section 5.2.3.

### 6.2.5 Data analysis

Significance tests were performed using a two-tailed homoscedastic Student's t test on Microsoft™ Excel platform and listed separately in Table 6.1 and Table 6.2.

## 6.3 RESULTS

### 6.3.1 Cell viability after treatment with the chemo- and gene- therapeutics co-delivery systems

To eliminate any potential influence of inherent MSNPs toxicity, all viability results of the co-delivery systems in Figure 6.1 were calibrated with their unloaded counterparts.

Under hypoxic conditions, duo@CMSNPs appeared to the most efficient drug delivery system in RH30 cells, and reduced cell viability to approx. 66.73 % of the control (Figure

6.1a). It should be noted that duo@CMSNPs were even more effective than LY@CMSNPs in reducing RH30 cell viability under hypoxic condition. The other co-delivery systems also showed a decrease in cell viability in RH30 cells under hypoxic conditions. Under normoxic conditions, duo@CMSNPs were also found to be the most effective candidate in RH30 cells (Figure 6.1b).

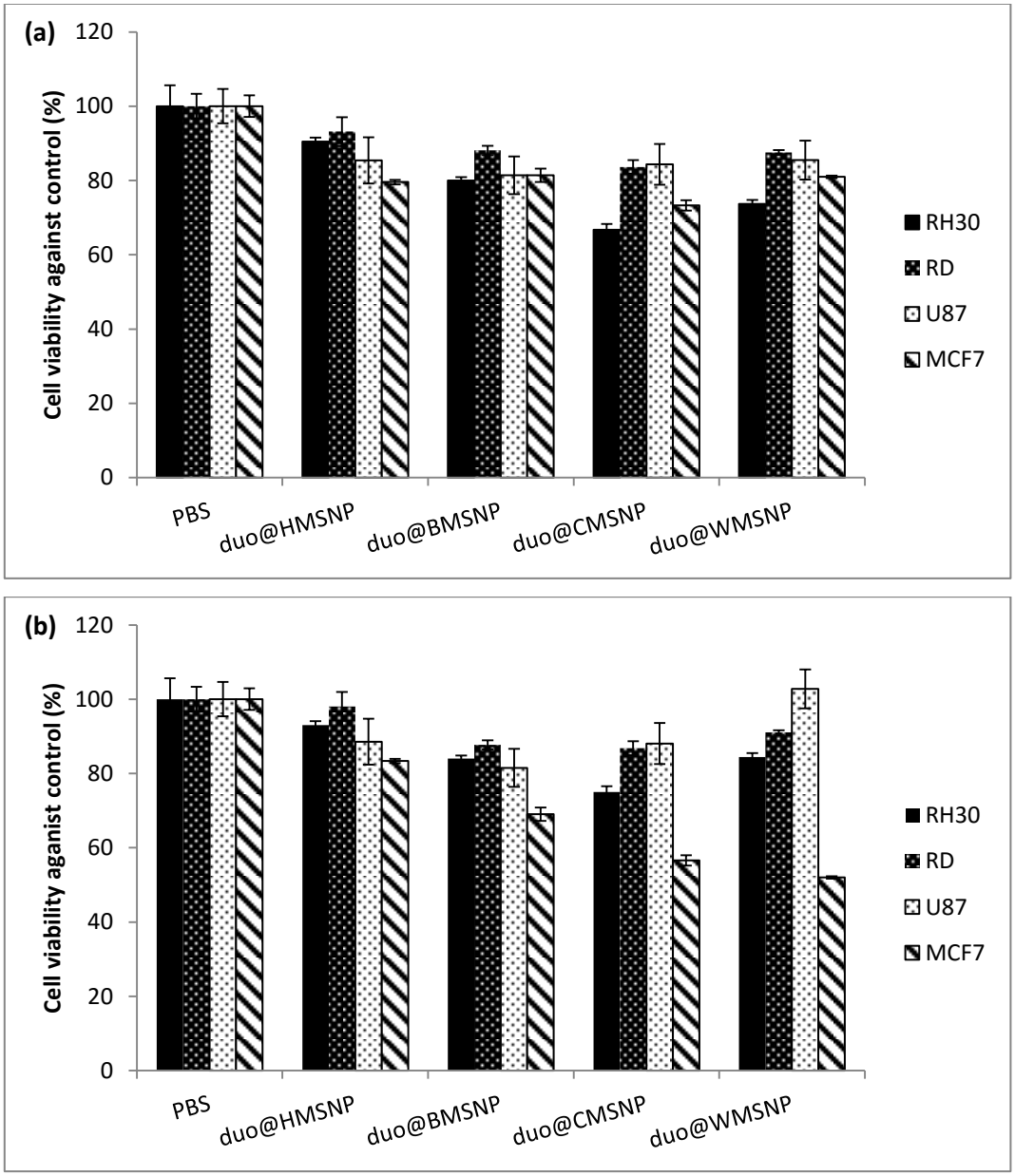


Figure 6.1 The cell viability of RH30, RD, U87-MG and MCF7 cells assessed using MTT assay after a treatment with duo@MSNPs co-delivery systems against the unloaded control for 24 hours under (a) hypoxic or (b) normoxic condition (the data are presented as the means ± standard deviation, n= 3)

In RD cells, duo@CMSNPs were found to be the most effective drug delivery system under either tested condition: after treatment of duo@CMSNPs, the viability of RD cells was reduced to approx. 83.64 % of the control under hypoxic condition, and to approx. 86.80 % of the control under normoxic condition (Figure 6.1). Besides, duo@BMSNPs and duo@WMSNPs were found to successfully reduce cell viability of RD cells under either oxidative condition. It was also noted that despite the fact that LY294002 alone appeared to be more effective in RD cells under normoxic conditions, no such phenomenon was observed when LY294002 was entrapped and released from a co-delivery system (Figure 3.9, Figure 6.1).

Despite the success of duo@CMSNPs in RH30 and RD cells, it was not the drug delivery platform that caused the most cell death in U87-MG cells. In U87-MG cells, duo@BMSNPs were seen to be the most promising candidate and caused a reduction of cell viability to 81.41 % of the control under hypoxic conditions, and approx. 81.52 % of the control under normoxic conditions (Figure 6.1). Other candidates were also found to be effective in reducing the cell viability under either oxidative condition.

In MCF7 cells, duo@CMSNPs appeared to be the most successful candidate in decreasing cell survival under hypoxic conditions, causing cell viability to be reduced to approx. 73.30 % of the control. duo@HMSNPs, duo@BMSNPs and duo@WMSNPs exhibited similar toxicity to MCF7 cells under the same conditions (Figure 6.1a). Under normoxic conditions, however, duo@WMSNPs were shown to be the most effective delivery system and reduced the viability of MCF7 cells to approx. 51.99 % of the control. duo@BMSNPs and duo@CMSNPs were both seen to be more effective in MCF7 cells under normoxic conditions than under hypoxic conditions: the viability reached 69.03 % and 56.60 % of the control respectively after treatment of duo@BMSNPs and

duo@CMSNPs, while the viability was only reduced to 81.39 % and 73.30 % of the control when treated under hypoxic conditions. duo@HMSNPs were also found to be valid in reducing cell survival. However the effectiveness was less than the other three candidates.

The results showed that almost all the co-delivery systems were able to cause a reduction in cell viability in all cell lines under either hypoxic or normoxic conditions.

### 6.3.2 ELMO1 gene expression after treatment with the chemo- and gene-therapeutics co-delivery system

To evaluate the effectiveness of the co-delivery systems with respect to gene silencing, ELMO1 gene expression in RD cells was measured using qRT-PCR. As demonstrated in section 5.3.3, only HMSNP-based and WMSNP-based delivery systems were tested.

LY@MSNPs were found to reduce ELMO1 expression: LY@HMSNP and LY@WMSNP caused 1.43 fold and 1.09 fold ELMO1 expression reduction in RD cells, respectively. This indicated the the released LY294002 could induce ELMO1 silencing in RD cells under normoxic condition. However, the co-delivery system with LY294002 and non-targeted siRNA loaded (labelled NT@LY@HMSNP and NT@LY@WMSNP in Figure 6.2) caused much less ELMO1 expression reduction. This may have resulted from a loss of LY294002 during the siRNA loading process.

As discussed in detail in Chapter 5, ELMO1-targeted siRNA was successfully delivered to RMS cells with both HMSNP and WMSNP. The co-delivery systems (loaded with both LY294002 and ELMO1-targeted siRNA; labelled ELMO1@LY@HMSNP and ELMO1@LY@WMSNP in Figure 6.2) also showed significantly high gene knock-down

efficiency ($P < 0.001$). Furthermore, the co-delivery system, ELMO1@LY@HMSNP, was found to be more efficient than ELMO1@HMSNP in gene silencing, while there was no significant difference between ELMO1@LY@WMSNP and ELMO1@WMSNP ($P > 0.05$) (Figure 6.2 b, Table 6.2).

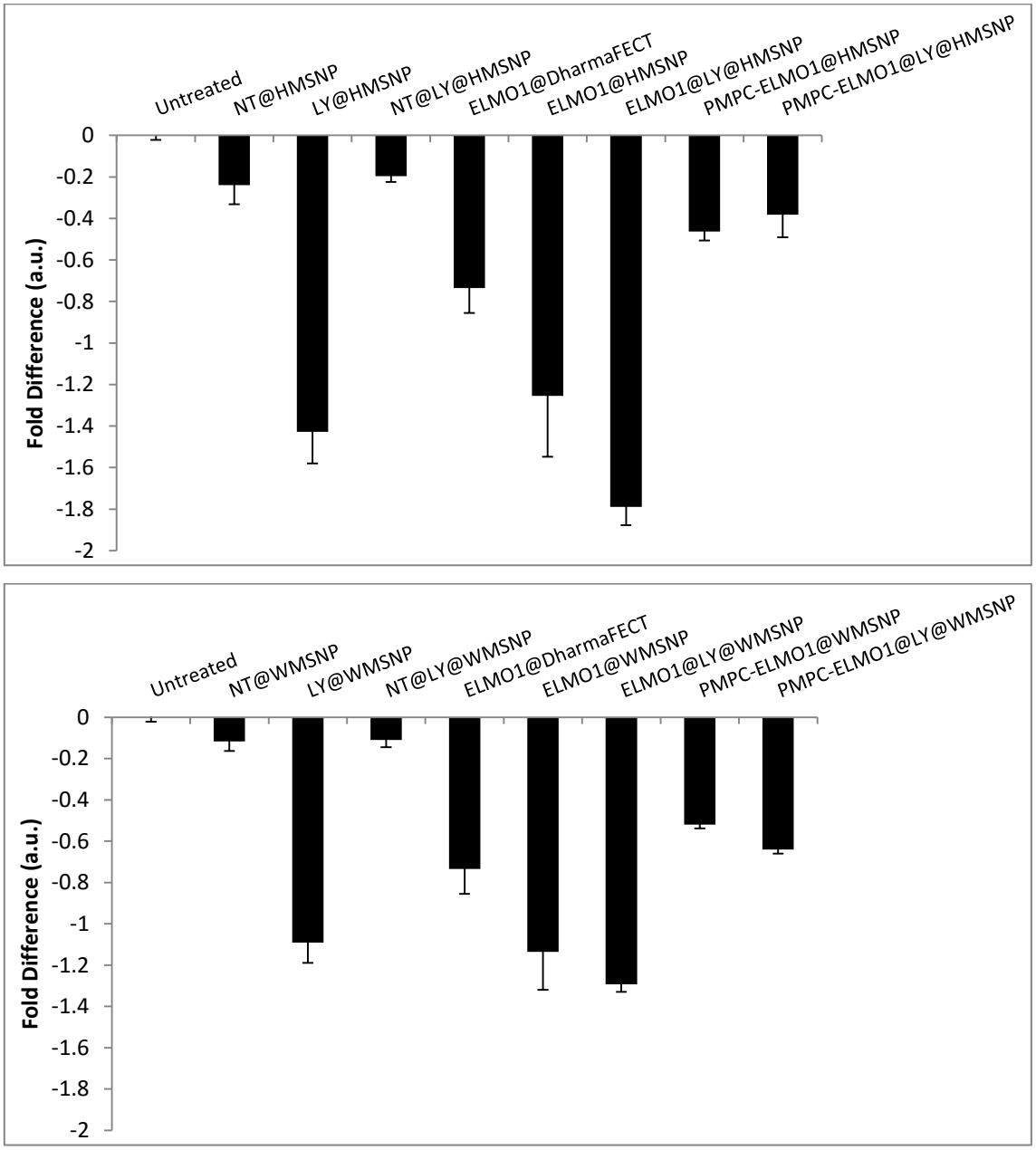


Figure 6.2 ELMO1 gene expression evaluated with quantitative RT-PCR analysis in RD cell lines after the cells were transfected for 24 hours with (a) HMSNP-based and (b) WMSNP-based delivery systems. The gene expression level was compared to β-actin as housekeeping gene. (The data are presented as the means ± standard deviation, n= 3). (Blank control: untreated; negative controls: transfected with non-targeted siRNA carried with (a) HMSNP or (b) WMSNP; positive control: transfected with ELMO1-targeted siRNA with DharmaFECT)

| Groups | NT@ HMSNP | LY@ HMSNP | NT@LY @HMSNP | ELMO1@ DharmaFECT | ELMO1@ HMSNP | ELMO1@ LY@HMSNP | PMPC-ELMO1@ HMSNP | PMPC-ELMO1@ LY@HMSNP |
|---|---|---|---|---|---|---|---|---|
| Untreated | *** | *** | *** | *** | *** | *** | *** | *** |
| NT@ HMSNP | | ** | n.s. | not tested | *** | *** | ** | n.s. |
| LY@ HMSNP | | | *** | *** | n.s. | * | *** | ** |
| NT@LY @HMSNP | | | | *** | *** | *** | *** | * |
| ELMO1@ DharmaFECT | | | | | ** | *** | *** | ** |
| ELMO1@ HMSNP | | | | | | * | *** | *** |
| ELMO1@ LY@HMSNP | | | | | | | *** | *** |
| PMPC-ELMO1@ HMSNP | | | | | | | | n.s. |

Table 6.1 The significance test performed on ELMO1 gene expression evaluated with quantitative RT-PCR analysis in RD cells after transfection for 24 hours with different HMSNP-based delivery systems presented in Figure 6.2a. n.s. = not significant, * $P < 0.05$, ** $P < 0.01$, *** $P < 0.001$

PMPC-PDPA capped co-delivery systems were found to be less efficient in silencing ELMO1 expression. PMPC-ELMO1@HMSNP and PMPC-ELMO1@LY@HMSNP only caused 0.46 fold and 0.38 fold ELMO1 expression reductions, respectively, after 24 hours transfection. This appeared to be significantly lower than the co-delivery system before capping ($P < 0.05$) (Figure 6.2a, Table 6.1). The results were seen to be similar to PMPC-ELMO1@WMSNP and PMPC-ELMO1@LY@WMSNP, which led to only 0.52 fold and 0.64 fold ELMO1 gene expression reductions respectively (Figure 6.2b, Table 6.2).

In summary, ELMO1 gene expression can be knocked down using the LY294002 / ELMO1-targeted siRNA co-delivery systems based on HMSNP and WMSNP. However, the gene knock-down was less significant when the co-delivery systems were capped with the pH-sensitive polymer, PMPC-PDPA.

| Groups | NT@WMSNP | LY@WMSNP | NT@LY@WMSNP | ELMO1@DharmaFECT | ELMO1@WMSNP | ELMO1@LY@WMSNP | PMPC-ELMO1@WMSNP | PMPC-ELMO1@LY@WMSNP |
|---|---|---|---|---|---|---|---|---|
| Untreated | ** | *** | *** | *** | *** | *** | *** | *** |
| NT@WMSNP | | *** | n.s. | not tested | *** | *** | *** | *** |
| LY@WMSNP | | | *** | ** | n.s. | * | *** | *** |
| NT@LY@WMSNP | | | | *** | *** | *** | *** | *** |
| ELMO1@DharmaFECT | | | | | *** | *** | * | n.s. |
| ELMO1@WMSNP | | | | | | n.s. | *** | ** |
| ELMO1@LY@WMSNP | | | | | | | *** | *** |
| PMPC-ELMO1@WMSNP | | | | | | | | ** |

Table 6.2 The significance test performed on ELMO1 gene expression evaluated with quantitative RT-PCR analysis in RD cells after transfection for 24 hours with different WMSNP-based delivery systems presented in Figure 6.2b. n.s. = not significant, * $P < 0.05$, ** $P < 0.01$, *** $P < 0.001$

## 6.4 DISCUSSION

### 6.4.1 Additive efficiency in gene silencing after treatment with the co-delivery systems

ELMO1 knock-down efficiency after transfection with the co-delivery system (1.79 fold ELMO1 knock-down compared to the blank control) was found to be higher than when

transfected with either LY@HMSNP (1.43 fold knock-down) or ELMO1@HMSNP (1.25 fold knock-down). This indicated an additive efficiency in ELMO1 gene knock-down when RD cells were treated with the co-delivery system.

Similar additive efficiency, or even synergistic effect, in gene knock-down, cell survival inhibition and tumour metastasis inhibition was also reported on other co-delivery systems. For example, Lee *et al.* claimed to use a micellar co-delivery system of doxorubicin and tumour necrosis factor -related apoptosis-inducing ligand to obtain a synergistic effect on cell death (Lee *et al.*, 2011a). Feng *et al.* reportedly achieved an additive effect on tumour growth inhibition when co-delivering VEGF-targeted siRNA and paclitaxel with a PEG-based core-shell nanoparticle platform (Feng *et al.*, 2014).

### 6.4.2 The function of the PI3K inhibitor, LY294002, to ELMO1 expression

ELMO1 expression has been shown to be largely dependent upon cell type, although ELMO1 regulation has not been fully studied to date (Patel *et al.*, 2011, Rapa *et al.*, 2012, Wang, 2006). It has been claimed that ELMO1 and PI3K work in parallel in human cells, and PI3K activation has not been found to affect ELMO1 regulation when studied in lymphocyte or neutrophil-like cells (Sai *et al.*, 2008, Stevenson *et al.*, 2014, Wang, 2006).

In this study, ELMO1 gene expression was found to be down-regulated in RD cells after treatment of LY294002@MSNPs (Figure 6.2). However, it was beyond the scope of this study to determine the role of PI3K in ELMO1 regulation in the different cell lines.

### 6.4.3 Cell viability after treatment with the co-delivery systems

Results from the Chapter 3 showed that under hypoxic conditions, the LY294002 drug alone was less effective than under normoxic conditions (Figure 3.6, Figure 3.7). This was also seen for the LY@MSNP under hypoxic conditions (Figure 4.7, Figure 4.8). After treatment with the co-delivery systems in most tested cell lines, however, there was negligible difference in cell viability whether tests were performed under hypoxic or normoxic conditions. The exception was the MCF7 breast cancer cell line, since duo@CMSNP and duo@WMSNP were shown to be more efficient under normoxic conditions than under hypoxic conditions.

It is possible that the internalisation of free LY294002 is compromised by oxidative stress, leading to the low physiological efficiency in tested cells. PEI capping and siRNA conjugation enables a more efficient internalisation of the co-delivery systems which is less influenced by oxygen level. Furthermore, PEI capping may also contribute to cell viability reduction, and the cytotoxicity of PEI is not oxygen-sensitive (data not shown). Therefore, cell viability after treatment with the co-delivery systems could be less affected by the environmental oxygen concentrations.

### 6.4.4 ELMO1 gene expression after treatment with the co-delivery systems under hypoxic conditions

Cell viability after treatment with the co-delivery systems was found to be less affected by the environmental oxygen level. In order to investigate whether hypoxia would affect the ELMO1 knock-down, RD cells were also transfected with the HMSNP based co-delivery system under hypoxic conditions.

LY294002 was confirmed to be less effective at reducing ELMO1 expression under hypoxic conditions. ELMO1 expression was only reduced by 0.62 fold when treated with LY@HMSNP under hypoxic condition, significantly lower than after treatment under normoxic conditions (1.43 fold reduction; $P < 0.001$).

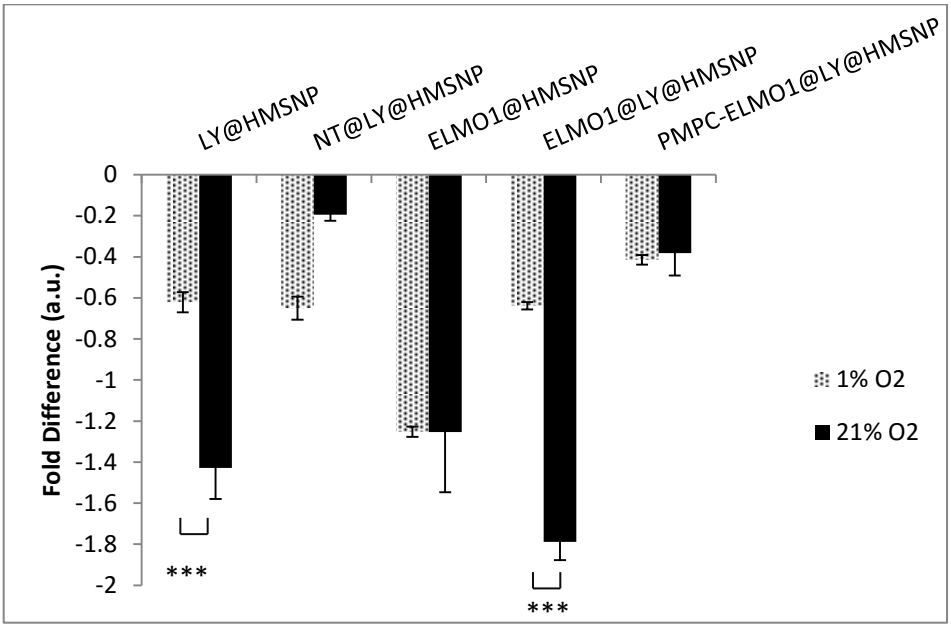


Figure 6.3 Comparing the expression of ELMO1 gene in RD cell lines after the cells were transfected for 24 hours with HMSNP-based co-delivery systems under hypoxic and normoxic conditions. The gene expression level was compared to β-actin as housekeeping gene. (The data are presented as the means ± standard deviation, n= 3)

Furthermore, there was no additive effect found after transfection with the co-delivery system. No significant difference was seen when RD cells were transfected with LY@HMSNP, NT@LY@HMSNP or ELMO1@LY@HMSNP under hypoxic conditions ($P > 0.05$). It was noted that ELMO1@LY@HMSNP was even less efficient in ELMO1 knock-down than ELMO1@HMSNP. Further experiments are required to explain this phenomenon.

### 6.4.5 PMPC-PDPA capped co-delivery system

As demonstrated in section 4.4.2, a number of problems remained when using PMPC-PDPA as a pH-sensitive capping on MSNPs. In addition, PMPC-PDPA was also found unsuitable to functionalise the co-delivery systems. The capped duo@MSNPs were less effective in reducing cell viability in all cell lines under either oxidative condition (data not shown). Furthermore, ELMO1 knock-down was also found to be less significant after transfection with PMPC-PDPA capped co-delivery systems (Figure 6.2, Figure 6.3).

Although PMPC-PDPA is found to be a biocompatible pH-sensitive polymer, it is not suitable as a functional capping on drug delivery systems based on MSNPs with the current capping procedures.

## 6.4.6 Future potential for the co-delivery system

### *6.4.6.1 Overcoming Multi-Drug Resistance (MDR)*

Co-delivery systems have been claimed to be an easy and effective means to overcome MDR in cancer (Xiong and Lavasanifar, 2011, Xiao *et al.*, 2012).

This possibility can also be investigated using MSNPs based co-delivery systems in the future, by loading anti-cancer drugs and siRNAs targeting MDR genes (such as ABC gene).

### *6.4.6.2 More efficient chemotherapeutics loading*

Despite the success in reducing cell viability with duo@MSNPs, most co-delivery systems were seen to be less efficient than their solo-LY294002 loaded counterparts.

This could be due to a loss of LY294002 during the assembly of the co-delivery systems. A more secure drug loading process is desired in future work. Previous literature reported a number of approaches to prevent premature release of cargo molecules such as capping pore-sized nanoparticles as gatekeepers (Colilla *et al.*, 2013). Those methods might enable a more efficient chemotherapeutics loading and reduce cargo loss.

#### *6.4.6.3 Environmental-responsive capping*

In order to control the release of cargo, PMPC-PDPA co-polymer was coated onto the surface of the MSNPs based co-delivery systems. However, it was found that the coating was not sufficient to enable an environmentally-stimulated release. Towards efficient control of environmental-responsive delivery, a more suitable surface capping candidate is desired. An appropriate candidate should be biocompatible, sensitive to tumour micro-environment (e.g. lower pH, lower oxygen concentration, or lower glucose than normal healthy tissue) and allow cargo release at the tumour site.

#### *6.4.6.3 Targeting delivery*

In order to achieve efficient delivery and minimise off-target release after systemic administration, the co-delivery system may also be further modified with a targeting ligand. As introduced in Chapter 4.1.3, a number of molecules (e.g. folic acid, IgG) could be used to target nanoparticles to tumours or cancer cells. Conjugation of a targeting ligand to a nanoparticle could potentially target an MSNP based co-delivery system specifically to tumours and therefore avoid unfavourable particle distribution in the body, enhance the efficiency of drug delivery, and mitigate off-target drug toxicity.

## 6.5 CONCLUSION

A multifunctional chemo- / gene- therapeutic co-delivery system can be established using functionalised MSNPs.

The co-delivery systems based on studied MSNPs were found to successfully deliver LY294002 and ELMO1-targeted siRNA to tested cancer cells at the same time, resulting in reduced cell viability reduction and ELMO1 knock-down. The reduction of cell viability was shown after treatments with the co-delivery systems for all four MSNP candidates studied, and also under either hypoxic or normoxic conditions.

Moreover, the LY294002 compound itself was found to suppress ELMO1 gene expression in both RH30 and RD cells. Further investigation is needed to understand the mechanism of ELMO1 gene knockdown in response to LY294002 in the RMS cell lines.

After transfection with the co-delivery system carrying both ELMO1-targeted siRNA and the LY294002, an additive effect was seen; further reducing ELMO1 gene expression in both RMS cell lines studied.

PMPC-PDPA co-polymer was found to be unsuitable for the functional capping of MSNPs for drug delivery systems. Using the current capping procedures, the co-polymer appeared to reduce the delivery efficacy of both the LY294002 and the ELMO1-targeted siRNA in the cell lines studied.

# Chapter 7

# Conclusion and Future

## 7.1 SUMMARY OF FINDINGS AND LIMITATIONS

Mesoporous silica nanoparticles have attracted attention in the field of drug delivery due to their biocompatibility, large surface area, controllable size, known surface chemistry for functionalization, and low synthesis cost. To date, however, most research on MSNPs has been limited to the hexagonal-aligned MSNPs (e.g. MCM-41 and SBA-15 in publications). In this study, four morphologically different MSNPs were synthesised, characterised, and assessed in detail, in order to analyse their suitability as *in vivo* drug carriers for anti-cancer reagents.

Four types of MSNPs were synthesised using sol-gel methods. Their physical properties were characterised in depth and compared with non-porous sold silica nanoparticles. The (bio-) degradability and biocompatibility of these particles was then assessed on different cancer cell lines. It has been demonstrated that:

1) In order to maximise cell uptake, minimise cytotoxicity, take advantage of the EPR effect, and minimize particle distribution to fenestrated organs, the optimal size range for intracellular drug delivery carriers should between 50 nm and 200 nm. HMSNPs, BMSNPs, and WMSNPs were shown to be of the correct size range. CMSNPs, with outer dimensions larger than 700 nm, were too large for efficient cellular uptake. Further investigation may be required to synthesize CMSNP style particles with the outer diameter reduced to below 200 nm. This may be possible to achieve by tuning the composition of the sol-gel system during the synthesis.

2) The nanoparticles had a high specific surface area which was desirable to allow efficient drug loading and surface functionalisation. All studied MSNPs showed high porosity with mesoscopic pores ranged between 1 nm and 10 nm (Table 2.1). Such pore sizes are approximately the same size of most chemotherapeutics, therefore allowing a sustained release of cargo due to the confinement effect (details in Chapter 4.4.1.2).

All studied MSNPs presented a negative or nearly neutral surface charge (Table 2.2). Due to a nanoparticle with negatively charged surface nanoparticles is more stable in suspension and beneficial for efficient endocytosis, HMSNPs, CMSNPs and WMSNPs are more suitable intracellular drug carriers than BMSNP (which was slightly positively charged). Furthermore, the exposed negatively charged silanol group also enable the studied MSNPs to be functionalised with other molecules, including environmental-responsive molecules and polymeric transfection reagents (e.g. PEI).

However, it was noticed that the current template removal processes are not sufficient in more than one candidate. A more effective method to remove the structure-directing templates would be beneficial to increase the specific surface area and/or reduce the surface charge of MSNPs, especially in BMSNPs.

3) The studied MSNPs were biocompatible with the tested cells up to 24 hours incubation (Figure 2.20). After longer incubation (96 hours), BMSNPs were seen to be more cytotoxic than the other candidates. The biocompatibility may be further enhanced with cell-compatible coatings, such as PEG.

4) HMSNPs appeared to be the best candidate with an optimal size, the largest surface area, a high absolute value for surface charge, and a relatively low cytotoxicity.

LY294002 is a drug with potent anti-cancer activity due to efficient PI3K pathway inhibition. We found that LY294002 was capable of inhibiting the phosphorylation of Akt and suppressing cell survival in four studied cancer cell lines. This efficiency was compromised when treated cells were under oxidative stress. LY294002 disturbed cellular metabolism in all tested cell lines. Cellular response to LY294002 was found to be dependent upon cell type, environmental oxygen and glucose levels. Further research will still be needed to fully understand the function of LY294002 in metabolism, proliferation and survival in different cell lines.

Different cargo molecules (positively charged model drug Rhodamine B, neutral hydrophobic chemotherapeutic LY294002, and negatively charged model drug calcein) were found to be successfully encapsulated into the MSNPs, and could be unloaded with different release profiles. The loading efficiency was seen to be dependent upon porosity / surface area of MSNPs, surface charges of MSNPs and electric potential difference between MSNPs and cargo molecules. The unloading behaviour was tuned by capping multi-layers polyelectrolytes or pH-sensitive co-polymers.

It is difficult to administer LY294002 systemically due to the insolubility, hydrophobicity and instability in aqueous solutions. We found that all studied MSNPs were able to deliver the LY294002 to cancer cells, and to cause efficient cell death. It was also found that the influence of hypoxia on the efficacy of the LY294002 to cause cell death was less profound when the compound was delivered using MSNPs. (i.e. under the hypoxic environment often found in tumours the physiological function of LY294002 was shown to be compromised).

siRNA is a useful tool to interfere with gene expression. Despite many approaches have been developed to deliver siRNA (including stimulating cells, chemically modifying siRNAs and using viral carriers of siRNAs), major challenges, such as high fatality, low cellular uptake efficiency and rapid systemic clearance, remain in current siRNA delivery methods. The MSNPs tested in this study were found to be able to successfully load and deliver siRNA to cancer cell lines causing efficient gene silencing. HMSNPs and WMSNPs were found to be better transfection reagents than one of the current products on market (DharmaFECT transfection reagent 1) under the same experimental procedures. Functionalised MSNPs appear to be more efficient siRNA carriers with higher transfection efficacy, lower cost and higher biocompatibility.

MSNP-based delivery systems were also found to successfully co-deliver both LY294002 and siRNA. LY294002 and ELMO1-targeted siRNA co-delivery systems utilising HMSNPs and WMSNPs were shown to be efficient in reducing cell viability and knocking-down ELMO1 expression.

## 7.2 FUTURE WORKS

Despite the success of current MSNPs synthesis methods, it may be particularly beneficial to concentrate further study on the template removal process for MSNPs that are intended for use in medical applications. Further work to reduce the outer dimension of CMSNPs is also needed. The methods for loading cargo into the MSNPs, and reducing the amount of drug which is not released into aqueous solution, would also benefit from follow-up study.

Future work could also include studies into more effective functionalisation of the MSNP surface for controlled release of cargo or targeting. Desirable properties for functionalization include 1) to be reactive with the silanol groups or the anionic surface of MSNPs; 2) biocompatible; 3) able to minimise premature cargo release, and 4) able to target specific cells or able to dissemble after trigger. Ideal nanoparticles functionalisation would therefore allow targeted delivery with minimal off-target cargo loss, and minimal harm to healthy cells.

The PMPC-PDPA co-polymer used in this study was found to be pH-sensitive albeit not sensitive enough in the physiological range under the current protocol. A further study could concentrate on the chemistry of PMPC-PDPA co-polymer in order to tune the pH-sensitivity.

Furthermore, the anti-cancer mechanisms of LY294002 and other PI3K inhibitors should be studied further. We observed many physiological functions of LY294002 in selected cells; however, there is a lack of focused studies on the mechanisms in metabolic altera-

tions after treatment. In particular, studies of chemotherapeutics to cancer cells under glucose, or other metabolite stress are lacking. Cancer cells in laboratories are mostly cultured in media with sufficient nutrients and oxygen, which is generally not found in real tumour microenvironments. It would therefore be beneficial for future research in pharmaceuticals, drug delivery and other cancer-related field to be mindful of the behaviours of the cancer cell lines to oxidative and/or metabolic stress in order to properly interpret results from *in vivo* studies, and clinical trials.

PEI coated MSNPs were found to be valid and efficient siRNA carriers. However, further research will be necessary to reduce the cytotoxicity of such delivery systems. This may include the development of new biocompatible polymers with high transfection efficacy..

In addition, the efficacy of stimuli-sensitive coating, drug unloading behaviours, system clearance and long-term fate of MSNPs based drug delivery systems will need to be performed  firstly on 3D-cultured cells (such as cell spheroids) and subsequently on *in vivo* models.

# Appendix

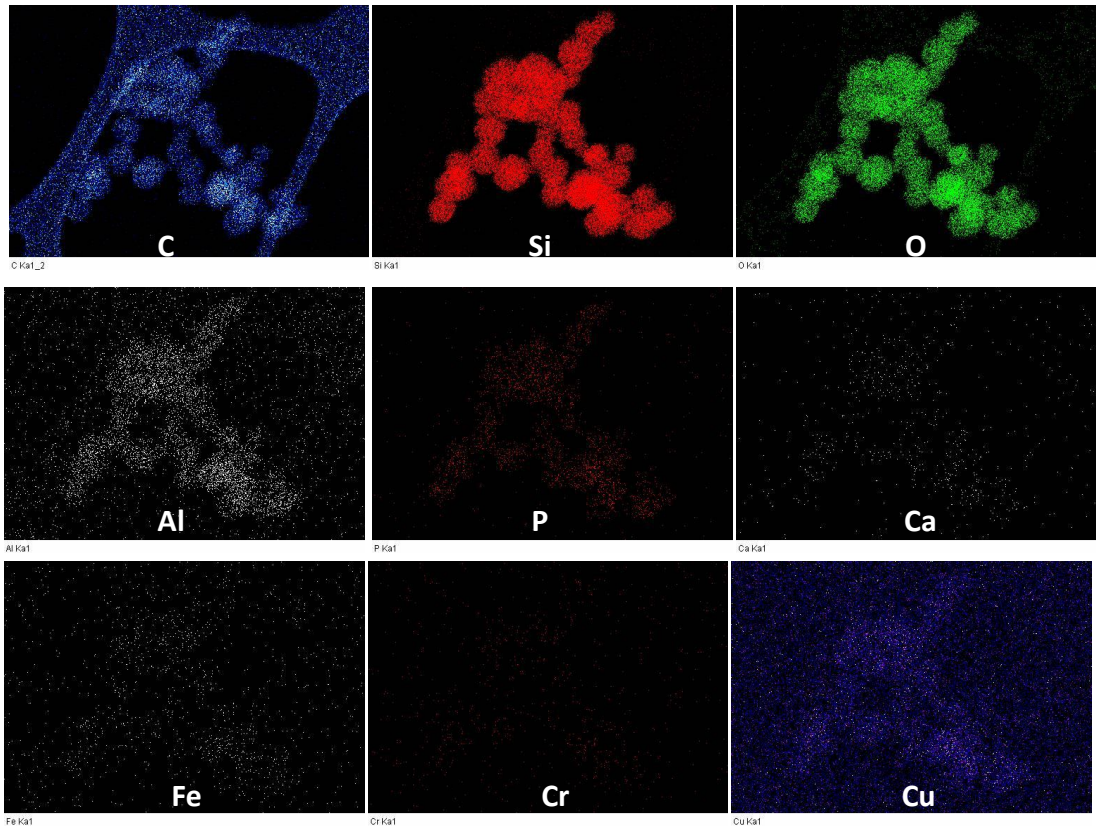


Figure S2.1 EDX mapping of a representative HMSNP sample measured using TEM. EDX mapping on those specific elements: Carbon, Silicon, Oxygen, Aluminium, Phosphor, Calcium, Iron, Chromium, and Copper

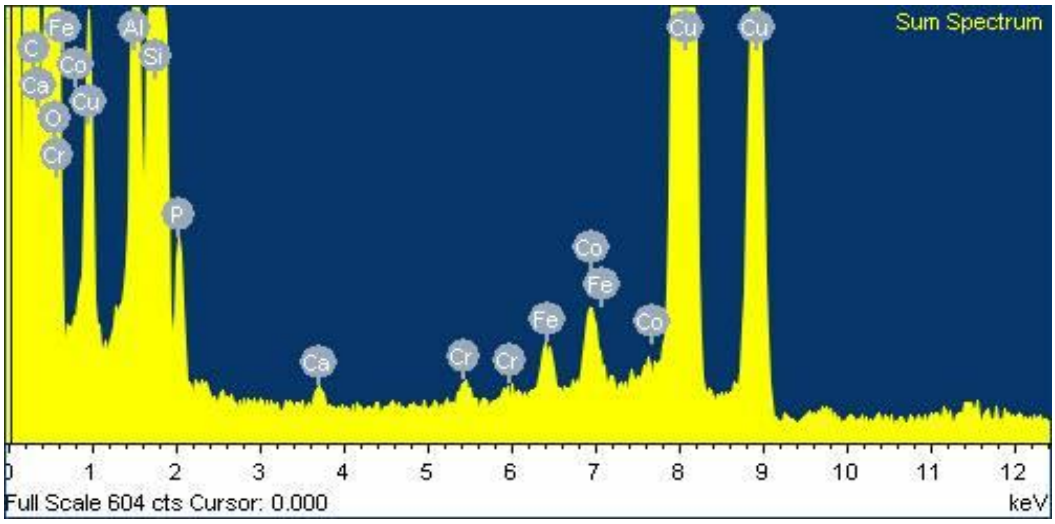


Figure S2.2 A sum EDX spectrum of a HMSNP sample with impurity elements detected

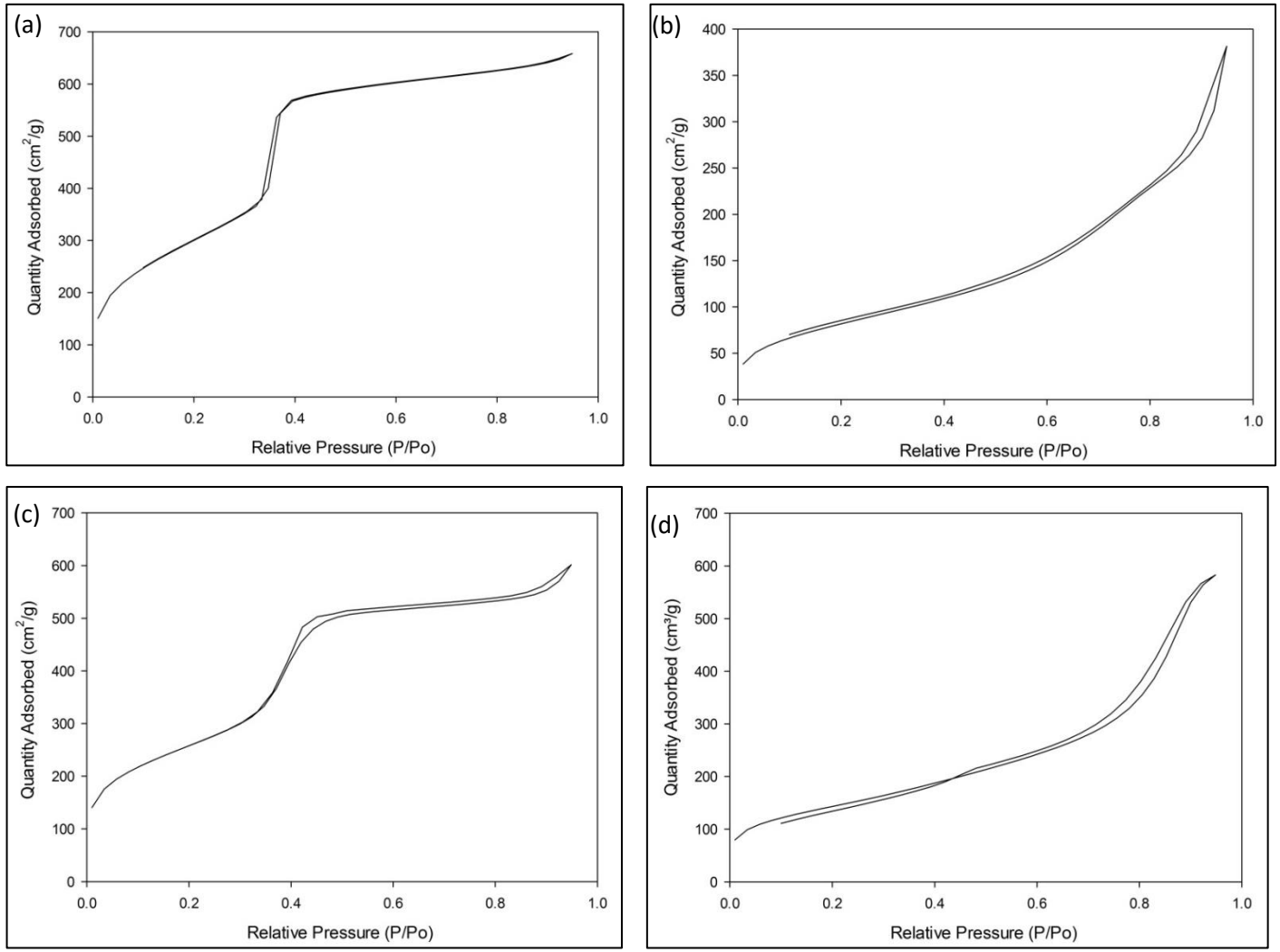


Figure S2.3 The isotherm linear plot of a) HMSNP, b) BMSNP, c) CMSNP and d) WMSNP from relative pressure 0.0 to 1.0

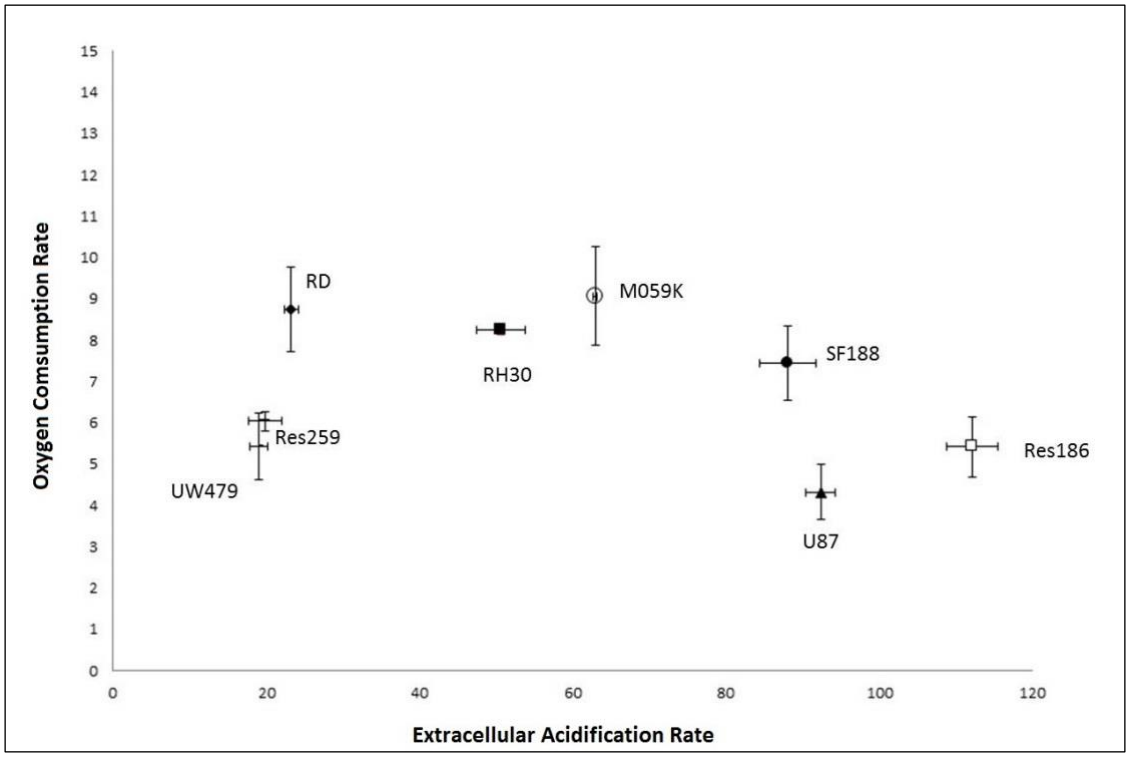


Figure S3.1 Bioenergetic profiles of immortalized cell lines UW249, Res259, RD, RH30, M059K, SF188, U87-MG, Res186 (Unpublished, Huang, et. al). Oxygen consumption rate and extracellular acidification rate are plotted to quantity mitochondrial respiration and to give an indication of glycolysis rates

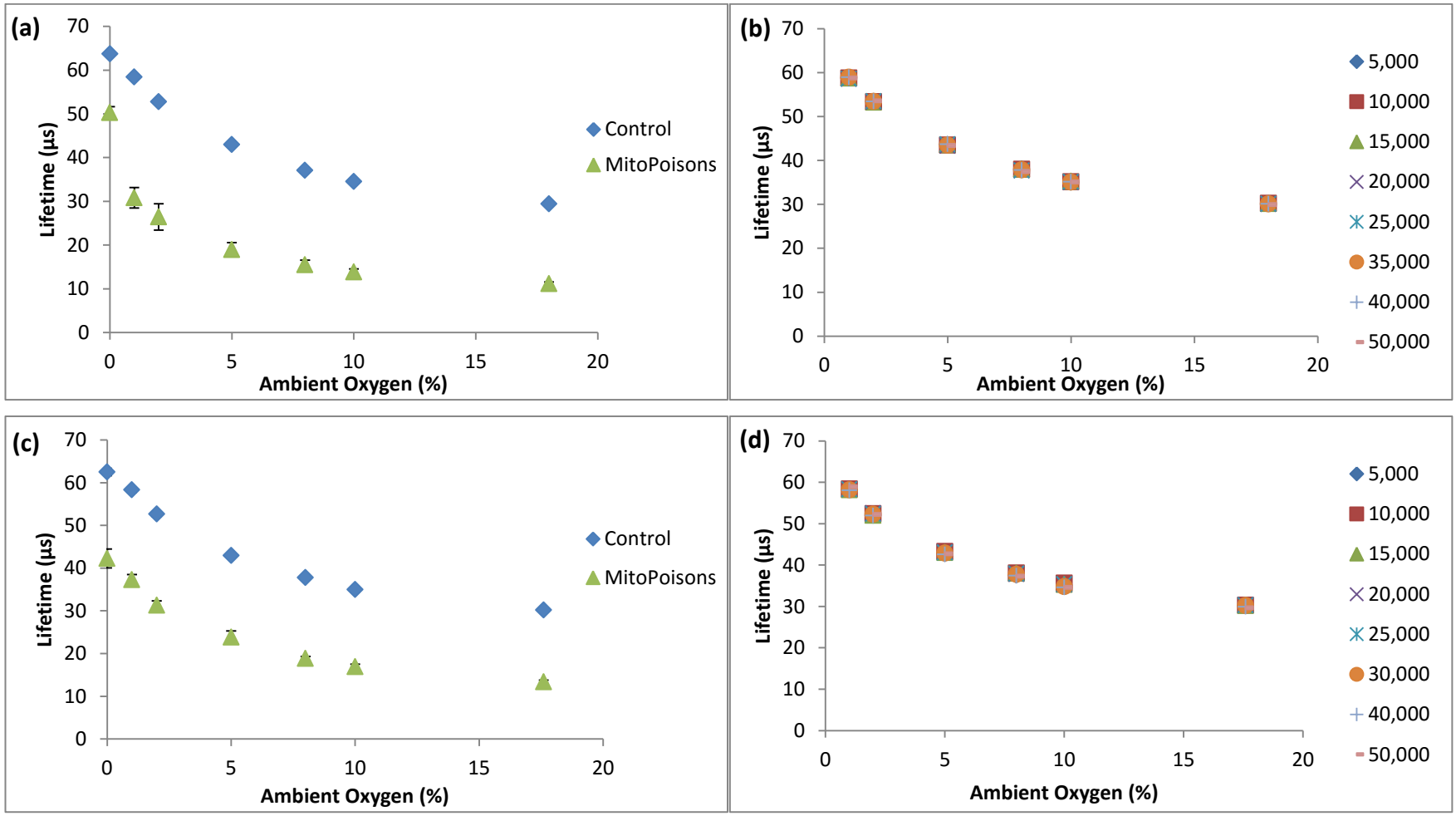


Figure S3.2 MitoXpress calibration curves of RD (a & b) or U87-MG (c & d) cells plotting lifetime values against ambient oxygen percentage. The lifetime was decreased after treatment with mito-poisons poisons (1 µM rotenone and 4 µM Antimycin-A ) (a & c); The lifetime was not shown dependence on cell number (b & d). (The data are presented as the means ± standard deviation, 24 points were taken from the plateau region from n = 3 replicates)

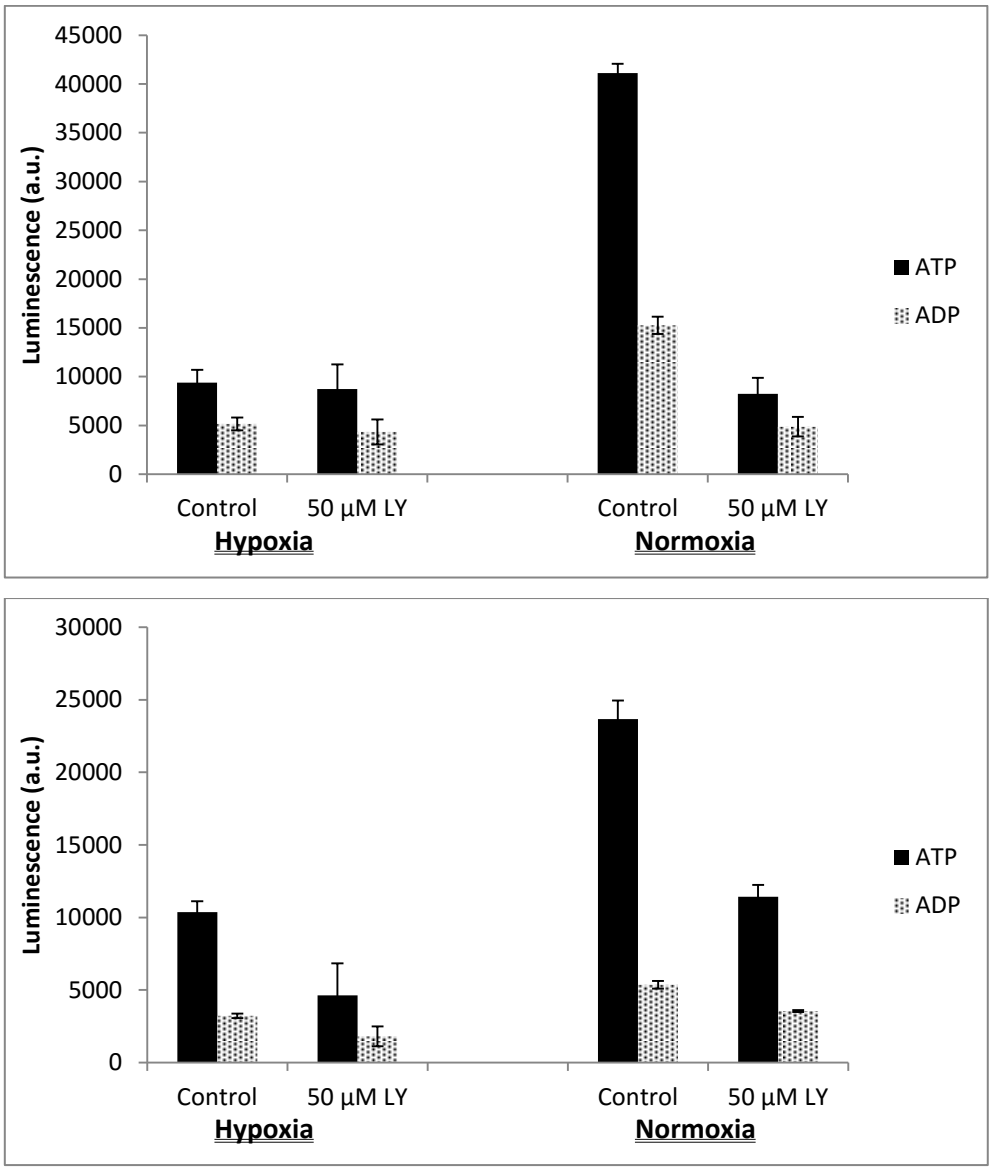


Figure S3.3 ATP, ADP production from a) RD or b) U87-MG cells after treatment with 50 µM LY294002 for 24 hours under either hypoxic (1% $O_2$) or normoxic (21% $O_2$) environment (The data are presented as the means ± standard deviation, n= 3)

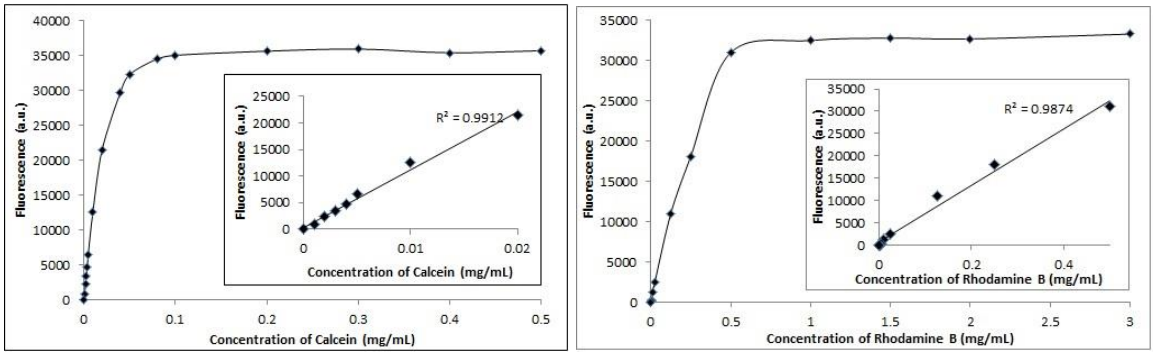


Figure S4.1 Concentration dependence of the fluorescence of Calcein (a) and Rhodamine B (b) plotting the concentration of model drug against fluorescence. Insets show detail of low concentration calcein or Rhodamine B

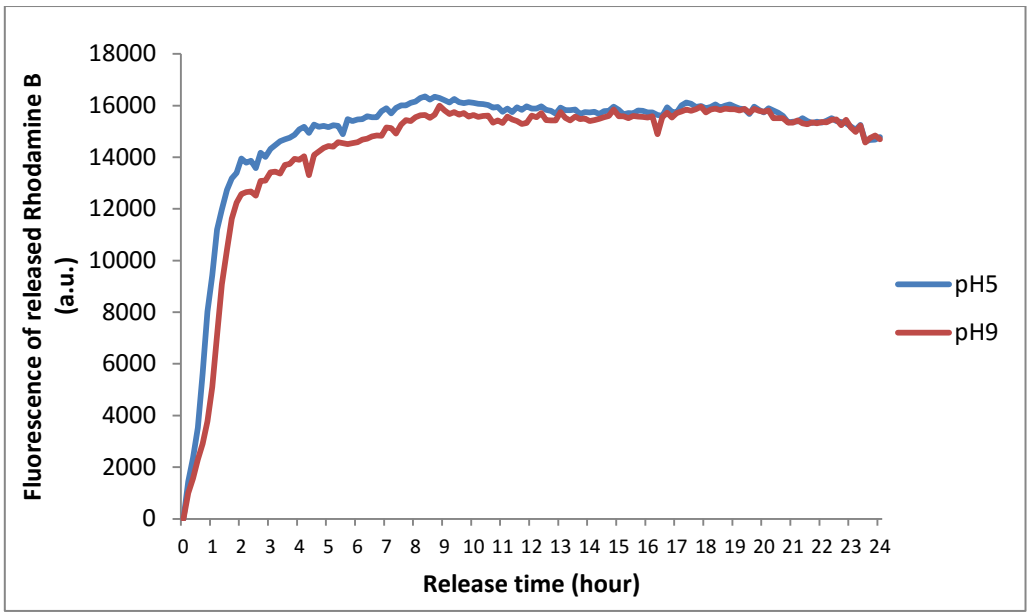


Figure S4.2 The release profile of PMPC-PDPA capped siRNA/Rhodamine B loaded HMSNP in release buffers with pH 5 or pH 9 over 24 hours

| Group | 0 | After 24 hours |
|---|---|---|
| Untreated | 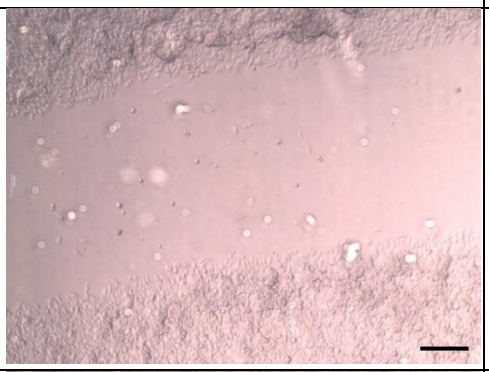 | 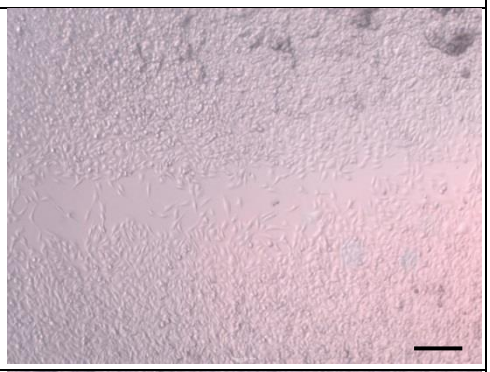 |
| bare ELMO1-targeted siRNA | 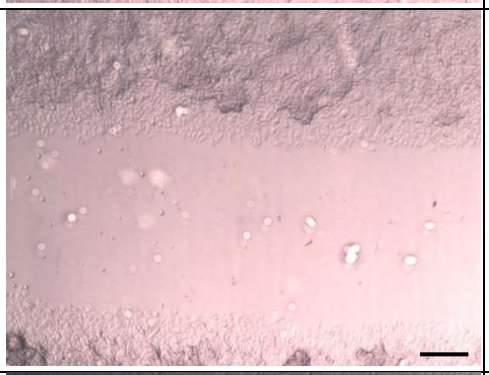 | 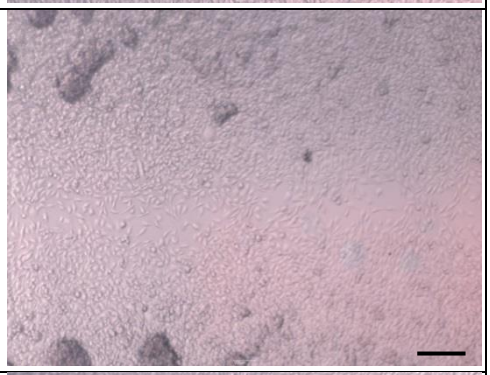 |
| NT@ Dhar-maFECT | 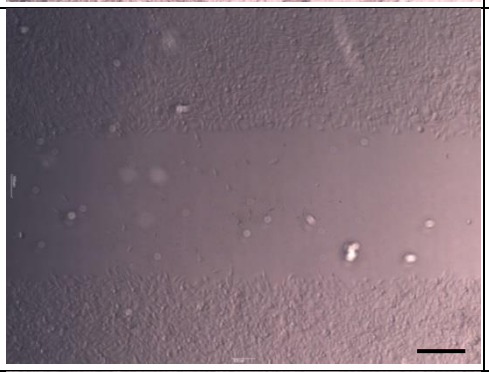 |  |
| ELMO1 @ Dhar-maFECT | 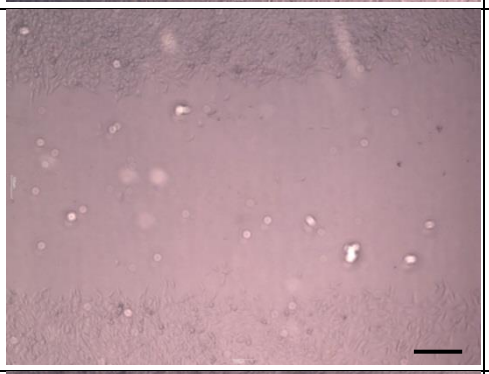 | 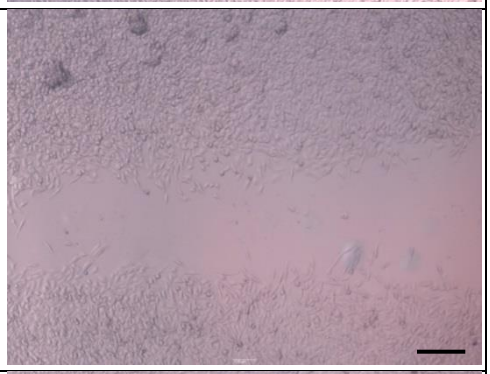 |
| ELMO1 @ SNP | 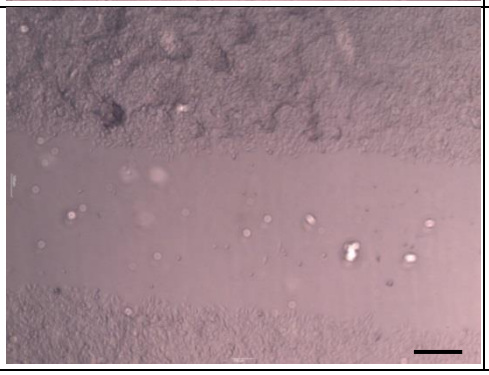 | 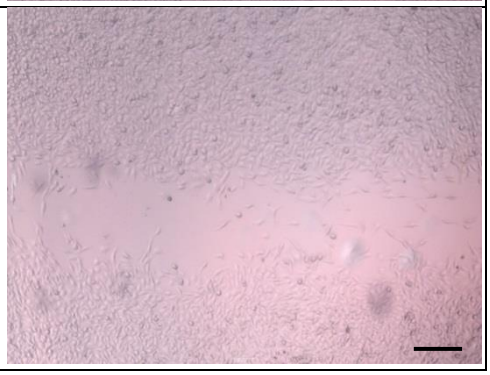 |

| | | |
|---|---|---|
| ELMO1 @ HMSNP | 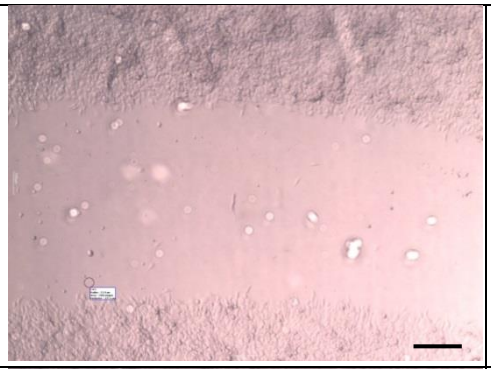 | 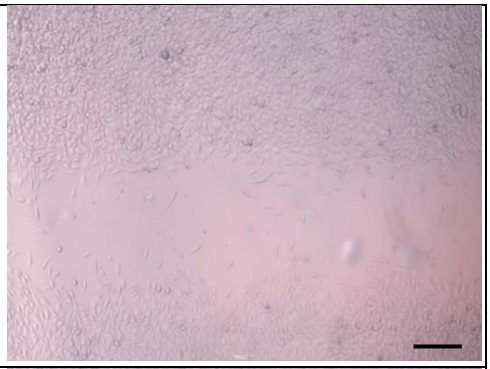 |
| ELMO1 @ BMSNP | 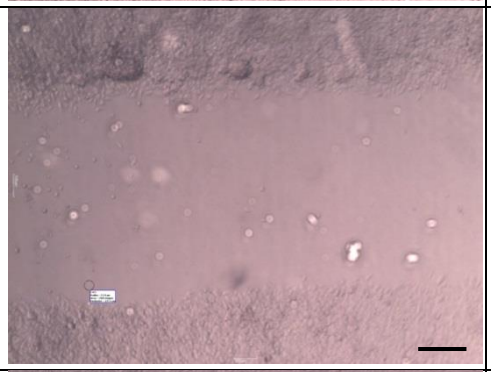 | 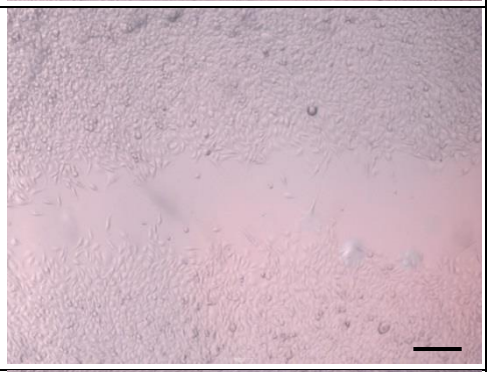 |
| ELMO1 @ CMSNP | 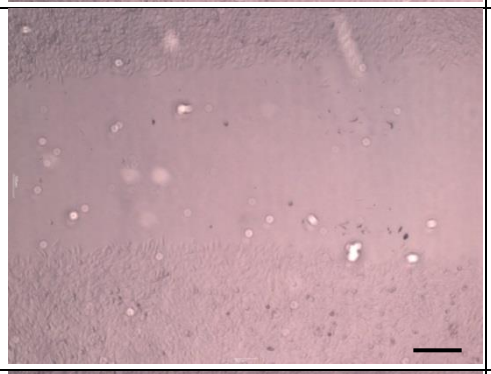 | 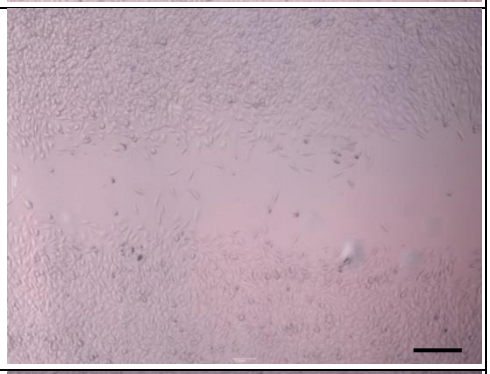 |
| ELMO1 @ WMSNP | 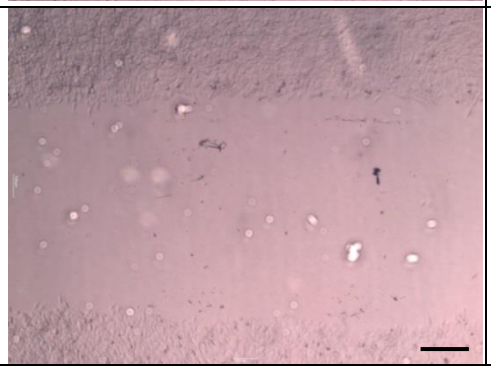 | 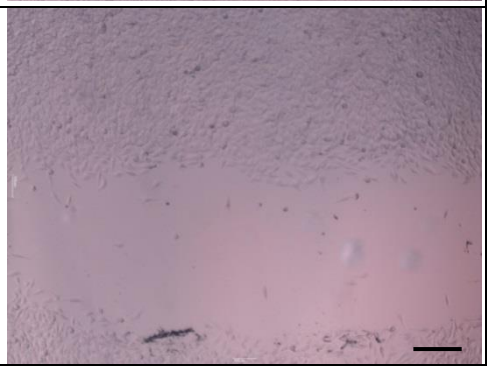 |

Table S5.1 A typical scratch test images after RH30 cells were transfected with ELMO1 for 72 hours on different carriers. Pictures were taken immediately after scratch (time 0) and after 24 hours incubation (scale bar: 200 μm)

# References


ABDUL-GHANI, R., SERRA, V., GYORFFY, B., JURCHOTT, K., SOLF, A., DIETEL, M. & SCHAFER, R. 2005. The PI3K Inhibitor LY294002 Blocks Drug Export from Resistant Colon Carcinoma Cells Overexpressing Mrp1. *Oncogene,* 25**,** 1743-1752.

ADAMS, J. M. & CORY, S. 2007. The Bcl-2 Apoptotic Switch in Cancer Development and Therapy. *Oncogene,* 26**,** 1324-37.

AKBAR, N., MOHAMED, T., WHITEHEAD, D. & AZZAWI, M. 2011. Biocompatibility of Amorphous Silica Nanoparticles: Size and Charge Effect on Vascular Function, in Vitro. *Biotechnology and Applied Biochemistry,* 58**,** 353-362.

ALBANESE, A., TANG, P. S. & CHAN, W. C. 2012. The Effect of Nanoparticle Size, Shape, and Surface Chemistry on Biological Systems. *Annu Rev Biomed Eng,* 14**,** 1-16.

ALESSI, D. R., ANDJELKOVIC, M., CAUDWELL, B., CRON, P., MORRICE, N., COHEN, P. & HEMMINGS, B. A. 1996. Mechanism of Activation of Protein Kinase B by Insulin and Igf-1. *The EMBO Journal,* 15**,** 6541-6551.

ALFAROUK, K. O., VERDUZCO, D., RAUCH, C., MUDDATHIR, A. K., ADIL, H. H., ELHASSAN, G. O., IBRAHIM, M. E., DAVID POLO OROZCO, J., CARDONE, R. A., RESHKIN, S. J. & HARGUINDEY, S. 2014. Glycolysis, Tumor Metabolism, Cancer Growth and Dissemination. A New Ph-Based Etiopathogenic Perspective and Therapeutic Approach to an Old Cancer Question. *Oncoscience,* 1**,** 777-802.

ALGARRA, M., CAMPOS, B. B., ALONSO, B., CASADO, C. M., ESTEVES DA SILVA, J. C. G. & BENAVENTE, J. 2013. Inclusion of Thiol Dab Dendrimer/Cdse Quantum Dots Based in a Membrane Structure: Surface and Bulk Membrane Modification. *Electrochimica Acta,* 89**,** 652-659.

ALI-BOUCETTA, H., AL-JAMAL, K. T. & KOSTARELOS, K. 2011. Cytotoxic Assessment of Carbon Nanotube Interaction with Cell Cultures. *Methods Mol Biol,* 726**,** 299-312.

ALLEN, T. M. & CULLIS, P. R. 2013. Liposomal Drug Delivery Systems: From Concept to Clinical Applications. *Adv Drug Deliv Rev,* 65**,** 36-48.

ALSHATWI, A. A., ATHINARAYANAN, J. & PERIASAMY, V. S. 2015. Biocompatibility Assessment of Rice Husk-Derived Biogenic Silica Nanoparticles for Biomedical Applications. *Mater Sci Eng C Mater Biol Appl,* 47**,** 8-16.

ALVAREZ-ERVITI, L., SEOW, Y., YIN, H., BETTS, C., LAKHAL, S. & WOOD, M. J. A. 2011. Delivery of siRNA to the Mouse Brain by Systemic Injection of Targeted Exosomes. *Nat Biotech,* 29**,** 341-345.

AMERICAN CANCER SOCIETY 2011. Global Cancer Facts & Figures 2nd Edition.

AMERICAN.DIABETES.ASSOCIATION 2000. Screening for Type 2 Diabetes. *Clinical Diabetes,* 18.

ANGELATOS, A. S., KATAGIRI, K. & CARUSO, F. 2006. Bioinspired Colloidal Systems Via Layer-by-Layer Assembly. *Soft Matter,* 2**,** 18-23.

ANGYAL, S. J., DOWNES, C. P., EISENBERG, F. J., IRVINE, R. F., MICHELL, R. H., PARTHASARATHY, R. & SHVETS, V. I. 1989. Numbering of Atoms in Myo-Inositol. Recommendations 1988. Nomenclature Committee of the International Union of Biochemistry. *Biochemical Journal,* 258**,** 1-2.

ARBAB, A. S., YOCUM, G. T., WILSON, L. B., PARWANA, A., JORDAN, E. K., KALISH, H. & FRANK, J. A. 2004. Comparison of Transfection Agents in Forming Complexes with Ferumoxides, Cell Labeling Efficiency, and Cellular Viability. *Molecular imaging,* 3**,** 24-32.

ARCARO, A. 2014. *Targeting PI3K/Mtor Signaling in Cancer*, Frontiers E-books.

ARDANA, A., WHITTAKER, A. K., MCMILLAN, N. A. J. & THURECHT, K. J. 2014. Polymeric siRNA Delivery Vectors: Knocking Down Cancers with Polymeric-Based Gene Delivery Systems. *Journal of Chemical Technology & Biotechnology*, n/a-n/a.

ARIGA, K., HILL, J. P. & JI, Q. 2007. Layer-by-Layer Assembly as a Versatile Bottom-up Nanofabrication Technique for Exploratory Research and Realistic Application. *Physical Chemistry Chemical Physics,* 9**,** 2319-2340.

ASEFA, T. & TAO, Z. 2012. Biocompatibility of Mesoporous Silica Nanoparticles. *Chemical Research in Toxicology,* 25**,** 2265-2284.

ATCC. *Culture Method of Rh30 (Crl-2061) and Rd (Atcc® Ccl-136™)* [Online]. Available: http://www.lgcstandards-atcc.org/Products/All/CRL-2061.aspx#culturemethod; http://www.lgcstandards-atcc.org/products/all/CCL-136.aspx?geo_country=gb#culturemethod.

AUFFAN, M., ROSE, J., BOTTERO, J.-Y., LOWRY, G. V., JOLIVET, J.-P. & WIESNER, M. R. 2009. Towards a Definition of Inorganic Nanoparticles from an Environmental, Health and Safety Perspective. *Nat Nano,* 4**,** 634-641.

BAE, Y. S., OH, H., RHEE, S. G. & YOO, Y. D. 2011. Regulation of Reactive Oxygen Species Generation in Cell Signaling. *Mol Cells,* 32**,** 491-509.

BANGHAM, A. D., STANDISH, M. M. & WATKINS, J. C. 1965. Diffusion of Univalent Ions across the Lamellae of Swollen Phospholipids. *Journal of Molecular Biology,* 13**,** 238-IN27.

BARRETT, E. P., JOYNER, L. G. & HALENDA, P. P. 1951. The Determination of Pore Volume and Area Distributions in Porous Substances. I. Computations from Nitrogen Isotherms. *Journal of the American Chemical Society,* 73**,** 373-380.

BARTHEL, A., SCHMOLL, D. & UNTERMAN, T. G. 2005. Foxo Proteins in Insulin Action and Metabolism. *Trends Endocrinol Metab,* 16**,** 183-9.

BERNARD, B. K., OSHEROFF, M. R., HOFMANN, A. & MENNEAR, J. H. 1990. Toxicology and Carcinogenesis Studies of Dietary Titanium Dioxide-Coated Mica in Male and Female Fischer 344 Rats. *Journal of Toxicology and Environmental Health,* 29**,** 417-429.

BERX, G. & VAN ROY, F. 2009. Involvement of Members of the Cadherin Superfamily in Cancer. *Cold Spring Harb Perspect Biol,* 1**,** a003129.

BHATTACHARYA, R. & MUKHERJEE, P. 2008. Biological Properties of "Naked" Metal Nanoparticles. *Advanced Drug Delivery Reviews,* 60**,** 1289-1306.

BISWAS, S., DESHPANDE, P. P., NAVARRO, G., DODWADKAR, N. S. & TORCHILIN, V. P. 2013. Lipid Modified Triblock Pamam-Based Nanocarriers for siRNA Drug Co-Delivery. *Biomaterials,* 34**,** 1289-1301.

BISWAS, S. & TORCHILIN, V. P. 2013. Dendrimers for siRNA Delivery. *Pharmaceuticals,* 6**,** 161-183.

BOOTHBY, L. A., DOERING, P. L. & KIPERSZTOK, S. 2004. Bioidentical Hormone Therapy: A Review. *Menopause,* 11**,** 356-67.

BOUSSIF, O., LEZOUALC'H, F., ZANTA, M. A., MERGNY, M. D., SCHERMAN, D., DEMENEIX, B. & BEHR, J. P. 1995. A Versatile Vector for Gene and Oligonucleotide Transfer into Cells in Culture and in Vivo: Polyethylenimine. *Proceedings of the National Academy of Sciences,* 92**,** 7297-7301.

BRAASCH, D. A., JENSEN, S., LIU, Y., KAUR, K., ARAR, K., WHITE, M. A. & COREY, D. R. 2003. RNA Interference in Mammalian Cells by Chemically-Modified RNA. *Biochemistry,* 42**,** 7967-75.

BRADBURY, M. S., PHILLIPS, E., MONTERO, P. H., CHEAL, S. M., STAMBUK, H., DURACK, J. C., SOFOCLEOUS, C. T., MEESTER, R. J. C., WIESNER, U. & PATEL, S. 2013. Clinically-Translated Silica Nanoparticles as Dual-Modality Cancer-Targeted Probes for Image-Guided Surgery and Interventions. *Integrative Biology,* 5**,** 74-86.

BROWN, H. A. 2007. *Lipidomics and Bioactive Lipids: Lipids and Cell Signaling: Lipids and Cell Signaling*, Elsevier Science.
BRUNAUER, S., EMMETT, P. H. & TELLER, E. 1938. Adsorption of Gases in Multimolecular Layers. *Journal of the American Chemical Society,* 60**,** 309-319.
BÜCHEL, G., UNGER, K. K., MATSUMOTO, A. & TSUTSUMI, K. 1998. A Novel Pathway for Synthesis of Submicrometer-Size Solid Core/Mesoporous Shell Silica Spheres. *Advanced Materials,* 10**,** 1036-1038.
BUCKNALL, D. G. 2012. Functional Supramolecular Architectures: For Organic Electronics and Nanotechnology, 2 Volume Set, Edited by P. Samorì and F. Cacialli. *Contemporary Physics,* 53**,** 281-282.
BUYENS, K., DE SMEDT, S. C., BRAECKMANS, K., DEMEESTER, J., PEETERS, L., VAN GRUNSVEN, L. A., DE MOLLERAT DU JEU, X., SAWANT, R., TORCHILIN, V., FARKASOVA, K., OGRIS, M. & SANDERS, N. N. 2012. Liposome Based Systems for Systemic siRNA Delivery: Stability in Blood Sets the Requirements for Optimal Carrier Design. *J Control Release,* 158**,** 362-70.
BUZEA, C., PACHECO, I. I. & ROBBIE, K. 2007. Nanomaterials and Nanoparticles: Sources and Toxicity. *Biointerphases,* 2.
ÇAĞDAŞ, M., SEZER, A. D. & BUCAK, S. 2014. *Liposomes as Potential Drug Carrier Systems for Drug Delivery*.
CAMPOS, S. M. & GHOSH, S. 2010. A Current Review of Targeted Therapeutics for Ovarian Cancer. *Journal of Oncology,* 2010.
CANCER RESEARCH UK. 2013. *Cancer Statistics for the Uk* [Online]. Available: http://www.cancerresearchuk.org/health-professional/cancer-statistics.
CANCER RESEARCH UK. 2014. *How Cancer Can Spread* [Online]. Available: http://www.cancerresearchuk.org/about-cancer/what-is-cancer/how-cancer-can-spread.
CARDONE, M. H., ROY, N., STENNICKE, H. R., SALVESEN, G. S., FRANKE, T. F., STANBRIDGE, E., FRISCH, S. & REED, J. C. 1998. Regulation of Cell Death Protease Caspase-9 by Phosphorylation. *Science,* 282**,** 1318-1321.
CHAHINE, N. O., COLLETTE, N. M., THOMAS, C. B., GENETOS, D. C. & LOOTS, G. G. 2014. Nanocomposite Scaffold for Chondrocyte Growth and Cartilage Tissue Engineering: Effects of Carbon Nanotube Surface Functionalization. *Tissue Engineering Part A,* 20**,** 2305-2315.
CHALHOUB, N. & BAKER, S. J. 2009. Pten and the Pi3-Kinase Pathway in Cancer. *Annu Rev Pathol,* 4**,** 127-50.
CHEN, C.-K., LAW, W.-C., AALINKEEL, R., YU, Y., NAIR, B., WU, J., MAHAJAN, S., REYNOLDS, J. L., LI, Y., LAI, C. K., TZANAKAKIS, E. S., SCHWARTZ, S. A., PRASAD, P. N. & CHENG, C. 2014. Biodegradable Cationic Polymeric Nanocapsules for Overcoming Multidrug Resistance and Enabling Drug-Gene Co-Delivery to Cancer Cells. *Nanoscale,* 6**,** 1567-1572.
CHEN, H., ZHEN, Z., TANG, W., TODD, T., CHUANG, Y.-J., WANG, L., PAN, Z. & XIE, J. 2013. Label-Free Luminescent Mesoporous Silica Nanoparticles for Imaging and Drug Delivery. *Theranostics,* 3**,** 650-657.
CHEN, M. Y., HOFFER, A., MORRISON, P. F., HAMILTON, J. F., HUGHES, J., SCHLAGETER, K. S., LEE, J., KELLY, B. R. & OLDFIELD, E. H. 2005. Surface Properties, More Than Size, Limiting Convective Distribution of Virus-Sized Particles and Viruses in the Central Nervous System. *Journal of Neurosurgery,* 103**,** 311-319.
CHENG-YU, A., BANG-SHANG, Z. & LU, Q.-H. Cytotoxicity of Polystyrene Nanospheres Internalization in Mouse Fibroblast Cells. Nanoelectronics Conference, 2008. INEC 2008. 2nd IEEE International, 24-27 March 2008 2008. 1087-1092.
CHENG, K. & MAHATO, R. I. 2013. *Advanced Delivery and Therapeutic Applications of Rnai*, Wiley.
CHENG, N., CHYTIL, A., SHYR, Y., JOLY, A. & MOSES, H. L. 2008a. Transforming Growth Factor-Beta Signaling-Deficient Fibroblasts Enhance Hepatocyte Growth Factor Signaling in

Mammary Carcinoma Cells to Promote Scattering and Invasion. *Mol Cancer Res,* 6**,** 1521-33.

CHENG, Y.-J., LUO, G.-F., ZHU, J.-Y., XU, X.-D., ZENG, X., CHENG, D.-B., LI, Y.-M., WU, Y., ZHANG, X.-Z., ZHUO, R.-X. & HE, F. 2015. Enzyme-Induced and Tumor-Targeted Drug Delivery System Based on Multifunctional Mesoporous Silica Nanoparticles. *ACS Applied Materials & Interfaces,* 7**,** 9078-9087.

CHENG, Y., WU, Q., LI, Y. & XU, T. 2008b. External Electrostatic Interaction Versus Internal Encapsulation between Cationic Dendrimers and Negatively Charged Drugs: Which Contributes More to Solubility Enhancement of the Drugs? *The Journal of Physical Chemistry B,* 112**,** 8884-8890.

CHITHRANI, B. D., GHAZANI, A. A. & CHAN, W. C. W. 2006. Determining the Size and Shape Dependence of Gold Nanoparticle Uptake into Mammalian Cells. *Nano Letters,* 6**,** 662-668.

CHO, E.-B., VOLKOV, D. O. & SOKOLOV, I. 2010. Ultrabright Fluorescent Mesoporous Silica Nanoparticles. *Small,* 6**,** 2314-2319.

CHO, K., WANG, X., NIE, S., CHEN, Z. & SHIN, D. M. 2008. Therapeutic Nanoparticles for Drug Delivery in Cancer. *Clinical Cancer Research,* 14**,** 1310-1316.

CHU, Z., HUANG, Y., TAO, Q. & LI, Q. 2011. Cellular Uptake, Evolution, and Excretion of Silica Nanoparticles in Human Cells. *Nanoscale,* 3**,** 3291-3299.

CHUNG, T.-H., WU, S.-H., YAO, M., LU, C.-W., LIN, Y.-S., HUNG, Y., MOU, C.-Y., CHEN, Y.-C. & HUANG, D.-M. 2007. The Effect of Surface Charge on the Uptake and Biological Function of Mesoporous Silica Nanoparticles in 3t3-L1 Cells and Human Mesenchymal Stem Cells. *Biomaterials,* 28**,** 2959-2966.

CLINE, G. W., JUCKER, B. M., TRAJANOSKI, Z., RENNINGS, A. J. M. & SHULMAN, G. I. 1998. *A Novel 13c Nmr Method to Assess Intracellular Glucose Concentration in Muscle, in Vivo*.

COLILLA, M., GONZÁLEZ, B. & VALLET-REGÍ, M. 2013. Mesoporous Silicananoparticles for the Design of Smart Delivery Nanodevices. *Biomater. Sci.,* 1**,** 114-134.

CONDE, J., AMBROSONE, A., HERNANDEZ, Y., TIAN, F., MCCULLY, M., BERRY, C. C., BAPTISTA, P. V., TORTIGLIONE, C. & DE LA FUENTE, J. M. 2015. 15 Years on siRNA Delivery: Beyond the State-of-the-Art on Inorganic Nanoparticles for Rnai Therapeutics. *Nano Today*.

COURTNAY, R., NGO, D. C., MALIK, N., VERVERIS, K., TORTORELLA, S. M. & KARAGIANNIS, T. C. 2015. Cancer Metabolism and the Warburg Effect: The Role of Hif-1 and PI3K. *Mol Biol Rep,* 42**,** 841-51.

COURTNEY, K. D., CORCORAN, R. B. & ENGELMAN, J. A. 2010. The PI3K Pathway as Drug Target in Human Cancer. *J Clin Oncol,* 28**,** 1075-83.

CRISCI, E., BÁRCENA, J. & MONTOYA, M. 2013. Virus-Like Particle-Based Vaccines for Animal Viral Infections. *Inmunología,* 32**,** 102-116.

CROISSANT, J. G., QI, C., MONGIN, O., HUGUES, V., BLANCHARD-DESCE, M., RAEHM, L., CATTOEN, X., WONG CHI MAN, M., MAYNADIER, M., GARY-BOBO, M., GARCIA, M., ZINK, J. I. & DURAND, J.-O. 2015. Disulfide-Gated Mesoporous Silica Nanoparticles Designed for Two-Photon-Triggered Drug Release and Imaging. *Journal of Materials Chemistry B,* 3**,** 6456-6461.

CROSS, D. & BURMESTER, J. K. 2006. Gene Therapy for Cancer Treatment: Past, Present and Future. *Clinical Medicine and Research,* 4**,** 218-227.

DATTA, S. R., DUDEK, H., TAO, X., MASTERS, S., FU, H., GOTOH, Y. & GREENBERG, M. E. 1997. Akt Phosphorylation of Bad Couples Survival Signals to the Cell-Intrinsic Death Machinery. *Cell,* 91**,** 231-41.

DAVIS, M. E. 2002. Ordered Porous Materials for Emerging Applications. *Nature,* 417**,** 813-821.

DAVIS, M. E., CHEN, Z. & SHIN, D. M. 2008. Nanoparticle Therapeutics: An Emerging Treatment Modality for Cancer. *Nat Rev Drug Discov,* 7**,** 771-782.

DE JONG, W. H. & BORM, P. J. A. 2008. Drug Delivery and Nanoparticles: Applications and Hazards. *International Journal of Nanomedicine,* 3**,** 133-149.
DE VILLIERS, M. M., ARAMWIT, P. & KWON, G. S. 2008. *Nanotechnology in Drug Delivery*, Springer New York.
DEAN, M., FOJO, T. & BATES, S. 2005. Tumour Stem Cells and Drug Resistance. *Nat Rev Cancer,* 5**,** 275-284.
DEGEN, A. & KOSEC, M. 2000. Effect of Ph and Impurities on the Surface Charge of Zinc Oxide in Aqueous Solution. *Journal of the European Ceramic Society,* 20**,** 667-673.
DETZER, A., OVERHOFF, M., WÜNSCHE, W., ROMPF, M., TURNER, J. J., IVANOVA, G. D., GAIT, M. J. & SCZAKIEL, G. 2009. Increased Rnai Is Related to Intracellular Release of siRNA Via a Covalently Attached Signal Peptide. *RNA,* 15**,** 627-636.
DEVANAND VENKATASUBBU, G., RAMASAMY, S., RAMAKRISHNAN, V. & KUMAR, J. 2013. Folate Targeted Pegylated Titanium Dioxide Nanoparticles as a Nanocarrier for Targeted Paclitaxel Drug Delivery. *Advanced Powder Technology,* 24**,** 947-954.
DI RENZO, F., CAMBON, H. & DUTARTRE, R. 1997. A 28-Year-Old Synthesis of Micelle-Templated Mesoporous Silica. *Microporous Materials,* 10**,** 283-286.
DOMB, A. J. & KHAN, W. 2014. *Focal Controlled Drug Delivery*, Springer US.
EDWARDS, D. A., PRAUSNITZ, M. R., LANGER, R. & WEAVER, J. C. 1995. Analysis of Enhanced Transdermal Transport by Skin Electroporation. *Journal of Controlled Release,* 34**,** 211-221.
ENGELMAN, J. A., LUO, J. & CANTLEY, L. C. 2006. The Evolution of Phosphatidylinositol 3-Kinases as Regulators of Growth and Metabolism. *Nat Rev Genet,* 7**,** 606-619.
ESFAND, R. & TOMALIA, D. A. 2001. Poly(Amidoamine) (Pamam) Dendrimers: From Biomimicry to Drug Delivery and Biomedical Applications. *Drug Discovery Today,* 6**,** 427-436.
FAN, Y. & ZHANG, Q. 2013. Development of Liposomal Formulations: From Concept to Clinical Investigations. *Asian Journal of Pharmaceutical Sciences,* 8**,** 81-87.
FANG, J., NAKAMURA, H. & MAEDA, H. 2011. The Epr Effect: Unique Features of Tumor Blood Vessels for Drug Delivery, Factors Involved, and Limitations and Augmentation of the Effect. *Advanced Drug Delivery Reviews,* 63**,** 136-151.
FENG, Q., YU, M.-Z., WANG, J.-C., HOU, W.-J., GAO, L.-Y., MA, X.-F., PEI, X.-W., NIU, Y.-J., LIU, X.-Y., QIU, C., PANG, W.-H., DU, L.-L. & ZHANG, Q. 2014. Synergistic Inhibition of Breast Cancer by Co-Delivery of Vegf siRNA and Paclitaxel Via Vapreotide-Modified Core–Shell Nanoparticles. *Biomaterials,* 35**,** 5028-5038.
FOLKMAN, J. 1995. Angiogenesis in Cancer, Vascular, Rheumatoid and Other Disease. *Nature Medicine,* 1**,** 27-31.
FOLKMAN, J., BACH, M., ROWE, J. W., DAVIDOFF, F., LAMBERT, P., HIRSCH, C., GOLDBERG, A., HIATT, H. H., GLASS, J. & HENSHAW, E. 1971. Tumor Angiogenesis - Therapeutic Implications. *New England Journal of Medicine,* 285**,** 1182-&.
FRANCI, G., FALANGA, A., GALDIERO, S., PALOMBA, L., RAI, M., MORELLI, G. & GALDIERO, M. 2015. Silver Nanoparticles as Potential Antibacterial Agents. *Molecules,* 20**,** 8856-74.
FU, Y. & KAO, W. J. 2011. Drug Release Kinetics and Transport Mechanisms of Non-Degradable and Degradable Polymeric Delivery Systems. *Expert opinion on drug delivery,* 7**,** 429-444.
FYRBERG, A. & LOTFI, K. 2010. Optimization and Evaluation of Electroporation Delivery of siRNA in the Human Leukemic Cem Cell Line. *Cytotechnology,* 62**,** 497-507.
GABIZON, A. & PAPAHADJOPOULOS, D. 1988. Liposome Formulations with Prolonged Circulation Time in Blood and Enhanced Uptake by Tumors. *Proceedings of the National Academy of Sciences of the United States of America,* 85**,** 6949-6953.
GARLICH, J. R., DE, P., DEY, N., SU, J. D., PENG, X., MILLER, A., MURALI, R., LU, Y., MILLS, G. B., KUNDRA, V., SHU, H.-K., PENG, Q. & DURDEN, D. L. 2008. A Vascular Targeted Pan Phos-

phoinositide 3-Kinase Inhibitor Prodrug, Sf1126, with Antitumor and Antiangiogenic Activity. *Cancer Research,* 68**,** 206-215.

GARY-BOBO, M., BREVET, D., BENKIRANE-JESSEL, N., RAEHM, L., MAILLARD, P., GARCIA, M. & DURAND, J.-O. 2012. Hyaluronic Acid-Functionalized Mesoporous Silica Nanoparticles for Efficient Photodynamic Therapy of Cancer Cells. *Photodiagnosis and Photodynamic Therapy,* 9**,** 256-260.

GAUMET, M., VARGAS, A., GURNY, R. & DELIE, F. 2008. Nanoparticles for Drug Delivery: The Need for Precision in Reporting Particle Size Parameters. *European Journal of Pharmaceutics and Biopharmaceutics,* 69**,** 1-9.

GHARBI, SEVERINE I., ZVELEBIL, MARKETA J., SHUTTLEWORTH, STEPHEN J., HANCOX, T., SAGHIR, N., TIMMS, JOHN F. & WATERFIELD, MICHAEL D. 2007. Exploring the Specificity of the PI3K Family Inhibitor LY294002. *Biochemical Journal,* 404**,** 15-21.

GIULIETTI, A., OVERBERGH, L., VALCKX, D., DECALLONNE, B., BOUILLON, R. & MATHIEU, C. 2001. An Overview of Real-Time Quantitative Pcr: Applications to Quantify Cytokine Gene Expression. *Methods,* 25**,** 386-401.

GLORIEUX, C., AUQUIER, J., DEJEANS, N., SID, B., DEMOULIN, J. B., BERTRAND, L., VERRAX, J. & CALDERON, P. B. 2014. Catalase Expression in Mcf-7 Breast Cancer Cells Is Mainly Controlled by PI3K/Akt/Mtor Signaling Pathway. *Biochem Pharmacol,* 89**,** 217-23.

GOLDBERG, I. 2013. *Cell Motility Factors*, Birkhäuser Basel.

GONZALEZ, G., SAGARZAZU, A. & ZOLTAN, T. 2013. Infuence of Microstructure in Drug Release Behavior of Silica Nanocapsules. *Journal of Drug Delivery,* 2013**,** 8.

GOTTLIEB, T. M., LEAL, J. F., SEGER, R., TAYA, Y. & OREN, M. 2002. Cross-Talk between Akt, P53 and Mdm2: Possible Implications for the Regulation of Apoptosis. *Oncogene,* 21**,** 1299-303.

GUO, D., WU, C., JIANG, H., LI, Q., WANG, X. & CHEN, B. 2008. Synergistic Cytotoxic Effect of Different Sized Zno Nanoparticles and Daunorubicin against Leukemia Cancer Cells under Uv Irradiation. *J Photochem Photobiol B,* 93**,** 119-26.

GUPTA, A. K. & GUPTA, M. 2005a. Cytotoxicity Suppression and Cellular Uptake Enhancement of Surface Modified Magnetic Nanoparticles. *Biomaterials,* 26**,** 1565-1573.

GUPTA, A. K. & GUPTA, M. 2005b. Synthesis and Surface Engineering of Iron Oxide Nanoparticles for Biomedical Applications. *Biomaterials,* 26**,** 3995-4021.

GUPTA, S. C., HEVIA, D., PATCHVA, S., PARK, B., KOH, W. & AGGARWAL, B. B. 2011. Upsides and Downsides of Reactive Oxygen Species for Cancer: The Roles of Reactive Oxygen Species in Tumorigenesis, Prevention, and Therapy. *Antioxidants & Redox Signaling,* 16**,** 1295-1322.

GUPTA, U., AGASHE, H. B. & JAIN, N. K. 2007. Polypropylene Imine Dendrimer Mediated Solubility Enhancement: Effect of Ph and Functional Groups of Hydrophobes. *Journal of Pharmacy and Pharmaceutical Sciences,* 10**,** 358-367.

HAMPTON, M. B. & ORRENIUS, S. 1997. Dual Regulation of Caspase Activity by Hydrogen Peroxide: Implications for Apoptosis. *FEBS Letters,* 414**,** 552-556.

HAN, M. & GAO, J.-Q. 2013. Nanotherapeutics in Multidrug Resistance. *In:* BAE, Y. H., MRSNY, R. J. & PARK, K. (eds.) *Cancer Targeted Drug Delivery: An Elusive Dream.* Springer.

HANAHAN, D. & WEINBERG, R. A. 2000. The Hallmarks of Cancer. *Cell,* 100**,** 57-70.

HARTONO, S. B., PHUOC, N. T., YU, M., JIA, Z., MONTEIRO, M. J., QIAO, S. & YU, C. 2014. Functionalized Large Pore Mesoporous Silica Nanoparticles for Gene Delivery Featuring Controlled Release and Co-Delivery. *Journal of Materials Chemistry B,* 2**,** 718-726.

HE, C., HU, Y., YIN, L., TANG, C. & YIN, C. 2010. Effects of Particle Size and Surface Charge on Cellular Uptake and Biodistribution of Polymeric Nanoparticles. *Biomaterials,* 31**,** 3657-3666.

HE, H., PHAM-HUY, L. A., DRAMOU, P., XIAO, D., ZUO, P. & PHAM-HUY, C. 2013. Carbon Nanotubes: Applications in Pharmacy and Medicine. *BioMed Research International,* 2013**,** 12.

HE, Q. & SHI, J. 2011. Mesoporous Silica Nanoparticle Based Nano Drug Delivery Systems: Synthesis, Controlled Drug Release and Delivery, Pharmacokinetics and Biocompatibility. *Journal of Materials Chemistry,* 21**,** 5845-5855.

HENNESSY, B. T., SMITH, D. L., RAM, P. T., LU, Y. & MILLS, G. B. 2005. Exploiting the PI3K/Akt Pathway for Cancer Drug Discovery. *Nat Rev Drug Discov,* 4**,** 988-1004.

HICKERSON, R. P., VLASSOV, A. V., WANG, Q., LEAKE, D., ILVES, H., GONZALEZ-GONZALEZ, E., CONTAG, C. H., JOHNSTON, B. H. & KASPAR, R. L. 2008. Stability Study of Unmodified siRNA and Relevance to Clinical Use. *Oligonucleotides,* 18**,** 345-354.

HOM, C., LU, J., LIONG, M., LUO, H., LI, Z., ZINK, J. I. & TAMANOI, F. 2010. Mesoporous Silica Nanoparticles Facilitate Delivery of siRNA to Shutdown Signaling Pathways in Mammalian Cells. *Small,* 6**,** 1185-1190.

HONARY, S. & ZAHIR, F. 2013. Effect of Zeta Potential on the Properties of Nano-Drug Delivery Systems - a Review (Part 1). *Tropical Journal of Pharmaceutical Research,* 12.

HSIANG, Y. H., HERTZBERG, R., HECHT, S. & LIU, L. F. 1985. Camptothecin Induces Protein-Linked DNA Breaks Via Mammalian DNA Topoisomerase-I. *Journal of Biological Chemistry,* 260**,** 4873-4878.

HU, L. M., ZALOUDEK, C., MILLS, G. B., GRAY, J. & JAFFE, R. B. 2000. In Vivo and in Vitro Ovarian Carcinoma Growth Inhibition by a Phosphatidylinositol 3-Kinase Inhibitor (LY294002). *Clinical Cancer Research,* 6**,** 880-886.

HUANG, X., P, N. & E, H. 2014. Characterization and Comparison of Mesoporous Silica Particles for Optimized Drug Delivery. *Nanomaterials and Nanotechnology***,** 1.

HUANG, X., TENG, X., CHEN, D., TANG, F. & HE, J. 2010. The Effect of the Shape of Mesoporous Silica Nanoparticles on Cellular Uptake and Cell Function. *Biomaterials,* 31**,** 438-48.

HUCKRIEDE, A., BUNGENER, L., TER VEER, W., HOLTROP, M., DAEMEN, T., PALACHE, A. M. & WILSCHUT, J. 2003. Influenza Virosomes: Combining Optimal Presentation of Hemagglutinin with Immunopotentiating Activity. *Vaccine,* 21**,** 925-31.

HUDSON, S. P., PADERA, R. F., LANGER, R. & KOHANE, D. S. 2008. The Biocompatibility of Mesoporous Silicates. *Biomaterials,* 29**,** 4045-55.

HUNTER, A. C. 2006. Molecular Hurdles in Polyfectin Design and Mechanistic Background to Polycation Induced Cytotoxicity. *Advanced Drug Delivery Reviews,* 58**,** 1523-1531.

IDE, M., WALLAERT, E., VAN DRIESSCHE, I., LYNEN, F., SANDRA, P. & VAN DER VOORT, P. 2011. Spherical Mesoporous Silica Particles by Spray Drying: Doubling the Retention Factor of Hplc Columns. *Microporous and Mesoporous Materials,* 142**,** 282-291.

ILER, R. K. 1979. *The Chemistry of Silica: Solubility, Polymerization, Colloid and Surface Properties and Biochemistry of Silica,* New York, Wiley-Interscience.

IRANI, K., XIA, Y., ZWEIER, J. L., SOLLOTT, S. J., DER, C. J., FEARON, E. R., SUNDARESAN, M., FINKEL, T. & GOLDSCHMIDT-CLERMONT, P. J. 1997. Mitogenic Signaling Mediated by Oxidants in Ras-Transformed Fibroblasts. *Science,* 275**,** 1649-1652.

IYER, A. K., KHALED, G., FANG, J. & MAEDA, H. 2006. Exploiting the Enhanced Permeability and Retention Effect for Tumor Targeting. *Drug Discovery Today,* 11**,** 812-818.

JACKSON, S. P. & BARTEK, J. 2009. The DNA-Damage Response in Human Biology and Disease. *Nature,* 461**,** 1071-8.

JAIN, S. 2012. Development of an Antibody Functionalized Carbon Nanotube Biosensor for Foodborne Bacterial Pathogens. *Journal of Biosensors & Bioelectronics,* 01.

JANG, W.-D., YIM, D. & HWANG, I.-H. 2014. Photofunctional Hollow Nanocapsules for Biomedical Applications. *Journal of Materials Chemistry B,* 2**,** 2202.

JEMAL, A., SIEGEL, R., WARD, E., HAO, Y. P., XU, J. Q., MURRAY, T. & THUN, M. J. 2008. Cancer Statistics, 2008. *Ca-a Cancer Journal for Clinicians,* 58**,** 71-96.

JIA, L., SHEN, J., LI, Z., ZHANG, D., ZHANG, Q., LIU, G., ZHENG, D. & TIAN, X. 2013. In Vitro and in Vivo Evaluation of Paclitaxel-Loaded Mesoporous Silica Nanoparticles with Three Pore Sizes. *Int J Pharm,* 445**,** 12-9.

JIAN-TAO, L., CHAO, W., YI, Z. & GUAN-HAI, W. 2014. Mesoporous Silica Nanoparticles with Controlled Loading of Cationic Dendrimer for Gene Delivery. *Materials Research Express,* 1**,** 035403.

JIANG, B. H., JIANG, G. Q., ZHENG, J. Z., LU, Z. M., HUNTER, T. & VOGT, P. K. 2001. Phosphatidylinositol 3-Kinase Signaling Controls Levels of Hypoxia-Inducible Factor. *Cell Growth & Differentiation,* 12**,** 363-369.

JIANG, T., MO, R., BELLOTTI, A., ZHOU, J. & GU, Z. 2014. Drug Delivery: Gel–Liposome-Mediated Co-Delivery of Anticancer Membrane-Associated Proteins and Small-Molecule Drugs for Enhanced Therapeutic Efficacy (Adv. Funct. Mater. 16/2014). *Advanced Functional Materials,* 24**,** 2258-2258.

JONES, R. G. & THOMPSON, C. B. 2009. Tumor Suppressors and Cell Metabolism: A Recipe for Cancer Growth. *Genes Dev,* 23**,** 537-48.

JONES, S. M., KLINGHOFFER, R., PRESTWICH, G. D., TOKER, A. & KAZLAUSKAS, A. 1999. Pdgf Induces an Early and a Late Wave of Pi 3-Kinase Activity, and Only the Late Wave Is Required for Progression through G1. *Current Biology,* 9**,** 512-521.

KALRA, N., DHANYA, V., SAINI, V. & JEYABALAN, G. 2013. Virosomes: As a Drug Delivery Carrier. *American Journal of Advanced Drug Delivery,* 1**,** 29-35.

KAMALHA, E., SHI, X., MWASIAGI, J. & ZENG, Y. 2012. Nanotechnology and Carbon Nanotubes; a Review of Potential in Drug Delivery. *Macromolecular Research,* 20**,** 891-898.

KANWAR, S. S., POOLLA, A. & MAJUMDAR, A. P. N. 2012. Regulation of Colon Cancer Recurrence and Development of Therapeutic Strategies. *World Journal of Gastrointestinal Pathophysiology,* 3**,** 1-9.

KAPITEIJN, E., MARIJNEN, C. A. M., NAGTEGAAL, I. D., PUTTER, H., STEUP, W. H., WIGGERS, T., RUTTEN, H. J. T., PAHLMAN, L., GLIMELIUS, B., VAN KRIEKEN, J., LEER, J. W. H., VAN DE VELDE, C. J. H. & DUTCH COLORECTAL CANC, G. 2001. Preoperative Radiotherapy Combined with Total Mesorectal Excision for Resectable Rectal Cancer. *New England Journal of Medicine,* 345**,** 638-646.

KAPSE-MISTRY, S., GOVENDER, T., SRIVASTAVA, R. & YERGERI, M. 2014. Nanodrug Delivery in Reversing Multidrug Resistance in Cancer Cells. *Frontiers in Pharmacology,* 5.

KARADAG, M., GEYIK, C., DEMIRKOL, D. O., ERTAS, F. N. & TIMUR, S. 2013. Modified Gold Surfaces by 6-(Ferrocenyl)Hexanethiol/Dendrimer/Gold Nanoparticles as a Platform for the Mediated Biosensing Applications. *Materials Science and Engineering C,* 33**,** 634-640.

KATOH, H., HIRAMOTO, K. & NEGISHI, M. 2006. Activation of Rac1 by Rhog Regulates Cell Migration. *Journal of Cell Science,* 119**,** 56-65.

KESHARWANI, P., JAIN, K. & JAIN, N. K. 2014. Dendrimer as Nanocarrier for Drug Delivery. *Progress in Polymer Science,* 39**,** 268-307.

KILIC-EREN, M., BOYLU, T. & TABOR, V. 2013. Targeting PI3K/Akt Represses Hypoxia Inducible Factor-1alpha Activation and Sensitizes Rhabdomyosarcoma and Ewing's Sarcoma Cells for Apoptosis. *Cancer Cell Int,* 13**,** 36.

KIM, D. H. & ROSSI, J. J. 2007. Strategies for Silencing Human Disease Using RNA Interference. *Nat Rev Genet,* 8**,** 173-184.

KIM, J.-Y., OH, M. H., BERNARD, L. P., MACARA, I. G. & ZHANG, H. 2011. The Rhog/Elmo1/Dock180 Signaling Module Is Required for Spine Morphogenesis in Hippocampal Neurons. *Journal of Biological Chemistry,* 286**,** 37615-37624.

KIM, T. H., KIM, M., ELTOHAMY, M., YUN, Y. R., JANG, J. H. & KIM, H. W. 2013. Efficacy of Mesoporous Silica Nanoparticles in Delivering Bmp-2 Plasmid DNA for in Vitro Osteogenic Stimulation of Mesenchymal Stem Cells. *J Biomed Mater Res A,* 101**,** 1651-60.

KITCHENS, K. M., EL-SAYED, M. E. H. & GHANDEHARI, H. 2005. Transepithelial and Endothelial Transport of Poly (Amidoamine) Dendrimers. *Advanced Drug Delivery Reviews,* 57**,** 2163-2176.

KOGANTI, S., JAGANI, H. V., PALANIMUTHU, V. R., MATHEW, J. A., RAO, M. C. & RAO, J. V. 2013. In Vitro and in Vivo Evaluation of the Efficacy of Nanoformulation of siRNA as an Adjuvant to Improve the Anticancer Potential of Cisplatin. *Experimental and Molecular Pathology,* 94**,** 137-147.

KONG, F., ZHANG, X., ZHANG, H., QU, X., CHEN, D., SERVOS, M., MÄKILÄ, E., SALONEN, J., SANTOS, H. A., HAI, M. & WEITZ, D. A. 2015. Inhibition of Multidrug Resistance of Cancer Cells by Co-Delivery of DNA Nanostructures and Drugs Using Porous Silicon Nanoparticles@Giant Liposomes. *Advanced Functional Materials,* 25**,** 3330-3340.

KOPPENOL, W. H., BOUNDS, P. L. & DANG, C. V. 2011. Otto Warburg's Contributions to Current Concepts of Cancer Metabolism. *Nat Rev Cancer,* 11**,** 325-37.

KOSMULSKI, M. 2004. Ph-Dependent Surface Charging and Points of Zero Charge Ii. Update. *Journal of Colloid and Interface Science,* 275**,** 214-224.

KOTEN, J. W., NEIJT, J. P., ZONNENBERG, B. A. & DEN OTTER, W. 1993. The Difference between Benign and Malignant Tumours Explained with the 4-Mutation Paradigm for Carcinogenesis. *Anticancer Res,* 13**,** 1179-82.

KUBOTA, Y., SHUIN, T., KAWASAKI, C., HOSAKA, M., KITAMURA, H., CAI, R., SAKAI, H., HASHIMOTO, K. & FUJISHIMA, A. 1994. Photokilling of T-24 Human Bladder Cancer Cells with Titanium Dioxide. *British Journal of Cancer,* 70**,** 1107-1111.

KULKARNI, S. A. & FENG, S. S. 2013. Effects of Particle Size and Surface Modification on Cellular Uptake and Biodistribution of Polymeric Nanoparticles for Drug Delivery. *Pharm Res,* 30**,** 2512-22.

KWON, S., SINGH, R. K., PEREZ, R. A., ABOU NEEL, E. A., KIM, H. W. & CHRZANOWSKI, W. 2013. Silica-Based Mesoporous Nanoparticles for Controlled Drug Delivery. *J Tissue Eng,* 4**,** 2041731413503357.

LAING, P., BACON, A., MCCORMACK, B., GREGORIADIS, G., FRISCH, B. & SCHUBER, F. 2006. The 'Co-Delivery' Approach to Liposomal Vaccines: Application to the Development of Influenza-a and Hepatitis-B Vaccine Candidates. *J Liposome Res,* 16**,** 229-35.

LAPPALAINEN, K., JAASKELAINEN, I., SYRJANEN, K., URTTI, A. & SYRJANEN, S. 1994. Comparison of Cell-Proliferation and Toxicity Assays Using 2 Cationic Liposomes. *Pharmaceutical Research,* 11**,** 1127-1131.

LEE, A. L. Z., DHILLON, S. H. K., WANG, Y., PERVAIZ, S., FAN, W. & YANG, Y. Y. 2011a. Synergistic Anti-Cancer Effects Via Co-Delivery of Tnf-Related Apoptosis-Inducing Ligand (Trail/Apo2l) and Doxorubicin Using Micellar Nanoparticles. *Molecular BioSystems,* 7**,** 1512-1522.

LEE, C. C., MACKAY, J. A., FRECHET, J. M. J. & SZOKA, F. C. 2005. Designing Dendrimers for Biological Applications. *Nat Biotech,* 23**,** 1517-1526.

LEE, J. E., LEE, D. J., LEE, N., KIM, B. H., CHOI, S. H. & HYEON, T. 2011b. Multifunctional Mesoporous Silica Nanocomposite Nanoparticles for Ph Controlled Drug Release and Dual Modal Imaging. *Journal of Materials Chemistry,* 21**,** 16869-16872.

LEE, J. S., GREEN, J. J., LOVE, K. T., SUNSHINE, J., LANGER, R. & ANDERSON, D. G. 2009. Gold, Poly(B-Amino Ester) Nanoparticles for Small Interfering RNA Delivery. *Nano Letters,* 9**,** 2402-2406.

LEROUEIL, P. R., BERRY, S. A., DUTHIE, K., HAN, G., ROTELLO, V. M., MCNERNY, D. Q., BAKER, J. R., ORR, B. G. & BANASZAK HOLL, M. M. 2008. Wide Varieties of Cationic Nanoparticles Induce Defects in Supported Lipid Bilayers. *Nano Letters,* 8**,** 420-424.

LESNIAK, A., SALVATI, A., SANTOS-MARTINEZ, M. J., RADOMSKI, M. W., DAWSON, K. A. & ÅBERG, C. 2013. Nanoparticle Adhesion to the Cell Membrane and Its Effect on Nanoparticle Uptake Efficiency. *Journal of the American Chemical Society,* 135**,** 1438-1444.

LI, D. & HANEDA, H. 2003. Morphologies of Zinc Oxide Particles and Their Effects on Photocatalysis. *Chemosphere,* 51**,** 129-137.

LI, J.-M., WANG, Y.-Y., ZHAO, M.-X., TAN, C.-P., LI, Y.-Q., LE, X.-Y., JI, L.-N. & MAO, Z.-W. 2012a. Multifunctional Qd-Based Co-Delivery of siRNA and Doxorubicin to Hela Cells for Reversal of Multidrug Resistance and Real-Time Tracking. *Biomaterials,* 33**,** 2780-2790.

LI, J., YANG, Y. & HUANG, L. 2012b. Calcium Phosphate Nanoparticles with an Asymmetric Lipid Bilayer Coating for siRNA Delivery to the Tumor. *Journal of Controlled Release,* 158**,** 108-114.

LI, X., XIE, Q. R., ZHANG, J., XIA, W. & GU, H. 2011. The Packaging of siRNA within the Mesoporous Structure of Silica Nanoparticles. *Biomaterials,* 32**,** 9546-9556.

LIANG, X.-J., CHEN, C., ZHAO, Y. & WANG, P. C. 2010. Circumventing Tumor Resistance to Chemotherapy by Nanotechnology. *Methods in molecular biology (Clifton, N.J.),* 596**,** 467-488.

LIN, Y.-S. & HAYNES, C. L. 2009. Synthesis and Characterization of Biocompatible and Size-Tunable Multifunctional Porous Silica Nanoparticles. *Chemistry of Materials,* 21**,** 3979-3986.

LIN, Y.-S. & HAYNES, C. L. 2010. Impacts of Mesoporous Silica Nanoparticle Size, Pore Ordering, and Pore Integrity on Hemolytic Activity. *Journal of the American Chemical Society,* 132**,** 4834-4842.

LIONG, M., LU, J., KOVOCHICH, M., XIA, T., RUEHM, S. G., NEL, A. E., TAMANOI, F. & ZINK, J. I. 2008. Multifunctional Inorganic Nanoparticles for Imaging, Targeting, and Drug Delivery. *Acs Nano,* 2**,** 889-896.

LIOTTA, L. A., STEEG, P. S. & STETLER-STEVENSON, W. G. 1991. Cancer Metastasis and Angiogenesis: An Imbalance of Positive and Negative Regulation. *Cell,* 64**,** 327-336.

LIU, Z., WINTERS, M., HOLODNIY, M. & DAI, H. 2007. siRNA Delivery into Human T Cells and Primary Cells with Carbon-Nanotube Transporters. *Angewandte Chemie - International Edition,* 46**,** 2023-2027.

LOPEZ-LAZARO, M. 2008. The Warburg Effect: Why and How Do Cancer Cells Activate Glycolysis in the Presence of Oxygen? *Anticancer Agents Med Chem,* 8**,** 305-12.

LOWE, S. W., CEPERO, E. & EVAN, G. 2004. Intrinsic Tumour Suppression. *Nature,* 432**,** 307-315.

LU, F., WU, S. H., HUNG, Y. & MOU, C. Y. 2009. Size Effect on Cell Uptake in Well-Suspended, Uniform Mesoporous Silica Nanoparticles. *Small,* 5**,** 1408-13.

LU, J., LIONG, M., LI, Z., ZINK, J. I. & TAMANOI, F. 2010. Biocompatibility, Biodistribution, and Drug-Delivery Efficiency of Mesoporous Silica Nanoparticles for Cancer Therapy in Animals. *Small,* 6**,** 1794-1805.

LU, J., LIONG, M., ZINK, J. I. & TAMANOI, F. 2007. Mesoporous Silica Nanoparticles as a Delivery System for Hydrophobic Anticancer Drugs. *Small,* 3**,** 1341-1346.

LUCCI, M. A., ORLANDI, R., TRIULZI, T., TAGLIABUE, E., BALSARI, A. & VILLA-MORUZZI, E. 2010. Expression Profile of Tyrosine Phosphatases in Her2 Breast Cancer Cells and Tumors. *Cell Oncol,* 32**,** 361-72.

LÜDERITZ, L. 2012. *An Afm Study of the Interactions between Colloidal Particles (Eine Afm-Untersuchung Der Wechselwirkungen Zwischen Kolloidteilchen).*

LUO, H., YANG, Y., DUAN, J., WU, P., JIANG, Q. & XU, C. 2013. Pten-Regulated Akt/Foxo3a/Bim Signaling Contributes to Reactive Oxygen Species-Mediated Apoptosis in Selenite-Treated Colorectal Cancer Cells. *Cell Death Dis,* 4**,** e481.

LUXCEL. 2015. *Mitoxpress™ Xtra Oxygen Consumption Assay (Hs Method)* [Online]. Available: http://luxcel.com/wp-content/uploads/2015/07/LUXCEL-MITOXPRESS-XTRA-BOOKLET-2015.pdf.

MAEDA, H., NOGUCHI, Y., SATO, K. & AKAIKE, T. 1994. Enhanced Vascular Permeability in Solid Tumor Is Mediated by Nitric Oxide and Inhibited by Both New Nitric Oxide Scavenger and Nitric Oxide Synthase Inhibitor. *Japanese Journal of Cancer Research,* 85**,** 331-334.

MAHAJAN, K. & MAHAJAN, N. P. 2012. PI3K-Independent Akt Activation in Cancers: A Treasure Trove for Novel Therapeutics. *Journal of Cellular Physiology,* 227**,** 3178-3184.

MALAIYANDI, L. M., HONICK, A. S., RINTOUL, G. L., WANG, Q. J. & REYNOLDS, I. J. 2005. Zn2+ Inhibits Mitochondrial Movement in Neurons by Phosphatidylinositol 3-Kinase Activation. *The Journal of Neuroscience,* 25**,** 9507-9514.

MALEK, A., CZUBAYKO, F. & AIGNER, A. 2008. Peg Grafting of Polyethylenimine (Pei) Exerts Different Effects on DNA Transfection and siRNA-Induced Gene Targeting Efficacy. *J Drug Target,* 16**,** 124-39.

MAMAEVA, V., ROSENHOLM, J. M., BATE-EYA, L. T., BERGMAN, L., PEUHU, E., DUCHANOY, A., FORTELIUS, L. E., LANDOR, S., TOIVOLA, D. M., LINDEN, M. & SAHLGREN, C. 2011a. Mesoporous Silica Nanoparticles as Drug Delivery Systems for Targeted Inhibition of Notch Signaling in Cancer. *Mol Ther,* 19**,** 1538-1546.

MAMAEVA, V., ROSENHOLM, J. M., BATE-EYA, L. T., BERGMAN, L., PEUHU, E., DUCHANOY, A., FORTELIUS, L. E., LANDOR, S., TOIVOLA, D. M., LINDÉN, M. & SAHLGREN, C. 2011b. Mesoporous Silica Nanoparticles as Drug Delivery Systems for Targeted Inhibition of Notch Signaling in Cancer. *Molecular Therapy,* 19**,** 1538-1546.

MANOHARAN, M. 2004. RNA Interference and Chemically Modified Small Interfering Rnas. *Curr Opin Chem Biol,* 8**,** 570-9.

MARSHALL, W. L. & CHEN, C.-T. A. 1982. Amorphous Silica Solubilities V. Predictions of Solubility Behavior in Aqueous Mixed Electrolyte Solutions to 300°C. *Geochimica et Cosmochimica Acta,* 46**,** 289-291.

MATSUMURA, Y. & MAEDA, H. 1986. A New Concept for Macromolecular Therapeutics in Cancer Chemotherapy: Mechanism of Tumoritropic Accumulation of Proteins and the Antitumor Agent Smancs. *Cancer Res,* 46**,** 6387-92.

MEDAROVA, Z., PHAM, W., FARRAR, C., PETKOVA, V. & MOORE, A. 2007. In Vivo Imaging of siRNA Delivery and Silencing in Tumors. *Nature Medicine,* 13**,** 372-377.

MENG, H., MAI, W. X., ZHANG, H., XUE, M., XIA, T., LIN, S., WANG, X., ZHAO, Y., JI, Z., ZINK, J. I. & NEL, A. E. 2013. Codelivery of an Optimal Drug/siRNA Combination Using Mesoporous Silica Nanoparticles to Overcome Drug Resistance in Breast Cancer in Vitro and in Vivo. *ACS Nano,* 7**,** 994-1005.

MILLER, A. B., HOOGSTRATEN, B., STAQUET, M. & WINKLER, A. 1981. Reporting Results of Cancer-Treatment. *Cancer,* 47**,** 207-214.

MITTAL, V. 2011. *Carbon Nanotubes Surface Modifications: An Overview* Wiley-VCH Verlag GmbH & Co. KGaA.

MOHANRAJ, V. J. & CHEN, Y. 2006. Nanoparticles - a Review. *Tropical Journal of Pharmaceutical Research,* 5**,** 561-573.

MOON, D.-S. & LEE, J.-K. 2012. Tunable Synthesis of Hierarchical Mesoporous Silica Nanoparticles with Radial Wrinkle Structure. *Langmuir,* 28**,** 12341-12347.

MOSQUEIRA, V. C. F., LEGRAND, P., GULIK, A., BOURDON, O., GREF, R., LABARRE, D. & BARRATT, G. 2001. Relationship between Complement Activation, Cellular Uptake and Surface Physicochemical Aspects of Novel Peg-Modified Nanocapsules. *Biomaterials,* 22**,** 2967-2979.

MURPHY, S. L., XU, J. & KOCHANEK, K. D. 2013. Deaths: Final Data for 2010. *National vital statistics reports : from the Centers for Disease Control and Prevention, National Center for Health Statistics, National Vital Statistics System,* 61**,** 1-117.

NAKAE, J., KITAMURA, T., SILVER, D. L. & ACCILI, D. 2001. The Forkhead Transcription Factor Foxo1 (Fkhr) Confers Insulin Sensitivity onto Glucose-6-Phosphatase Expression. *The Journal of Clinical Investigation,* 108**,** 1359-1367.

NANDIYANTO, A. B. D., KIM, S.-G., ISKANDAR, F. & OKUYAMA, K. 2009. Synthesis of Spherical Mesoporous Silica Nanoparticles with Nanometer-Size Controllable Pores and Outer Diameters. *Microporous and Mesoporous Materials,* 120**,** 447-453.

NAVRATILOVA, J., HANKEOVA, T., BENES, P. & SMARDA, J. 2013. Low-Glucose Conditions of Tumor Microenvironment Enhance Cytotoxicity of Tetrathiomolybdate to Neuroblastoma Cells. *Nutr Cancer,* 65**,** 702-10.

NEUN, B. W. & DOBROVOLSKAIA, M. A. 2011. Qualitative Analysis of Total Complement Activation by Nanoparticles. *Methods Mol Biol,* 697**,** 237-45.

NEWMAN, P., MINETT, A., ELLIS-BEHNKE, R. & ZREIQAT, H. 2013. Carbon Nanotubes: Their Potential and Pitfalls for Bone Tissue Regeneration and Engineering. *Nanomedicine: Nanotechnology, Biology and Medicine,* 9**,** 1139-1158.

NHS 2015. Radiotherapy - Side Effects.

OBERDORSTER, G., MAYNARD, A., DONALDSON, K., CASTRANOVA, V., FITZPATRICK, J., AUSMAN, K., CARTER, J., KARN, B., KREYLING, W., LAI, D., OLIN, S., MONTEIRO-RIVIERE, N., WARHEIT, D., YANG, H. & GROUP, I. R. F. R. S. I. N. T. S. W. 2005. Principles for Characterizing the Potential Human Health Effects from Exposure to Nanomaterials: Elements of a Screening Strategy. *Part Fibre Toxicol,* 2**,** 8.

OLIN, M. R., ANDERSEN, B. M., LITTERMAN, A. J., GROGAN, P. T., SARVER, A. L., ROBERTSON, P. T., LIANG, X., CHEN, W., PARNEY, I. F., HUNT, M. A., BLAZAR, B. R. & OHLFEST, J. R. 2011. Oxygen Is a Master Regulator of the Immunogenicity of Primary Human Glioma Cells. *Cancer Research,* 71**,** 6583-6589.

OLIVEIRA, S., STORM, G. & SCHIFFELERS, R. M. 2006. Targeted Delivery of siRNA. *J Biomed Biotechnol,* 2006**,** 63675.

ONOZUKA, H., TSUCHIHARA, K. & ESUMI, H. 2011. Hypoglycemic/Hypoxic Condition in Vitro Mimicking the Tumor Microenvironment Markedly Reduced the Efficacy of Anticancer Drugs. *Cancer Science,* 102**,** 975-982.

OSORIO, J. 2012. Metabolism: An Akt-Independent Pathway for Regulation of Gluconeogenesis. *Nat Rev Endocrinol,* 8**,** 257-257.

OVERHOFF, M. & SCZAKIEL, G. 2005. *Phosphorothioate-Stimulated Uptake of Short Interfering RNA by Human Cells*.

OZBEN, T. 2007. Oxidative Stress and Apoptosis: Impact on Cancer Therapy. *Journal of Pharmaceutical Sciences,* 96**,** 2181-2196.

OZIN, G. A., ARSENAULT, A. C. & ROYAL SOCIETY OF, C. 2005. *Nanochemistry: A Chemical Approach to Nanomaterials*, Royal Society of Chemistry.

OZPOLAT, B., SOOD, A. K. & LOPEZ-BERESTEIN, G. 2009. Nanomedicine Based Approaches for the Delivery of siRNA in Cancer. *Journal of Internal Medicine,* 267**,** 44-53.

PACK, D. W., HOFFMAN, A. S., PUN, S. & STAYTON, P. S. 2005. Design and Development of Polymers for Gene Delivery. *Nat Rev Drug Discov,* 4**,** 581-593.

PARK, I. Y., KIM, I. Y., YOO, M. K., CHOI, Y. J., CHO, M.-H. & CHO, C. S. 2008a. Mannosylated Polyethylenimine Coupled Mesoporous Silica Nanoparticles for Receptor-Mediated Gene Delivery. *International Journal of Pharmaceutics,* 359**,** 280-287.

PARK, J.-H., VON MALTZAHN, G., ZHANG, L., SCHWARTZ, M. P., RUOSLAHTI, E., BHATIA, S. N. & SAILOR, M. J. 2008b. Magnetic Iron Oxide Nanoworms for Tumor Targeting and Imaging. *Advanced Materials,* 20**,** 1630-1635.

PATEL, H., TSCHEKA, C. & HEERKLOTZ, H. 2009. Characterizing Vesicle Leakage by Fluorescence Lifetime Measurements. *Soft Matter,* 5**,** 2849-2851.

PATEL, M., PELLETIER, A. & CÔTÉ, J.-F. 2011. Opening up on Elmo Regulation: New Insights into the Control of Rac Signaling by the Dock180/Elmo Complex. *Small GTPases,* 2**,** 268-275.
PEARSON, R. T., WARREN, N. J., LEWIS, A. L., ARMES, S. P. & BATTAGLIA, G. 2013. Effect of Ph and Temperature on Pmpcâ€"Pdpa Copolymer Self-Assembly. *Macromolecules,* 46**,** 1400-1407.
PFEIFFER, T., SCHUSTER, S. & BONHOEFFER, S. 2001. Cooperation and Competition in the Evolution of Atp-Producing Pathways. *Science,* 292**,** 504-7.
PHYSICAL CHEMISTRY DIVISION COMMISSION ON COLLOID, SURFACE CHEMISTRY INCLUDING CATALYSIS, MCCUSKER, L. B., LIEBAU, F. & ENGELHARDT, G. 2003. Nomenclature of Structural and Compositional Characteristics of Ordered Microporous and Mesoporous Materials with Inorganic Hosts: (Iupac Recommendations 2001). *Microporous and Mesoporous Materials,* 58**,** 3-13.
QUARESMA, M., COLEMAN, M. P. & RACHET, B. 2015. 40-Year Trends in an Index of Survival for All Cancers Combined and Survival Adjusted for Age and Sex for Each Cancer in England and Wales, 1971-2011: A Population-Based Study. *Lancet,* 385**,** 1206-18.
RAGELLE, H., VANDERMEULEN, G. & PREAT, V. 2013. Chitosan-Based siRNA Delivery Systems. *J Control Release,* 172**,** 207-18.
RAMPAZZO, E., VOLTAN, R., PETRIZZA, L., ZACCHERONI, N., PRODI, L., CASCIANO, F., ZAULI, G. & SECCHIERO, P. 2013. Proper Design of Silica Nanoparticles Combines High Brightness, Lack of Cytotoxicity and Efficient Cell Endocytosis. *Nanoscale,* 5**,** 7897-905.
RAO, K. S., EL-HAMI, K., KODAKI, T., MATSUSHIGE, K. & MAKINO, K. 2005. A Novel Method for Synthesis of Silica Nanoparticles. *Journal of Colloid and Interface Science,* 289**,** 125-131.
RAPA, E. 2008. *Characterisation of the Differences in Gene Expression between Rhabdomyosarcoma Cells and Myoblasts.* Doctor of Philosophy, University of Oxford.
RAPA, E., HILL, S., MORTEN, K., POTTER, M. & MITCHELL, C. 2012. The over-Expression of Cell Migratory Genes in Alveolar Rhabdomyosarcoma Could Contribute to Metastatic Spread. *Clinical and Experimental Metastasis***,** 1-11.
RASMUSSEN, J. W., MARTINEZ, E., LOUKA, P. & WINGETT, D. G. 2010. Zinc Oxide Nanoparticles for Selective Destruction of Tumor Cells and Potential for Drug Delivery Applications. *Expert opinion on drug delivery,* 7**,** 1063-1077.
RAVAL, A., PARIKH, J. & ENGINEER, C. 2010. Mechanism of Controlled Release Kinetics from Medical Devices. *Brazilian Journal of Chemical Engineering,* 27**,** 211-225.
REN, Y., KANG, C. S., YUAN, X. B., ZHOU, X., XU, P., HAN, L., WANG, G. X., JIA, Z., ZHONG, Y., YU, S., SHENG, J. & PU, P. Y. 2010. Co-Delivery of as-Mir-21 and 5-Fu by Poly(Amidoamine) Dendrimer Attenuates Human Glioma Cell Growth in Vitro. *J Biomater Sci Polym Ed,* 21**,** 303-14.
ROBERTS, J. C., BHALGAT, M. K. & ZERA, R. T. 1996. Preliminary Biological Evaluation of Polyamidoamine (Pamam) Starburst Dendrimers. *J Biomed Mater Res,* 30**,** 53-65.
ROCHE. *Transfection Success Factors* [Online].
ROSENHOLM, J. M., SAHLGREN, C. & LINDEN, M. 2010. Towards Multifunctional, Targeted Drug Delivery Systems Using Mesoporous Silica Nanoparticles--Opportunities & Challenges. *Nanoscale,* 2**,** 1870-83.
ROSENHOLM, J. M., SAHLGREN, C. & LINDEN, M. 2011. Multifunctional Mesoporous Silica Nanoparticles for Combined Therapeutic, Diagnostic and Targeted Action in Cancer Treatment. *Curr Drug Targets,* 12**,** 1166-86.
SAAD, M., GARBUZENKO, O. B. & MINKO, T. 2008. Co-Delivery of siRNA and an Anticancer Drug for Treatment of Multidrug-Resistant Cancer. *Nanomedicine (Lond),* 3**,** 761-76.
SAHA, S., MALIK, M. M. & QURESHI, M. S. 2014. Comparative Study of Synergistic Effects of Antibiotics with Triangular Shaped Silver Nanoparticles, Synthesized Using Uv-Light Irradia-

tion, on ≪I≫Staphylococcus Aureus≪/I≫ and ≪I≫Pseudomonas Aeruginosa≪/I&Gt. *Journal of Biomaterials and Nanobiotechnology,* 05**,** 186-193.
SAI, J., RAMAN, D., LIU, Y., WIKSWO, J. & RICHMOND, A. 2008. Parallel Phosphatidylinositol 3-Kinase (PI3K)-Dependent and Src-Dependent Pathways Lead to Cxcl8-Mediated Rac2 Activation and Chemotaxis. *Journal of Biological Chemistry,* 283**,** 26538-26547.
SANTY, L. C., RAVICHANDRAN, K. S. & CASANOVA, J. E. 2005. The Dock180/Elmo Complex Couples Arno-Mediated Arf6 Activation to the Downstream Activation of Rac1. *Current Biology,* 15**,** 1749-1754.
SCHACHTER, D. 2013. *The Source of Toxicity in Ctab and Ctab-Stabilized Gold Nanorods.*
SCHWAB, A. J. & PANG, K. S. 2000. The Multiple Indicator Dilution Method and Its Utility in Risk Assessment. *Environmental Health Perspectives,* 108**,** 861-872.
SENGER, D. R., GALLI, S. J., DVORAK, A. M., PERRUZZI, C. A., HARVEY, V. S. & DVORAK, H. F. 1983. Tumor Cells Secrete a Vascular Permeability Factor That Promotes Accumulation of Ascites Fluid. *Science,* 219**,** 983-985.
SHANKAR, A., MITTAL, J. & JAGOTA, A. 2014. Binding between DNA and Carbon Nanotubes Strongly Depends Upon Sequence and Chirality. *Langmuir,* 30**,** 3176-3183.
SHEN, J., HE, Q., GAO, Y., SHI, J. & LI, Y. 2011. Mesoporous Silica Nanoparticles Loading Doxorubicin Reverse Multidrug Resistance: Performance and Mechanism. *Nanoscale,* 3**,** 4314-22.
SHERRILL, M. S. 1936. The Contributions of Arthur A. Noyes to Science. *Science,* 84**,** 217-220.
SIGMA-ALDRICH. Available: http://www.sigmaaldrich.com/life-science/functional-genomics-and-rnai/sirna/learning-center/mission-sup-reg0/experimental-design0.html#s12.
SILVER, I. & ERECINSKA, M. 1994. Extracellular Glucose Concentration in Mammalian Brain: Continuous Monitoring of Changes During Increased Neuronal Activity and Upon Limitation in Oxygen Supply in Normo-, Hypo-, and Hyperglycemic Animals. *The Journal of Neuroscience,* 14**,** 5068-5076.
SKINNER, S. A., TUTTON, P. J. M. & O'BRIEN, P. E. 1990. Microvascular Architecture of Experimental Colon Tumors in the Rat. *Cancer Research,* 50**,** 2411-2417.
SLOWING, II, VIVERO-ESCOTO, J. L., WU, C. W. & LIN, V. S. 2008. Mesoporous Silica Nanoparticles as Controlled Release Drug Delivery and Gene Transfection Carriers. *Adv Drug Deliv Rev,* 60**,** 1278-88.
SONG, G., OUYANG, G. & BAO, S. 2005. The Activation of Akt/Pkb Signaling Pathway and Cell Survival. *Journal of Cellular and Molecular Medicine,* 9**,** 59-71.
SPENCE, R. A. J. & JOHNSTON, P. G. 2001. *Oncology*, Oxford University Press.
SPONCHIA, G., MARIN, R., FRERIS, I., MARCHIORI, M., MORETTI, E., STORARO, L., CANTON, P., LAUSI, A., BENEDETTI, A. & RIELLO, P. 2014. Mesoporous Silica Nanoparticles with Tunable Pore Size for Tailored Gold Nanoparticles. *Journal of Nanoparticle Research,* 16.
STANEVA, D., BOSCH, P. & GRABCHEV, I. 2012. Ultrasonic Synthesis and Spectral Characterization of a New Blue Fluorescent Dendrimer as Highly Selective Chemosensor for Fe 3+ Cations. *Journal of Molecular Structure,* 1015**,** 1-5.
STEVENSON, C., DE LA ROSA, G., ANDERSON, C. S., MURPHY, P. S., CAPECE, T., KIM, M. & ELLIOTT, M. R. 2014. Essential Role of Elmo1 in Dock2-Dependent Lymphocyte Migration. *J Immunol,* 192**,** 6062-70.
STEWART, B. W. & WILD, C. P. 2014. *World Cancer Report 2014,* Lyon, IARC Press.
STEWART, D. J. 2010. Tumor and Host Factors That May Limit Efficacy of Chemotherapy in Non-Small Cell and Small Cell Lung Cancer. *Critical reviews in oncology/hematology,* 75**,** 173-234.
SU, J. D., MAYO, L. D., DONNER, D. B. & DURDEN, D. L. 2003. Pten and Phosphatidylinositol 3'-Kinase Inhibitors up-Regulate P53 and Block Tumor-Induced Angiogenesis: Evidence for an Effect on the Tumor and Endothelial Compartment. *Cancer Res,* 63**,** 3585-92.

SUTEEWONG, T., SAI, H., LEE, J., BRADBURY, M., HYEON, T., GRUNER, S. M. & WIESNER, U. 2010. Ordered Mesoporous Silica Nanoparticles with and without Embedded Iron Oxide Nanoparticles: Structure Evolution During Synthesis. *Journal of Materials Chemistry,* 20**,** 7807.

TAO, C., ZHU, Y., XU, Y., ZHU, M., MORITA, H. & HANAGATA, N. 2014. Mesoporous Silica Nanoparticles for Enhancing the Delivery Efficiency of Immunostimulatory DNA Drugs. *Dalton Transactions,* 43**,** 5142-5150.

TARN, D., ASHLEY, C. E., XUE, M., CARNES, E. C., ZINK, J. I. & BRINKER, C. J. 2013. Mesoporous Silica Nanoparticle Nanocarriers: Biofunctionality and Biocompatibility. *Accounts of Chemical Research,* 46**,** 792-801.

THAKOR, A. S. & GAMBHIR, S. S. 2013. Nanooncology: The Future of Cancer Diagnosis and Therapy. *CA: A Cancer Journal for Clinicians,* 63**,** 395-418.

THERMOFISHER. *Low Transfection Efficiency and Low Cell Viability Are the Most Frequent Causes of Unsuccessful Gene Silencing Experiments* [Online]. Available: http://www.thermofisher.com/uk/en/home/references/ambion-tech-support/rnai-sirna/tech-notes/optimizing-sirna-transfection-for-rnai.html.

THOMAS, M. & KLIBANOV, A. M. 2002. Enhancing Polyethylenimine's Delivery of Plasmid DNA into Mammalian Cells. *Proceedings of the National Academy of Sciences of the United States of America,* 99**,** 14640-14645.

TÓTH, J., BERGER, F. & DÉKÁNY, I. 1999. Calculation of the Bet Compatible Surface Area from Any Type I Isotherms Measured Below the Critical Temperature. *Journal of Colloid and Interface Science,* 212**,** 402-410.

TREWYN, B. G., NIEWEG, J. A., ZHAO, Y. & LIN, V. S. Y. 2008. Biocompatible Mesoporous Silica Nanoparticles with Different Morphologies for Animal Cell Membrane, Penetration. *Chemical Engineering Journal,* 137**,** 23-29.

TSOURIS, V., JOO, M. K., KIM, S. H., KWON, I. C. & WON, Y.-Y. 2014. Nano Carriers That Enable Co-Delivery of Chemotherapy and Rnai Agents for Treatment of Drug-Resistant Cancers. *Biotechnology Advances,* 32**,** 1037-1050.

URATA, C., YAMAUCHI, Y., AOYAMA, Y., IMASU, J., TODOROKI, S., SAKKA, Y., INOUE, S. & KURODA, K. 2008. Fabrication of Hierarchically Porous Spherical Particles by Assembling Mesoporous Silica Nanoparticles Via Spray Drying. *J Nanosci Nanotechnol,* 8**,** 3101-5.

VALLET-REGI, M., RÁMILA, A., DEL REAL, R. P. & PÉREZ-PARIENTE, J. 2001. A New Property of Mcm-41: Drug Delivery System. *Chemistry of Materials,* 13**,** 308-311.

VAN ETTEN, E. W. M., TEN KATE, M. T., SNIJDERS, S. V. & BAKKER-WOUDENBERG, I. A. J. M. 1998. Administration of Liposomal Agents and Blood Clearance Capacity of the Mononuclear Phagocyte System. *Antimicrobial Agents and Chemotherapy,* 42**,** 1677-1681.

VERMA, A., UZUN, O., HU, Y., HU, Y., HAN, H. S., WATSON, N., CHEN, S., IRVINE, D. J. & STELLACCI, F. 2008. Surface-Structure-Regulated Cell-Membrane Penetration by Monolayer-Protected Nanoparticles. *Nat Mater,* 7**,** 588-95.

VESELY, E. & MICHIGAN, U. O. 2009. *Glut1 Induced Cflip Expression Promotes Proliferation and Prevents Apoptosis in Vsmcs*, University of Michigan.

VIVERO-ESCOTO, J. L., SLOWING, I. I., TREWYN, B. G. & LIN, V. S. Y. 2010. Mesoporous Silica Nanoparticles for Intracellular Controlled Drug Delivery. *Small,* 6**,** 1952-1967.

VONARBOURG, A., PASSIRANI, C., SAULNIER, P. & BENOIT, J.-P. 2006. Parameters Influencing the Stealthiness of Colloidal Drug Delivery Systems. *Biomaterials,* 27**,** 4356-4373.

WALKEY, C. D., OLSEN, J. B., GUO, H., EMILI, A. & CHAN, W. C. W. 2012. Nanoparticle Size and Surface Chemistry Determine Serum Protein Adsorption and Macrophage Uptake. *Journal of the American Chemical Society,* 134**,** 2139-2147.

WANG, H., WINGETT, D., ENGELHARD, M. H., FERIS, K., REDDY, K. M., TURNER, P., LAYNE, J., HANLEY, C., BELL, J., TENNE, D., WANG, C. & PUNNOOSE, A. 2009a. Fluorescent Dye En-

capsulated Zno Particles with Cell-Specific Toxicity for Potential Use in Biomedical Applications. *J Mater Sci Mater Med,* 20**,** 11-22.
WANG, H., ZHAO, P., SU, W., WANG, S., LIAO, Z., NIU, R. & CHANG, J. 2010. Plga/Polymeric Liposome for Targeted Drug and Gene Co-Delivery. *Biomaterials,* 31**,** 8741-8.
WANG, J. 2006. *Dock180/Elmo Proteins Are Critical Regulators of Phagocytosis,Macropinocytosis and Chemotaxis in Dictyostelium.* Doctor of Philosophy, University of Dundee.
WANG, L. Y., YAN, R. X., HAO, Z. Y., WANG, L., ZENG, J. H., BAO, H., WANG, X., PENG, Q. & LI, Y. D. 2005. Fluorescence Resonant Energy Transfer Biosensor Based on Upconversion-Luminescent Nanoparticles. *Angewandte Chemie-International Edition,* 44**,** 6054-6057.
WANG, X., LI, Q., XIE, J., JIN, Z., WANG, J., LI, Y., JIANG, K. & FAN, S. 2009b. Fabrication of Ultralong and Electrically Uniform Single-Walled Carbon Nanotubes on Clean Substrates. *Nano Letters,* 9**,** 3137-3141.
WARBURG, O. 1956. Origin of Cancer Cells. *Science,* 123**,** 309-314.
WARBURG, O., WIND, F. & NEGELEIN, E. 1927. The Metabolism of Tumors in the Body. *J Gen Physiol,* 8**,** 519-30.
WARIS, G. & AHSAN, H. 2006. *Reactive Oxygen Species: Role in the Development of Cancer and Various Chronic Conditions*.
WEIDNER, N., SEMPLE, J. P., WELCH, W. R. & FOLKMAN, J. 1991. Tumor Angiogenesis and Metastasis - Correlation in Invasive Breast-Carcinoma. *New England Journal of Medicine,* 324**,** 1-8.
WEINBERG, F., HAMANAKA, R., WHEATON, W. W., WEINBERG, S., JOSEPH, J., LOPEZ, M., KALYANARAMAN, B., MUTLU, G. M., BUDINGER, G. R. S. & CHANDEL, N. S. 2010. Mitochondrial Metabolism and Ros Generation Are Essential for Kras-Mediated Tumorigenicity. *Proceedings of the National Academy of Sciences,* 107**,** 8788-8793.
WEINBERG, R. A. 2007. *The Biology of Cancer*, Garland Science.
WHITEHEAD, K. A., LANGER, R. & ANDERSON, D. G. 2009. Knocking Down Barriers: Advances in siRNA Delivery. *Nat Rev Drug Discov,* 8**,** 129-138.
WIN, K. Y. & FENG, S. S. 2005. Effects of Particle Size and Surface Coating on Cellular Uptake of Polymeric Nanoparticles for Oral Delivery of Anticancer Drugs. *Biomaterials,* 26**,** 2713-22.
WU, L. P., FICKER, M., CHRISTENSEN, J. B., TROHOPOULOS, P. N. & MOGHIMI, S. M. 2015. Dendrimers in Medicine: Therapeutic Concepts and Pharmaceutical Challenges. *Bioconjug Chem,* 26**,** 1198-211.
WU, W., HODGES, E., REDELIUS, J. & HÖÖG, C. 2004. A Novel Approach for Evaluating the Efficiency of Sirnas on Protein Levels in Cultured Cells. *Nucleic Acids Research,* 32**,** e17.
WYSOCZYNSKI, M., SHIN, D.-M., KUCIA, M. & RATAJCZAK, M. Z. 2010. Selective Upregulation of Interleukin-8 by Human Rhabdomyosarcomas in Response to Hypoxia: Therapeutic Implications. *International Journal of Cancer,* 126**,** 371-381.
XIAO, Y., JASKULA-SZTUL, R., JAVADI, A., XU, W., EIDE, J., DAMMALAPATI, A., KUNNIMALAIYAAN, M., CHEN, H. & GONG, S. 2012. Co-Delivery of Doxorubicin and siRNA Using Octreotide-Conjugated Gold Nanorods for Targeted Neuroendocrine Cancer Therapy. *Nanoscale,* 4**,** 7185-7193.
XIONG, X. B. & LAVASANIFAR, A. 2011. Traceable Multifunctional Micellar Nanocarriers for Cancer-Targeted Co-Delivery of Mdr-1 siRNA and Doxorubicin. *Acs Nano,* 5**,** 5202-13.
XU, L., ZHANG, H. & WU, Y. 2014. Dendrimer Advances for the Central Nervous System Delivery of Therapeutics. *ACS Chem Neurosci,* 5**,** 2-13.
YANAGISAWA, T., SHIMIZU, T., KURODA, K. & KATO, C. 1990. The Preparation of Alkyltriinethylaininonium&Ndash;Kaneinite Complexes and Their Conversion to Microporous Materials. *Bulletin of the Chemical Society of Japan,* 63**,** 988-992.

YANG, Y., HUI, L. V., YUQIN, C. H. E., JIE, L. I., SHUAI, H. O. U., TIEZHU, Z. & WEI, W. 2014. Effect of Saw Palmetto Extract on PI3K Cell Signaling Transduction in Human Glioma. *Experimental and Therapeutic Medicine,* 8**,** 563-566.

YASUN, E., LI, C., BARUT, I., JANVIER, D., QIU, L., CUI, C. & TAN, W. 2015. Bsa Modification to Reduce Ctab Induced Nonspecificity and Cytotoxicity of Aptamer-Conjugated Gold Nanorods. *Nanoscale,* 7**,** 10240-8.

YEN, S. K., PADMANABHAN, P. & SELVAN, S. T. 2013. Multifunctional Iron Oxide Nanoparticles for Diagnostics, Therapy and Macromolecule Delivery. *Theranostics,* 3**,** 986-1003.

YILMAZ, M. D., XUE, M., AMBROGIO, M. W., BUYUKCAKIR, O., WU, Y., FRASCONI, M., CHEN, X., NASSAR, M. S., STODDART, J. F. & ZINK, J. I. 2015. Sugar and Ph Dual-Responsive Mesoporous Silica Nanocontainers Based on Competitive Binding Mechanisms. *Nanoscale,* 7**,** 1067-1072.

YOO, J.-W., IRVINE, D. J., DISCHER, D. E. & MITRAGOTRI, S. 2011. Bio-Inspired, Bioengineered and Biomimetic Drug Delivery Carriers. *Nat Rev Drug Discov,* 10**,** 521-535.

ZHANG, H., LI, Z., XU, P., WU, R. & JIAO, Z. 2010. A Facile Two Step Synthesis of Novel Chrysanthemum-Like Mesoporous Silica Nanoparticles for Controlled Pyrene Release. *Chemical Communications,* 46**,** 6783-6785.

ZHANG, H., LI, Z., XU, P., WU, R., WANG, L., XIANG, Y. & JIAO, Z. 2011. Synthesis of Novel Mesoporous Silica Nanoparticles for Loading and Release of Ibuprofen. *J Control Release,* 152 Suppl 1**,** e38-9.

ZHENG, J. I. E. 2012. Energy Metabolism of Cancer: Glycolysis Versus Oxidative Phosphorylation (Review). *Oncology Letters,* 4**,** 1151-1157.

ZU, X. L. & GUPPY, M. 2004. Cancer Metabolism: Facts, Fantasy, and Fiction. *Biochem Biophys Res Commun,* 313**,** 459-65.